



POLITECNICO

MILANO 1863

Politecnico di Milano, Milan, Italy
Department of Aerospace Science and Technology
Doctoral programme in Aerospace Engineering

Engineering ballistic capture for autonomous interplanetary spacecraft with limited onboard resources

PhD dissertation of:
Gianmario Merisio

Supervisor:
Prof. Francesco Topputo

Tutor:
Prof. Sergio Ricci

Coordinator:
Prof. Pierangelo Masarati

Cycle XXXV

Gianmario Merisio: *Engineering ballistic capture for autonomous interplanetary spacecraft with limited onboard resources*

Supervisor:

Prof. Francesco Topputo

Location:

Milano, Italy

*To Arianna,
with whom I set sail into the wide blue yonder,
flying on the back of a magnificent Dragon.*

Copyright © 2023, Gianmario Merisio

All Rights Reserved

Abstract

Current deep-space missions heavily count on ground-based operations. Although reliable, ground slots will saturate soon, so hampering the current momentum in space exploration. EXTREMA is an ERC-funded project enabling self-driving spacecraft, challenging the current paradigm and aiming, among others, at autonomously engineering ballistic capture. This work presents at first a characterization of ballistic capture corridors, time-varying manifolds supporting capture that can be targeted far away from the planet. Then, an autonomous ballistic capture algorithm is discussed. The aim is to devise an algorithm suitable for interplanetary spacecraft with limited control authority and onboard resources. The algorithm is applied to synthesize corridors at Mars. It envisages a novel methodology to construct families of ballistic capture orbits and compute the backbone of capture sets. Families are obtained by solving a sequence of well-posed three-point boundary value problems. The backbone is derived by exploiting a method based on Lagrangian descriptors. The algorithm performance is assessed and its limitations are discussed.

Sommario

Attualmente le missioni interplanetarie fanno pesantemente uso delle operazioni da terra. Sebbene affidabili, gli slot a terra verranno presto saturati, ostacolando l'attuale impulso dell'esplorazione spaziale. EXTREMA è un progetto finanziato dall'ERC che abilita veicoli spaziali a guida autonoma, sfidando il paradigma attuale e mirando, tra le altre cose, ad ingegnerizzare la cattura gravitazionale autonoma. Questo lavoro presenta dapprima una caratterizzazione dei corridoi di cattura gravitazionale, varietà tempo-varianti che supportano la cattura e che possono essere bersagliati lontano dal pianeta. Successivamente, viene discusso l'algoritmo di cattura gravitazionale autonoma. L'obiettivo è quello di concepire un algoritmo adatto a veicoli spaziali interplanetari con autorità di controllo e risorse di bordo limitate. L'algoritmo viene applicato per sintetizzare corridoi di cattura a Marte ed implementa una metodologia innovativa per costruire famiglie di orbite di cattura gravitazionale e calcolare la struttura portante, denominata *backbone*, degli insiemi di cattura. Le famiglie di orbite sono ottenute risolvendo una sequenza di problemi al contorno a tre punti. La *backbone* viene ricavata sfruttando un metodo basato sui descrittori lagrangiani. Le prestazioni dell'algoritmo sono valutate ed i suoi limiti vengono discussi.

Acknowledgments

My heartfelt appreciation to Prof. Francesco Topputo, my supervisor, who advised me in the most ardent, meticulous, and brilliant way. Other than being a sensational mentor who constantly encouraged me to enhance, you passionately inspired me to do research. I am extremely grateful for all the time and effort you devoted to me.

To the staff and colleagues in the Department of Aerospace Science and Technology (DAER) at Politecnico di Milano, thanks for the fruitful discussions fostering my doctoral research, especially Prof. F. Ferrari, Prof. P. Di Lizia, and Prof. M. Massari. I also acknowledge the contribution of Prof. J. J. Masdemont and Dr. E. M. Alessi for reviewing my doctoral dissertation and providing fruitful feedback.

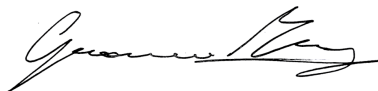
My thanks extend to present and past members of the Deep-space Astrodynamics Research and Technology (DART) Group. Each of you either is or was a very valuable teammate, but above all, I consider you trusted friends. A special thank goes to Mattia, we started this crazy journey together, managed to support each other through difficulties, and shared the pleasure of successes, I sincerely appreciate this. To Dr. V. Franzese, Dr. P. Panicucci, Dr. A. Morselli, and Dr. K. V. Mani, you taught me a lot but Dr. C. Giordano twice as much, I cannot thank you all enough. To Gianfranco, you are my treasured desk mate even if a little too messy. To Carmine, Felice, Andrea, Stefano, Pelayo, Eleonora, Antonio, Alessandra, Claudio, and all the others, thanks for the great time spent together at DART Lab.

To Michele, Marco, Federico, Giovanni, Emanuele, and Alessandro, I was extremely fortunate to meet you during this journey, thanks for your priceless moral and technical support, you are all wonderful friends. To Giacomo, thanks for all the times you cooked appetizing delicacies for the both of us and for all the after-work chats that helped me release the tension accumulated doing research. Thanks also to all the people here not mentioned who covered a role in this experience.

A huge thanks to my dear friends, Emanuele and Sarah, postgraduate life tends to rift old friends apart, but in our case, it has not succeeded yet. A sincere thanks go to Matteo, my companion of adventures, whose precious sharp statements are never frivolous. To all of you, career doesn't leave much room to have a beer together, but we did better.

I would like to thank my entire family, which constantly supported me in all possible forms. I am especially grateful to my brother Luca and my sister Celeste, your fondness was always present. My deepest gratitude to *Mamma* and *Papà* who raised me with unconditional love, I could not have done it without you. *Grazie*.

The utmost appreciation is dedicated to my beloved Arianna. Despite your denying it, you have been an essential element in this spectacular journey. Through your presence and affection, you assisted me during adversities, when I was lost in frustration and struggling to overcome obstacles. Most importantly, your thorough confidence in me fueled the necessary motivation to strive for more sophisticated ambitions and never settle. I treasure all our moments, which sustain me through tough times. I am profoundly beholden to have you by my side.



Gianmario Merisio
Milan, February 2023

Table of contents

Abstract	v
Sommario	vii
Acknowledgments	ix
1 Introduction	1
1.1 Context	1
1.2 EXTREMA	3
1.3 Motivation	5
1.4 Research questions	5
1.5 Dissertation overview	6
1.6 Publications and contribution to the field	7
1.7 Notation and conventions	13
2 Dynamical model	15
2.1 Reference frames	15
2.2 Ephemerides	16
2.3 Equations of motion	16
2.4 Variational equations	19
2.5 Cauchy–Green strain tensor	21
2.6 Poincaré and stroboscopic maps	22
2.7 Material surface	23
2.8 Numerical propagation	23
3 The ballistic capture mechanism	25
3.1 Weak stability boundary	26
3.2 Definition of particle stability	26
3.3 Design of ballistic capture orbits	28
3.4 The role of solar gravity gradient	28
3.5 Effect of physical parameters	30
3.6 Influence of moons and perturbations	31
3.7 GRATIS	35

4	Lagrangian coherent structures	37
4.1	Finite-time Lyapunov exponents	39
4.2	Variational theory for LCSs	40
4.3	Lagrangian descriptors	42
4.4	Application to ballistic capture	44
4.5	LCSs extraction techniques trade-off	45
5	Characterization of ballistic capture corridors	47
5.1	Definitions	47
5.2	Characterization	50
5.3	Results	54
5.4	Final remarks	68
6	Autonomous ballistic capture algorithm	69
6.1	On-ground tasks	69
6.2	Onboard tasks	71
7	Generation of ballistic capture orbit families	75
7.1	Problem statement	75
7.2	Methodology	76
7.3	Results	86
7.4	Final remarks	97
8	Backbone of capture set	99
8.1	Problem statement	99
8.2	Methodology	100
8.3	Results	105
8.4	Final remarks	117
9	Synthesis of ballistic capture corridors	119
9.1	Problem statement	119
9.2	Methodology	119
9.3	Results	122
9.4	Final remarks	125
10	Conclusion	127
10.1	Summary of results	127
10.2	Recommendations for future work	128
A	Verification and validation campaign of GRATIS	131
A.1	V&V of DOPRI8 integration scheme	132
A.2	Integration schemes comparison	140
A.3	RHS V&V against GMAT	143
A.4	Siding Spring comet (C/2013 A1) benchmark	151
A.5	2006 RH ₁₂₀ benchmark	155

A.6	2020 CD ₃ benchmark	160
A.7	V&V of stable sets extraction and manipulation	165
	References	173
	List of figures	i
	List of tables	v
	List of algorithms	vii
	List of acronyms	ix

Introduction

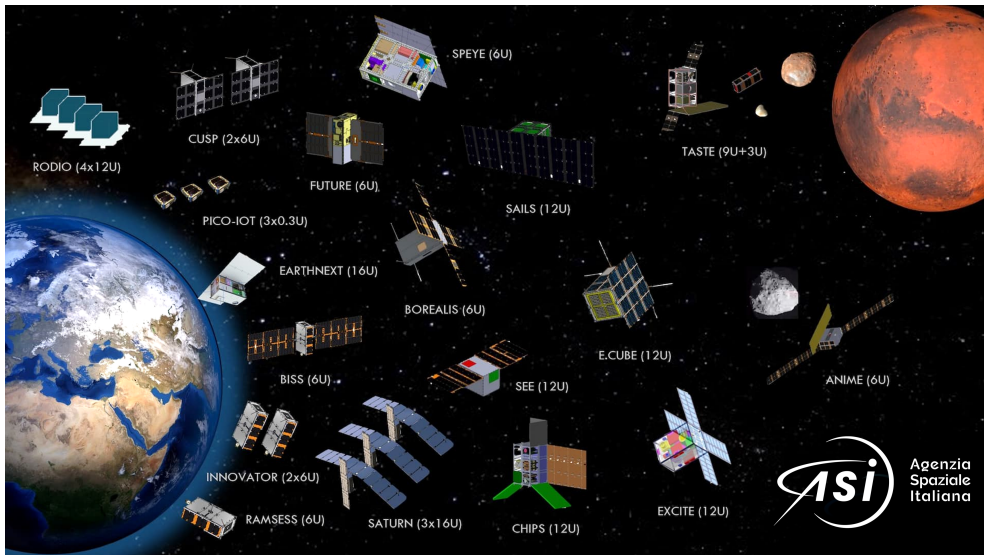
The space sector is experiencing a flourishing growth. The space economy is booming. Integrated, space-based services will soon benefit mankind at unprecedented levels. The momentum characterizing the near-Earth space will soon affect outer space as well. Evidence is mounting that the near future will be characterized by a large amount of deep-space missions [1–4]. In the last decade, CubeSats have granted affordable access to space due to their reduced manufacturing costs compared to traditional missions. At the present-day, most miniaturized spacecraft has thus far been deployed into near-Earth orbits, but soon a multitude of interplanetary CubeSats will be employed for deep-space missions as well [5, 6].

1.1 Context

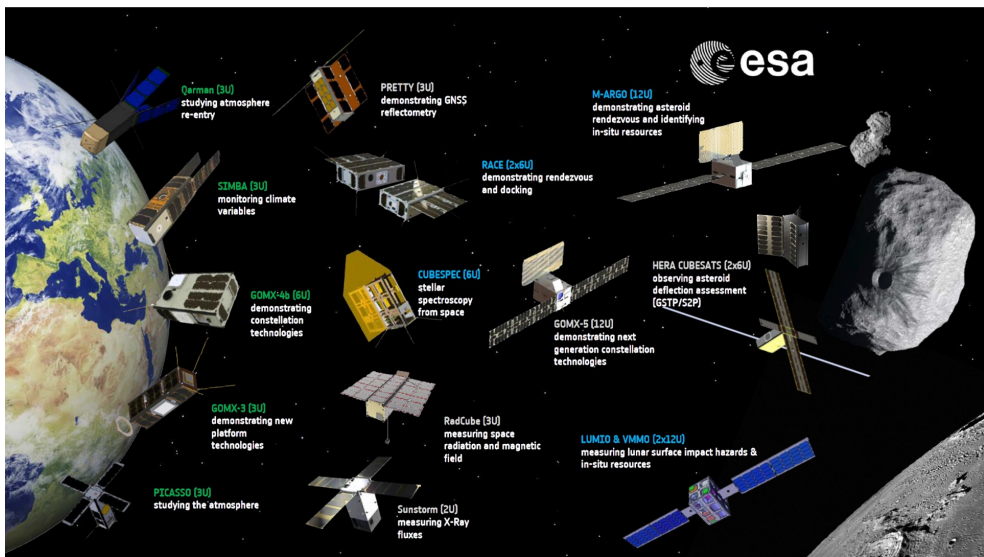
The great amount of nano satellite missions recently launched or currently under study is the most concrete proof of what is expected to be the next CubeSat revolution. The infographic in Figure 1.1a shows the Agenzia Spaziale Italiana (ASI)'s CubeSats fleet funded through the recently launched ALCOR programme¹. On the other hand, the European Space Agency (ESA)'s technology CubeSat fleet funded in General Support Technology Programme (GSTP) Fly Element² is proposed in Figure 1.1b. These are just two, non-exhaustive examples. Other space agencies like the National Aeronautics and Space Administration (NASA) and the Japan Aerospace Exploration Agency (JAXA), and numerous private companies are presently operating or designing miniaturized platforms. Advancement in services to support the thriving small satellite market is ongoing, thereby encouraging formation of CubeSat fleets for the future massive exploration of the inner solar system.

¹<https://www.asi.it/2022/05/lagenzia-spaziale-italiana-investe-sui-nanosatelliti-at-traverso-un-nuovo-programma-di-sviluppo-per-tecnologie-e-missioni-satellitari/> [last accessed Dec 1, 2022].

²https://www.esa.int/Enabling_Support/Space_Engineering_Technology/Shaping_the_Future/About_the_General_Support_Technology_Programme_GSTP [last accessed Dec 1, 2022].



(a) ASI's CubeSat fleet funded through ALCOR programme. *Image credits:* ASI.



(b) ESA's technology CubeSat fleet funded in GSTP Fly Element. *Image credits:* ESA.

Figure 1.1: Non-exhaustive examples of the multitude of miniaturized probes (e. g., CubeSats) that will soon permeate the inner solar system.

Nevertheless, the current paradigm for deep-space missions strongly relies on ground-based operations [7]. Although reliable, this approach will rapidly cause saturation of ground slots, so hampering the current momentum in space exploration. At the actual pace, human-in-the-loop, flight-related operations for deep-space missions will soon become unsustainable.

1.2 EXTREMA

EXTREMA³ (short for *Engineering Extremely Rare Events in Astrodynamics for Deep-Space Missions in Autonomy*) enables self-driving spacecraft. By challenging the current paradigm under which spacecraft are piloted in interplanetary space, EXTREMA addresses the following big research question (RQ) [5, 6, 8]

EXTREMA big research question

To what extent can we navigate the solar system free of human supervision?

Self-driving spacecraft become the main focus: machines capable of traveling in deep space and autonomously reaching their destination. These systems are used to engineer ballistic capture (BC) [9–12], thereby proving the effectiveness of autonomy in a complex scenario. The project has been awarded a European Research Council (ERC) Consolidator Grant in 2019.

Successfully freeing deep-space probes from human supervision will significantly reduce the overall operation costs. The disruptive innovation of EXTREMA is summarized in the following key aspects [5]:

- i) autonomous determination of the spacecraft position is enabled by extracting information from the surrounding environment;
- ii) increased operational risks is facilitated by the rising multitude of miniaturized, low-cost, deep-space probes.
- iii) temporary orbiting about a planet is unlocked by proving the feasibility of BC for systems characterized by low or no control authority.

A comprehensive overview of EXTREMA is given in Figure 1.2. The project is erected on three pillars, each one designed to answer a specific operational research question (ORQ):

- **Pillar 1** is about autonomous navigation, so aiming to develop algorithms and techniques to reconstruct the state of the spacecraft through optical navigation [13–15];
- **Pillar 2** faces autonomous guidance and control, so aiming to develop state-of-the-art trajectory computing algorithms under a closed-loop guidance paradigm, in which a new trajectory is re-computed on board whenever required [16, 17];
- **Pillar 3** is the focus of this dissertation and deals with autonomous ballistic capture (ABC), so aiming to validate algorithms developed in Pillars 1 and 2 in a complex scenario appealing for CubeSats missions.

Three experiments producing intermediate results are foreseen, one within each pillar. They are instrumental for the EXTREMA simulation hub (ESH), an integrated experimental facility to perform dynamical simulations of the spacecraft–environment interaction, so allowing high-fidelity testing of autonomous guidance, navigation, and control (GNC) systems for interplanetary CubeSats.

³<https://dart.polimi.it/extrema-erc/> [last accessed Dec 1, 2022].

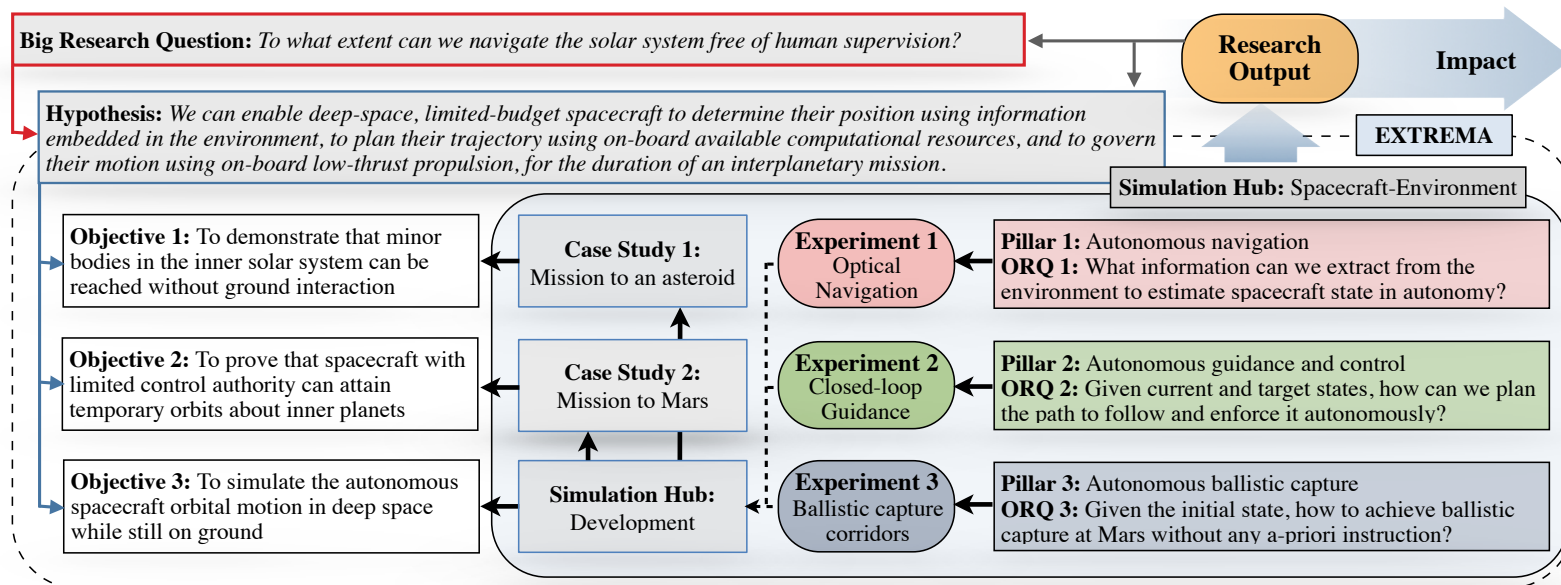


Figure 1.2: Overview of the EXTREMA project objectives and structure. EXTREMA (short for *Engineering Extremely Rare Events in Astrodynamics for Deep-Space Missions in Autonomy*) enables self-driving spacecraft, challenging the current paradigm under which spacecraft are piloted in interplanetary space. *Image credits:* EXTREMA team at DART Group [5].

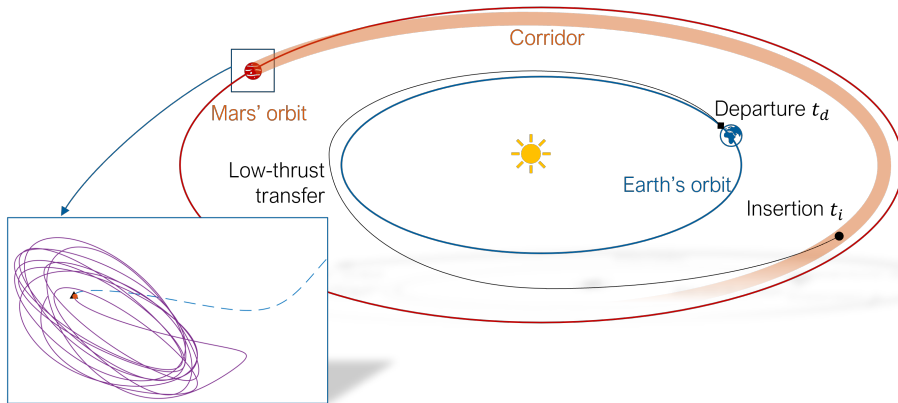


Figure 1.3: Earth–Mars low-thrust transfer culminating in ballistic capture at Mars.

1.3 Motivation

In EXTREMA, BC is used because it is a desirable solution for limited-control platforms, which cannot afford to enter into orbits about a planet due to a lack of significant control authority. The key is to accomplish low-thrust orbits culminating in BC, as shown in Figure 1.3 [10, 12]. Massive numerical simulations are required to find the specific conditions supporting capture. In the method shown in [18], stable sets are computed via grid sampling and propagation. Then, BC orbits with prescribed features are extracted [19]. Millions of initial conditions are integrated and classified according to the orbits they generate. Initial conditions (ICs) granting capture define a capture set, which in turn is used to find ballistic capture corridors (BCCs) [11]: time-varying manifold supporting capture that can be targeted far away from the planet.

To grant spacecraft the capability to manipulate stable sets in order to self-compute a BCC is crucial. Nevertheless, stable sets onboard computation is not an option. Moreover, these sets depend on both capture epoch and osculating eccentricity, so they cannot be computed once for all [18]. Thus, the challenge in EXTREMA Pillar 3 is to develop and validate an algorithm compatible with the onboard resources.

1.4 Research questions

BC mechanism is suited for limited-control platforms, which cannot afford to enter into orbits about a planet because of the lack of proper means. In Pillar 3, the object of study is attaining BC in autonomy. The spacecraft assumed already in deep space has to acquire BC at Mars without relying on any information provided from ground. Mars is chosen without loss of generality due to its relevance in the long-term exploration [5, 6]. This leads to EXTREMA's third ORQ.

Operational research question 3

Given the initial state, how can we achieve ballistic capture at Mars without any a priori instruction?

Starting from the ORQ3, a set of detailed RQs is elaborated to specifically drive the research presented in this dissertation and provide a proper answer to the ORQ3.

Research questions

- i) How can we characterize ballistic capture corridors?
- ii) How to synthesize high-fidelity ballistic capture corridors that are computationally inexpensive for onboard usage?
 - a) How can we generate new ballistic capture orbits on board?
 - b) To what extent can we exploit Lagrangian indicators to extract dynamical insight and build ballistic capture corridors?
 - c) How accurate are ballistic capture corridors constructed on board?

Two research objectives (ROs) related to the RQs are set as well.

Research objectives

- i) Characterize ballistic capture corridors.
- ii) Develop an autonomous ballistic capture algorithm for inexpensive synthesis of high-fidelity ballistic capture corridors.

1.5 Dissertation overview

Chapter 1 introduces the context, the motivation, the research questions, and the objectives of this study. The dynamics, variational equations, and some useful mathematical tools exploited throughout the work are discussed in Chapter 2. Chapters 3 and 4 present the state of the art for the ballistic capture mechanism and Lagrangian coherent structures, respectively. Chapter 4 terminates with a trade-off among extraction techniques. In Chapter 5, ballistic capture corridors are characterized to answer research question i) and achieve the associated research objective. Chapter 6 provides a detailed overview of the autonomous ballistic capture algorithm. In Chapters 7–9, the core methods implemented in the autonomous ballistic capture algorithm are covered, one per chapter. The problem statements associated with each method are established, methodologies are discussed, and results are presented. Eventually, chapters conclude by summarizing the major findings. As a whole, Chapters 6–9 answer research question ii). Final remarks and recommendations for future work are given in Chapter 10.

1.6 Publications and contribution to the field

During the years of my Philosophiæ Doctor (PhD), I had the chance to present my work at several conferences and to publish on peer-reviewed journals. I contributed to several proposals writing. Furthermore, I actively partook in the Phase A study of the Lunar Meteoroid Impacts Observer (LUMIO) lunar CubeSat mission and I am a member of the team currently involved in Phase B. Additionally, I conducted research activity on qualitative analysis of the dynamics in non-autonomous systems for Centre National d'Études Spatiales (CNES).

LUMIO is a 12U CubeSat that will be placed on a halo orbit at Earth–Moon L_2 to observe, quantify, and characterize meteoroid impacts on the lunar farside [20, 21]. LUMIO wants to quantify the luminous energy of meteoroid impacts to the Moon in the equivalent impact kinetic energy range at the Earth from 10^{-6} to 10^{-4} kton TNT Equivalent. Additionally, the mission aims to detect new meteoroid impacts on the Moon in the equivalent kinetic energy range from 10^{-4} to 10^{-1} kton TNT Equivalent [22]. The expected temporal distribution of the detected lunar impact flashes is shown on the left y -axis of Figure 1.4. Figure 1.5 shows the potential scientific contribution of the LUMIO CubeSat compared to data of previous programmes [23]. The comparison shows how LUMIO will detect new impacts in the range at higher energy (green background) and will contribute to refining the knowledge in the lower energetic range (light blue background). Some of the impacts in the high-energy range cannot be successfully detected by the LUMIO-Cam (yellow diamonds in the plot). They saturate both detectors due to their high energy [20].

The research activity funded by CNES and titled “*Généralisation du concept de variétés invariantes at applications à la conception des missions d’exploration de petits corps*” is briefly introduced [24]. The study exploited generalization of invariant manifolds theory to non-autonomous dynamical systems to perform a qualitative analysis of the dynamics around small bodies in order to highlight practical stability regions. The methodology was applied to the case studies of Martian Moons eXploration (MMX) and Hera missions. My contribution was in relation to Hera mission. Specifically, a qualitative analysis of the natural motion about the Didymos binary asteroid system was carried out to compute bounded orbits useful for the global characterization of the asteroids belonging to the system and to investigate potential landing trajectories. Results were obtained in the perturbed bi-elliptic restricted 4-body problem (BER4BP). Figures 1.6 and 1.7 show the resulting Lagrangian descriptor (LD) scalar fields used to search for islands of bounded motion. Figure 1.6 focuses on the case of distant retrograde orbits (DROs), while Figure 1.7 is about Sun-synchronous terminator orbits (SSTOs).

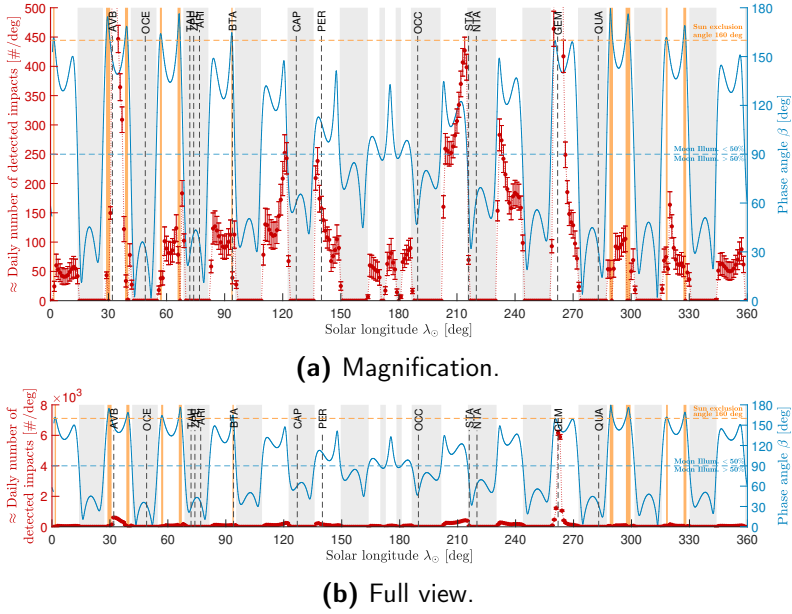


Figure 1.4: Estimation of the temporal distribution of detected lunar impacts of LUMIO lunar CubeSat. On the left y-axis, the approximately daily number of impacts in 1 deg bins of solar longitude. Impact kinetic energy $KE \geq 10^{-6}$ kton TNT Equivalent, Earth equivalent. On the right y-axis, the phase angle β .

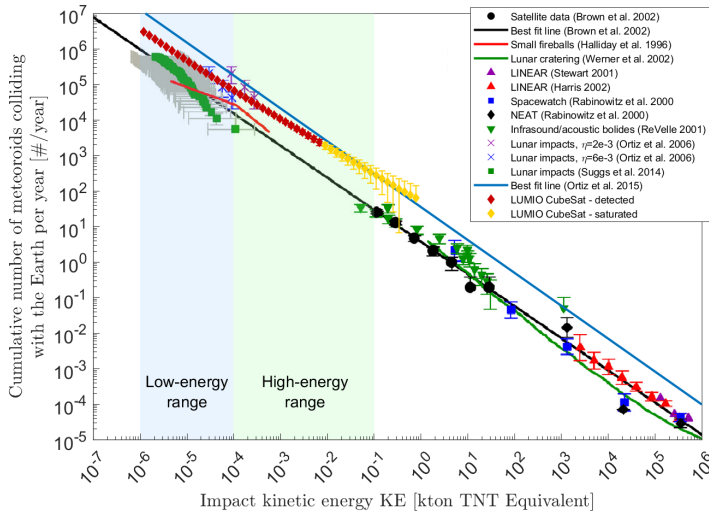


Figure 1.5: Comparison of the estimated LUMIO lunar CubeSat scientific return with the scientific return of previous programmes. Logarithmic scale plot. The plot is an elaborated version of Figure 9 in [23], courtesy of Dr. R. M. Suggs, Dr. D. E. Moser, Dr. W. J. Cooke, and Dr. R. J. Suggs.

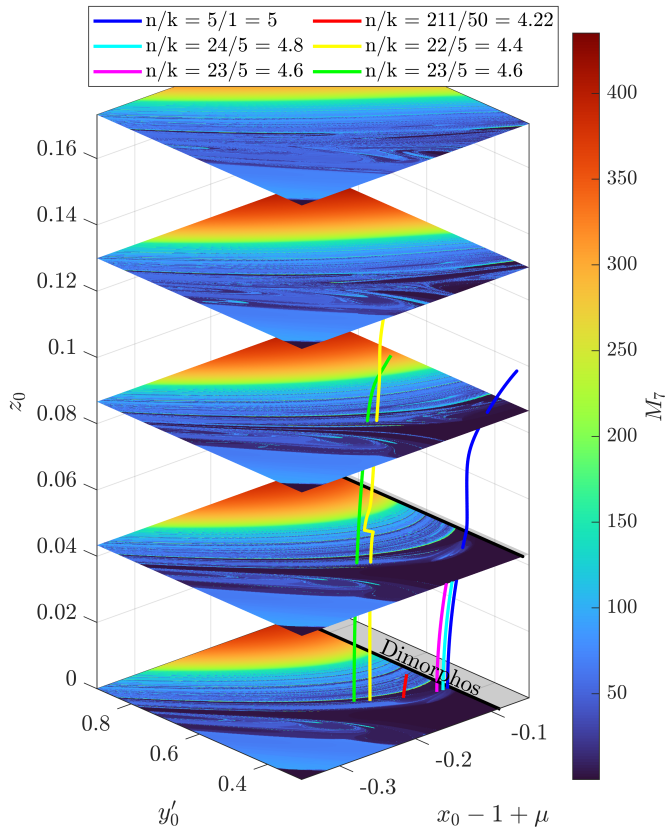


Figure 1.6: Forward LD scalar field in the spatial perturbed BER4BP. Families of resonant three-dimensional DROs are computed in the spatial CR3BP.

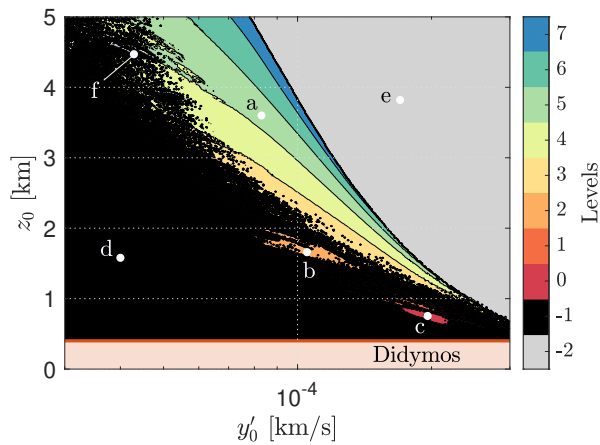


Figure 1.7: Levels of LD in the perturbed BER4BP computed while looking for SSTOs.

Most of the research activity outcome was already presented in various forms (i. e., papers, presentations, technical reports). The list of contributions to the field split among journal articles, book chapters, conference papers, and workshop presentations is provided below.

Journal articles

- [J6] Quinci A, **Merisio G**, et al. “Qualitative study of ballistic capture at Mars via lagrangian descriptors”. In: *Communications in Nonlinear Science and Numerical Simulation* (-). Submitted on April 13, 2022. Under review.
- [J5] Raffa S, **Merisio G**, et al. “Finding regions of bounded motion in binary asteroid environment using Lagrangian descriptors”. In: *Communications in Nonlinear Science and Numerical Simulation* (-). Submitted on March 14, 2022. Under review (3rd round).
- [J4] Caleb T, **Merisio G**, et al. “Stable sets mapping with Taylor differential algebra with application to ballistic capture orbits around Mars”. In: *Celestial Mechanics and Dynamical Astronomy* 134.39 (2022). DOI: [10.1007/s10569-022-10090-8](https://doi.org/10.1007/s10569-022-10090-8).
- [J3] Cervone A, Topputo F, Speretta S, Menicucci A, Turan E, Di Lizia P, Massari M, Franzese V, Giordano C, **Merisio G**, et al. “LUMIO: A CubeSat for observing and characterizing micro-meteoroid impacts on the lunar far side”. In: *Acta Astronautica* 195 (2022), pp. 309–317. DOI: [10.1016/j.actaastro.2022.03.032](https://doi.org/10.1016/j.actaastro.2022.03.032).
- [J2] **Merisio G** and Topputo F. “Present-day model of lunar meteoroids and their impact flashes for LUMIO mission”. In: *Icarus* 389 (2023), p. 115180. DOI: [10.1016/j.icarus.2022.115180](https://doi.org/10.1016/j.icarus.2022.115180).
- [J1] Topputo F, **Merisio G**, et al. “Meteoroids detection with the LUMIO lunar CubeSat”. In: *Icarus* 389 (2023), p. 115213. DOI: [10.1016/j.icarus.2022.115213](https://doi.org/10.1016/j.icarus.2022.115213).

Book chapters

- [B1] Di Domenico G, Andreis E, Morelli AC, **Merisio G**, et al. “The ERC-funded EXTREMA project: Achieving self-driving interplanetary CubeSats”. In: *Modeling and Optimization in Space Engineering — New Concepts and Approaches*. Accepted on March 31, 2022. In press. Springer.

Conference papers

- [C17] **Merisio G** and Topputo F. “Backbone of ballistic capture set”. In: *33rd AAS/AIAA Space Flight Mechanics Meeting* (Austin, Texas, USA). 2023, pp. 1–22.

- [C16] Bernardini N, **Merisio G**, et al. “Exploiting coherent patterns for the analysis of qualitative motion and the design of bounded orbits around small bodies”. In: *73rd International Astronautical Congress (IAC 2022)* (Paris, France). 2022, pp. 1–16.
- [C15] **Merisio G** and Topputo F. “An algorithm to engineer autonomous ballistic capture at Mars”. In: *73rd International Astronautical Congress (IAC 2022)* (Paris, France). 2022, pp. 1–16.
- [C14] Franzese V, **Merisio G**, et al. “Current status of LUMIO: A lunar CubeSat mission at Earth–Moon L2”. In: *4S Symposium* (Vilamoura, Portugal). 2022, pp. 1–15.
- [C13] Morselli A, Di Domenico G, Andreis E, Morelli AC, **Merisio G**, et al. “The EXTREMA orbital simulation hub: A facility for GNC testing of autonomous interplanetary CubeSat”. In: *4S Symposium* (Vilamoura, Portugal). 2022, pp. 1–13.
- [C12] Speretta S, Turan E, Cervone A, Menicucci A, Topputo F, Franzese V, Giordano C, **Merisio G**, Di Lizia P, Massari M, et al. “LUMIO: A CubeSat to monitor micro-meteroid impacts on the lunar farside”. In: *2022 IEEE Aerospace Conference (AERO)* (Big Sky, Montana, USA). IEEE. 2022, pp. 1–8.
- [C11] Morelli AC, **Merisio G**, et al. “A convex guidance approach to target ballistic capture corridors at Mars”. In: *44th AAS Guidance, Navigation and Control Conference* (Breckenridge, Colorado, USA). 2022, pp. 1–24.
- [C10] Cervone A, Speretta S, Menicucci A, Bertels E, Topputo F, and **Merisio G**. “Selection of the propulsion system for the LUMIO mission: An intricate trade-off between cost, reliability and performance”. In: *72nd International Astronautical Congress* (Dubai, United Arab Emirates). 2021.
- [C9] Cervone A, Topputo F, Speretta S, Menicucci A, Di Lizia P, Massari M, Franzese V, Giordano C, **Merisio G**, et al. “Design challenges and opportunities offered by the LUMIO spacecraft: A CubeSat for observing and characterizing micro-meteoroid impacts on the lunar far side”. In: *72nd International Astronautical Congress* (Dubai, United Arab Emirates). 2021.
- [C8] Di Domenico G, Andreis E, Morelli AC, **Merisio G**, et al. “Toward self-driving interplanetary CubeSats: The ERC-funded project EXTREMA”. In: *72nd International Astronautical Congress* (Dubai, United Arab Emirates). 2021.
- [C7] Topputo F, **Merisio G**, et al. “Current status of LUMIO mission: Characterizing lunar meteoroid impacts with a CubeSat”. In: *72nd International Astronautical Congress* (Dubai, United Arab Emirates). 2021.
- [C6] **Merisio G**, Franzese V, et al. “LUMIO: A CubeSat to monitor the lunar farside”. In: *Europlanet Science Congress 2021 (EPSC2021)* (Virtual). 2021. DOI: [10.5194/epsc2021-282](https://doi.org/10.5194/epsc2021-282).

- [C5] **Merisio G** and Topputo F. "Characterization of ballistic capture corridors aiming at autonomous ballistic capture at Mars". In: *2021 AAS/AIAA Astrodynamics Specialist Conference* (Big Sky, Montana, USA/Virtual). 2021.
- [C4] Topputo F, **Merisio G**, et al. "LUMIO CubeSat: A mission to refine meteoroid population knowledge". In: *7th IAA Planetary Defense Conference (PDC 2021)* (Virtual). 2021.
- [C3] Cervone A, Topputo F, Speretta S, Menicucci A, Biggs J, Di Lizia P, Massari M, Franzese V, Giordano C, **Merisio G**, et al. "Phase A design of the LUMIO spacecraft: A CubeSat for observing and characterizing micro-meteoroid impacts on the lunar far side". In: *71st International Astronautical Congress* (Virtual). 2020.
- [C2] **Merisio G**, Giordano C, et al. "Predicting the scientific outcome of the LUMIO lunar CubeSat". In: *71st International Astronautical Congress* (Virtual). 2020.
- [C1] **Merisio G**, Topputo F, et al. "LUMIO CubeSat: Toward a lunar situational awareness". In: *EPSC-DPS Joint Meeting 2019* (Geneva, Switzerland). 2019.

Presentations

- [P4] **Merisio G**, Franzese V, et al. "LUMIO: A CubeSat to monitor the lunar farside". In: *Fireballs Workshop #3 on Fireball Databases and Machine Learning* (Glasgow, United Kingdom). 2022.
- [P3] **Merisio G** and Topputo F. "Ballistic capture corridors at Mars: Co-orbital, time-varying manifolds supporting capture". In: *COOMOT International Workshop on Co-orbital Motion: Modeling, Understanding and Exploitation* (Milan, Italy). 2022.
- [P2] **Merisio G** and Topputo F. "High-fidelity trajectory design of ballistic capture exploiting coherent patterns". In: *1st Aerospace PhD Day* (Virtual). 2021.
- [P1] Topputo F, **Merisio G**, et al. "LUMIO CubeSat: Toward a lunar situational awareness". In: *iCubeSat 2019, 8th Interplanetary CubeSat Workshop* (Milan, Italy). 2019.

1.7 Notation and conventions

The notation and conventions used throughout the manuscript are herewith introduced. Scalars are indicated with lower-case letters (e. g., a). Vectors are indicated with bold lower-case letters (e. g., $\mathbf{p} = [a \ b \ c]^\top$), while their magnitudes with the same letter but in regular font (e. g., $p = \|\mathbf{p}\|$). Reference quantities are written with a hat (e. g., $\hat{\mathbf{p}}$). Small variations are prepended by δ (e. g., $\delta\mathbf{p}$). Usually, the position vector is $\mathbf{r} = [x \ y \ z]^\top$, the velocity vector is $\mathbf{v} = [\dot{x} \ \dot{y} \ \dot{z}]^\top = [v_x \ v_y \ v_z]^\top$, the state space vector is $\mathbf{x} = [\mathbf{r}^\top \ \mathbf{v}^\top]^\top$, and the angular momentum is $\mathbf{h} = \mathbf{r} \times \mathbf{v} = [\mathbf{r}^\wedge] \mathbf{v}$, where the skew-symmetric matrix $[\mathbf{r}^\wedge]$ is defined as

$$[\mathbf{r}^\wedge] := \begin{bmatrix} 0 & -z & y \\ z & 0 & -x \\ -y & x & 0 \end{bmatrix}. \quad (1.1)$$

Specific notation is introduced contextually on an as-needed basis.

Acknowledgments The work presented in this dissertation has received funding from the ERC under the European Union’s Horizon 2020 research and innovation programme (Grant Agreement No. 864697). In Section 1.6, research on the LUMIO CubeSat mission has been conducted under ESA Contract No. 4000130257/20/NL/AS within the GSTP, and has received support from the national delegations of Italy (ASI), the Netherlands (NSO), and Norway (NOSA). The author also acknowledge the members of the LUMIO team for their support and the ESA experts for reviewing the Phase A design. Research on project “*Généralisation du concept de variétés invariantes at applications à la conception des missions d’exploration de petits corps*” introduced in Section 1.6 has received funding from the French space agency CNES under the Research and Technology programme (Contract R-S20/BS-0005-066, Reference DCAS/689/2022). The author would like to thank the EXTREMA team at the Deep-space Astrodynamics Research & Technology (DART) Group⁴, Politecnico di Milano, for the extremely valuable content provided to write parts of Sections 1.1 and 1.2.

“Che importa il nome dell’autore in copertina? Trasportiamoci col pensiero di qui a tremila anni. Chissà quali libri della nostra epoca si saranno salvati, e di chissà quali autori si ricorderà ancora il nome. Ci saranno libri che resteranno famosi ma che saranno considerati opere anonime come per noi l’epopea di Ghilgamesh; ci saranno autori di cui sarà sempre famoso il nome ma di cui non resterà nessuna opera, come è successo a Socrate; o forse tutti libri superstiti saranno attribuiti a un unico autore misterioso, come Omero.”

Italo Calvino, *Se una notte d’inverno un viaggiatore*

⁴<https://dart.polimi.it/> [last accessed Dec 1, 2022].

Dynamical model

Following the nomenclature in [25], a *target* and a *primary* are defined. The target is the body around which the ballistic capture is studied. The primary is the main body around which the target revolves. Target and primary masses are m_t and m_p , respectively. The mass ratio of the system is $\mu = m_t / (m_t + m_p)$. This work is focused on ballistic capture having Mars as target and the Sun as primary⁵.

2.1 Reference frames

The following reference frames are used: J2000, ECLIPJ2000, RTN@ t_i , and RPF.

J2000. Defined on Earth's mean equator and equinox, J2000 is an inertial frame determined from observations of planetary motions, which was realized to coincide almost exactly with the International Celestial Reference Frame (ICRF) [26]. The J2000 inertial frame (also known as EMEJ2000) is built-in in SPICE⁶ [27, 28]. In SPICE, the ICRF and J2000 frames are considered the same. The origin of the J2000 can be chosen arbitrarily.

ECLIPJ2000. This is an inertial frame built-in in SPICE, which is defined on the ecliptic coordinates and based on the J2000 inertial frame. The origin of the ECLIPJ2000 frame can be chosen arbitrarily.

RTN@ t_i . The radial-tangential-normal of date frame (RTN@ t_i) is an inertial frame frozen at a prescribed epoch t_i . The frame is centered at the target. The x-axis is aligned with the primary–secondary direction, the z-axis is normal to the

⁵See Table 2 in [25] for a complete list of targets and their primaries.

⁶SPICE is the information system developed by Navigation and Ancillary Information Facility (NAIF) to assist NASA scientists and engineers in mission modeling, planning, interpreting scientific observations, and executing activities. <https://naif.jpl.nasa.gov/naif/> [last accessed Dec 1, 2022]

primary–secondary plane in the direction of their angular momentum, and the y -axis completes the dextral orthonormal triad.

RPF. The roto-pulsating frame (RPF) is a rotating frame centered at the primary–target system barycenter. The rotation is such that both the target and the primary are at rest in the RPF. In this frame, the x -axis points from the primary to the target, the z -axis is directed as the angular momentum of the system, and the y -axis completes the dextral orthonormal triad. The transformation from and to the RPF involves a change of origin, a rotation, and a scaling [29].

2.2 Ephemerides

The precise states of the Sun and the major planets are retrieved from the Jet Propulsion Laboratory (JPL)’s planetary ephemerides `de440s.bsp`⁷ (or DE440s) [30]. Additionally, the ephemerides `mar097.bsp` of Mars (the target) and its moons are employed⁸. Unless otherwise specified, the following generic leap seconds kernel (LSK) and planetary constant kernel (PCK) were used: `naif0012.tls`, `pck00010.tpc`, and `gm_de440.tpc`⁹.

2.3 Equations of motion

The Equations of motion (EoM) of the restricted n -body problem are considered. Unless otherwise specified, the gravitational attractions of the Sun, Mercury, Venus, Earth–Moon (B¹⁰), Mars (central body), Jupiter (B), Saturn (B), Uranus (B), Neptune (B), Pluto (B), Phobos, and Deimos are taken into account. Additionally, solar radiation pressure (SRP), Mars’ non-spherical gravity (NSG), and relativistic corrections [31] (Schwarzschild solution, geodesic precession, and Lense–Thirring precession) are also included in the model. The assumed spacecraft parameters needed to evaluate the SRP perturbation are collected in Table 2.1. They are compatible with the parameters of a 12U deep-space CubeSat [32]. Terms of the infinite series modeling NSG are considered up to degree $n_{deg} = 20$ and order $n_{ord} = 20$ [10]. The coefficients to evaluate the NSG perturbation are retrieved from the MRO120F gravity field model of Mars. Data are publicly available in the file `jgmro_120f_sha.tab`, archived in the Geosciences Node of NASA’s

⁷Data publicly available at: https://naif.jpl.nasa.gov/pub/naif/generic_kernels/spk/planets/de440s.bsp [retrieved Dec 1, 2022].

⁸`~/spk/satellites/mar097.bsp` [retrieved Dec 1, 2022].

⁹Data publicly available at: https://naif.jpl.nasa.gov/pub/naif/generic_kernels/lsc/naif0012.tls, and `~/generic_kernels/pck/pck00010.tpc` [retrieved Dec 1, 2022]. The `gm_de440.tpc` PCK kernel was written from scratch, courtesy of Dr. C. Giordano, because the version consistent with ephemerides DE440s is not released yet.

¹⁰Here B stands for barycenter.

Table 2.1: Spacecraft parameters for SRP evaluation [32].

Parameter	Unit	Value
Mass–SRP area ratio m/A	kg m^{-2}	75
Coefficient of reflectivity C_r	-	1.3

Planetary Data System¹¹. Far from Mars, when in heliocentric motion, the NSG perturbation is neglected. EoM are integrated in the J2000 inertial frame.

The EoM in a non-rotating Mars-centered reference frame are [10, 25, 31]

$$\ddot{\mathbf{r}} = -\frac{\mu_t}{r^3}\mathbf{r} - \sum_{i \in \mathbb{P}} \mu_i \left(\frac{\mathbf{r}_i}{r_i^3} + \frac{\mathbf{r} - \mathbf{r}_i}{\|\mathbf{r} - \mathbf{r}_i\|^3} \right) + \frac{QA}{m} \frac{\mathbf{r} - \mathbf{r}_\odot}{\|\mathbf{r} - \mathbf{r}_\odot\|^3} - \mathcal{R} \frac{\mu_t}{r^2} \left(\Lambda \frac{\mathcal{R}^\top \mathbf{r}}{r} - \begin{bmatrix} J \\ K \\ H \end{bmatrix} \right) + \quad (2.1)$$

$$+ \frac{\mu_t}{c^2 r^3} \left[\left(4 \frac{\mu_t}{r} - v^2 \right) \mathbf{r} + 4 (\mathbf{r} \cdot \dot{\mathbf{r}}) \dot{\mathbf{r}} \right] + 2 (\boldsymbol{\Omega} \times \dot{\mathbf{r}}) + 2 \frac{\mu_t}{c^2 r^3} \left[\frac{3}{r^2} (\mathbf{r} \times \dot{\mathbf{r}}) (\mathbf{r} \cdot \mathbf{J}) + (\dot{\mathbf{r}} \times \mathbf{J}) \right]$$

where μ_t is the gravitational parameter of the target body (i. e., Mars in this work); \mathbf{r} and $\dot{\mathbf{r}} = \mathbf{v}$ are the position and velocity vectors of the spacecraft with respect to the target, respectively, being r and v their magnitudes; \mathbb{P} is a set of $n - 2$ indexes (where n concerns the n -body problem) each one referring to the perturbing bodies; μ_i and \mathbf{r}_i are the gravitational parameter and position vector of the i -th body with respect to the target, respectively; A is the Sun-projected area on the spacecraft for SRP evaluation; m is the spacecraft mass; \mathbf{r}_\odot is the position vector of the Sun with respect to the target; \mathcal{R} is the time-dependent matrix transforming vector components from the Mars-fixed frame to the non-rotating frame in which the EoM are written; Λ , J , K , and H are defined as in [33]; $c = 299792458 \text{ m s}^{-1}$ (from SPICE [27, 28]) is the speed of light in vacuum; \mathbf{J} is the rotating central body's angular momentum per unit mass in the J2000 frame. Then, $Q = LC_r / (4\pi c)$ where C_r is the spacecraft coefficient of reflectivity, and $L = S_\odot 4\pi d_{\text{AU}}^2$ is the luminosity of the Sun. The latter is computed from the solar constant¹² $S_\odot = 1367.5 \text{ W m}^{-2}$ evaluated at $d_{\text{AU}} = 1 \text{ AU}$. Lastly, $\boldsymbol{\Omega} = \frac{3}{2} \dot{\mathbf{r}}_{\odot/t} \times (-\mu_\odot \mathbf{r}_{\odot/t}) / (c^2 r_{\odot/t}^3)$ where μ_\odot is the gravitational parameter of the Sun; $\mathbf{r}_{\odot/t}$ and $\dot{\mathbf{r}}_{\odot/t} = \mathbf{v}_{\odot/t}$ are the position and velocity vectors, respectively, of the target body with respect to the Sun, being $r_{\odot/t}$ and $\dot{r}_{\odot/t} = v_{\odot/t}$ their magnitudes.

Contributions of individual terms in Eq. (2.1) are compared in Figure 2.1. The specific force f_i in km s^{-2} associated to each term is plotted as a function of the distance r from the central body expressed in Mars' radii. Distances reach up to twice the semi-major axis of Mars.

¹¹Data publicly available at: https://pds-geosciences.wustl.edu/mro/mro-m-rss-5-sdp-v1/mrors_1xxx/data/shadr/ [retrieved Dec 1, 2022].

¹²https://extapps.ksc.nasa.gov/Reliability/Documents/Preferred_Practices/2301.pdf [last accessed Dec 1, 2022].

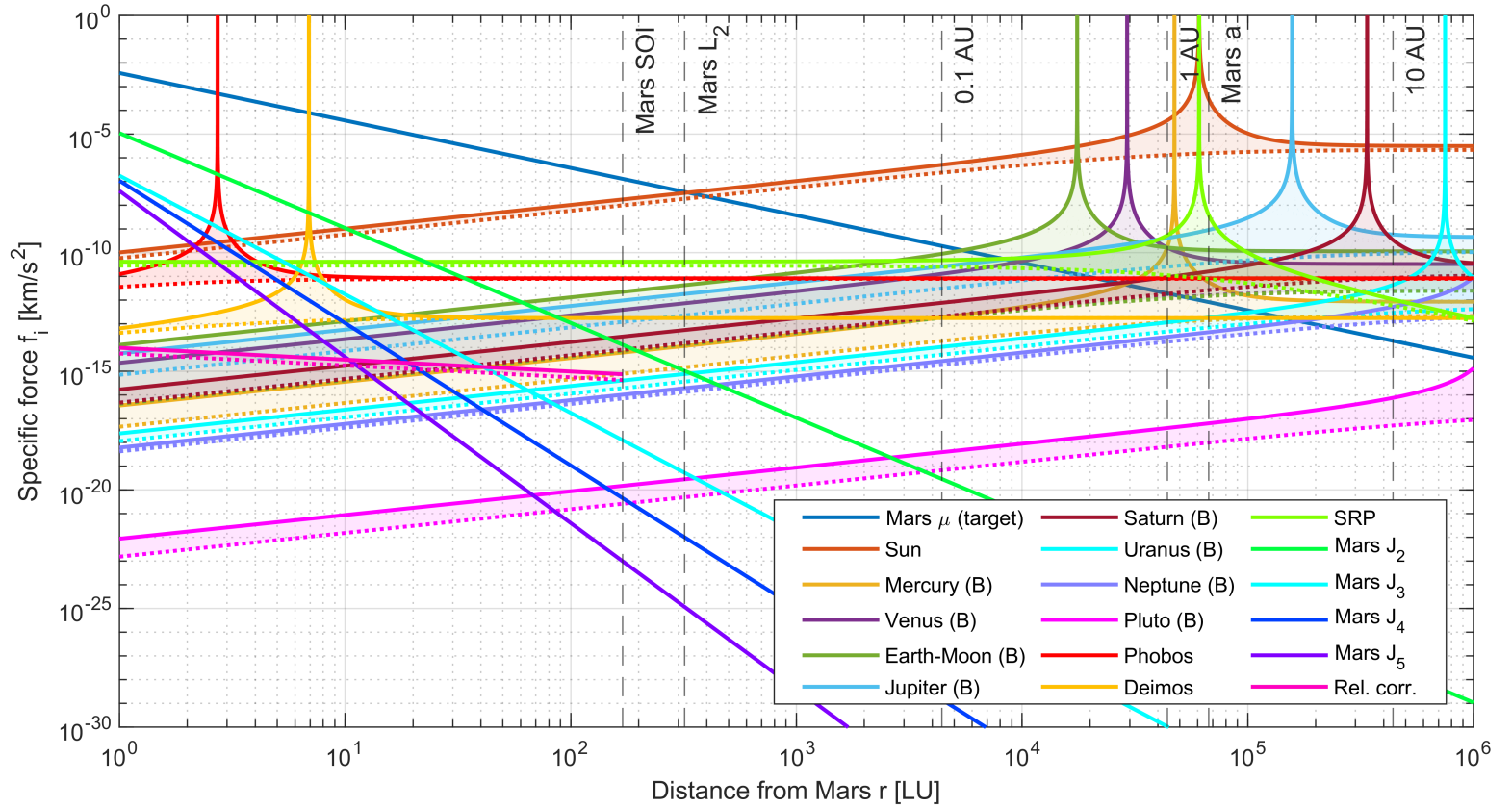


Figure 2.1: Contributions of individual terms in Eq. (2.1). Specific force f_i associated to each term is plotted as a function of distance r from the central body expressed in Mars' radii, $\text{LU} = R_{\text{Mars}} = 3396.0\text{km}$. Dashed lines mark peculiar distances from Mars: Mars SOI, Mars Lagrange point L_2 , 0.1 AU, 1 AU, Mars semi-major axis, and 10 AU.

2.4 Variational equations

Given the EoM of a dynamical system, the motion of a particle is described by

$$\begin{cases} \dot{\mathbf{x}}(t) = \mathbf{f}(\mathbf{x}, t) \\ \mathbf{x}(t_0) = \mathbf{x}_0 \end{cases} \quad (2.2)$$

with $\mathbf{x}(t) \in \Omega \subseteq \mathbb{R}^n$ being the state vector of the system and $t \in [t_a, t_b] \subseteq \mathbb{R}$ is the independent variable representing time. Eq. (2.2) is a first-order differential equation (also referred to as velocity map). In Section 2.3, the dynamics of the system is described by second-order differential equations, which is then transformed to a system of first-order differential equations. The transformation implies doubling the number of equations. When the dynamics \mathbf{f} explicitly depend on the independent variable (typically, but not always, the time t) the system is labeled as non-autonomous.

Integrating Eq. (2.2) gives the flow map of the system

$$\varphi_{t_0}^t : \Omega \mapsto \Omega, \quad \mathbf{x}_0 \mapsto \varphi_{t_0}^t(\mathbf{x}_0) = \mathbf{x}(\mathbf{x}_0, t_0; t) \quad (2.3)$$

which returns the state at time epoch t for each initial state \mathbf{x}_0 and initial time t_0 . From the flow map, the definition of the state transition matrix (STM) follows [34]

$$\Phi := \Phi(\mathbf{x}_0, t_0; t) = D_{\mathbf{x}_0} \varphi_{t_0}^t(\mathbf{x}_0) = D_{\mathbf{x}_0} \mathbf{x}(\mathbf{x}_0, t_0; t) \quad (2.4)$$

where D is the differential operator. The STM Φ can be propagated through

$$\begin{cases} \dot{\Phi} = D_{\mathbf{x}} \mathbf{f}(\mathbf{x}, t) \Phi = \mathbf{A}(\mathbf{x}, t) \Phi \\ \Phi(\mathbf{x}_0, t_0; t_0) = \mathbf{I}_{n \times n} \end{cases} \quad (2.5)$$

where \mathbf{A} is the Jacobian of the velocity map and $\mathbf{I}_{n \times n}$ is the identity matrix of size n . Due to the term $\mathbf{A}(\mathbf{x}(t), t) = D_{\mathbf{x}} \mathbf{f}(\mathbf{x}(t), t)$ that depends on $\mathbf{x}(t)$, the integration of Eqs. (2.2) and (2.5) must be carried out simultaneously. The joint system of Eqs. (2.2) and (2.5) characterized by $n + n^2$ relations constitutes what is usually referred to as variational equations

$$\begin{cases} \dot{\mathbf{x}}(t) = \mathbf{f}(\mathbf{x}(t), t) \\ \mathbf{x}(t_0) = \mathbf{x}_0 \\ \dot{\Phi} = \mathbf{A}(\mathbf{x}, t) \Phi \\ \Phi(\mathbf{x}_0, t_0; t_0) = \mathbf{I}_{n \times n} \end{cases} \quad (2.6)$$

2.4.1 Analytical derivatives of the velocity map

When referring to dynamical systems, the representation of the state is not unique. In fact, there is an infinite set of equivalent formulations. In this section, a Cartesian representation is used, such that

$$\mathbf{x}(t) = \begin{bmatrix} \mathbf{r}(t) \\ \mathbf{v}(t) \end{bmatrix} = \begin{bmatrix} \mathbf{r}(t) \\ \dot{\mathbf{r}}(t) \end{bmatrix} \quad \text{and} \quad \dot{\mathbf{x}}(t) = \mathbf{f}(\mathbf{x}, t) = \begin{bmatrix} \mathbf{v}(t) \\ \mathbf{a}(\mathbf{r}, \mathbf{v}, t) \end{bmatrix} = \begin{bmatrix} \dot{\mathbf{r}}(t) \\ \ddot{\mathbf{r}}(\mathbf{r}, \dot{\mathbf{r}}, t) \end{bmatrix}. \quad (2.7)$$

The Jacobian of the velocity map is

$$\mathbf{A}(\mathbf{x}, t) = \frac{\partial \mathbf{f}(\mathbf{x}, t)}{\partial \mathbf{x}(t)} = \begin{bmatrix} \frac{\partial \mathbf{v}(t)}{\partial \mathbf{r}(t)} & \frac{\partial \mathbf{v}(t)}{\partial \mathbf{v}(t)} \\ \frac{\partial \mathbf{a}(\mathbf{r}, \mathbf{v}, t)}{\partial \mathbf{r}(t)} & \frac{\partial \mathbf{a}(\mathbf{r}, \mathbf{v}, t)}{\partial \mathbf{v}(t)} \end{bmatrix}_{6 \times 6} = \begin{bmatrix} \mathbf{0}_{3 \times 3} & \mathbf{I}_{3 \times 3} \\ \frac{\partial \ddot{\mathbf{r}}(\mathbf{r}, \dot{\mathbf{r}}, t)}{\partial \mathbf{r}(t)} & \frac{\partial \ddot{\mathbf{r}}(\mathbf{r}, \dot{\mathbf{r}}, t)}{\partial \dot{\mathbf{r}}(t)} \end{bmatrix}_{6 \times 6} \quad (2.8)$$

where $\mathbf{0}_{3 \times 3}$ and $\mathbf{I}_{3 \times 3}$ are the null and identity matrices of size 3, respectively. If $\ddot{\mathbf{r}}(\mathbf{r}, t)$ does not depend on velocity $\dot{\mathbf{r}}$, then

$$\frac{\partial \ddot{\mathbf{r}}(\mathbf{r}, t)}{\partial \dot{\mathbf{r}}(t)} = \mathbf{0}_{3 \times 3}. \quad (2.9)$$

In this peculiar case, to obtain the Jacobian of the dynamics is therefore necessary to compute only one term [35], the south-west block of the matrix in Eq. (2.8). The Jacobian $\mathbf{A}(\mathbf{x}, t)$ of the velocity field in Eq. (2.8), is computed as the sum of the following terms, which are then individually derived,

$$\frac{\partial \ddot{\mathbf{r}}(\mathbf{r}, \dot{\mathbf{r}}, t)}{\partial \mathbf{r}(t)} = \left. \frac{\partial \ddot{\mathbf{r}}}{\partial \mathbf{r}} \right|_{\text{sg}} + \left. \frac{\partial \ddot{\mathbf{r}}}{\partial \mathbf{r}} \right|_{\text{3b}} + \left. \frac{\partial \ddot{\mathbf{r}}}{\partial \mathbf{r}} \right|_{\text{srp}} + \left. \frac{\partial \ddot{\mathbf{r}}}{\partial \mathbf{r}} \right|_{\text{nsg}} + \left. \frac{\partial \ddot{\mathbf{r}}}{\partial \mathbf{r}} \right|_{\text{relc}}, \quad (2.10)$$

$$\frac{\partial \ddot{\mathbf{r}}(\mathbf{r}, \dot{\mathbf{r}}, t)}{\partial \dot{\mathbf{r}}(t)} = \left. \frac{\partial \ddot{\mathbf{r}}}{\partial \dot{\mathbf{r}}} \right|_{\text{relc}}. \quad (2.11)$$

Central body spherical gravity field. The contribution arising from the term associated with the central gravity field of the target body is given by [35]

$$\left. \frac{\partial \ddot{\mathbf{r}}}{\partial \mathbf{r}} \right|_{\text{sg}} = -\mu_t \left(\frac{1}{r^3} \mathbf{I}_{3 \times 3} - 3 \frac{\mathbf{r} \mathbf{r}^\top}{r^5} \right) \quad (2.12)$$

where the subscript 'sg' stands for 'spherical gravity' and $\mathbf{r} \mathbf{r}^\top$ represents the dyadic product, which results in a 3×3 matrix and should not be confused with the dot product $\mathbf{r}^\top \mathbf{r} = \mathbf{r} \cdot \mathbf{r} = \langle \mathbf{r}, \mathbf{r} \rangle$.

Third-body perturbations. The partial derivative of the acceleration generated by third-body perturbations is given by [35]

$$\left. \frac{\partial \ddot{\mathbf{r}}}{\partial \mathbf{r}} \right|_{\text{3b}} = - \sum_{i \in \mathbb{P}} \mu_i \left(\frac{1}{\|\mathbf{r} - \mathbf{r}_i\|^3} \mathbf{I}_{3 \times 3} - 3 \frac{(\mathbf{r} - \mathbf{r}_i)(\mathbf{r} - \mathbf{r}_i)^\top}{\|\mathbf{r} - \mathbf{r}_i\|^5} \right) \quad (2.13)$$

where the subscript '3b' stands for 'third-body'.

Solar radiation pressure For the SRP term, the expression of the partial derivative assumes the following form [35]

$$\left. \frac{\partial \ddot{\mathbf{r}}}{\partial \mathbf{r}} \right|_{\text{srp}} = \frac{C_{RLS} A}{4 \pi c m} \left(\frac{1}{\|\mathbf{r} - \mathbf{r}_s\|^3} \mathbf{I}_{3 \times 3} - 3(\mathbf{r} - \mathbf{r}_s) \frac{(\mathbf{r} - \mathbf{r}_s)^\top}{\|\mathbf{r} - \mathbf{r}_s\|^5} \right) \quad (2.14)$$

where the subscript 'srp' stands for 'solar radiation pressure'.

Non-spherical gravity. The partial derivative for the NSG contribution is [33, 35]

$$\begin{aligned} \left. \frac{\partial \ddot{\mathbf{r}}}{\partial \mathbf{r}} \right|_{\text{nsg}} = & \frac{\mu_t}{r^3} \left(\begin{bmatrix} \mathcal{R}^\top \mathbf{r}/r & \alpha \end{bmatrix} \begin{bmatrix} F & G \\ G & M \end{bmatrix} \begin{bmatrix} (\mathcal{R}^\top \mathbf{r}/r)^\top \\ \alpha^\top \end{bmatrix} + \right. \\ & + \begin{bmatrix} \mathcal{R}^\top \mathbf{r}/r & \mathbf{d} \end{bmatrix} \begin{bmatrix} 0 & -1 \\ -1 & 0 \end{bmatrix} \begin{bmatrix} (\mathcal{R}^\top \mathbf{r}/r)^\top \\ \mathbf{d}^\top \end{bmatrix} + \\ & \left. + \begin{bmatrix} N-\Lambda & -O & Q \\ -O & -(N+\lambda) & R \\ Q & R & -\Lambda \end{bmatrix} \right) \end{aligned} \quad (2.15)$$

where the subscript ‘nsg’ stands for ‘non-spherical gravity’. Terms α , \mathbf{d} , F , G , M , N , O , Q , R , and Λ are defined as in [33].

Relativistic corrections. Partial derivatives of relativistic corrections are¹³

$$\begin{aligned} \left. \frac{\partial \ddot{\mathbf{r}}}{\partial \mathbf{r}} \right|_{\text{relc}} = & \frac{1}{c^2 r^5} \left(\frac{1}{r^2} \mathbf{I}_{3 \times 3} - 3 \mathbf{r} \mathbf{r}^\top \right) \left(\frac{4}{r} - v^2 \right) - \frac{4 \mathbf{r} \mathbf{r}^\top}{c^2 r^6} - \frac{12}{c^2 r^5} (\mathbf{r} \cdot \dot{\mathbf{r}}) \dot{\mathbf{r}} \mathbf{r}^\top + \\ & + \frac{4}{c^2 r^3} \dot{\mathbf{r}} \dot{\mathbf{r}}^\top - \frac{6}{c^2 r^5} \left(\frac{3}{r^2} (\mathbf{r} \times \dot{\mathbf{r}}) \mathbf{r}^\top \mathbf{J} + \dot{\mathbf{r}} \times \mathbf{J} \right) \mathbf{r}^\top + \\ & + \frac{2}{c^2 r^3} \left(-\frac{6}{r^4} (\mathbf{r} \times \dot{\mathbf{r}}) \mathbf{r}^\top \mathbf{J} \mathbf{r}^\top + \frac{3}{r^2} (\mathbf{r} \times \dot{\mathbf{r}}) \mathbf{J}^\top - \frac{3}{r^2} (\mathbf{r} \cdot \mathbf{J}) [\dot{\mathbf{r}}^\wedge] \right), \end{aligned} \quad (2.16)$$

$$\begin{aligned} \left. \frac{\partial \ddot{\mathbf{r}}}{\partial \mathbf{r}} \right|_{\text{relc}} = & -\frac{2}{c^2 r^3} \mathbf{r} \dot{\mathbf{r}}^\top + \frac{4}{c^2 r^3} \left(\dot{\mathbf{r}} \mathbf{r}^\top + (\mathbf{r} \cdot \dot{\mathbf{r}}) \mathbf{I}_{3 \times 3} \right) + 2 [\Omega^\wedge] + \\ & + \frac{2}{c^2 r^3} \left(\frac{3}{r^2} (\mathbf{r} \cdot \mathbf{J}) [\mathbf{r}^\wedge] - [\mathbf{J}^\wedge] \right) \end{aligned} \quad (2.17)$$

where the subscript ‘relc’ stands for ‘relativistic corrections’.

2.5 Cauchy–Green strain tensor

Consider a perturbed state $\mathbf{x}_0 = \hat{\mathbf{x}}_0 + \delta \mathbf{x}_0$ at time t_0 , the evolution of the infinitesimal perturbation after a time span T is [34]

$$\delta \mathbf{x}(t_0 + T) = \boldsymbol{\Phi}_{t_0}^{t_0+T}(\mathbf{x}_0) - \boldsymbol{\Phi}_{t_0}^{t_0+T}(\hat{\mathbf{x}}_0) = \boldsymbol{\Phi}_{t_0}^{t_0+T} \delta \mathbf{x}_0 + \mathcal{O}(\|\delta \mathbf{x}_0\|^2) \quad (2.18)$$

where $\boldsymbol{\Phi}_{t_0}^{t_0+T} = \boldsymbol{\Phi}(\mathbf{x}_0, t_0; t_0 + T)$ is the STM for a finite time $t = t_0 + T$. Thus, the distance after a time span T due to the initial perturbation is given by the Euclidean norm of $\delta \mathbf{x}(t_0 + T)$

$$\|\delta \mathbf{x}(t_0 + T)\|^2 = \langle \boldsymbol{\Phi}_{t_0}^{t_0+T} \delta \mathbf{x}_0, \boldsymbol{\Phi}_{t_0}^{t_0+T} \delta \mathbf{x}_0 \rangle = \delta \mathbf{x}_0^\top [\boldsymbol{\Phi}_{t_0}^{t_0+T}]^\top \boldsymbol{\Phi}_{t_0}^{t_0+T} \delta \mathbf{x}_0 = \delta \mathbf{x}_0^\top \boldsymbol{\Delta}_{t_0}^{t_0+T} \delta \mathbf{x}_0 \quad (2.19)$$

where $\boldsymbol{\Delta}(\mathbf{x}_0, t_0; t_0 + T) = [\boldsymbol{\Phi}_{t_0}^{t_0+T}]^\top \boldsymbol{\Phi}_{t_0}^{t_0+T}$ is the finite-time Cauchy–Green strain tensor (CGST). $\boldsymbol{\Delta}_{t_0}^{t_0+T}$ is a symmetric, positive definite tensor. Its n eigenvalues

¹³Equations (2.16) and (2.17) are courtesy of Dr. C. Giordano, who derived and implemented them in GRATIS (see Section 3.7).

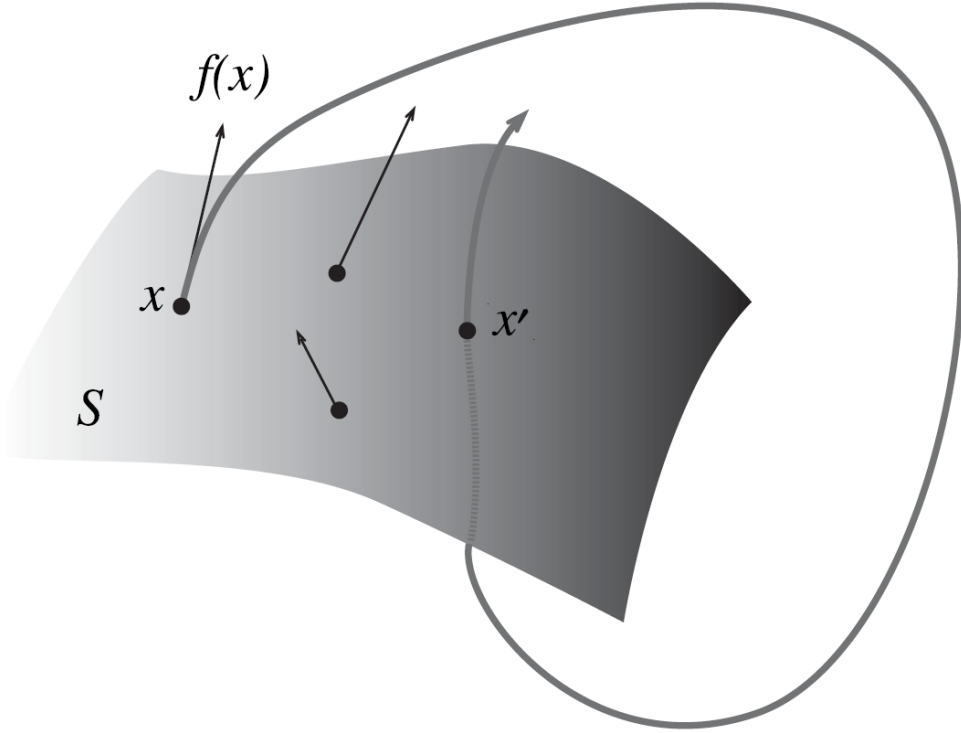


Figure 2.2: Poincaré map \mathcal{P} transforming \mathbf{x} into $\mathbf{x}' = \mathcal{P}(\mathbf{x})$ onto the Poincaré section \mathcal{S} . Figure from [37].

inform on the stretching magnitude along corresponding eigenvectors directions. The eigenvalues $\lambda_i(\mathbf{x}_0)$ and eigenvectors $\xi_i(\mathbf{x}_0)$ of $\Delta_{t_0}^{t_0+T}(\mathbf{x}_0)$ satisfy [36]

$$\Delta_{t_0}^{t_0+T} \xi_i = \lambda_i \xi_i, \quad \text{and} \quad \|\xi_i\| = 1, \quad i = 1, \dots, n. \quad (2.20)$$

Moreover,

$$0 < \lambda_1 \leq \dots \leq \lambda_n, \quad \text{and} \quad \xi_i \perp \xi_j, \quad i \neq j. \quad (2.21)$$

The CGST $\Delta_{t_0}^t$ quantifies the relative stretching of nearby trajectories for a given time interval.

2.6 Poincaré and stroboscopic maps

Among dynamical systems mathematical tools, a useful construct is represented by the Poincaré map (also referred to as first recurrence map) [37]. They are obtained by intersecting the flow with a lower-dimensional surface, named Poincaré section, transversal to the flow itself (see Figure 2.2). Stroboscopic maps are special types of Poincaré maps defined when investigating a non-autonomous periodic dynamics, so studying the system in intervals of period T time units.

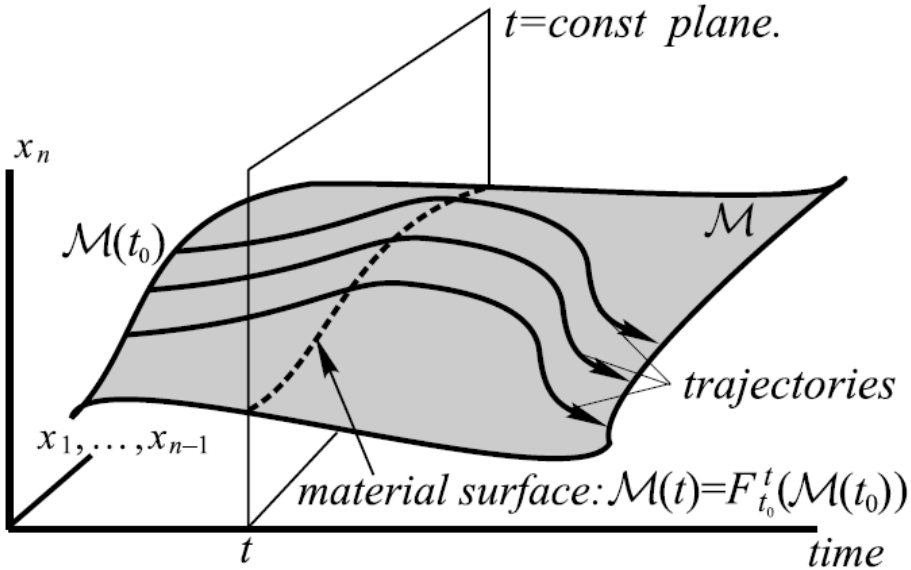


Figure 2.3: Material surface $\mathcal{M}(t)$ generated in the extended phase space by the flow map from $\mathcal{M}(t_0)$. Figure from [36].

2.7 Material surface

A material surface \mathcal{M} is a manifold of the phase space $\Omega \times [\alpha, \beta]$ generated by the advection of a $(n-1)$ -dimensional manifold $\mathcal{M}(t_0) \subset \Omega$ by the flow map. Hence,

$$\mathcal{M}(t) := \varphi_{t_0}^t(\mathcal{M}(t_0)). \quad (2.22)$$

Then, it is the time- t position of the initial surface $\mathcal{M}(t_0)$ evolving under the flow. Since $\varphi_{t_0}^t(\mathbf{x}_0)$ is a diffeomorphism, the material surface at time t is as smooth as the initial surface $\mathcal{M}(t_0)$ and it is $(n-1)$ -dimensional $\forall t$ [36] (see Figure 2.3).

2.8 Numerical propagation

The EoM in Eq. (2.1) are integrated with the GRavity Tidal Slide (GRATIS) tool [38] (see Section 3.7) in their nondimensional form to avoid ill-conditioning [25]. Normalization units are reported in Table 2.2. Numerical integration is carried out either with MATLAB[®]'s `ode113` [39] or `my_ode78` routines. The former is a multistep, variable-step, variable-order (VSVO), Adams–Bashforth–Moulton (ABM), predictor-corrector (PECE) solver of orders 1st to 13th¹⁴. The latter

¹⁴The highest order used appears to be 12th since a formula of order 13th is used to form the error estimate and the function does local extrapolation to advance the integration at order 13th. <https://www.mathworks.com/help/matlab/ref/ode113.html> [last accessed Dec 1, 2022].

Table 2.2: Nondimensionalization units.

Unit	Symbol	Value	Comment
Gravity parameter	MU	$42\,828.376\text{ km}^3\text{ s}^{-2}$	Mars' gravity parameter μ_t
Length	LU	3396.0000 km	Mars' radius R_{Mars}
Time [†]	TU	$956.281\,42\text{ s}$	$(\text{LU}^3/\text{MU})^{0.5}$
Velocity	VU	$3.551\,255\,8\text{ km s}^{-1}$	LU/TU

[†] Time unit chosen such that the nondimensional period of a circular orbit of radius LU equals 2π .

implements the Dormand–Prince 8th-order embedded Runge–Kutta (DOPRI8) propagation scheme [35], also known as RK8(7)13M¹⁵. This is an adaptive step, 8th-order Runge–Kutta (RK) integrator with 7th-order error control. Coefficients were derived by Prince and Dormand [40]. Usually, the dynamics are propagated with relative and absolute tolerances both set to 10^{-12} [25].

Two's a company, three's a crowd.

Proverb

¹⁵The notation RK $p(q)s$ M is used when referring to a RK method of order p , with an embedded step-size control of q th-order, and a total of s stages [35].

The ballistic capture mechanism

Ballistic capture allows a spacecraft to approach a planet and enter a temporary orbit about it without requiring maneuvers in between. As part of the low-energy transfers, it is a valuable alternative to Keplerian approaches. Exploiting BC grants several benefits in terms of both cost reduction [41] and mission versatility [9, 42], in general at the cost of longer transfer times [43, 44]. In the past, the BC mechanism was used to rescue Hiten [45], and to design insertion trajectories in lunar missions like SMART-1 [46] and GRAIL [47]. In the near future, BepiColombo will exploit BC orbits to be weakly captured by Mercury [48, 49]. BC is an extremely rare event [50] and requires acquiring a proper state far away from the target planet [9].

BC orbits are characterized by ICs escaping the target when integrated backward and performing n revolutions about it when propagated forward, neither impacting or escaping the target. In forward time, particles flying on BC orbits approach the target coming from outside its sphere of influence (SOI) and remain temporarily captured about it. After a certain time, the particle escapes if an energy dissipation mechanism does not take place. To make the capture permanent, either a braking maneuver or the target atmosphere (if available) could be used [51, 52].

When searching for BC opportunities, most of the trajectories found are spurious solutions typically not useful for mission design purposes [25]. Practical solutions are detected via the regularity index¹⁶ S and regularity coefficient $\Delta S\%$ [54]. The aim is seeking for ideal orbits that present regular post-capture legs resulting in n revolutions about the target similar in both orientation and shape. Numerical experiments showed that high-quality, post-capture orbits are associated to small regularity index and coefficient [25, 50, 53, 54]. Capture occurrence is quantitatively measured through the capture ratio \mathcal{R}_C [50]. Typically, search spaces characterized by a large capture ratio are desirable when looking for BC orbits.

¹⁶In previous works, this was referred to as stability index [25, 50, 53]. However, the adjustment from *stability* to *regularity* index was proposed in [54] to avoid misunderstandings with the periodic orbit stability index. The same nomenclature introduced in [54] is used in this dissertation.

3.1 Weak stability boundary

Over the years, the weak stability boundary (WSB) was defined in several different ways. It was initially identified as a fuzzy boundary region placed at approximately 1.5×10^6 km from the Earth in the Sun–Earth direction [45, 55]. An algorithmic definition followed in [56], later extended in [18, 57, 58]. Then, it was interpreted as the intersection of three sub-sets of the phase space [59, 60]. The WSB being closely connected to BC [56], a formal definition and a methodology for its derivation from weakly stable and unstable sets were finally proposed in [19]. The fascinating idea of extending the WSB concept to the interstellar space including dark matter was discussed in [61]. To date, despite the effort put in numerous works [57, 59, 60, 62, 63], both WSB and BC are still not completely understood. Nonetheless, a connection between celestial and quantum mechanics was recently found exploiting the WSB [64], providing a fresh perspective to tackle the problem.

3.2 Definition of particle stability

A particle stability is inferred using a plane in the three-dimensional physical space [41]. According to the spatial stability definition provided in [25]. The following indications are used to classify stability (see [25] for more details):

- 1) a particle completes a revolution around the target according to *Remark 1* and Eq. (5) in [25];
- 2) a particle escapes from the target according to *Remark 2* and Eq. (6) in [25];
- 3) a particle impacts with the target according to *Remark 3* and Eq. (7) in [25].

Variants of Eq. (7) in [25] can be derived to locate impacts with target's moons.

Based on its dynamical behavior, a propagated trajectory is said to be:

- i) *weakly stable* (sub-set \mathcal{W}_i) if the particle performs i complete revolutions around the target without escaping or impacting with it or its moons;
- ii) *unstable* (sub-set \mathcal{X}_i) if the particle escapes from the target before completing the i th revolution;
- iii) *target–crash* (sub-set \mathcal{K}_i) if the particle impacts with the target before completing the i th revolution;
- iv) *moon–crash* (sub-set \mathcal{M}_i) if the particle impacts with one of the target's moons before completing the i th revolution;
- v) *acrobatic* (sub-set \mathcal{D}_i) if none of the previous conditions occurs within the integration time span.

Conditions ii)-v) apply after the particle performs $(i - 1)$ revolutions around the target (see Figure 3.1). The sub-sets are defined for $i \in \mathbb{Z} \setminus \{0\}$, where the sign of i informs on the propagation direction. When $i > 0$ ($i < 0$) the IC is propagated forward (backward) in time. The overall domain, union of all sub-sets, is defined Ω . A graph clarifying the relations between sub-sets is shown in Figure 3.2. A capture set is defined as $\mathcal{C}_{-1}^n := \mathcal{W}_n \cap \mathcal{X}_{-1}$. Therefore, it is the intersection between the stable set in forward time \mathcal{W}_n and the unstable set in backward time \mathcal{X}_{-1} [25].

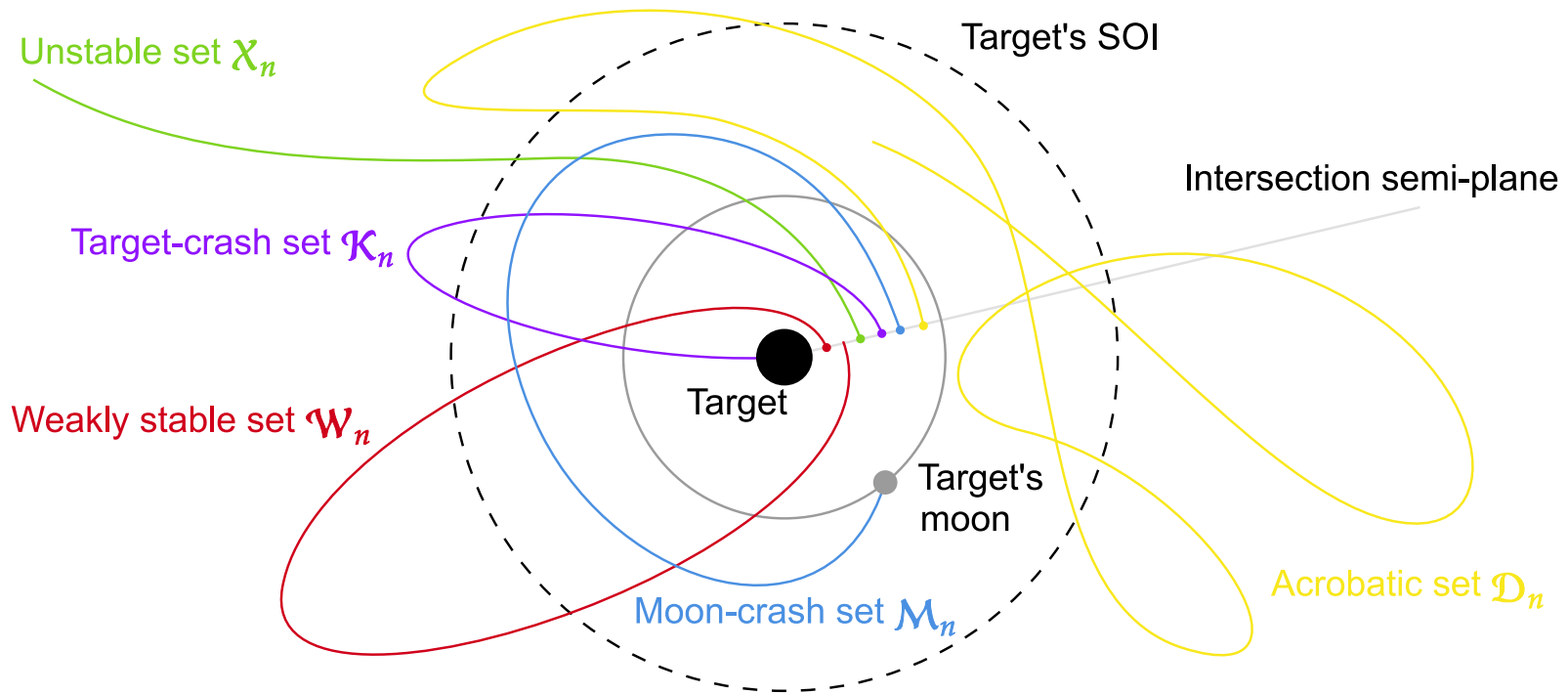


Figure 3.1: Illustration of particle stability. Weakly stable set \mathcal{W}_n in red, unstable set \mathcal{X}_n in green, target-crash set \mathcal{K}_n in purple, moon-crash set \mathcal{M}_n in blue, and acrobatic set \mathcal{D}_n in yellow. Example with $n = 1$.

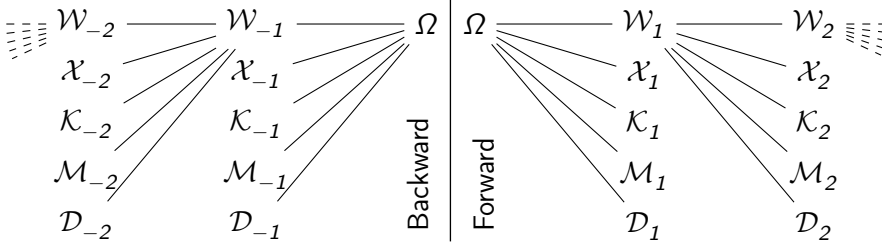


Figure 3.2: Sets relations according to the algorithmic definition of WSB.

3.3 Design of ballistic capture orbits

Currently, two approaches are known for designing BC orbits: the technique stemmed from invariant manifolds [62, 65], and the method based on stable sets manipulation [19, 25]. The former gives insights into the dynamics but it is only applicable to autonomous systems akin to the circular restricted three-body problem (CR3BP), while the latter can be applied to more representative, non-autonomous models, although it being computationally expensive [18, 50]. Lately, continuation from periodic orbits computed in the autonomous case [54], the variational theory for Lagrangian coherent structures (LCSs) [36, 66], and the Taylor differential algebra [67] were applied to derive BC orbits and the WSB more efficiently [68, 69].

3.4 The role of solar gravity gradient

Previous works highlight the fundamental role covered by the solar gravity gradient in the BC mechanism [43, 52]. The solar gravity gradient is computed as the first order term of the Taylor expansion w.r.t. the position vector about the origin of the Mars-centered frame. In the RPF, it is computed as

$$\delta\ddot{\mathbf{r}}_{\odot} \approx -\mu_{\odot} \left(\frac{1}{\|\mathbf{r}_{\odot}\|^3} \mathbf{I}_{3 \times 3} - 3 \frac{\mathbf{r}_{\odot} \mathbf{r}_{\odot}^{\top}}{\|\mathbf{r}_{\odot}\|^5} \right) \delta \mathbf{r} \quad (3.1)$$

with $\mathbf{r}_{\odot} = \mathbf{r}_{\odot}(t)$ and $\delta \mathbf{r} = [x \ y \ z]^{\top}$ since the expansion is computed about the origin of the Mars-centered frame. In the RPF, it is computed as

$$\delta\ddot{\boldsymbol{\rho}}_{\odot} \approx -\frac{a_{\odot}^3 (1 - \mu)}{\|\mathbf{r}_{\odot}\|^3} \begin{bmatrix} -2 & 1 & 1 \end{bmatrix} \delta \boldsymbol{\rho} \quad (3.2)$$

where $a_{\odot} = 2.279 \times 10^8$ km is the semi-major axis of the Sun–Mars system, and $\delta \boldsymbol{\rho} = [(X - 1 + \mu) \ Y \ Z]^{\top}$.

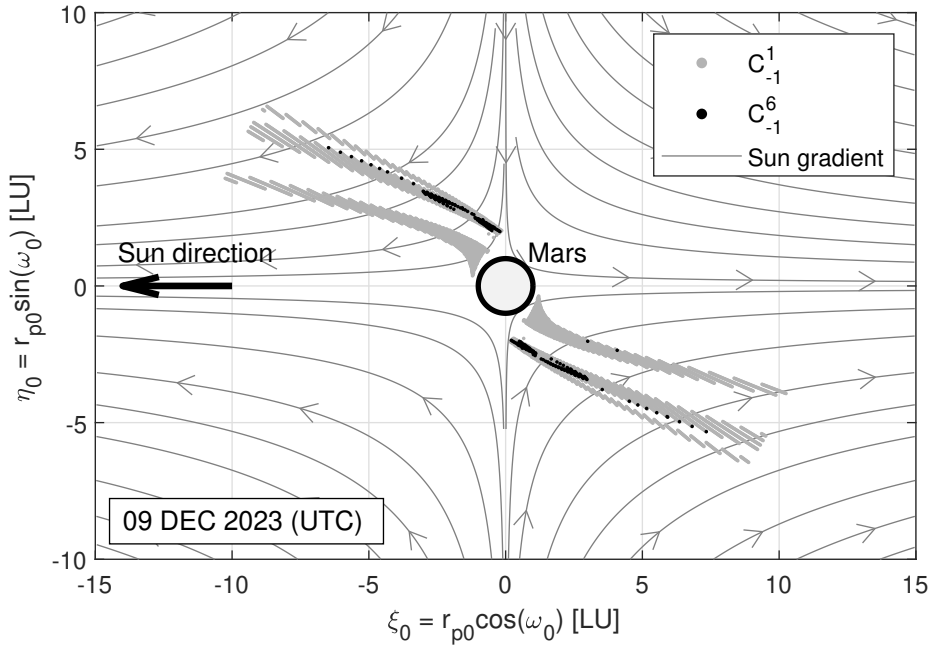


Figure 3.3: Capture sets \mathcal{C}_{-1}^1 and \mathcal{C}_{-1}^6 inspected against solar gravity gradient. Capture sets and solar gravity gradient computed at capture epoch t_0 set to December 9, 2023 at 12:00:00.00 (UTC). Nondimensional coordinates on the orbital plane $i_0 = \Omega_0 = 0$ rad defined in the Mars-centered $\text{RTN}@t_0$ frame.

Depending on where a spacecraft is currently flying, the solar gravity gradient differently affects the spacecraft velocity. In particular, tangential velocity and solar gravity field lines [43, 52]:

- i) have opposite directions in the I and III quadrants;
- ii) have the same directions in the II and IV quadrants.

The further the spacecraft is from Mars, the stronger is the solar gravity gradient. The strongest effect is in correspondence of osculating apocenters of the orbit, where the solar gravity gradient slowly raises or reduces the osculating semi-major axis a of the orbits by small amounts [43]. In light of the considerable time spent by the spacecraft in the apocenter region, the energy increases or decreases based on the actual quadrant in which the spacecraft is flying [43].

Figure 3.3 shows an example¹⁷ where streamlines of the solar gravity gradient are plotted on the background of capture sets \mathcal{C}_{-1}^1 and \mathcal{C}_{-1}^6 . Results are represented in the Mars-centered $\text{RTN}@t_0$ frame. As a consequence, the Sun direction is aligned with the $-x$ direction. In Figure 3.4, an example \mathcal{C}_{-1}^1 trajectory is inspected against streamlines of the solar gravity gradient in the RPF.

¹⁷EoM include gravitational attractions of the Sun, Mercury, Venus, Earth–Moon (B), Mars (central body), Jupiter (B), Saturn (B), Uranus (B) and Neptune (B), and SRP.

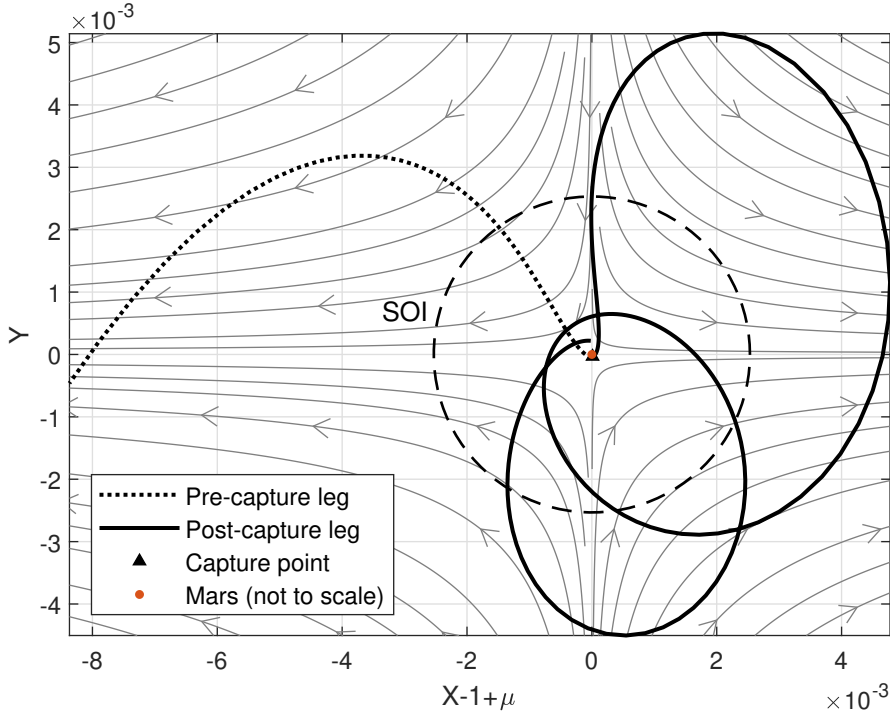


Figure 3.4: C_{-1}^1 trajectory inspected against the solar gravity gradient. Trajectory capture epoch t_0 set to December 9, 2023 at 12:00:00.00 (UTC). Capture point located in the IV quadrant. Nondimensional coordinates in the RPF.

3.5 Effect of physical parameters

The influence on the BC phenomenon of the central body eccentricity and true anomaly, the mass ratio, and the osculating orbital plane orientation of the particle are herewith summarized based on the results reported in [50, 70].

Target eccentricity. Increasing eccentricity results in higher values of the capture ratio \mathcal{R}_C and thus denser capture sets [50]. Moreover, trajectories obtained in the CR3BP qualitatively differ from those computed in more realistic dynamics like the elliptic restricted three-body problem (ER3BP) or n -body models. Therefore, variations in the regularity index S are likely to be observed as well [50].

Target true anomaly. Variations in both \mathcal{R}_C and S are observed considering different true anomalies f_t of the target body. In particular [50]:

- i) \mathcal{R}_C is maximized (i. e., capture set is larger) when:
 - a) $f_t \in [\pi/2, 3\pi/2]$ for prograde orbits;
 - b) $f_t \in [0, \pi/2] \vee [3\pi/2, 2\pi]$ for retrograde orbits;
- ii) S_{\min} is minimized (i. e., orbits are more regular) when $f_t \in [0, \pi/2]$ for both prograde and retrograde orbits.

Mass ratio. The mass ratio μ covers a fundamental role in the capture probability (quantitatively) and capability (qualitatively). The major findings of the assessment carried out in [70] are:

- i) the larger the mass ratio μ , the easier is the BC manifestation;
- ii) for similar mass ratio μ , capture capability may be increased by the primary and/or secondary having minuscule normalized radii;
- iii) capture sets of systems with large mass ratios are structurally different from those of exhibiting small mass ratios;
- iv) post-capture stability with respect to primaries is nearly independent of the mass ratio μ , but post-capture stability regarding their primaries is not;
- v) ranges of Jacobi constant guaranteeing high capture probability and fine capture capability exist and are obtained by merging results of prograde and retrograde branches.

Particle osculating orbital plane orientation. The orientation of the plane associated with the particle IC covers a role too. In particular, according to [50]:

- two inclination ranges maximize the capture ratio: $i_0 \in [40, 70]$ deg and $i_0 \in [150, 160]$ deg, thus the maximum chance for capture does not occur in the Sun–target plane;
- capture is sensitive to right ascension of the ascending node (RAAN) Ω_0 , but no distinct pattern is appreciated;
- prograde orbits evolve in more regular post-capture dynamics;
- the minimum regularity index S_{\min} depends on i_0 and Ω_0 (i. e., on the initial osculating plane orientation), especially for polar orbits.

3.6 Influence of moons and perturbations

Effects on BC by gravitational attractions of many bodies besides the primaries and SRP have been investigated in previous works [10, 11, 50, 53], with [11], and [10] also considering the target NSG perturbations. Compared to the restricted three-body problem, the restricted n -body model is more adequate for constructing ballistic capture orbits as proved in [50], with a particle being more easily captured when considering additional gravitational attractions. The presence of moons increases the capture ratio \mathcal{R}_c and improves the regularity of post-capture orbits while accommodating larger pre-capture energies [53]. In fact, fly-bys of target's moons can be exploited to achieve a zero-cost permanent capture [53]. In some cases, upon completion of the fly-by, the Kepler energy is decreased such that the particle remains thereafter trapped about the central body. However, to achieve a significant change in the energy of the particle, the moon should have a strong enough gravitational influence. Consequently, only large natural satellites such as the Moon or those orbiting the outer planets are viable options in a real case scenario [53]. Similarly, SRP may increase the chances of being temporarily captured about the target and regularizes the post-capture legs [10, 11]. Even if not duly discussed,

the aforementioned remarks are observed also in the results of this work. Overall, supplementary terms in the dynamics seem to favor the manifestation of the BC phenomenon, so increasing capture chances.

To illustrate quantitative and qualitative variations in capture sets when additional perturbations are considered, ten \mathcal{C}_{-1}^6 capture sets are constructed¹⁸ following the methodology discussed in [25]. The search space is chosen to maximize the capture ratio \mathcal{R}_C based on the analysis reported in [50]. It is defined in the Mars-centered RTN@ t_i reference frame at ten capture epochs t_0 uniformly distributed from January 1, 2030 at 12:00:00.000 (UTC) to February 20, 2032 at 10:32:39.144 (UTC), so covering a complete Earth–Mars synodic period of ≈ 780 days. The selected plane is defined by inclination i_0 and RAAN Ω_0 set both equal to 0.2π rad, so maximizing the capture ratio for Mars (according to Figure 10 in [50]). Sought trajectories have osculating eccentricity $e_0 = 0.99$ [9], and true anomaly $\theta_0 = 0$ rad at initial epochs t_0 . Let $R_{\mathcal{O}^*}$ be the radius of Mars in km, then the search space on the plane defined above is a circular crown centered at Mars, from radius $R_{\mathcal{O}^*} + 100$ km up to radius $11R_{\mathcal{O}^*}$. Hence,

$$(r_{p0}, \omega_0) \in [R_{\mathcal{O}^*} + 100 \text{ km}, 11R_{\mathcal{O}^*}] \times [0, 2\pi] \quad (3.3)$$

with r_{p0} the pericenter radius and ω_0 the argument of pericenter. The circular crown is made of $N_{r_{p0}} = 678$ and $N_{\omega_0} = 360$ evenly spaced points of pericenter radius r_{p0} and argument of pericenter ω_0 , respectively.

Figure 3.5 summarizes the quantitative and qualitative information about all the ten \mathcal{C}_{-1}^6 capture sets computed. Among those shown, the best capture set is the one having capture epoch t_0 at November 25, 2031 at 18:40:49.054 (UTC). It shows a large capture ratio and it seems regular. In fact, both the minimum regularity index and coefficient are small. For similar reasons, another valid option would have been the capture set with capture epoch t_{CAP} occurring at January 1, 2030 at 12:00:00.000 (UTC). The best capture set is compared against a poor one in Figure 3.6. The plot in Figure 3.6a shows how the poor capture set is fragmented, unstructured, and irregular when compared to the best one. Results confirm the knowledge already present in the literature [50].

Data availability The data set supporting the findings of this study are available on Zenodo¹⁹ with the identifier <https://doi.org/10.5281/zenodo.5931461>.

¹⁸EoM include gravitational attractions of the Sun, Mercury, Venus, Earth–Moon (B), Mars (central body), Jupiter (B), Saturn (B), Uranus (B) and Neptune (B), SRP, Mars' NSG, and relativistic corrections.

¹⁹<https://zenodo.org/> [last accessed Dec 1, 2022].

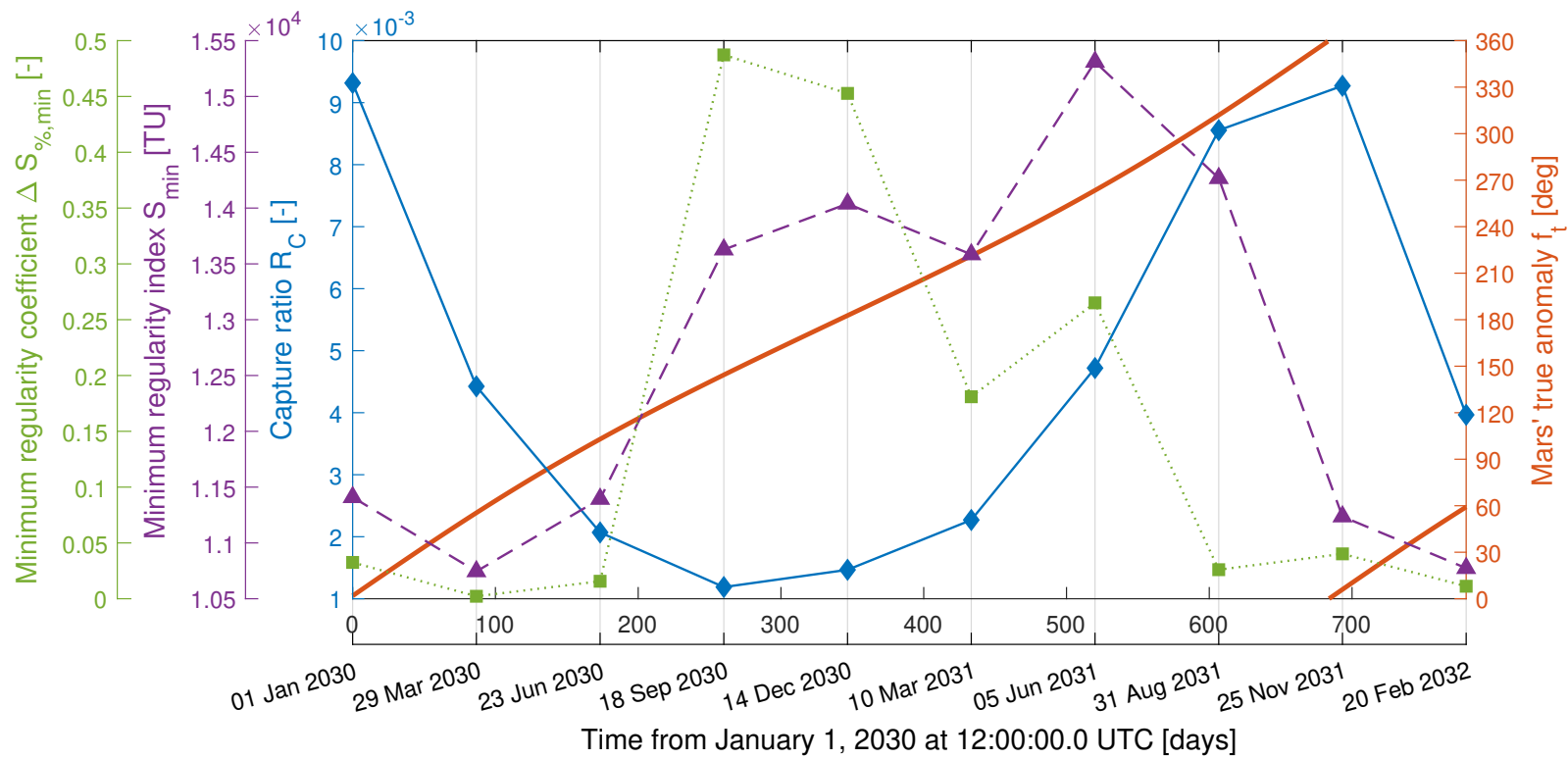
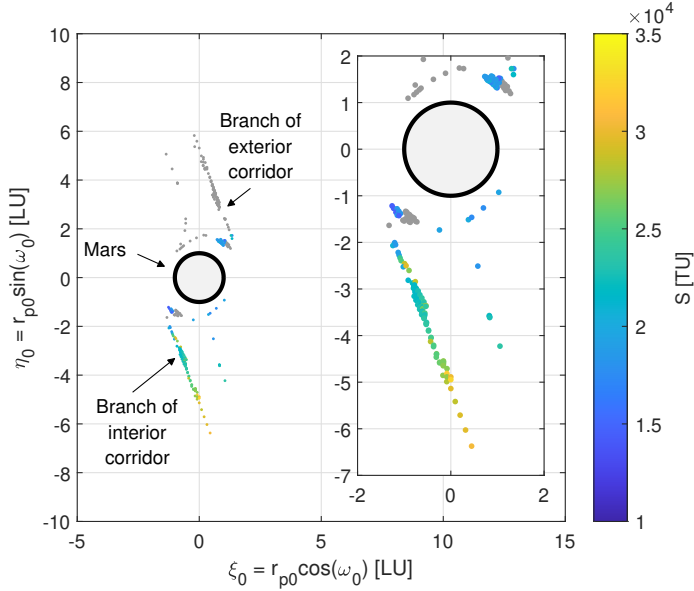
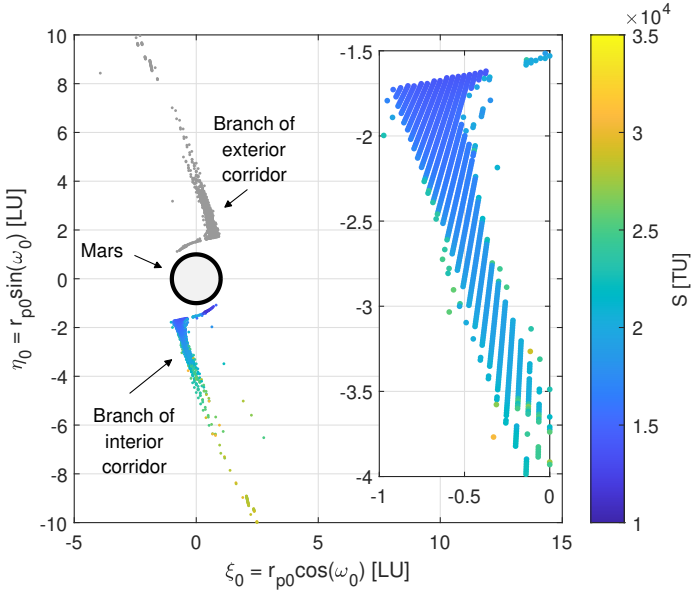


Figure 3.5: Qualitative and quantitative indexes of the ten C_{-1}^6 capture sets as a function of the time past January 1, 2030 at 12:00:00.0 (UTC). Capture epochs of capture sets also shown. On the left y-axes, capture ratio \mathcal{R}_C (thick, blue, filled diamonds line), minimum regularity index S (dashed, purple, filled triangles line), and minimum regularity coefficient $\Delta S_{\%}$ (dotted, green, filled squares line). On the right y-axis, Mars' true anomaly f_t (thick, orange line).



(a) Capture set \mathcal{C}_{-1}^6 at $t_0 =$ September 18, 2030 at 11:30:18.396 (UTC). In the magnification, details close to Mars where capture set is fragmented, unstructured, and irregular. Clusters close to Mars' surface present ICs developing both interior and exterior BCCs.



(b) Capture set \mathcal{C}_{-1}^6 at $t_0 =$ November 25, 2031 at 18:40:49.054 (UTC). In the magnification, details close to Mars where a continuous, structured, and regular region of the capture set is located and from which ICs develop the interior BCC.

Figure 3.6: Capture sets \mathcal{C}_{-1}^6 . Branches developing exterior BBCs are colored in gray. Regularity index of ICs belonging to branches developing interior BCCs. Nondimensional coordinates on the orbital plane $i_0 = \Omega_0 = 0.2\pi$ rad defined in the Mars-centered RTN@ t_0 frame. Mars is the gray circle with black surround.

3.7 GRATIS

GRATIS, which stands for GRavity Tidal Slide, is a toolkit to search for BC opportunities. Based on the algorithmic definition of ballistic capture, the software tool computes, extracts, and manipulates stable sets to derive capture conditions [38]. The BC mechanism arises in highly sensitive regimes where a particle or spacecraft approaches a celestial body and starts revolving around it, completely free of any maneuvers. It being a highly sensitive phenomenon, the implementation of a high-fidelity model is necessary. Currently, GRATIS features a restricted n -body problem. Additionally, it takes into account SRP as well as the central body NSG and relativistic corrections. Essentially, GRATIS can be used to design trajectory branches exhibiting capture about a celestial body.

Pursuing the answers to the research questions posed in this dissertation and achieving the goal set, a modification of the original implementation in GRATIS of the algorithm discussed in [10, 25] was needed. Therefore, to ascertain that GRATIS achieved its purpose in an ideally error-free way, a verification and validation (V&V) campaign was carried out (see Appendix A).

Acknowledgments The author would like to thank T. Caleb, E. La Paglia, and A. Quinci for the extremely valuable content provided to write parts of Chapter 3.

“Everything we see, everyone we meet, is caught up in a great unseen flow. But it’s bigger than that. It’s the entire world, the entire universe even. And compared to something as big as that, AI, you and I are tiny, not even the size of ants. Only one small part within a much greater flow. Nothing more than a fraction of the whole. But by putting all those ‘ones’ together, you get one great ‘All’, just like Teacher said. The flow of this universe follows laws of such magnitude that you and I can’t even imagine them.” – Edward Elric

Hiromu Arakawa, *Fullmetal Alchemist*

Lagrangian coherent structures

A mathematical tool suited for studying complex, non-linear, non-autonomous dynamical systems is represented by LCSs [24, 36, 71–78]. The word Lagrangian highlights the evolution of such structures in the state space throughout time, as opposed to the Eulerian specification of the flow. The behavior of an autonomous dynamical system, with respect to its IC, can be completely studied via fixed points. Unfortunately, this property is lost for non-linear, non-autonomous dynamical systems linked to complex dynamical phenomena. Nevertheless, LCSs represent a robust skeleton of special material surfaces distinguishing regions of qualitatively different dynamics [79].

LCSs can be considered as a generalization of invariant manifolds in non-autonomous systems with arbitrary time dependence. They are time-evolving structures in the phase space of a generic dynamical system forming the skeleton of observed tracer patterns. They are defined on two key properties [36]:

- a LCS should be a material surface, it must have sufficiently high dimension to have visible impact (i. e., acting as transport barrier) and it must move with the flow to operate as an observable core of evolving Lagrangian patterns;
- a LCS should exhibit locally the strongest attraction, repulsion or shearing in the flow, which is essential to distinguish it from all nearby material surfaces.

LCSs can be defined as the point-wise strongest repelling, attracting or shearing material surfaces in the flow over a finite horizon of interest, as shown in Figure 4.1. In particular, repelling LCSs are the core structures responsible for stretching. On the other hand, attracting LCSs act as centerpieces of folding. Finally, shear LCSs delineate swirling and jet-type patterns [66].

From their physical interpretation, LCSs result of very interest for the study of the dynamics. They separate different dynamics of the flow in space and time, acting as the most important barriers for material flux across them [66]. LCSs can be classified following the same rationale used when analyzing invariant manifolds:

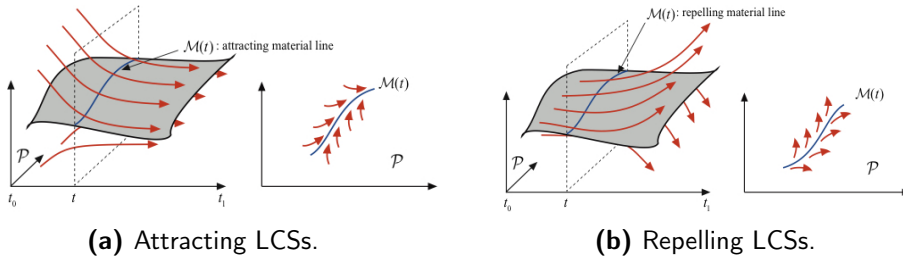


Figure 4.1: Attracting and repelling LCSs in the extended phase space of a two-dimensional dynamical system²⁰.

- hyperbolic LCSs are characterized by the strongest attraction or repulsion;
- elliptic LCSs are closed material surfaces;
- parabolic LCSs are structures defined by the strongest shearing.

When considering autonomous dynamical systems, examples of LCSs are stable and unstable manifolds of fixed points and periodic orbits. The big advantage of LCSs is that they remain applicable to more complex flows with arbitrary time dependence or only defined over a finite horizon (computed or measured). In fact, time-dependent flows admit patterns ruling tracers transport. While in autonomous systems LCSs correspond to invariant manifolds, they evolve with the flow in time-dependent ones, so continuing to bound distinct regions of behavior [66].

In the literature, several indicators were successfully applied to the study of complex, non-linear systems for dynamical structures identification. They are defined by: the Fourier analysis of the solutions, e. g., frequency map [80, 81]; the variation of phase-space variables during the motion, e. g., sup-map analysis [82] and LDs [83]; the solutions of variational equations, e. g., Lyapunov indicators [84], finite-time Lyapunov exponent (FTLE) [71, 72], mean exponential growth factor of nearby orbits (MEGNO) [85], and fast Lyapunov indicator (FLI) [86]. Several comparison papers are available [87–89].

The choice of an indicator is goal oriented. For instance, frequency map discerns regions of regular and chaotic motion [80, 81]. Similarly, Lyapunov indicators discriminate between regular and chaotic motions. Additionally, they can successfully compute stable, unstable, and Lagrangian manifolds [84]. Sup-map analysis [82] and LDs [83] rely on tailored integral norms computed along the motion. FLI informs on the precision loss during the numerical integrations [86, 90]. Modified FLIs identify chaotic regions and L_1 – L_2 manifolds when applied to the three-body problem [91]. Hereafter, selected theories about LCSs and methods for their identification and computation are presented. They include the FTLE [71, 72, 74, 76], the variational theory for LCS [36, 74, 75, 77, 92], and the LD method [24, 76, 83, 93].

²⁰Retrieved from Wikiwand, *Lagrangian Coherent Structures*, https://www.wikiwand.com/en/Lagrangian_coherent_structure [last accessed Dec 1, 2022].

4.1 Finite-time Lyapunov exponents

In a dynamical system of the form like Eq. (2.2), the local measure of the largest separation rate between neighboring ICs can be defined as the maximum FTLE. Essentially, a FTLE is a finite-time average of the maximum expansion rate for close ICs advected by the flow map. Therefore, the FTLE scalar field can be used to locate LCSs in the phase space. According to [71], LCSs are ridges of the FTLE scalar field.

Considering an infinitesimal perturbation $\delta\mathbf{x}(t_0) = \delta\mathbf{x}_0$ to the trajectory and propagating it under the linearized flow over the time interval $[t_0, t_0 + T]$, the largest possible infinitesimal stretching along $\varphi_{t_0}^{t_0+T}(\mathbf{x}_0)$ at $t_0 + T$ is given by the largest eigenvalue of the STM $\Phi_{t_0}^{t_0+T}(\mathbf{x}_0)$. Recalling Eq. (2.19), the linearized evolution of the infinitesimal perturbation $\delta\mathbf{x}_0$ after a finite time T can be analyzed exploiting the CGST. The maximum stretching occurs when $\delta\mathbf{x}_0$ is aligned with the eigenvector associated with the maximum eigenvalue λ_n of the CGST $\Delta_{t_0}^{t_0+T}$. Then, the associated FTLE is defined as

$$\Lambda_{t_0}^{t_0+T}(\mathbf{x}_0) = \frac{1}{|T|} \|\Phi_{t_0}^{t_0+T}(\mathbf{x}_0)\| = \frac{1}{2|T|} \ln(\lambda_n) \quad (4.1)$$

where $\|\Phi_{t_0}^{t_0+T}(\mathbf{x}_0)\|$ is the operator norm of the deformation gradient that is equal to the square root of the maximum eigenvalue $\lambda_n(\mathbf{x}_0, t_0; t_0 + T)$ of the CGST.

The finite horizon $T = t - t_0$ can be chosen both positive and negative. In particular, forward-time integration locates repelling LCSs (i. e., stable manifolds in autonomous systems), while backward-time propagation locates attracting LCSs (i. e., unstable manifolds in autonomous systems). Specifically, LCSs are defined as the ridges of FTLE field that is computed for each point inside the domain of interest. At time t_0 a repelling LCS over $[t_0, t]$ should appear as a ridge of the FTLE field. Conversely, an attracting LCS over $[t_0, t]$ should be a ridge of the backward-time field [71, 94]. For instance, consider a generic hyperbolic point and its stable and unstable manifolds, as shown in Figure 4.2. The two points on either side of the stable manifold will diverge after a sufficient amount of time. Therefore, large values of the FTLE field are expected along the stable manifold and, roughly speaking, as T increases the LCS becomes better resolved [71].

The drawback of relying on the FTLE field is that there are not mathematical theorems supporting LCSs existence. As a consequence, FTLE ridges may fail in detecting LCSs, so producing false positives or missing existing LCSs. This even in simple two-dimensional steady flows [36]. Examples where FTLE ridges indicate maxima of shear, as opposed to repelling LCSs, exist too. In fact, observed LCSs are not necessarily FTLE field ridges, and FTLE field ridges are not necessarily hyperbolic LCSs²¹ [36]. Nevertheless, the approach is useful for preliminary quick explorations of the phase space. In a two-dimensional phase space, ridges identification is even easier because they can be found by visual inspection.

²¹This because the procedure completely ignores the direction of the eigenvector associated to the largest eigenvalue and it can be considered only statistically robust [79].

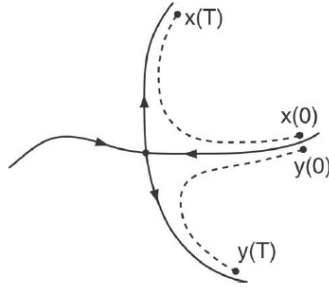


Figure 4.2: Qualitative behavior of two example points straddling a stable manifold that diverges after a sufficient amount of time. Figure from [71].

4.2 Variational theory for LCSs

To solve for inconsistencies in LCSs detection when relying on the FTLE ridges, a variational theory has been developed by Haller [36, 92]. Haller defined hyperbolic LCSs as locally most repelling or attracting material surfaces [95]. He derived a variational theory providing sufficient and necessary conditions for hyperbolic LCS in terms of the CGST invariants.

The variational theory seeks special material surfaces that act as organizing centers of observed trajectory patterns [36]. Such material surfaces distinguish themselves by attracting or repelling nearby trajectories at locally the highest rate in the flow. Consider a material surface $\mathcal{M}(t_0)$ that is advected by the flow map into a time evolving material surface $\mathcal{M}(t) = \varphi_{t_0}^t(\mathcal{M}(t_0))$ (see Figure 4.3). The time evolving material surface $\mathcal{M}(t)$ has codimension 1 with respect to the state vector \mathbf{x} . For each point $\mathbf{x}_0 \in \mathcal{M}(t_0)$, the evolution of the unit \mathbf{n}_0 normal to $\mathcal{M}(t_0)$ advected by the linearized flow map is monitored. The normal repulsion rate $\rho_{t_0}^t(\mathbf{x}_0, \mathbf{n}_0)$ is the length of the surface-normal component of the advected vector $D_{\mathbf{x}_0} \varphi_{t_0}^t(\mathbf{x}_0) \mathbf{n}_0$, and quantifies the normal attraction or repulsion of $\mathcal{M}(t)$. Furthermore, the advected normal also has a tangential component of length $\sigma_{t_0}^t(\mathbf{x}_0, \mathbf{n}_0)$ (see Figure 4.3). If $\rho_{t_0}^t(\mathbf{x}_0, \mathbf{n}_0) > 1$, then the evolving material surface exerts net normal repulsion on nearby particles. Conversely, when $\rho_{t_0}^t(\mathbf{x}_0, \mathbf{n}_0) < 1$ means that it attracts particles along its normal direction. On the other hand, $\sigma_{t_0}^t(\mathbf{x}_0, \mathbf{n}_0) > 0$ signals shear exerted by $\mathcal{M}(t)$ on nearby elements [66].

The normal repulsion rate can be computed in terms of the CGST as [36]

$$\rho_{t_0}^t(\mathbf{x}_0, \mathbf{n}_0) = \frac{1}{\sqrt{\langle \mathbf{n}_0, [\Delta_{t_0}^t(\mathbf{x}_0)]^{-1} \mathbf{n}_0 \rangle}}. \quad (4.2)$$

The repulsion ratio $\nu_{t_0}^t(\mathbf{x}_0, \mathbf{n}_0)$ is defined to assess which effect is dominant between repulsion and shearing. It is computed as [36]

$$\nu_{t_0}^t(\mathbf{x}_0, \mathbf{n}_0) = \min_{\substack{|\mathbf{e}_0|=1 \\ \mathbf{e}_0 \in \mathcal{T}_{\mathbf{x}_0} \mathcal{M}(t_0)}} \frac{\rho_{t_0}^t(\mathbf{x}_0, \mathbf{n}_0)}{\sqrt{\langle \mathbf{e}_0, \Delta_{t_0}^t(\mathbf{x}_0) \mathbf{e}_0 \rangle}}, \quad (4.3)$$

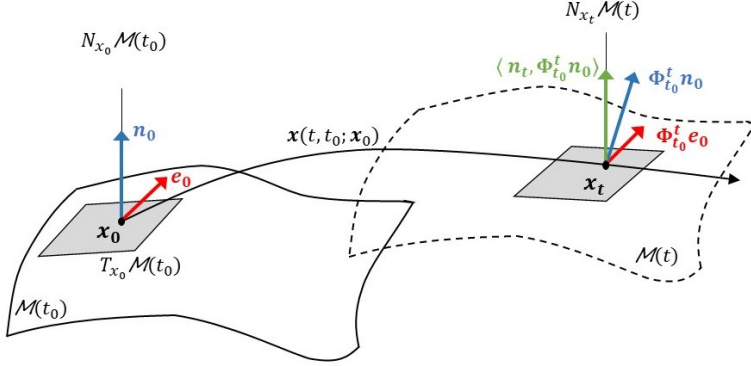


Figure 4.3: Advection of $\mathcal{M}(t_0)$, $\mathcal{T}_{x_0} \mathcal{M}(t_0)$, and \mathbf{n}_0 . Figure from [36].

where \mathbf{e}_0 is a unit tangent vector lying in the tangent space $\mathcal{T}_{x_0} \mathcal{M}(t_0)$. If inequality $\nu_{t_0}^t(\mathbf{x}_0, \mathbf{n}_0) > 1$ is verified, then the normal growth is larger than the tangential one. Under this condition, a repelling (attracting) LCS is a material surface $\mathcal{M}(t)$ whose net repulsion $\rho_{t_0}^t(\mathbf{x}_0, \mathbf{n}_0)$ is pointwise maximal (minimal) when perturbing \mathbf{n}_0 (see Figure 4.4). A shear LCSs is a material surface maximizing the net shear $\sigma_{t_0}^t(\mathbf{x}_0, \mathbf{n}_0)$ and satisfying $\nu_{t_0}^t(\mathbf{x}_0, \mathbf{n}_0) < 1$ [66]. Sufficient and necessary conditions for a material surface to be a repelling LCS were derived in [36].

Theorem 4.2.1. Considering a compact material surface $\mathcal{M}(t) \subset U \subset \mathbb{R}^n$ over a time interval $[t_0, t]$, it is a repelling LCS over the given time interval if and only if the following conditions are satisfied $\forall \mathbf{x}_0 \in \mathcal{M}(t_0)$:

1. $\lambda_{n-1}(\mathbf{x}_0, t_0; t) \neq \lambda_n(\mathbf{x}_0, t_0; t) > 1$;
2. $\xi_n(\mathbf{x}_0, t_0; t) \perp \mathcal{T}_{x_0} \mathcal{M}(t_0)$;
3. $\langle D_{x_0} \lambda_n(\mathbf{x}_0, t_0; t), \xi_n(\mathbf{x}_0, t_0; t) \rangle = 0$;
4. $\mathbf{L}(\mathbf{x}_0, t_0; t)$ positive definite²² $\forall \mathbf{x}_0 \in \mathcal{M}(t_0)$.

with

$$\mathbf{L} = \begin{bmatrix} D_{x_0}^2 \Delta^{-1} [\xi_n, \xi_n, \xi_n, \xi_n] & 2 \frac{\lambda_n - \lambda_1}{\lambda_1 \lambda_n} \langle \xi_1, D_{x_0} \xi_n \xi_n \rangle & \dots & 2 \frac{\lambda_n - \lambda_{n-1}}{\lambda_{n-1} \lambda_n} \langle \xi_{n-1}, D_{x_0} \xi_n \xi_n \rangle \\ 2 \frac{\lambda_n - \lambda_1}{\lambda_1 \lambda_n} \langle \xi_1, D_{x_0} \xi_n \xi_n \rangle & \frac{2\lambda_n - \lambda_1}{\lambda_1 \lambda_n} & \dots & 0 \\ \vdots & \vdots & \ddots & \vdots \\ 2 \frac{\lambda_n - \lambda_{n-1}}{\lambda_{n-1} \lambda_n} \langle \xi_{n-1}, D_{x_0} \xi_n \xi_n \rangle & 0 & \dots & \frac{2\lambda_n - \lambda_{n-1}}{\lambda_{n-1} \lambda_n} \end{bmatrix} \quad (4.4)$$

where the first diagonal term in Eq. (4.4) is

$$D_{x_0}^2 \Delta^{-1} [\xi_n, \xi_n, \xi_n, \xi_n] = -\frac{1}{\lambda_n^2} \langle \xi_n, D_{x_0}^2 \lambda_n \xi_n \rangle + 2 \sum_{q=1}^{n-1} \frac{\lambda_n - \lambda_q}{\lambda_n \lambda_q} \langle \xi_q, D_{x_0} \xi_n \xi_n \rangle^2. \quad (4.5)$$

²²At the present-day, $\mathbf{L}(\mathbf{x}_0, t_0, t)$ is not associated to any physical meaning.

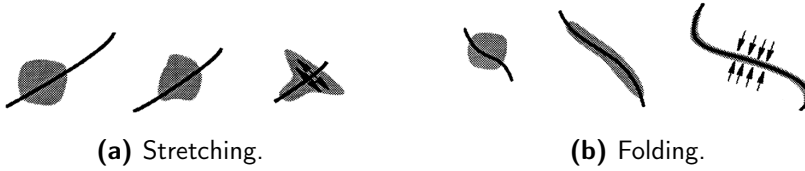


Figure 4.4: The role of coherent structures. Figure from [95].

In Theorem 4.2.1, condition 1 ensures that the normal repulsion rate is larger than the tangential stretch due to shear along the LCS. Together, conditions 2 and 3 guarantee that repulsion rate attains a local extremum along the LCS relative to all C^1 -close material surfaces. Finally, condition 4 ensures that this extremum is a strict local maximum [96]. Theorem 4.2.1 is valid in general for n -dimensional problems. Conditions of Theorem 4.2.1 are reformulated specializing the theorem for two-dimensional flows and accounting for numerical sensitivity and implementation robustness as follows [36, 92, 96]:

- A. $\lambda_1(\mathbf{x}_0, t_0; t) \neq \lambda_2(\mathbf{x}_0, t_0; t) > 1$;
- B. $\langle \xi_2(\mathbf{x}_0, t_0; t), D_{\mathbf{x}_0}^2 \lambda_2(\mathbf{x}_0, t_0; t) \xi_2(\mathbf{x}_0, t_0; t) \rangle \leq 0$;
- C. $\xi_1(\mathbf{x}_0, t_0; t) \parallel \mathcal{M}(t_0)$;
- D. $\bar{\lambda}_2(\gamma)$, the average of λ_2 over a curve γ , is maximal on $\mathcal{M}(t_0)$ among all nearby curves γ satisfying $\gamma \parallel \xi_1(\mathbf{x}_0, t_0; t)$.

According to condition C, repelling LCSs are material curves tangent to ξ_1 , the eigenvector field associated with the smallest eigenvalue of the CGST. Lines tangent to ξ_1 are called strainlines [96]. Numerical algorithms implementing LCSs variational theory are based on the computation of strainlines constituting LCS candidates set. Then, effective LCSs are extracted from the candidates set through filtering [96].

To compute an attracting LCSs a similar procedure can be adopted. As counterparts of strainlines, stretchlines are the curves of the phase space that exhibit compressing forces and are associated to attracting LCSs. They are material curves tangent to the ξ_2 vector field. Attracting and repelling LCSs can be constructed from a single forward-time propagation [97].

4.3 Lagrangian descriptors

LDs are heuristic quantities for revealing the underlying template of geometrical structures that determine transport in phase space for a generic dynamical system [83]. They are based on the integration of a bounded, positive property of the trajectory over a finite horizon. The first definition of LDs relied on the computation of the arc length of particle trajectories as they evolve forward and backward in time [98]. Later, the method was extended to include other positive quantities. The methodology found several applications in different scientific areas, such as ocean currents, atmospheric sciences, and chemistry [83, 98].

LDs provide insight that appears to be linked with the the geometric pattern

of structures that govern transport in phase space. Their definition and heuristic arguments explaining why they are effective are presented in [83]. A theoretical framework is discussed in [93]. However, the connection between LDs and geometric patterns governing the transport in phase space is controversial and largely disputed in the literature. Indeed, LDs are not derived from mathematically well defined variational principles, thus their relation to invariant manifolds is unclear and mathematically not well defined [66, 89]. Moreover, LDs are not objective, i. e., structures resulting from the scalar field depend on the frame of the observer, whereas material curves such as periodic orbits are frame-indifferent [99, 100]. Finally, counter-examples to the method of Lagrangian descriptors are discussed in the literature. Specifically, they face smooth contour lines of LD at invariant manifolds, singular features of LD at irrelevant points, and failure when dealing with Hamiltonian systems [99].

Let us consider a general time-dependent vector field on \mathbb{R}^n

$$\frac{d\mathbf{x}(t)}{dt} = \mathbf{f}(\mathbf{x}, t), \quad \text{with } \mathbf{x} \in \mathbb{R}^n, \quad \text{and } t \in \mathbb{R}. \quad (4.6)$$

Assuming the velocity field C^r ($r \geq 1$) in \mathbf{x} and continuous in t , a unique solution allowing for linearization exists. Given the initial time t_0 and the integration time span $[t_0 - \tau, t_0 + \tau]$, the Euclidean arc length \tilde{M} of the curve in the phase space defined by propagating an IC $\mathbf{x}(t_0) = \mathbf{x}_0$ through Eq. (4.6) is [83]

$$\tilde{M}(\mathbf{x}_0, t_0, \tau) = \int_{t_0 - \tau}^{t_0 + \tau} \sqrt{\sum_{i=1}^n \left(\frac{dx_i(t)}{dt} \right)^2} dt = \int_{t_0 - \tau}^{t_0 + \tau} \|\mathbf{f}(\mathbf{x}, t)\| dt. \quad (4.7)$$

Results depend on the finite horizon chosen. \tilde{M} can be computed appending its integrand to the space state equations with a zero initial value and propagating the extended dynamics. Trajectories propagated from close ICs remaining close as they evolve in time are expected to have similar \tilde{M} [83]. Differently, abrupt changes in the field are associated to separatrices of the dynamics. Such features are expected to exhibit a discontinuity in the derivative of \tilde{M} along the direction perpendicular to the separatrix [83, 93].

There exist other positive intrinsic physical or geometrical properties of trajectories that can be integrated to successfully identify geometric patterns. The general formulation is [83]

$$\begin{cases} M(\mathbf{x}_0, t_0, \tau) = \int_{t_0 - \tau}^{t_0 + \tau} |\mathcal{F}(\mathbf{x}(t))|^\gamma dt & \text{for } \gamma \leq 1 \\ M(\mathbf{x}_0, t_0, \tau) = \left(\int_{t_0 - \tau}^{t_0 + \tau} |\mathcal{F}(\mathbf{x}(t))|^\gamma dt \right)^{\frac{1}{\gamma}} & \text{for } \gamma > 1 \end{cases} \quad (4.8)$$

where γ defines the L^γ norm of the integrand. An extensive class of different LDs was defined in [83] based on the integrand, the selected norm, and the integration interval (see Table 4.1). The definition of any function M_i can be broken in a

Table 4.1: Class of LDs with integrand and norm [83, 93].

LD	$ \mathcal{F}(\mathbf{x}(t)) $	Integrand description	Norm
M_1	$\ \mathbf{v}(t)\ $	Magnitude of velocity	L^1
M_2	$\ \mathbf{a}(t)\ $	Magnitude of acceleration	L^1
$M_{3,1}$	$\ \mathbf{v}(t)\ $	Magnitude of velocity	$L^{1/2}$
$M_{3,2}$	$\ \mathbf{a}(t)\ $	Magnitude of acceleration	$L^{1/2}$
M_4	$\ \dot{\mathbf{a}}(t)\ $	Magnitude of acceleration derivative	L^1
M_5	$(\kappa + a)^{-1}$	Positive quantity related to curvature [†]	L^1
M_6	$\ \mathbf{x}(t)\ $	Magnitude of space state	L^1
M_7	$\ \mathbf{x}(t)\ $	Magnitude of space state	$L^{1/2}$
M_8	$\sum_{i=1}^n x_i(t) ^p$	Sum of p -root terms [‡]	L^p

[†] With $\kappa = [(\mathbf{v} \cdot \mathbf{v})(\mathbf{a} \cdot \mathbf{a}) - (\mathbf{v} \cdot \mathbf{a})^2] / v^3$ and $1 \leq a \leq 5$ to avoid singularities [83].

[‡] It is suggested to choose $p = 1/\tau$ [93].

natural way into forward and backward integration to obtain LDs M_i^f and M_i^b , respectively. The forward propagation should highlight stable manifolds of the dynamical system, while the backward one recovers unstable ones [101]. Their combination is capable to detect all invariant manifolds simultaneously.

A key property common to all LDs is that they monotonically increase along a trajectory. Indeed, they are integrals of positive quantities. It being a heuristic approach, similarly to the FTLE, there is the possibility that they may fail in identifying LCSs correctly. This is due to the lack of mathematical proofs providing necessary and/or sufficient conditions supporting LCSs existence.

4.4 Application to ballistic capture

Different studies investigated LCSs applied to the restricted three-body problem in the frame of BC. In the CR3BP context, FTLE fields reveal intersections of invariant manifolds of periodic orbits with Poincaré cuts [72]. However, the FTLE approach becomes helpful when the ER3BP model is considered. The existence of periodically pulsating LCSs in the phase space of the ER3BP exploiting the FTLE method was demonstrated in [72]. These pulsating structures proved to be the time-dependent analogues of invariant manifolds in the circular problem.

WSBs play the role of dynamics separatrices, distinguishing phase space regions with different global behavior. In previous works, the FTLE field proved to be a convenient tool to get the shape of the WSB [102, 103]. LCSs extraction from their variational theory was also applied to the computation and understanding of BC orbits in the area of stable sets manipulation both in the planar [68, 102, 103] and spatial [77, 78, 104] ER3BP. Results show that repelling LCSs obtained with their variational theory match with boundaries of stable sets [68, 78]. However, correspondence between strainlines and the WSB is not perfect. The reason could

reside in the high sensitivity of LCSs to different particle dynamics and in the usage of a fixed finite horizon [68, 103]. Indeed, times of flight in stable sets are not constant [19, 69].

More recently, a characterization of the ER3BP dynamics in the Mars proximity based on the LD method was discussed in [105]. Geometrical structures featured by LD scalar fields were extracted through an edge detection algorithm and inspected against the WSB derived over similar finite horizons. For a fair comparison, the particle stability definition was modified to relax the geometrical constraint on the number of completed revolutions [19, 25]. Eventually, capture sets at Mars were identified in the intricate plot of separatrices, thereby showing a strong correlation between extracted separatrices and the WSB.

4.5 LCSs extraction techniques trade-off

The presented approaches identify separate regions in which qualitatively different dynamical behaviors arise. In non-autonomous dynamical systems (e. g., ER3BP, n -body problem) families of hyperbolic material surfaces may be leveraged to organize tracer mixing. Different heuristic approaches can be exploited to highlight material surfaces, such as FTLEs and LDs. Them being heuristic, these methods could fail in LCSs detection, underlining false positives or false negatives. Nevertheless, they are computationally inexpensive tools useful for a qualitative description of the dynamics. On the other hand, LCSs computation from their variational theory requires additional effort, but eliminates theoretical inconsistencies. Based on the trade-off presented in Table 4.2, LDs appears to be the most suited technique among the three LCS-like methods covered in this chapter.

Acknowledgments The author would like to thank A. Quinci, S. Raffa, and E. Zulli for the extremely valuable content provided to write parts of Chapter 4.

“See that new color on the dial? There’s a new portal. It’s a present for you. Come see.” – Howl

Hayao Miyazaki, *Howl’s Moving Castle (film)*

Table 4.2: LCS-like methods trade-off.

Method	Mathematical proofs	Act as transport barriers	Time information	Difficulty of generalization from 2D to nD	Implementation effort	Computational effort
FTLE field	<u>yellow</u> Weak (heuristic arguments)	<u>blue</u> Not in general (counterexamples available)	<u>blue</u> Forward <u>or</u> backward [†]	<u>green</u> Low	<u>blue</u> Medium (variational eqs.)	<u>blue</u> Medium ($n + n^2$ eqs. to propagate)
Variational theory for LCSs	<u>green</u> Strong (theorems available)	<u>green</u> Yes (mathematically proved)	<u>blue</u> Forward <u>or</u> backward	<u>yellow</u> High (2D & 3D methods available, not nD [‡])	<u>yellow</u> High (variational eqs., PDEs in nD [‡])	<u>yellow</u> High (Cauchy problem plus nested propagation)
Lagrangian descriptors	<u>yellow</u> Weak (heuristic arguments)	<u>blue</u> Not in general (counterexamples available)	<u>green</u> Forward <u>and</u> backward	<u>green</u> Low	<u>green</u> Low (augmented state)	<u>green</u> Low ($n + m$ eqs. to propagate, m small)

green Excellent blue Good yellow Correctable deficiencies red Unacceptable

[†] One could try to use the CGST from $t_0 - T$ to $t_0 + T$, then changing into forward and backward. Alternatively, forward and backward FTLEs can be summed up.

[‡] Methods to solve nD issue are available. Maps from 2D to nD and viceversa can be exploited [68]. 3D method based on reduced strainlines and stretchlines [77, 78, 104]. Alternatively, strainlines (stretchlines) could be constructed along the intersection of a 2D domain and the $(n - 1)$ tangent space perpendicular to the maximum (minimum) stretch direction.

Characterization of ballistic capture corridors

This chapter presents the characterization of BCCs, time-varying manifolds supporting capture. Corridors are mathematically defined, computed via backward propagation in a high-fidelity model, characterized, and studied.

5.1 Definitions

A trajectory is defined as:

Definition. Let $(\mathbf{x}_0, t_0) \in \mathbb{R}^6 \times \mathbb{R}$ and $\varphi(\mathbf{x}_0, t_0; t)$ be the starting point and the solution at time t , respectively, of the Cauchy problem

$$\begin{cases} \dot{\mathbf{x}} = \mathbf{f}(\mathbf{x}, t) \\ \mathbf{x}(t_0) = \mathbf{x}_0 \end{cases} \quad (5.1)$$

where the first relation is the state-space representation of the EoM in Eq. (2.1). Then, a trajectory γ is defined as

$$\gamma(\mathbf{x}_0, t_0) := \{\varphi(\mathbf{x}_0, t_0; t) \forall t \in \mathbb{R}\}. \quad (5.2)$$

Similarly, backward and forward legs γ_b and γ_f , respectively, are defined as

$$\gamma_b(\mathbf{x}_0, t_0) := \{\varphi(\mathbf{x}_0, t_0; t) \forall t \in [t_0 - 10T_{\sigma}, t_0]\}, \quad (5.3)$$

$$\gamma_f(\mathbf{x}_0, t_0) := \{\varphi(\mathbf{x}_0, t_0; t) \forall t \in [t_0, t_0 + 10T_{\sigma}]\}, \quad (5.4)$$

where $T_{\sigma} = 2\pi\sqrt{a_{\sigma}^3/\mu_{\odot}} = 687$ days is the revolution period of Mars, with $a_{\sigma} = 2.279 \times 10^8$ km and $\mu_{\odot} = 1.327 \times 10^{11}$ km³s⁻² the semi-major axis of the Sun–Mars system and the gravitational parameter of the Sun, respectively.

Sets $\Gamma_{\mathcal{W}_n}$, $\Gamma_{\mathcal{X}_{-1}}$, and $\Gamma_{\mathcal{C}_{-1}^n}$ of trajectories $\gamma(\mathbf{x}_0, t_0)$ whose ICs (\mathbf{x}_0, t_0) belong to weakly-stable set \mathcal{W}_n , escape set \mathcal{X}_{-1} , and capture set \mathcal{C}_{-1}^n , respectively, are

$$\Gamma_{\mathcal{W}_n} = \{\gamma(\mathbf{x}_0, t_0) \mid \forall (\mathbf{x}_0, t_0) \in \mathcal{W}_n\}, \quad (5.5)$$

$$\Gamma_{\mathcal{X}_{-1}} = \{\gamma(\mathbf{x}_0, t_0) \mid \forall (\mathbf{x}_0, t_0) \in \mathcal{X}_{-1}\}, \quad (5.6)$$

$$\Gamma_{\mathcal{C}_{-1}^n} = \{\gamma(\mathbf{x}_0, t_0) \mid \forall (\mathbf{x}_0, t_0) \in \mathcal{C}_{-1}^n\}. \quad (5.7)$$

A corridor is obtained backward propagating ICs belonging to a capture sets \mathcal{C}_{-1}^n , where $n > 0$ is the number of revolutions after capture. Similarly to a capture set \mathcal{C}_{-1}^n , a corridor is designated as $\check{\mathcal{B}}_{-1}^n$ and it is defined as

$$\check{\mathcal{B}}_{-1}^n = \{\gamma_b(\mathbf{x}_0, t_0) \mid \forall (\mathbf{x}_0, t_0) \in \mathcal{C}_{-1}^n\}. \quad (5.8)$$

An exterior corridor $\check{\mathcal{E}}_{-1}^n$ is a subset of a corridor $\check{\mathcal{B}}_{-1}^n$ including pre-capture trajectories having heliocentric semi-major axis a_\odot greater than the target body's one (i. e., Mars, whose semi-major axis $a_t = a_\sigma = 1.5237$ AU). It is defined as

$$\check{\mathcal{E}}_{-1}^n = \{\gamma_b(\mathbf{x}_0, t_0) \in \check{\mathcal{B}}_{-1}^n : a_\odot(\varphi(\mathbf{x}_0, t_0; t)) > a_t \forall t \in [t_0 - 10T_\sigma, \hat{t}]\} \quad (5.9)$$

where $\hat{t} < t_0$ is a certain time before capture epoch t_0 when the escape (or pre-capture) leg ends in backward time. Contrarily, an interior corridor $\check{\mathcal{I}}_{-1}^n$ is the subset of a corridor $\check{\mathcal{B}}_{-1}^n$ including all trajectories having semi-major axis smaller than the central body's one (i. e., Mars). It is defined as

$$\check{\mathcal{I}}_{-1}^n = \{\gamma_b(\mathbf{x}_0, t_0) \in \check{\mathcal{B}}_{-1}^n : a_\odot(\varphi(\mathbf{x}_0, t_0; t)) < a_t \forall t \in [t_0 - 10T_\sigma, \hat{t}]\}. \quad (5.10)$$

Consequently, $\check{\mathcal{B}}_{-1}^n = \check{\mathcal{E}}_{-1}^n \cup \check{\mathcal{I}}_{-1}^n$. In the context of EXTREMA (see Section 1.2), the interior corridor is of interest because it extends between Mars and Earth's orbits. A subcorridor $\check{\mathcal{S}}_{-1}^n$, a generic subset of a corridor $\check{\mathcal{B}}_{-1}^n$, is defined as

$$\check{\mathcal{S}}_{-1}^n = \{\gamma_b(\mathbf{x}_0, t_0) \mid \forall (\mathbf{x}_0, t_0) \in \mathcal{D}_{-1}^n\}, \quad (5.11)$$

where the generic domain \mathcal{D}_{-1}^n is

$$\mathcal{D}_{-1}^n = \{\mathbf{x}_0 : \mathbf{x}_0 \in \mathcal{C}_{-1}^n \wedge \mathbf{g}(\mathbf{x}_0) \leq \mathbf{0} \wedge \mathbf{h}(\mathbf{x}_0) = \mathbf{0}\}, \quad (5.12)$$

with $\mathbf{g}(\mathbf{x}_0)$ and $\mathbf{h}(\mathbf{x}_0)$ being two sets of $m \geq 0$ inequality constraints and $n \geq 0$ equality constraints, respectively, with m and p finite. Finally, the envelope $\partial\check{\mathcal{S}}_{-1}^n$ of a subcorridor $\check{\mathcal{S}}_{-1}^n$ is constructed backward propagating the subcorridor domain border $\partial\mathcal{D}_{-1}^n$. Therefore, it is defined as

$$\partial\check{\mathcal{S}}_{-1}^n = \{\gamma_b(\mathbf{x}_0, t_0) \mid \forall (\mathbf{x}_0, t_0) \in \partial\mathcal{D}_{-1}^n\}. \quad (5.13)$$

An illustration of prior definitions is proposed in Figure 5.1.

5.2 Characterization

Two corridors are built and characterized starting from two peculiar capture sets²³. The capture sets are constructed from the same initial grid following the methodology discussed in [25]. The search space is chosen to maximize the capture ratio \mathcal{R}_C based on the analysis reported in [50]. It is defined in the Mars-centered RTN@ t_i reference frame at capture epoch t_0 set to December 9, 2023 at 00:45:18.363 (UTC). At this epoch, Mars' true anomaly with respect to the Sun is equal to 270 deg, maximizing \mathcal{R}_C [50]. The selected plane is defined by inclination i_0 and RAAN Ω_0 set both equal to 0.2π rad, so maximizing the capture ratio (according to Figure 10 in [50]). At initial epochs t_0 , sought Mars-orbiting trajectories have osculating eccentricity $e_0 = 0.99$ [9], and true anomaly $\theta_0 = 0$ rad. Let $R_{\mathcal{M}}$ be the radius of Mars in km, then the search space on the plane defined above is a circular crown centered at Mars, from radius $R_{\mathcal{M}} + 100$ km up to radius $11R_{\mathcal{M}}$. Hence, $(r_{p0}, \omega_0) \in [R_{\mathcal{M}} + 100 \text{ km}, 11R_{\mathcal{M}}] \times [0, 2\pi)$. The circular crown is made of $N_{r_{p0}} = 339$ and $N_{\omega_0} = 360$ evenly spaced points of radius of pericenter r_{p0} and argument of pericenter ω_0 , respectively.

The characterization procedure consists of the following: i) critical analysis of trends and rates of corridor's osculating elements when orbiting the Sun; ii) visualization of time snapshots showing corridor's heliocentric Keplerian elements and consequent pattern identification; iii) opportunistic selection of a subdomain in the capture sets to derive the corresponding subcorridor; iv) investigation of subcorridor dimensions and shape; v) study of Poincaré sections.

5.2.1 Step i) trends and rates of Keplerian elements

The first characterization step provides a first look into the behavior of the corridor when observed in heliocentric coordinates, which should be that typical of trajectories designed in non-Keplerian models (e. g., CR3BP). The expectation is to observe trajectories similar to each other far from the target body. This is expected because a spacecraft is affected mainly by the Sun's gravitational attraction when far from Mars. Consequently, the features of highly irregular trajectories, essential elements of the BC phenomenon, should not be observed far from the target body. Additionally, the rate of change of the Keplerian elements is computed using a finite differences scheme to further confirm how variations of the corridor's Keplerian elements are small when far from the central body.

5.2.2 Step ii) time snapshots

The dynamics being non-autonomous, a time snapshot is a collection of states taken at a fixed time epoch. Based on the considerations made in Section 5.2.1, time snapshots of a corridor's heliocentric Keplerian elements are expected to

²³EoM include gravitational attractions of the Sun, Mercury, Venus, Earth–Moon (B), Mars (central body), Jupiter (B), Saturn (B), Uranus (B) and Neptune (B), SRP, and Mars' NSG.

show similar patterns. Specifically, the aim of this step is to visualize how states spread, thereby assessing by visual inspection if clusters of ICs rift apart or remain connected. Due to the presence of many IC clusters typical of capture sets and the potential Cantor-like structure claimed in [106], a corridor is expected to be made of various subsets. However, the major concern is about the possibility to find holes in their structure, so recognizing such subsets as not continuous entities.

5.2.3 Step iii) opportunistic selection of a corridor subset

A subcorridor \check{S}_{-1}^n , is investigated in detail. A circular domain within the capture set is opportunistically chosen to derive the corresponding subcorridor. Location and size of the domain are selected based on the local value of regularity index S and regularity coefficient $\Delta S_{\%}$ of the capture set. They are defined as [54]

$$S = \frac{t_{N_r} - t_0}{N_r}, \quad S^{(2b)} = \frac{2\pi}{\sqrt{\mu_t}} \left(\frac{r_0}{1 - e_0} \right)^{3/2}, \quad \Delta S_{\%} = 100 \left| \frac{S}{S^{(2b)}} - 1 \right| \quad (5.14)$$

where N_r is the number of forward or backward revolutions, t_0 is the initial time, and t_{N_r} is the time required to complete the N_r revolutions. The regularity index of a Keplerian orbit $S^{(2b)}$ is used as reference. The regularity coefficient $\Delta S_{\%}$ measures the distance between S and $S^{(2b)}$, so indicating how far an orbit is from being Keplerian [54]. The smaller the regularity index and coefficient, the more regular the post-capture trajectory [50].

5.2.4 Step iv) dimension and shape

Dimensions and shape of the subcorridor (for the sake of conciseness also referred to as corridor from now on) are investigated as well. This is to study its size variation with time (i. e., how much the corridor is stretched, compressed, tilted), what shape it takes on, and shape changes over time. Specifically, two- and three-dimensional representations of the corridor are plotted to get confidence with its shape and size. The result is achieved by propagating and visualizing the envelope $\partial \check{S}_{-1}^n$ of the subcorridor \check{S}_{-1}^n .

5.2.5 Step v) Poincaré sections

Poincaré sections of the subcorridor are computed at prescribed solar longitudes λ_{\odot} . The selection of longitude values is performed based on the physical space spanned by the corridor in the time frame of the backward propagation performed. Therefore, the corridor is intersected in the physical space by half-planes originating from the z-axis. The shapes of these cuts in the physical space are derived and plotted for various solar longitudes. Velocity surfaces corresponding to Poincaré sections are computed as well. Differently from time snapshots, corridor's trajectories reach the Poincaré sections at different time epochs. Poincaré sections are computed because they are expected to provide precise estimates of corridor dimensions and a clear insight on its shape.

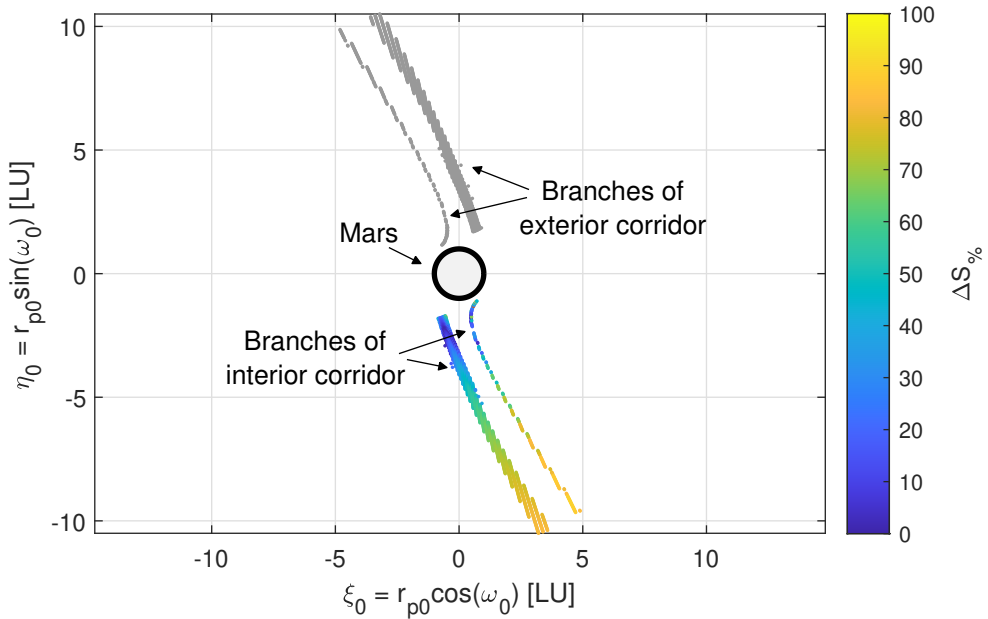
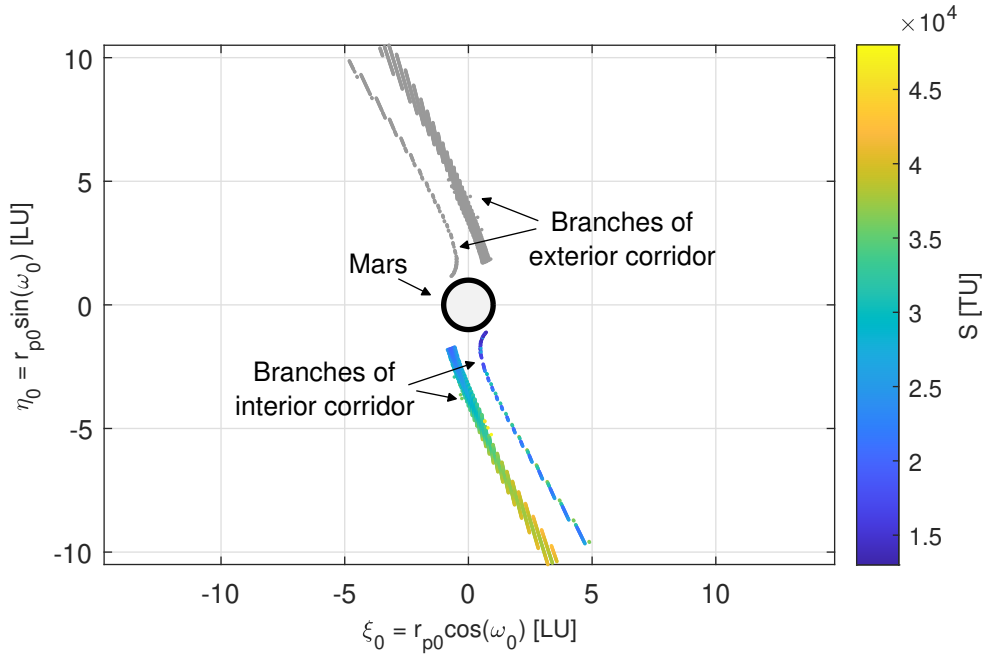


Figure 5.2: Capture set \mathcal{C}_{-1}^2 . Branches developing exterior ballistic capture corridors are colored in gray. Nondimensional coordinates on the orbital plane $i_0 = \Omega_0 = 0.2\pi$ rad defined in the Mars-centered RTN@ t_0 frame. Mars is the gray circle with black surround.

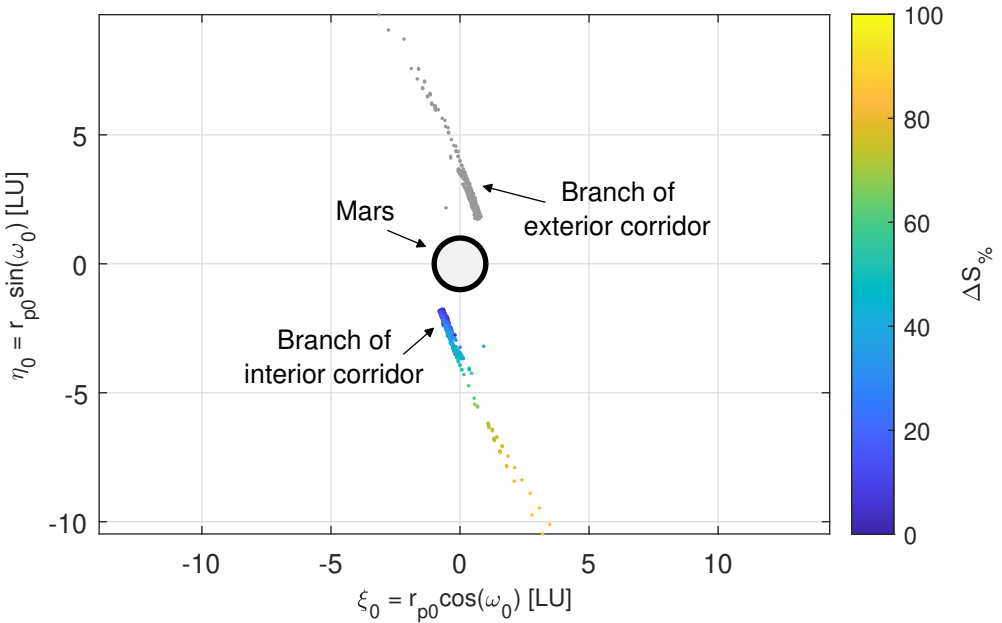
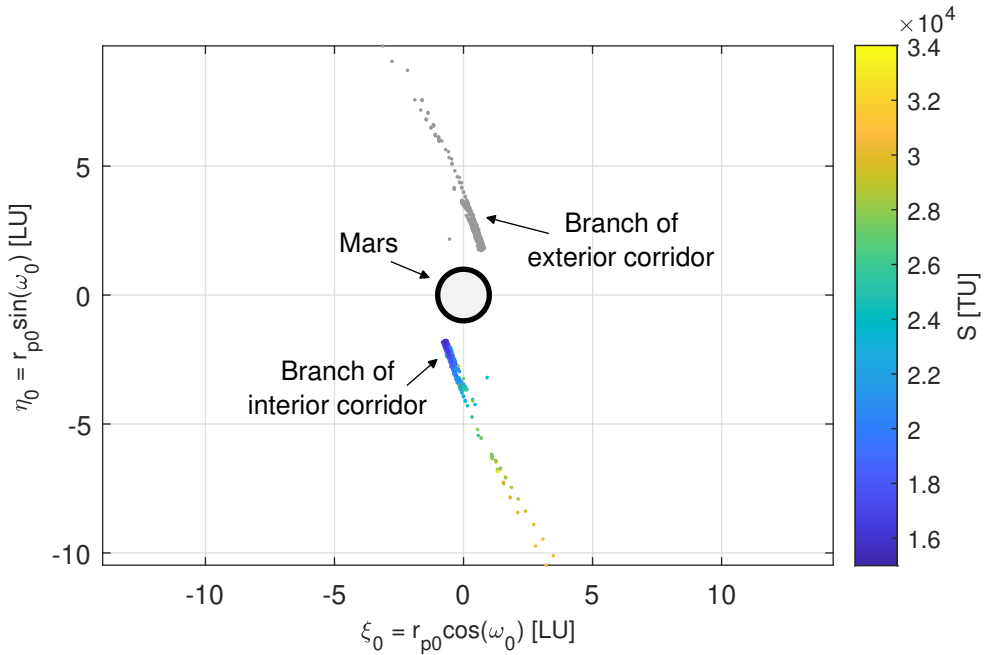


Figure 5.3: Capture set \mathcal{C}_{-1}^6 . Branches developing exterior ballistic capture corridors are colored in gray. Nondimensional coordinates on the orbital plane $i_0 = \Omega_0 = 0.2\pi$ rad defined in the Mars-centered RTN@ t_0 frame. Mars is the gray circle with black surround.

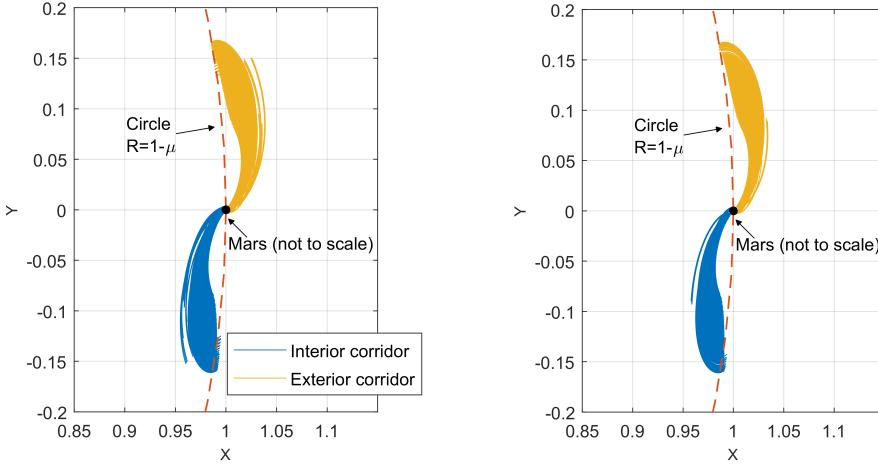
(a) Corridor \check{B}_{-1}^2 by capture set C_{-1}^2 .(b) Corridor \check{B}_{-1}^6 by capture set C_{-1}^6 .

Figure 5.4: BCCs from t_0 to t_0-600 days. Interior and exterior corridors colored in blue and yellow, respectively. Nondimensional coordinates in the RPF.

5.3 Results

The peculiar capture sets C_{-1}^2 and C_{-1}^6 from which corridors \check{B}_{-1}^2 and \check{B}_{-1}^6 are developed can be seen in Figures 5.2 and 5.3, respectively. In the capture set C_{-1}^2 , four sickle-shaped clusters of ICs are distinguishable. The two of them located in the half-plane $y > 0$, colored in gray, develop the exterior corridor. Differently, the other two branches develop the interior corridor. On the other hand, the set C_{-1}^6 is made of by only two clusters. The branch in the bottom half-plane gives rise to the interior corridor, while the gray one generates the exterior corridor.

In Figure 5.4, corridors \check{B}_{-1}^2 and \check{B}_{-1}^6 are shown. Interior and exterior corridors are colored in blue and yellow, respectively. As expected, \check{B}_{-1}^2 looks thicker and more packed than \check{B}_{-1}^6 [19]. By definition of capture set, $C_{-1}^n \subseteq C_{-1}^m$ with m and n both positive, and $n > m$. Consequently, $\check{B}_{-1}^n \subseteq \check{B}_{-1}^m$ is verified too, therefore \check{B}_{-1}^6 is a subset of \check{B}_{-1}^2 . In general, the same applies to \check{I}_{-1}^n and \check{E}_{-1}^n .

5.3.1 Step i) trends and rates of Keplerian elements

Osculating elements of corridors about the Sun in the ECLIPJ2000 frame are investigated. Figure 5.5 shows the six Keplerian elements from t_0 to t_0-1000 days of both \check{B}_{-1}^2 and \check{B}_{-1}^6 . In the plots, they are compared to Mars' orbit Keplerian elements. Except for initial short transients close to the capture epoch t_0 characterized by huge variations, all elements but true anomaly θ stabilize rapidly. After approximately 300 days in backward time, curves look completely flat. Such time span is in line with typical times of flight on pre-capture legs belonging to the unstable set \mathcal{X}_{-1} . After the initial (from the right), strong, short transient,

true anomaly varies accordingly with Mars' true anomaly as expected. From plots showing the trend of semi-major axis a (see top-left corner in Figures 5.5a and 5.5b), the distinction between interior and exterior corridors is clear. However, the four peculiar branches of \mathcal{C}_{-1}^2 cannot be distinguished within the two bundles of curves.

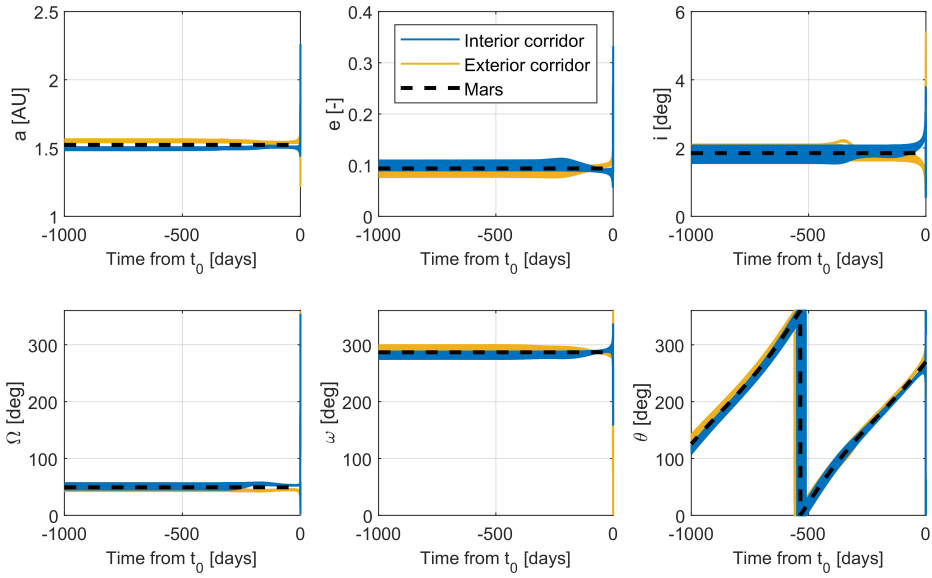
Claims in Section 5.2.1 are confirmed by results in Figure 5.6 on the yearly rates of the heliocentric osculating elements. In the plots, they are compared to the yearly rates of Mars' orbit (dotted horizontal lines). As expected, the strong, short transients are characterized by large rates (see right hand sides in Figure 5.6).

5.3.2 Step ii) time snapshots

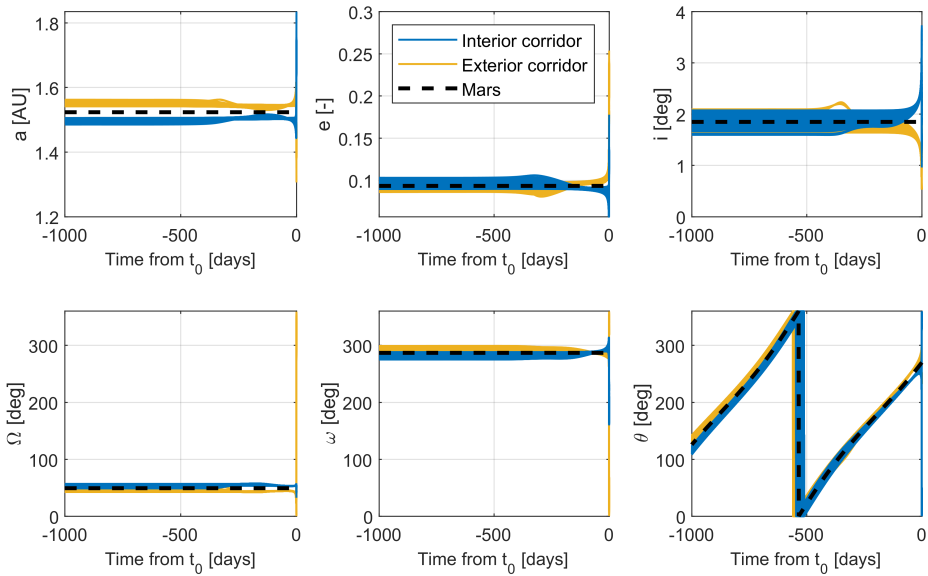
Two time snapshots at $t = t_0 - 600$ days are taken. One about $\check{\mathcal{B}}_{-1}^2$, found in Figure 5.7, and the other of $\check{\mathcal{B}}_{-1}^6$, visible in Figure 5.8. They show instantaneous values of Keplerian elements about the Sun of the two corridors, seen in the ECLIPJ2000 frame 600 days before capture epoch at Mars. They correspond to states at end points of trajectories in Figure 5.4.

Conversely to Figure 5.5a, in Figure 5.7 the four branches are easily identifiable. Interior and exterior corridors features are nearly symmetric. Indeed, they almost exhibit a point symmetry with respect to Mar's Keplerian elements, marked by red crosses. In this time snapshot, each branch is well resolved, thin, and relatively long. This is a peculiarity of the specific corridor and not a common feature. Indeed, numerical experiments here omitted show that such characteristics are typical of highly regular capture sets like those presented in this chapter (see Figure 5.2 and Figure 5.3). Differently, less regular capture sets produce corridors whose time snapshots present poorly resolved, sparse, and large clusters that are hardly distinguishable to each other. Except that only two clusters are identified, similar considerations can be done for the time snapshot in Figure 5.8. The other two branches are lost increasing the number of revolutions n from 2 to 6.

Results in Figures 5.7 and 5.8 are connected with hyperbolic manifolds. Indeed, relations between the WSB and invariant manifolds were already proved to exist in the CR3BP [62]. Specifically, trajectories belonging to escape sets in backward time are responsible for transport phenomena from the secondary (i. e., Mars) realm either to the primary (i. e., the Sun) realm or to the exterior realm. On the other hand, trajectories propagated from the WSB reach Lagrange points [62]. However, the latter are trajectories exhibiting in general different Jacobi constants since they are not obtained starting from the very same periodic orbit. Therefore, they belong to different stable invariant manifolds. Extending the concept to the non-autonomous case under study, interior corridors $\check{\mathcal{I}}_{-1}^n$ should be a set of trajectories responsible for transport phenomena from the secondary realm to the primary realm. Conversely, exterior corridors $\check{\mathcal{E}}_{-1}^n$ should transport material towards the exterior realm. Trajectories in both $\check{\mathcal{I}}_{-1}^n$ and $\check{\mathcal{E}}_{-1}^n$ are expected to travel firstly within stable hyperbolic manifolds and then into unstable hyperbolic manifolds.



(a) Trends of heliocentric osculating elements of \check{B}_{-1}^2 .



(b) Trends of heliocentric osculating elements of \check{B}_{-1}^6 .

Figure 5.5: Trends of heliocentric osculating elements of BCCs in the ECLIPJ2000 frame from t_0 to $t_0 - 1000$ days. From top-left to bottom-right: semi-major axis a , eccentricity e , inclination i , RAAN Ω , argument of pericenter ω , and true anomaly θ as a function of time from capture epoch t_0 .

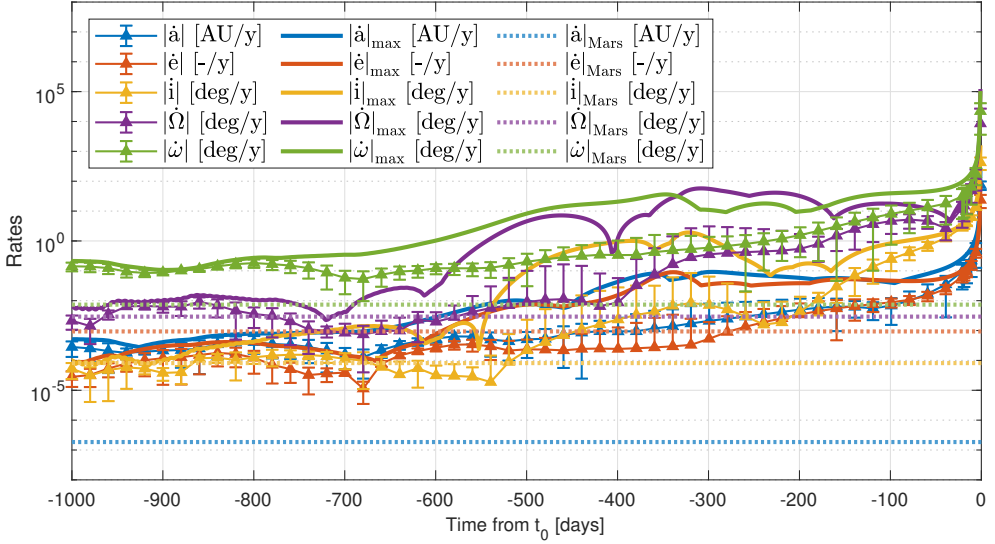
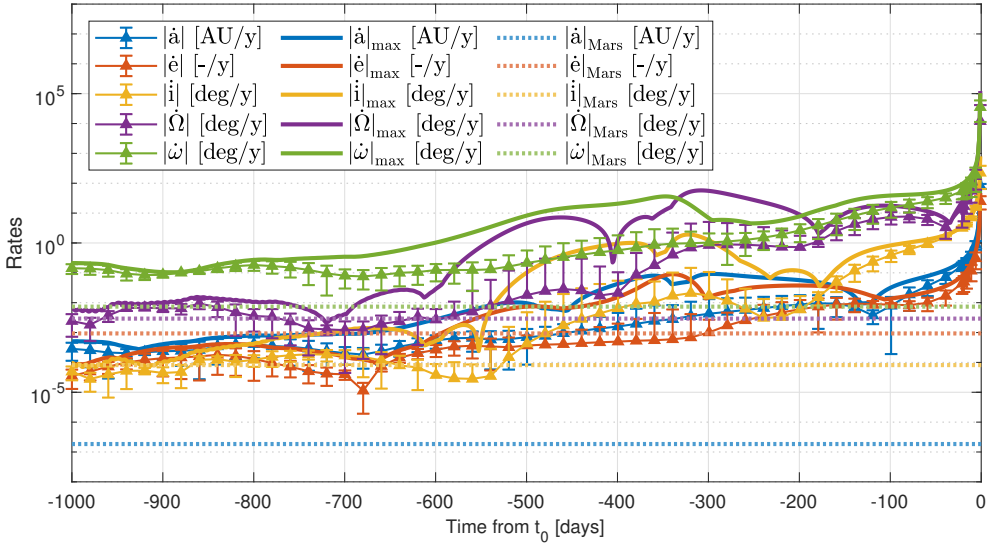
(a) Corridor \check{B}_{-1}^2 .(b) Corridor \check{B}_{-1}^6 .

Figure 5.6: Rates of heliocentric osculating elements for BBCs in the ECLIPJ2000 frame from t_0 to $t_0 - 1000$ days. Triangles and error bars mark mean rates and their standard deviations, respectively. Solid lines represent maximum rates, while dotted horizontal lines indicate rates of Mars' orbit.

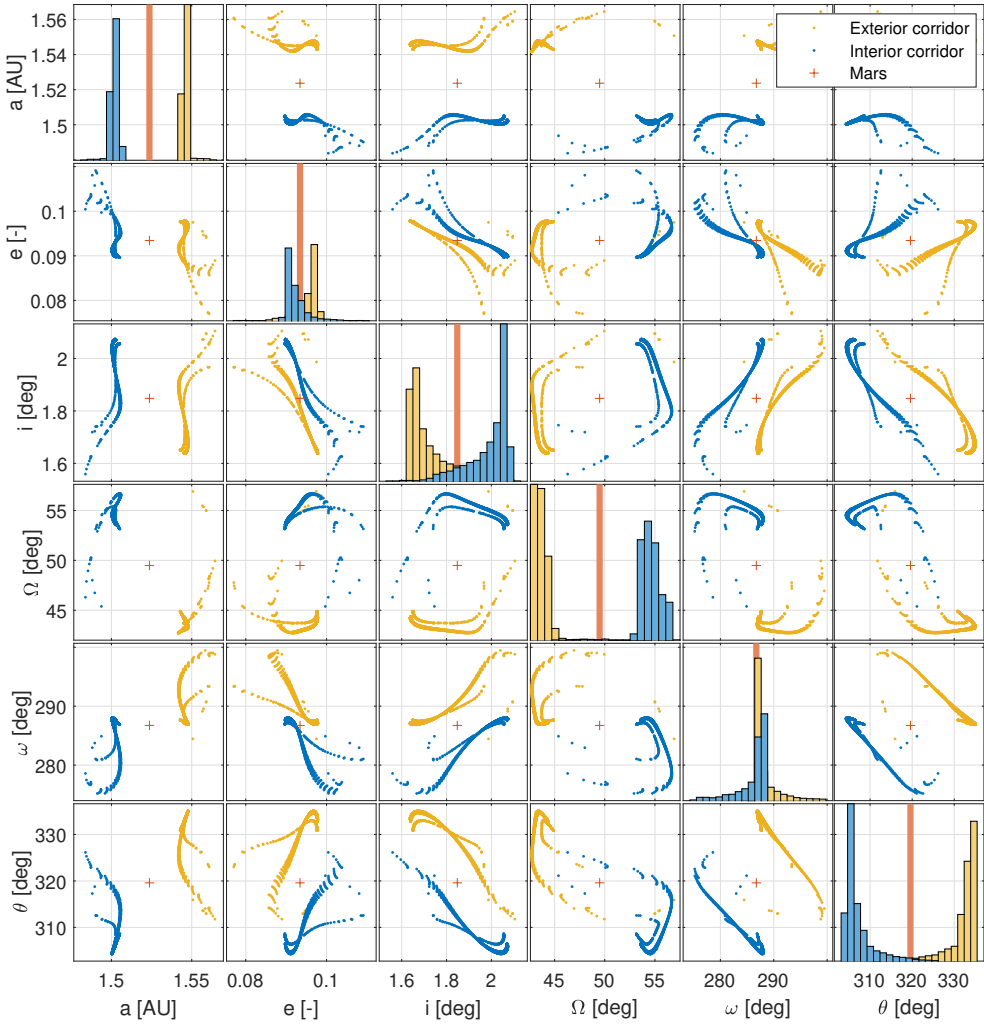


Figure 5.7: Time snapshot at $t_0 - 600$ days of \tilde{B}_{-1}^2 . Scatterplot matrix of heliocentric osculating elements in the ECLIPJ2000 frame. The patterns of the two interior corridor branches, in blue, and the two exterior corridor branches, in yellow, are clearly visible. Red crosses represent Mars' Keplerian elements.

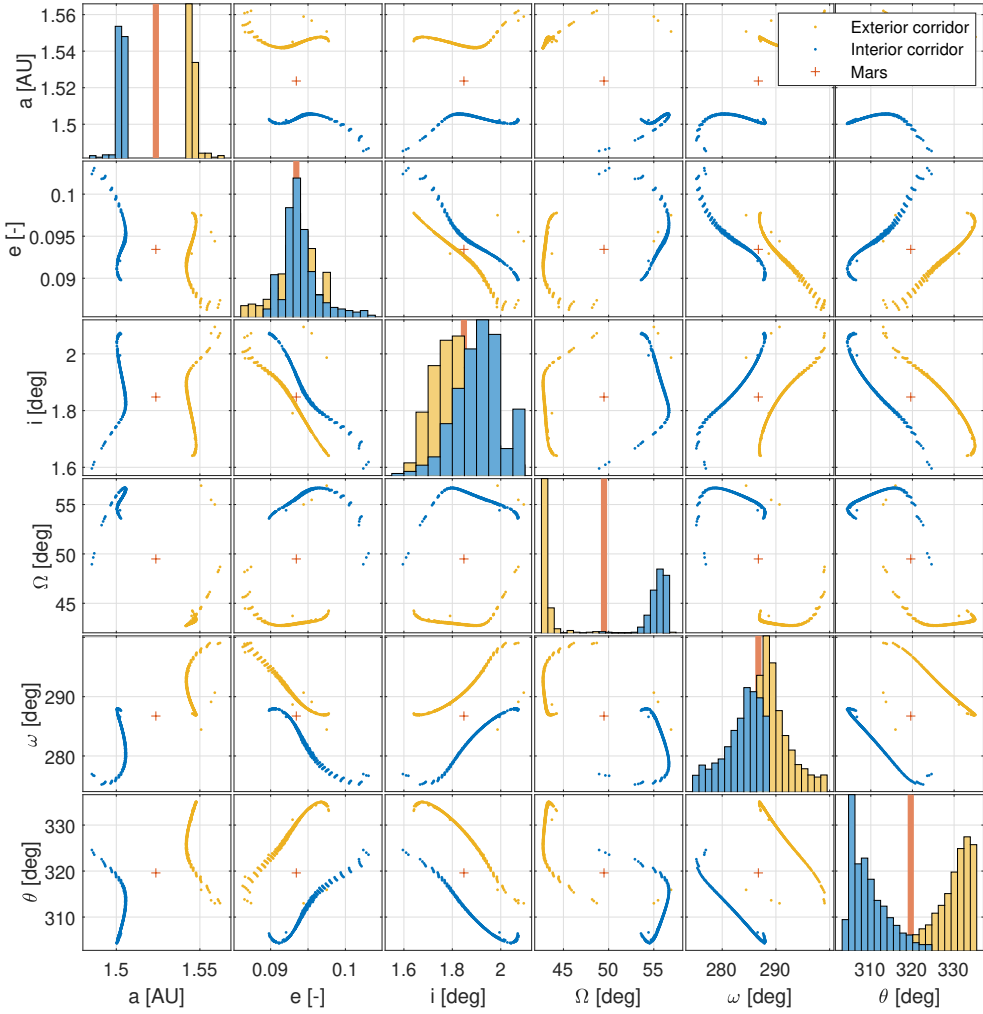


Figure 5.8: Time snapshot at $t_0 - 600$ days of \check{B}_{-1}^6 . Scatterplot matrix of heliocentric osculating elements in the ECLIPJ2000 frame. The patterns of the only interior corridor branch, in blue, and the only exterior corridor branch, in yellow, are clearly identified. Red crosses represent Mars' Keplerian elements.

5.3.3 Step iii) opportunistic selection of a corridor subset

A subcorridor $\check{\mathcal{S}}_{-1}^6$ is built starting from the \mathcal{C}_{-1}^6 branch developing the interior corridor. Specifically, a circular domain within the capture set is selected to fulfill the purpose. A circle of radius $\Delta r_p = 250$ km, and centered in $(r_c, \omega_c) = (R_{\odot} + 3400 \text{ km}, 250 \text{ deg})$ is constructed on the orbital plane of the capture set, as shown in Figure 5.9a. The circle is placed at the top of the cluster because of the strong regularity peculiar of that region. Indeed, both regularity index and coefficient are small as shown by plots in Figure 5.3. A magnification of the red circle in Figure 5.9a is reported in Figure 5.9b.

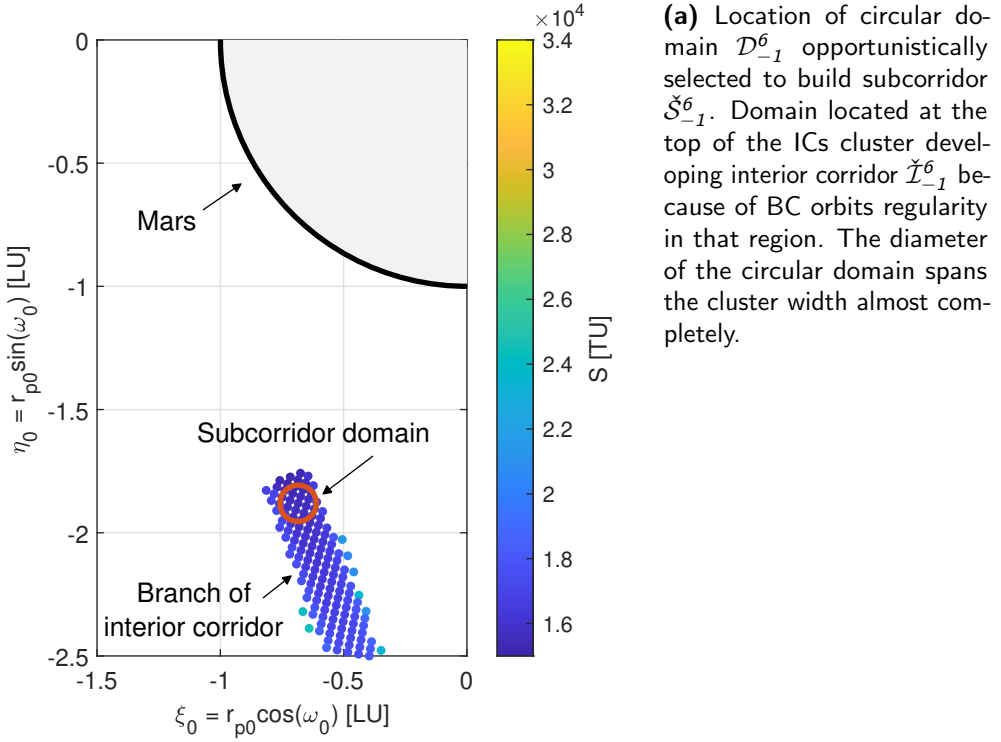
5.3.4 Step iv) dimension and shape

The subcorridor dimension and shape are studied backward propagating from t_0 to $t_0 - 600$ days the central point and the 20 ICs uniformly distributed along the border of the red circular domain in Figure 5.9. The resulting set of trajectories are used to build the corridor's envelope $\partial \check{\mathcal{S}}_{-1}^6$ in the physical space. The corridor is reported in Figures 5.10 and 5.11 from different points of view and in various reference frames.

Figure 5.10a shows the corridor, in light blue, from a top view of the xy -plane in the Sun-centered ECLIPJ2000 frame. The corridor is backward propagated from capture points, visible in the bottom-left, for 600 days. This is almost a revolution period of Mars, whose orbit is plotted in black. The corridor remains closely attached to Mars' orbit and stretches in backward time. The latter is a desirable feature, since it eases targeting the corridor for spacecraft with limited control authority like CubeSats. The corridor being a stream of trajectories, its characteristics should be similar to what already discovered regarding individual Earth–Mars transfers relying on BC [9].

The plot in Figure 5.10b offers a three-dimensional representation of the corridor in the Mars-centered ECLIPJ2000 frame. Far from Mars, the initial tiny circular region is stretched considerably. The envelope, initially shaped as a relatively small circle, increases remarkably in size and becomes almost a segment when backward propagated. That seems to reflect what observed in Figure 5.8, which shows thin and very long clusters of trajectories. Two-dimensional Mars-centered views of the corridor are given in Figure 5.11. Specifically, Figure 5.11 collects the three views of the whole corridor, while Figure 5.12 offers magnifications of the corridor and post-capture²⁴ envelopes at a closer range from Mars.

²⁴Trajectories of post-capture legs are obtained forward propagating ICs belonging to $\partial \mathcal{D}_{-1}^n$ from t_0 to t_{r, \mathcal{W}_6} (time epoch at which the 6th revolution is achieved).



(b) Detail of circular subcorridor domain $\mathcal{D}_{-1}^{\epsilon}$. The red solid curve and the red cross represent the domain's border and center, respectively. The black dots within the red surround represent an example 715 points Fibonacci lattice used to sample the subcorridor domain $\mathcal{D}_{-1}^{\epsilon}$ (see Chapter 9). Some points of capture set's grid can be seen in the background.

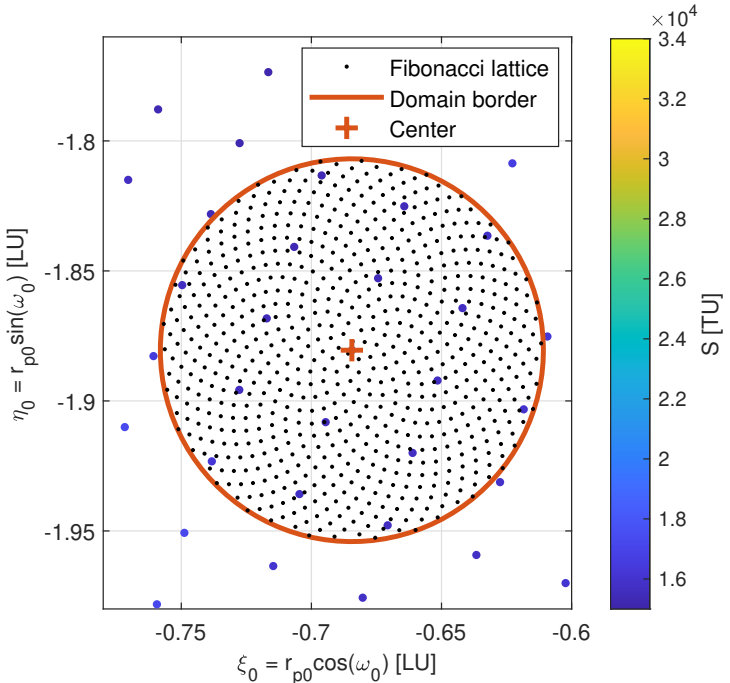
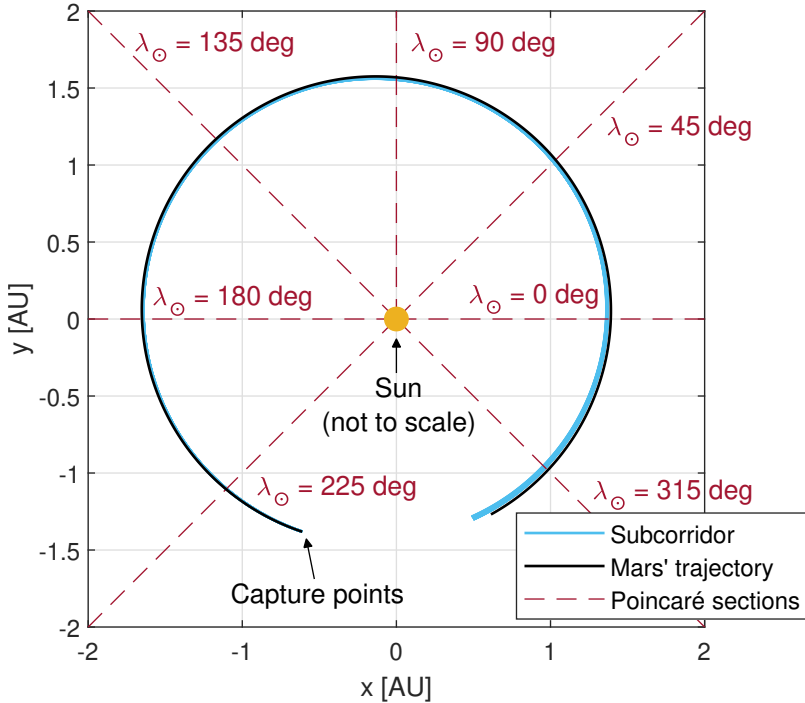
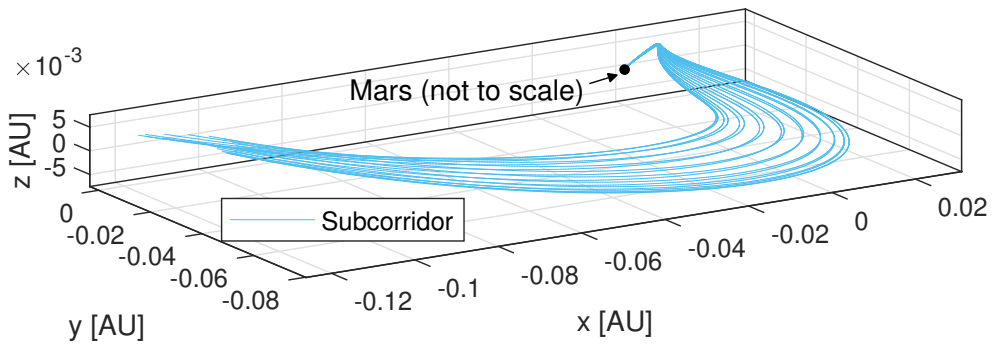


Figure 5.9: Detail of capture set $\mathcal{C}_{-1}^{\epsilon}$ showing regularity index S of ICs belonging to the set. Nondimensional coordinates on the orbital plane $i_0 = \Omega_0 = 0.2\pi$ rad defined in the Mars-centered RTN@ t_0 frame. Mars is partially shown in gray with black surround.



(a) Subcorridor envelope, in light blue, in the Sun-centered ECLIPJ2000 frame compared to Mars' orbit, in black. Dashed dark red segments, and corresponding solar longitudes, identify Poincaré sections shown in Figure 5.13. View xy -plane.



(b) Three-dimensional view of subcorridor envelope in Mars-centered ECLIPJ2000 frame.

Figure 5.10: Representations in the physical space of the subcorridor envelope $\partial\check{\mathcal{S}}_{-1}^6$ built from the red circular domain border shown in Figure 5.9. Envelope backward propagated from t_0 to $t_0 - 600$ days.

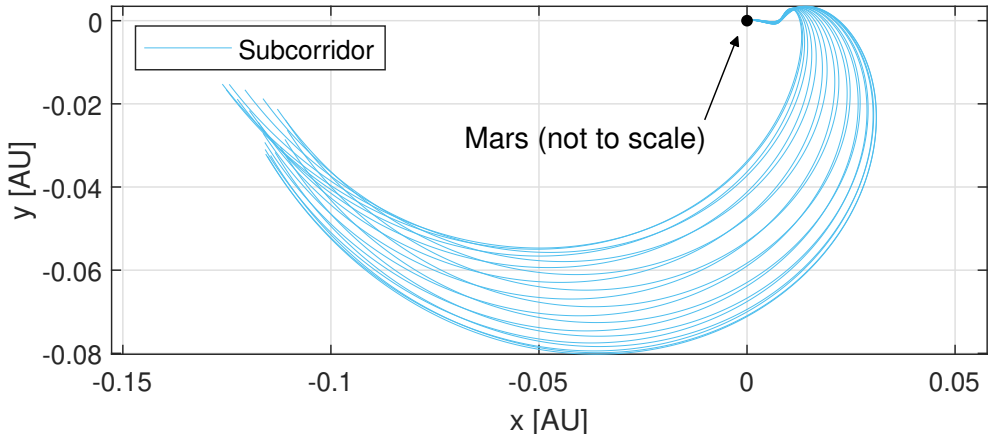
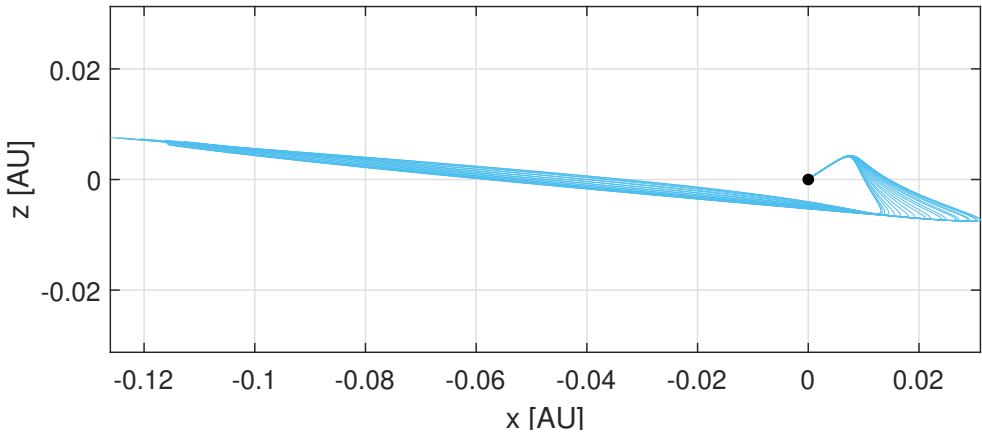
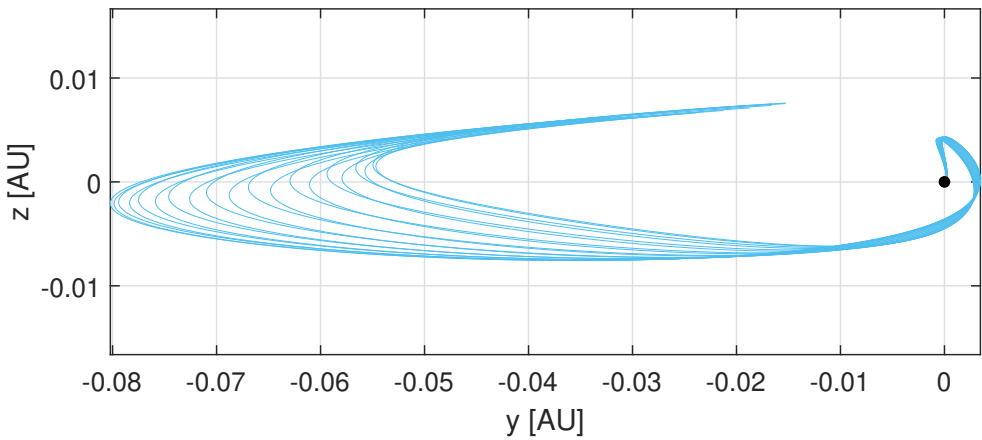
(a) View xy -plane.(b) View xz -plane.(c) View yz -plane.

Figure 5.11: Views in the physical space of subcorridor envelope $\partial\mathcal{S}_{-1}^{\mathfrak{S}^6}$ far from Mars built from red circular domain border shown in Figure 5.9. Subcorridor backward propagated from t_0 to t_0-600 days. Trajectories plotted in the Mars-centered ECLIPJ2000 frame.

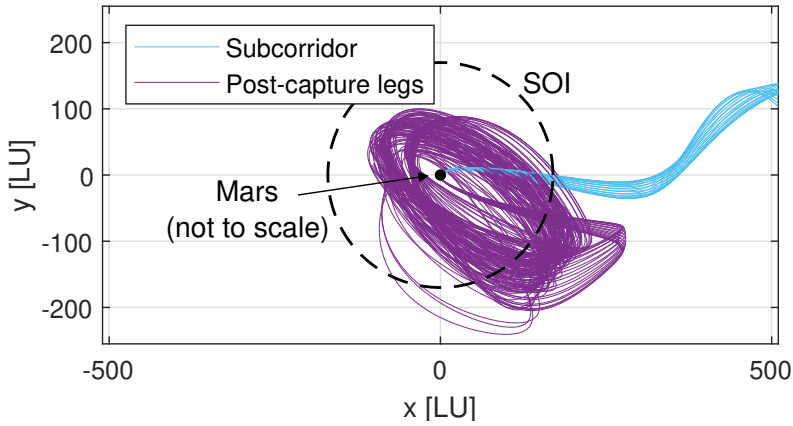
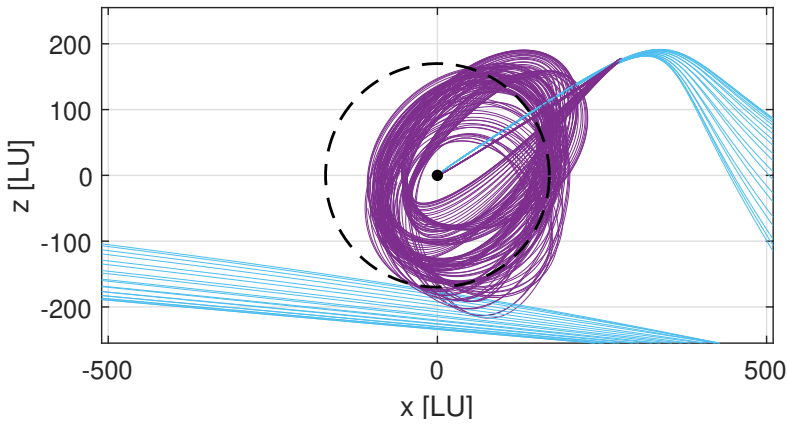
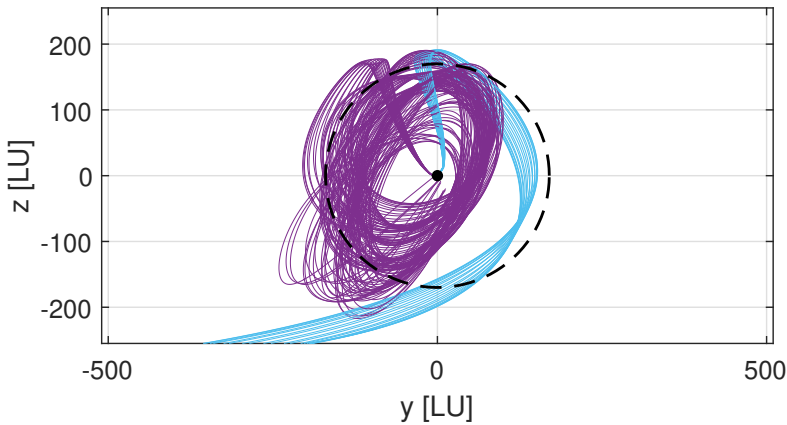
(a) View xy -plane.(b) View xz -plane.(c) View yz -plane.

Figure 5.12: Views in the physical space of subcorridor envelope $\partial\mathcal{S}_{-1}^{\check{6}}$ built from red circular domain border shown in Figure 5.9. Magnifications of subcorridor and post-capture envelopes at a closer range from Mars. Subcorridor backward propagated from t_0 to $t_0 - 600$ days. Trajectories plotted in the Mars-centered ECLIPJ2000 frame.

5.3.5 Step v) Poincaré sections

Poincaré sections at prescribed solar longitudes of corridor's envelope (grid made of 100 ICs uniformly distributed along the border of the red circular domain in Figure 5.9) and center are computed to better understand how the envelope shape changes over time and to estimate more precisely its characteristic dimensions. Seven half-planes in the physical space perpendicular to the xy -plane are selected at corresponding solar longitudes λ_{\odot} equal to 225 deg, 180 deg, 135 deg, 90 deg, 45 deg, 0 deg, and 315 deg. They are represented in Figure 5.10a as dashed red segments starting from the origin. The sequence is in accordance with the order in which the corridor crosses Poincaré sections. Selected longitudes cover almost uniformly and completely the corridor from t_0 to $t_0 - 600$ days.

Results are shown in plots of Figure 5.13. They display Poincaré sections of positions and velocities of the envelope $\partial\check{S}_{-1}^6$, marked by blue crosses, with respect to the corridor \check{S}_{-1}^6 center, represented by the red diamond. Coordinates are computed in the ECLIPJ2000 frame. The sequence of Poincaré sections about positions allows visualizing how the envelope changes shape over time. In particular, its size at $\lambda_{\odot} = 315$ deg is more than one order of magnitude larger than its size at $\lambda_{\odot} = 225$ deg. At $\lambda_{\odot} = 90$ deg, the envelope twists around itself, while at $\lambda_{\odot} = 45$ deg it takes on a bizarre shape. Numerical experiments here excluded show that around $\lambda_{\odot} = 90$ deg the corridor twists completely on itself. Differently, at around $\lambda_{\odot} = 45$ deg the top part of the envelope undergoes a deformation resembling a wavy movement. The twist lasts approximately from $\lambda_{\odot} = 105$ deg to $\lambda_{\odot} = 75$ deg, while the deformation persists roughly from $\lambda_{\odot} = 60$ deg to $\lambda_{\odot} = 30$ deg. Likely, such behaviors are the results of the peculiar distribution of Keplerian elements characterizing the trajectories belonging to the corridor and of how they geometrically interact in the physical space.

The characteristic dimensions of the envelope are retrieved from charts in Figure 5.13. Specifically, at $\lambda_{\odot} = 225$ deg, the two characteristic dimensions are approximately $d = 6.1 \times 10^{-5}$ AU (*i. e.*, the smaller dimension) and $D = 4.6 \times 10^{-4}$ AU (*i. e.*, the larger one). On the other hand, at $\lambda_{\odot} = 315$ deg, d and D are about 2.8×10^{-4} AU and 1.7×10^{-2} AU, respectively. In the latter case, d is relatively large ($\approx 4.2 \times 10^4$ km), albeit it being two orders of magnitude smaller than D . This implies targeting a section perhaps large enough for limited control authority spacecraft, so verifying that BCC targeting is a viable option for CubeSats [12].

The Sun-centered states of the points belonging to the envelope and shown in Poincaré sections of Figure 5.13 can be retrieved summing the corresponding states of the center collected in Tables 5.1 and 5.2 (position and velocities, respectively). For the sake of completeness, time epochs and time intervals from t_0 of when the center crosses the sections are reported in Table 5.3. The center trajectory takes 224.76 days to escape from Mars in backward time. At the escape, the solar longitude is approximately 144 deg.

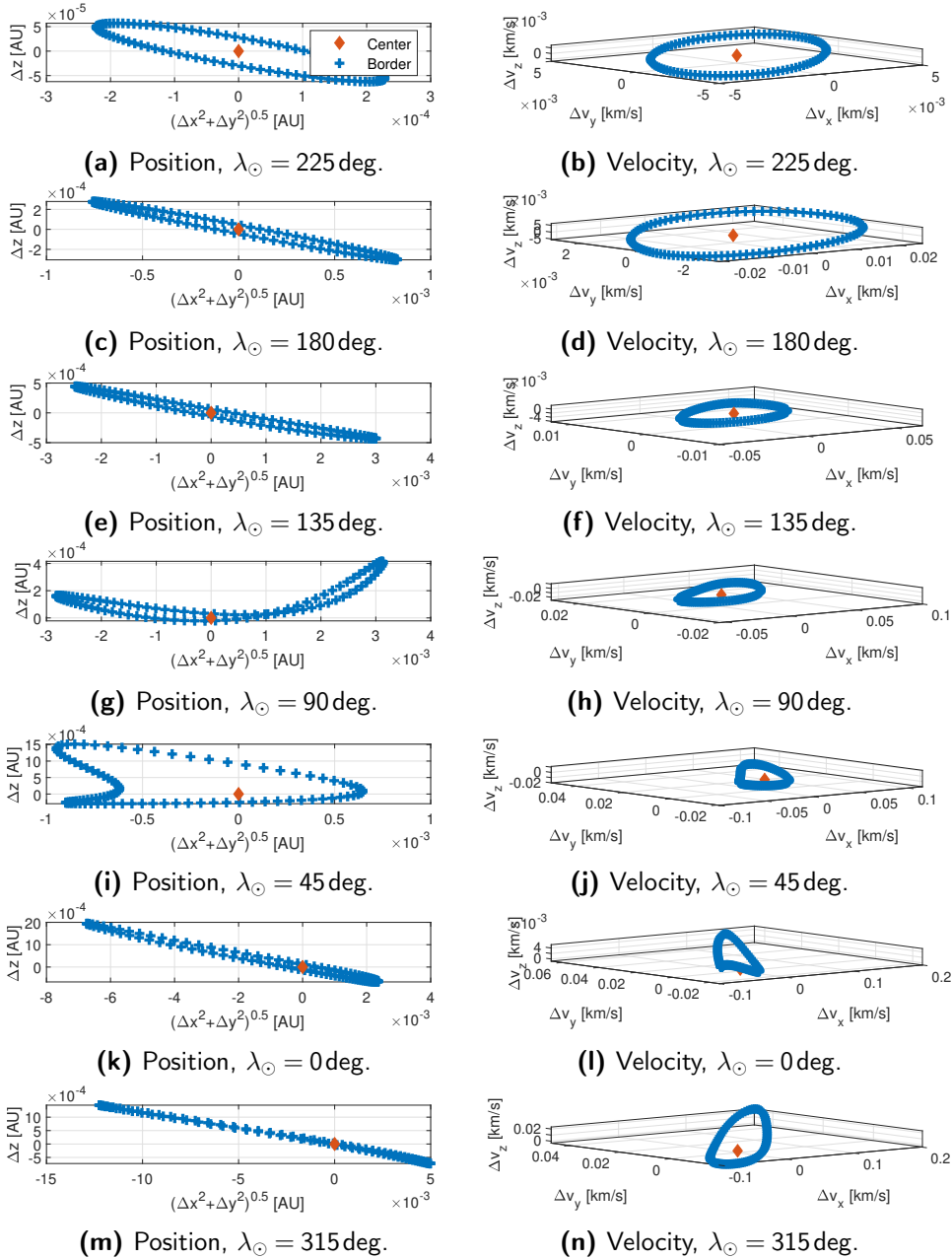


Figure 5.13: Poincaré sections of subcorridor \mathcal{S}_{-1}^6 in the ECLIPJ2000 frame for solar longitudes λ_{\odot} shown in Figure 5.10a. Blue crosses represent points sampled on subcorridor domain border. Center of circular domain identified by the red diamond. On the left, positions with respect to center. On the right, velocities with respect to center. Center time epochs, positions, and velocities collected in Tables 5.3, 5.1, and 5.2, respectively.

Table 5.1: Positions of center in Poincaré sections.

Solar longitude	Position		
λ_{\odot} [deg]	x [AU]	y [AU]	z [AU]
225	-1.102 808	-1.102 808	$7.844\,357 \times 10^{-3}$
180	-1.641 041	$1.554\,104 \times 10^{-13}$	$4.293\,343 \times 10^{-2}$
135	-1.162 058	1.162 058	$5.006\,461 \times 10^{-2}$
90	$-6.957\,004 \times 10^{-15}$	1.557 277	$2.662\,889 \times 10^{-2}$
45	1.020 845	1.020 845	$-8.854\,905 \times 10^{-3}$
0	1.367 875	$7.111\,910 \times 10^{-13}$	$-3.521\,404 \times 10^{-2}$
315	$9.624\,945 \times 10^{-1}$	$-9.624\,945 \times 10^{-1}$	$-4.120\,283 \times 10^{-2}$

Table 5.2: Velocities of center in Poincaré sections.

Solar longitude	Velocity		
λ_{\odot} [deg]	v_x [km s $^{-1}$]	v_y [km s $^{-1}$]	v_z [km s $^{-1}$]
225	$1.787\,586 \times 10^1$	$-1.510\,174 \times 10^1$	$-8.164\,564 \times 10^{-1}$
180	$8.595\,426 \times 10^{-1}$	$-2.222\,691 \times 10^1$	$-4.055\,608 \times 10^{-1}$
135	$-1.623\,405 \times 10^1$	$-1.507\,938 \times 10^1$	$1.683\,084 \times 10^{-1}$
90	$-2.333\,669 \times 10^1$	2.152 594	$6.396\,673 \times 10^{-1}$
45	$-1.617\,810 \times 10^1$	$1.940\,766 \times 10^1$	$7.479\,764 \times 10^{-1}$
0	1.080 975	$2.655\,486 \times 10^1$	$4.253\,387 \times 10^{-1}$
315	$1.832\,666 \times 10^1$	$1.940\,964 \times 10^1$	$-1.405\,752 \times 10^{-1}$

Table 5.3: Time epochs t_0 and time intervals Δt at which center crosses Poincaré sections.

Solar longitude	Time epoch	Time intervals
λ_{\odot} [deg]	t_c [UTC]	$\Delta t_c = t_c - t_0$ [days]
225	October 28, 2023 at 11:14:06.557	-41.563
180	July 24, 2023 at 08:52:44.062	-137.66
135	April 13, 2023 16:33:00.264	-239.34
90	January 7, 2023 at 05:22:50.146	-335.81
45	October 15, 2022 at 00:19:38.723	-420.02
0	August 2, 2022 at 12:51:56.425	-493.50
315	May 25, 2022 at 11:05:11.527	-562.57

5.4 Final remarks

Corridors are streams of trajectories [107] guaranteeing capture that can be targeted far away from the central body [5, 11]. From a different perspective, corridors are time-varying manifolds supporting capture that are approximately in 1:1 mean-motion resonance with the target body. After a short transient, corridor heliocentric Keplerian elements flatten out and their variation, initially characterized by large rates, decreases rapidly in backward time. Time snapshots highlight symmetries and patterns in interior and exterior corridor branches. Subcorridors are developed from specific domains contained in capture sets that are opportunistically selected to fulfill missions purposes. Domains of various shapes (e. g., circular, elliptic, square, strip) can be exploited. Targeting of corridors with strongly constrained platform (e. g., CubeSat) is facilitated by the stretching in backward time. This translates in a compression of the dynamics when propagated forwardly. Eventually, characteristic dimensions of corridors range from $\approx 9.0 \times 10^3$ -by- 6.9×10^4 km up to $\approx 4.2 \times 10^4$ -by- 1.8×10^6 km over a time span roughly from -40 to -560 days.

Acknowledgments The author would like to thank A. Martinelli for the fruitful suggestions provided in the making of Figure 5.1.

“All men dream – but not equally. Those who dream by night, in the dusty recesses of their minds, wake in the day to find that it was vanity. . . . But the dreamers of the day are dangerous men, for they may act their dream with open eyes, to make it possible. This I did.” – T. E. Lawrence, *Seven Pillars of Wisdom*

Autonomous ballistic capture algorithm

The chapter introduces an ABC algorithm tailored for spacecraft with reduced computational capability and that could potentially see the implementation onboard of interplanetary autonomous CubeSat. An overview about the ABC algorithm and the generation of new capture orbits directly onboard are provided. The flowchart in Figure 6.1 gives the overview of the ABC algorithm. The algorithm is composed by two major segments. The first is carried out on ground and aims to prepare a BCC database [11] necessary for the second part of the procedure. The second segment is carried out on board and foresees the CubeSat (or a spacecraft in general) computing new BC sets from which desired BCCs are synthesized [11].

6.1 On-ground tasks

The segment carried out on ground has the purpose of preparing a database of BC orbits to be later used on board as educated guesses for the core algorithm devised for the onboard computation of capture sets and BCCs. Tasks envisioned in the on-ground segment can be performed by a calculator (e. g., workstation, cluster) leveraging on the usual methods for BC design (see Section 3.3). Inputs required by the on-ground module are:

- maximum number of forward revolutions n ;
- list of capture epochs $t_0^{(i)}$;
- initial eccentricity e_0 ;
- initial orbital plane expressed through inclination i_0 and RAAN Ω_0 ;
- initial true anomaly θ_0 (typically ICs are assumed at pericenter, so $\theta_0 = 0$);
- search space on the orbital plane as a circular crown expressed in terms of radius of pericenter r_{p0} and argument of pericenter ω_0 together with the number of grid points.

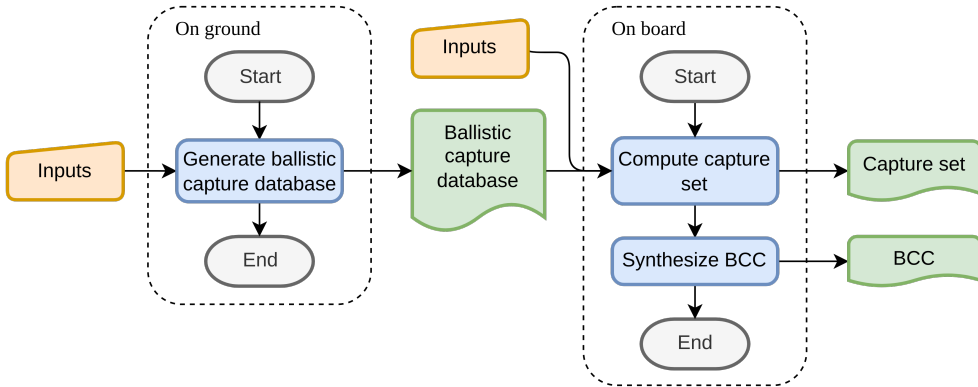


Figure 6.1: ABC algorithm flowchart.

Keplerian elements refer to the $\text{RTN}@t_0^{(i)}$ frame. The output of the module, corresponding to the information stored in the BC database, includes:

- capture sets from \mathcal{C}_{-1}^1 to \mathcal{C}_{-1}^n ;
- regularity indices S ;
- regularity coefficients $\Delta S\%$;
- separatrices extracted from LD fields (i. e., according to [105]).

Once inputs are provided, the following actions are taken for each given time epoch $t_0^{(i)}$: i) computation of subsets \mathcal{W} , \mathcal{X} , and \mathcal{K} ; ii) derivation of capture sets from \mathcal{C}_{-1}^1 to \mathcal{C}_{-1}^n through sets manipulation; iii) computation of regularity index S and coefficient $\Delta S\%$ for all capture sets; iv) computation of finite horizons τ_b (pre-capture leg) and τ_f (post-capture leg) required for LD method; v) extraction of separatrices featured by LD fields to bound locations of capture sets in the phase space; vi) storage of results into the BC database. In step v), separatrices can be extracted according to the methodology in [105], where LD fields are computed over finite horizons consistent with revolution periods of post-capture legs. Alternatively, methods based on LCSs [78], stroboscopic strainlines [68], or Taylor differential algebra (DA) combined with automatic domain splitting [69] are solid options too.

The quantity of information contained in the database strictly depends on the number of capture epochs considered and the grid size. A collection of stable sets ICs plus metadata computed from a grid of 10^5 ICs requires ≈ 0.12 GB of storage. Assuming to store 10 collections characterized by capture epochs covering a time window of 300 days by steps of 30 days, which should be enough to properly catch major variations in the sets about a baseline capture epoch, then the database is estimated to be ≈ 1.2 GB. Nevertheless, the exact amount of data included in the database will depend on the specific mission under design. The detailed flowchart of the on-ground module is shown in Figure 6.2.

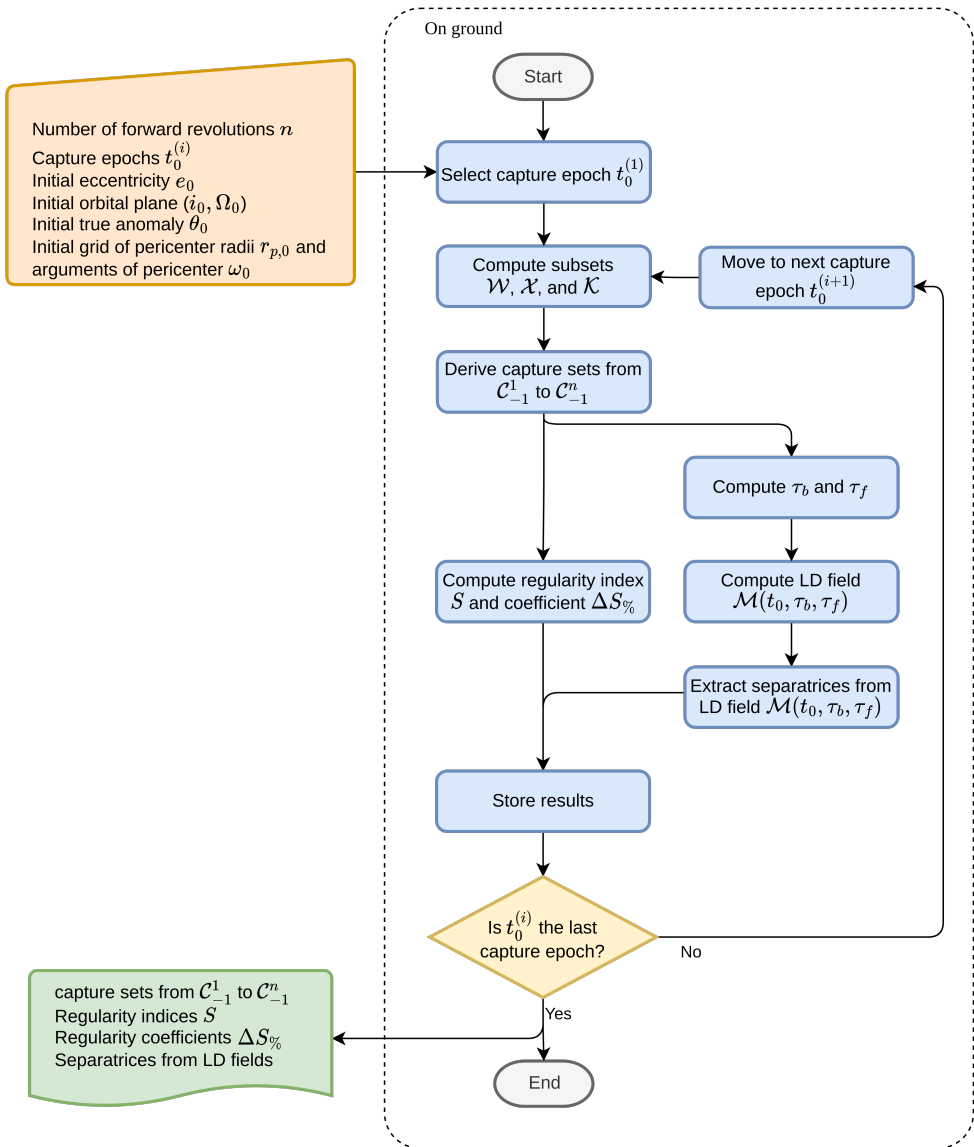


Figure 6.2: ABC algorithm on-ground tasks.

6.2 Onboard tasks

The final goal of the onboard module is to compute capture sets and synthesize BCCs on the fly, while autonomously cruising in the interplanetary space and on an as-needed basis. Inputs required by the algorithm are:

- desired capture epoch t_0 (from autonomous guidance and control unit);
- output of the on-ground module (see Section 6.1).

The output, calculated on requests of the autonomous guidance and control unit [5, 12], includes:

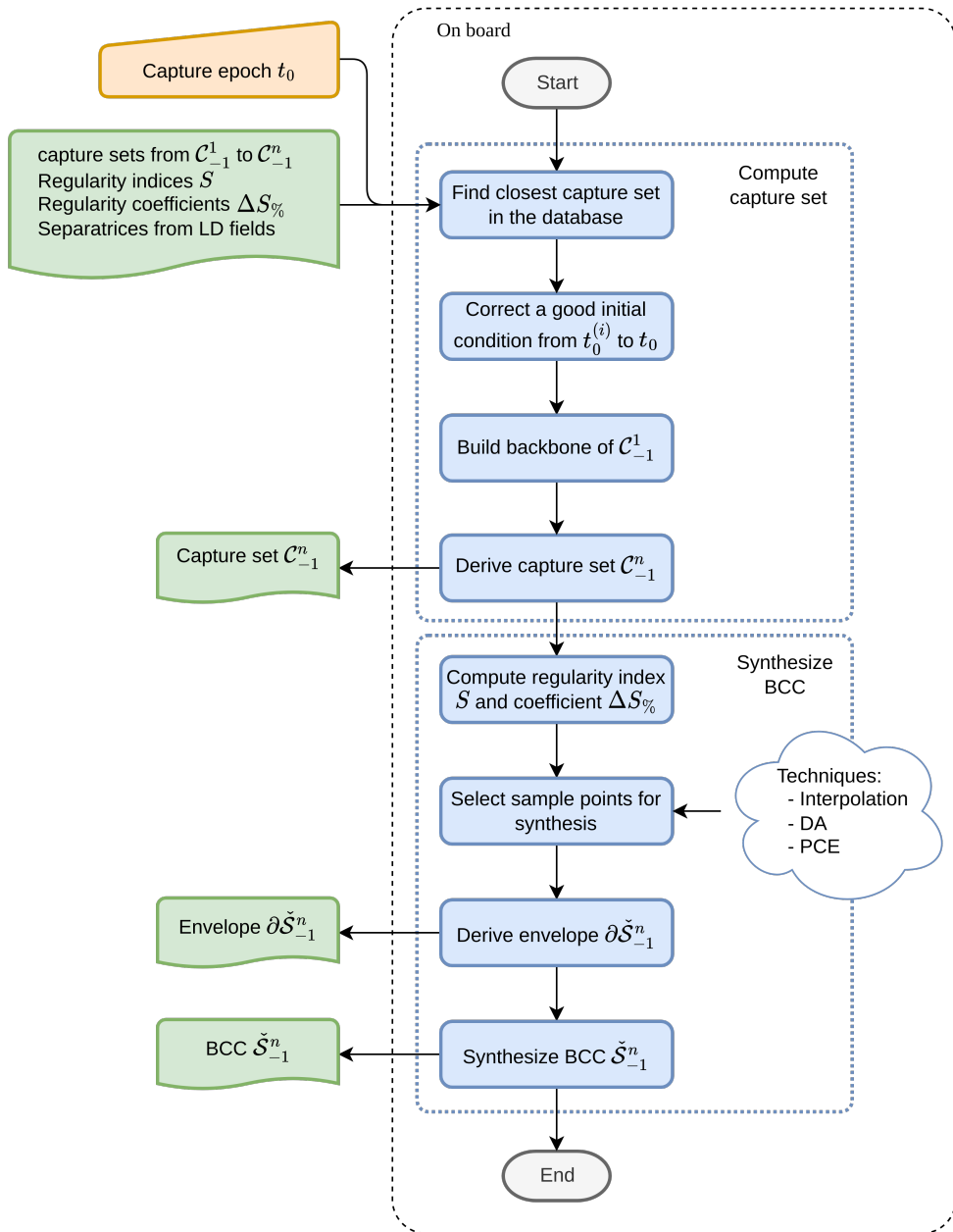


Figure 6.3: ABC algorithm onboard tasks.

- capture set \mathcal{C}_{-1}^n ;
- envelope $\partial \check{S}_{-1}^n$;
- subcorridor \check{S}_{-1}^n .

All outputs are calculated such that the capture epoch corresponds to the desired t_0 in input. In general, the database available is coarse and it does not store sets

guaranteeing capture at the desired time t_0 .

Given the inputs, the following processes are executed: i) search for the i th capture set available in the BC database whose capture epoch $t_0^{(i)}$ is the closest to the desired capture epoch t_0 ; ii) correction of a good IC stored in the database but featuring capture at $t_0^{(i)}$ into a new IC exhibiting capture at time epoch t_0 ; iii) build of capture set \mathcal{C}_{-1}^I backbone using as educated guess the new IC derived in step ii); iv) derivation of capture set \mathcal{C}_{-1}^n (or a portion of it) leveraging on the backbone; v) computation of regularity index S and coefficient $\Delta S\%$ for BC orbits belonging to \mathcal{C}_{-1}^n found in step iv); vi) selection of sample points for synthesis of a BCC numerical approximation; vii) derivation of subcorridor envelope $\partial\check{\mathcal{S}}_{-1}^n$; viii) synthesis of a numerical approximation representative of subcorridor $\check{\mathcal{S}}_{-1}^n$; The detailed flowchart of the onboard segment is presented in Figure 6.3. Steps i)–iv) focus on the computation of capture sets on the fly. The correction of a known BC orbit into a new solution in step ii) is of paramount importance. Generation of families of BC orbits correcting the initial condition is discussed in Chapter 7. The definition, computation, and exploitation of backbones, which are required to complete steps iii) and iv), are covered in Chapter 8. The synthesis of the subcorridor $\check{\mathcal{S}}_{-1}^n$ is in charge of steps v)–viii). Several options are available for BCC synthesis. In this dissertation, a linear interpolation for a fast and inexpensive evaluation of states in the BCC is considered (see Chapter 9). Alternatively, techniques typically used for nonlinear uncertainty propagation like DA [67] or polynomial chaos expansion (PCE) [108, 109] could be successfully employed as well.

Acknowledgments The suggestion of using DA to synthesize BCCs was proposed by Dr. A. Morselli and Dr. P. Panicucci during a meeting of the EXTREMA team at DART, Politecnico di Milano. The suggestion relied on their knowledge and familiarity with DA. Later, synthesis of BCCs using DA was studied by T. Caleb, G. Merisio, Prof. P. Di Lizia, and Prof. F. Topputo. Results were satisfactory but they remain unpublished. The concept of using PCE to synthesize BCCs was conceived by Dr. C. Giordano, supported by his past experience in working with PCE. The concept is currently under study at DART, Politecnico di Milano. The investigation is being carried out by M. Liotta, G. Merisio, Dr. C. Giordano, and Prof. F. Topputo. Preliminary results are promising.

“If you don’t take risks, you can’t create a future.” – Monkey D. Luffy

Eiichiro Oda, *One Piece*

Generation of ballistic capture orbit families

In this chapter, a novel methodology to generate families of BC orbits characterized by succeeding capture epochs is proposed. The problem of finding a new capture orbit at the desired capture epoch correcting a known reference solution is stated. The families are built by sequentially correcting ICs of enough regular BC orbits. New orbits are obtained solving a well-posed three-point boundary value problem (3PBVP) exhibiting 8 linearized boundary conditions. The problem is solved for a finite set of variables with the multiple shooting technique. Effort is put in making the method suitable for autonomous spacecraft with limited onboard resources (e. g., CubeSats). Details of the correction procedure are provided. The methodology is applied to generate families of orbits belonging to capture sets \mathcal{C}_{-1}^1 and \mathcal{C}_{-1}^6 starting from a baseline capture orbit selected for its remarkable regularity. Performance and limitations of the algorithm are assessed. Finally, results are inspected against streamlines of the solar gravity gradient to reveal the nature of corrections applied on reference capture orbits.

7.1 Problem statement

Provided that an enough regular BC orbit is known, then the goal is to derive a modified IC at a desired capture epoch retaining the dynamical behavior of the original BC orbit. Thus, the known reference IC $(\hat{\mathbf{x}}_0, \hat{t}_0) \in \mathcal{C}_{-1}^n$ is corrected into a new IC $(\mathbf{x}_0, t_0) \in \mathcal{C}_{-1}^n$. According to definitions in Section 5.1 and under the dynamics in Eq. (2.1), orbits $\gamma(\hat{\mathbf{x}}_0, \hat{t}_0)$ and $\gamma(\mathbf{x}_0, t_0)$ are necessarily different because the problem is non-autonomous and $\delta t_0 = t_0 - \hat{t}_0 \neq 0$. A schematic representation of the problem is proposed in Figure 7.1. Throughout the chapter, $\gamma(\hat{\mathbf{x}}_0, \hat{t}_0)$ and $(\hat{\mathbf{x}}_0, \hat{t}_0)$ are also referred to as reference BC orbit and IC, respectively. On the other hand, $\gamma(\mathbf{x}_0, t_0)$ and (\mathbf{x}_0, t_0) are indicated as corrected or new BC orbit and IC, respectively. The problem can be thus mathematically stated as follows:

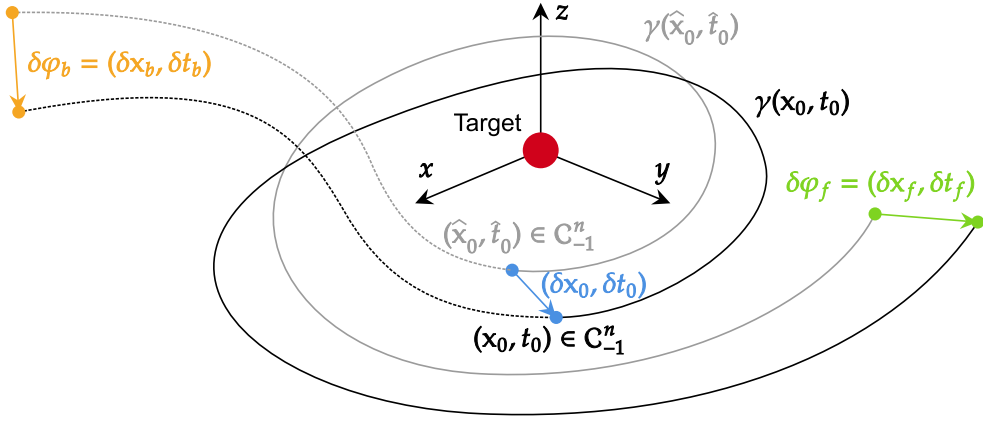


Figure 7.1: Correction of capture orbit.

Problem. Find a modified initial condition \mathbf{x}_0 at a given time t_0 such that $\gamma(\mathbf{x}_0, t_0)$ retains the dynamical behavior of $\gamma(\hat{\mathbf{x}}_0, \hat{t}_0)$. In particular, if $(\hat{\mathbf{x}}_0, \hat{t}_0) \in \mathcal{C}_{-1}^n$ and $\gamma(\hat{\mathbf{x}}_0, \hat{t}_0)$ is a ballistic capture orbit, then $\hat{\mathbf{x}}_0$ shall be corrected into \mathbf{x}_0 such that $(\mathbf{x}_0, t_0) \in \mathcal{C}_{-1}^n$ and $\gamma(\mathbf{x}_0, t_0)$ is a ballistic capture orbit.

7.2 Methodology

The methodology devised to tackle the problem envisages five steps:

1. expansion of the flow $\varphi(\mathbf{x}_0, t_0; t_f)$ about the reference solution $\gamma(\hat{\mathbf{x}}_0, \hat{t}_0)$ at final forward time $t_f > t_0$, after the particle has performed n revolutions about the target, so satisfying condition $(\mathbf{x}_0, t_0) \in \mathcal{W}_n$;
2. expansion of the flow $\varphi(\mathbf{x}_0, t_0; t_b)$ about the reference solution $\gamma(\hat{\mathbf{x}}_0, \hat{t}_0)$ at final backward time $t_b < t_0$, when the particle escapes from the target, so satisfying condition $(\mathbf{x}_0, t_0) \in \mathcal{X}_{-1}$;
3. specification of enough boundary conditions to well-pose the 3PBVP [110];
4. linearization of nonlinear boundary conditions;
5. solution of the 3PBVP through multiple shooting.

This is the core part of a larger algorithm where a number N_p of 3PBVPs are sequentially solved to compute a new family of BC orbits at subsequent capture epochs. Provided that the time step δt_0 is small enough²⁵, the new BC orbit $\gamma(\mathbf{x}_0, t_0)$ is expected to be similar to the reference one. Consequently, boundary conditions are linearized about the reference BC orbit $\gamma(\hat{\mathbf{x}}_0, \hat{t}_0)$. The linearization is beneficial for two reasons: i) it makes boundary conditions consistent with the flow expansion; ii) the problem becomes completely linear, so solving the 3PBVP requires

²⁵Numerical experiments here not reported have shown that the maximum time step δt_0 granting convergence of the algorithm is approximately the 1% of the target orbital period about the primary. Therefore, a maximum time step of a few days is suggested when targeting Mars. Specifically, $\delta t_0 < 7$ days.

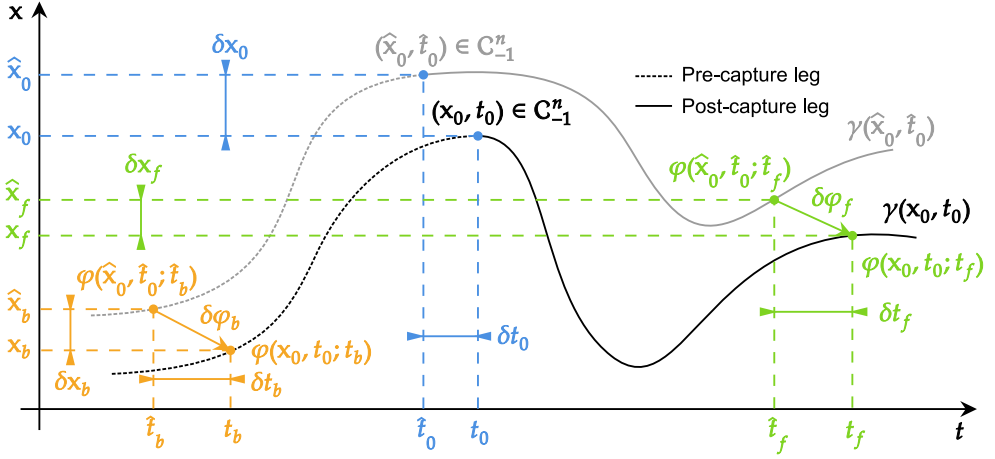


Figure 7.2: Representation of flow expansion.

just a matrix inversion. Throughout the chapter, $\mathbf{r}_0 = \hat{\mathbf{r}}_0 + \delta\mathbf{r}_0$, $\mathbf{v}_0 = \hat{\mathbf{v}}_0 + \delta\mathbf{v}_0$, and $\mathbf{h}_0 = \hat{\mathbf{h}}_0 + \delta\mathbf{h}_0$ are the position, velocity, and angular momentum vectors, respectively. In first approximation, $\delta\mathbf{h} = \mathbf{r} \times \delta\mathbf{v} - \mathbf{v} \times \delta\mathbf{r} = [\mathbf{r}^\wedge] \delta\mathbf{v} - [\mathbf{v}^\wedge] \delta\mathbf{r}$. Finally, the 20-dimensional vector \mathbf{z} is defined as $\mathbf{z} = [\mathbf{x}_0^\top \ \mathbf{x}_f^\top \ \mathbf{x}_b^\top \ t_f \ t_b]^\top$.

7.2.1 Flow expansion

The Taylor expansion truncated at the first order of the flow $\varphi(\mathbf{x}_0, t_0; t_f)$ is

$$\begin{aligned} \varphi(\mathbf{x}_0, t_0; t_f) &= \varphi(\hat{\mathbf{x}}_0 + \delta\mathbf{x}_0, \hat{t}_0 + \delta t_0; \hat{t}_f + \delta t_f) \approx \\ &\approx \varphi(\hat{\mathbf{x}}_0, \hat{t}_0; \hat{t}_f) + \frac{\partial \varphi}{\partial \mathbf{x}_0} \delta\mathbf{x}_0 + \frac{\partial \varphi}{\partial t_0} \delta t_0 + \frac{\partial \varphi}{\partial t_f} \delta t_f \end{aligned} \quad (7.1)$$

where partial derivatives are

$$\frac{\partial \varphi}{\partial \mathbf{x}_0} = \Phi(\mathbf{x}_0, t_0; t_f) = \Phi_{t_0}^{t_f}, \quad (7.2)$$

$$\frac{\partial \varphi}{\partial t_0} = -\Phi_{t_0}^{t_f} \mathbf{f}(\mathbf{x}_0, t_0), \quad (7.3)$$

$$\frac{\partial \varphi}{\partial t_f} = \mathbf{f}(\mathbf{x}_f, t_f). \quad (7.4)$$

They are evaluated at $(\hat{\mathbf{x}}_0, \hat{t}_0; \hat{t}_f)$. Φ is the STM [111]. The derivative in Eq. (7.3) is computed according to [112]. Hence, the expansion becomes

$$\delta\varphi_f \approx \Phi_{\hat{t}_0}^{\hat{t}_f} \delta\mathbf{x}_0 - \Phi_{\hat{t}_0}^{\hat{t}_f} \mathbf{f}(\hat{\mathbf{x}}_0, \hat{t}_0) \delta t_0 + \mathbf{f}(\hat{\mathbf{x}}_f, \hat{t}_f) \delta t_f \quad (7.5)$$

where $\delta\varphi_f = \varphi_f - \hat{\varphi}_f = \varphi(\mathbf{x}_0, t_0; t_f) - \varphi(\hat{\mathbf{x}}_0, \hat{t}_0; \hat{t}_f)$. Similarly, the Taylor expansion truncated at the first order of the flow $\varphi(\mathbf{x}_0, t_0; t_b)$ is

$$\delta\varphi_b \approx \Phi_{\hat{t}_0}^{\hat{t}_b} \delta\mathbf{x}_0 - \Phi_{\hat{t}_0}^{\hat{t}_b} \mathbf{f}(\hat{\mathbf{x}}_0, \hat{t}_0) \delta t_0 + \mathbf{f}(\hat{\mathbf{x}}_b, \hat{t}_b) \delta t_b \quad (7.6)$$

where $\delta\varphi_b = \varphi_b - \hat{\varphi}_b = \varphi(\mathbf{x}_0, t_0; t_b) - \varphi(\hat{\mathbf{x}}_0, \hat{t}_0; \hat{t}_b)$. Overall, Eqs. (7.5) and (7.6) provide 12 relations. Given $\delta t_0 = t_0 - \hat{t}_0$, 20 terms still remain unknown. They are $\delta\mathbf{x}_0$, $\delta\varphi_f = \delta\mathbf{x}_f$, δt_f , $\delta\varphi_b = \delta\mathbf{x}_b$, and δt_b . Therefore, 8 boundary conditions must be specified to well-pose the problem. To better clarify, Figure 7.2 proposes a representation of the flow expansion on the $t\mathbf{x}$ -plane. For the sake of simplicity, the 6-dimensional state space \mathbf{x} is represented as 1-dimensional in Figure 7.2. The Taylor expansion of the flow $\varphi(\mathbf{x}_0, t_0; t_{f|b})$ may be written more compactly as

$$\delta\varphi_{f|b} = \varphi_{f|b} - \hat{\varphi}_{f|b} \approx \Phi_{\hat{t}_0}^{\hat{t}_{f|b}} \delta\mathbf{x}_0 - \Phi_{\hat{t}_0}^{\hat{t}_{f|b}} \mathbf{f}(\hat{\mathbf{x}}_0, \hat{t}_0) \delta t_0 + \mathbf{f}(\hat{\mathbf{x}}_{f|b}, \hat{t}_{f|b}) \delta t_{f|b} \quad (7.7)$$

where the notation $(\bullet|\star)$ means either (\bullet) or (\star) shall be used in the overall relation.

7.2.2 Boundary conditions

The necessary 8 boundary conditions are obtained as follows. Firstly, 3 relations (1 vector and 2 scalar equations) are enforced at capture epoch (i. e., at initial time t_0). Then, other 3 are imposed after n revolutions about the target (i. e., at final forward time t_f). Finally, 1 condition is prescribed at the escape (i. e., at final backward time t_b). They are individually discussed in the next paragraphs.

Boundary condition i_0) The IC \mathbf{x}_0 belongs to a certain orbital plane at t_0 (defined in the RTN@ t_0 frame). It is required that the new IC belongs to the same plane but defined at time $t_0 + \delta t_0$. This is to follow Mars in its orbital revolution about the Sun. $\mathbf{h} = \mathbf{r} \times \mathbf{v}$ In mathematical terms

$$\mathbf{h}_0^{\text{RTN}@ (t_0 + \delta t_0)} = \hat{\mathbf{h}}_0^{\text{RTN}@ t_0}. \quad (7.8)$$

Linearizing Eq. (7.8), it is obtained

$$\mathbf{R}_1 \hat{\mathbf{h}}_0 \times \mathbf{R}_2 \hat{\mathbf{h}}_0 + \mathbf{R}_1 \hat{\mathbf{h}}_0 \times \mathbf{R}_2 \delta \mathbf{h}_0 = \mathbf{0} \quad (7.9)$$

where $\mathbf{R}_1 = \mathbf{R}_{\text{J2000} \rightarrow \text{RTN}@ t_0}$ is the rotation matrix from the J2000 frame to the RTN@ t_0 frame, and $\mathbf{R}_2 = \mathbf{R}_{\text{J2000} \rightarrow \text{RTN}@ (t_0 + \delta t_0)}$ is the rotation matrix from the J2000 frame to the RTN@($t_0 + \delta t_0$) frame. The relation is rewritten as

$$\left[\left(\mathbf{R}_1 \hat{\mathbf{h}}_0 \right)^\wedge \right] \mathbf{R}_2 \mathbf{A}_0 \mathbf{x}_0 + \mathbf{a} = \mathbf{0} \quad (7.10)$$

with $\mathbf{A}_0 = [-[\hat{\mathbf{v}}_\delta] \quad [\hat{\mathbf{r}}_\delta]]$, and $\mathbf{a} = \mathbf{R}_1 \hat{\mathbf{h}}_0 \times \mathbf{R}_2 (-\hat{\mathbf{h}}_0)$. In a more compact form

$$\mathbf{M}_I \mathbf{z} + \mathbf{b}_I = \mathbf{0} \quad (7.11)$$

with

$$\mathbf{M}_I = \mathbf{P} \left[\left[\left(\mathbf{R}_1 \hat{\mathbf{h}}_0 \right)^\wedge \right] \mathbf{R}_2 \mathbf{A}_0 \quad \mathbf{0}_{3 \times 14} \right], \quad \mathbf{b}_I = \mathbf{P} \mathbf{a}, \quad \text{and} \quad \mathbf{P} = \begin{bmatrix} 1 & 0 & 0 \\ 0 & 1 & 0 \end{bmatrix} \quad (7.12)$$

where $\mathbf{0}_{n \times m}$ is the null matrix of dimension $n \times m$. The auxiliary matrix \mathbf{P} is used to extract the first 2 rows in Eq. (7.10) because only 2 out of the 3 relations available are linearly independent.

Boundary condition ii₀) The new IC shall be a pericenter. This means

$$\mathbf{r}_0 \cdot \mathbf{v}_0 = 0, \quad (7.13)$$

a scalar equation that once linearized gives

$$\hat{\mathbf{r}}_0 \cdot \delta \mathbf{v}_0 + \hat{\mathbf{v}}_0 \cdot \delta \mathbf{r}_0 = \mathbf{b}_0^\top \mathbf{x}_0 = 0 \quad (7.14)$$

with $\mathbf{b}_0 = [\hat{\mathbf{v}}_0^\top \ \hat{\mathbf{r}}_0^\top]^\top$. More compactly

$$\mathbf{m}_2^\top \mathbf{z} + b_2 = 0 \quad (7.15)$$

where

$$\mathbf{m}_2 = [\mathbf{b}_0^\top \ \mathbf{0}_{1 \times 14}]^\top, \quad \text{and} \quad b_2 = 0. \quad (7.16)$$

Boundary condition iii₀) The new IC is enforced to have osculating orbital elements with eccentricity $e_0 = \hat{e}_0$, so meaning $\delta e_0 = 0$. This is done exploiting the two-body problem orbit equation. Since $\theta_0 = 0$, we can write

$$\|\mathbf{r}_0\| = \frac{\mathbf{h}_0 \cdot \mathbf{h}_0}{\mu_t(1 + e_0)} = \frac{\mathbf{h}_0 \cdot \mathbf{h}_0}{\mu_t(1 + \hat{e}_0)} \quad (7.17)$$

that can be rewritten as

$$\|\mathbf{r}_0\| \hat{e}_0 = \frac{\mathbf{h}_0 \cdot \mathbf{h}_0}{\mu_t} - \|\mathbf{r}_0\|. \quad (7.18)$$

Once linearized, it provides the following scalar relation

$$2\hat{\mathbf{h}}_0 \cdot \delta \mathbf{h}_0 - \hat{h}_0^2 \frac{\hat{\mathbf{r}}_0 \cdot \delta \mathbf{r}_0}{\hat{r}_0^2} = 2\hat{\mathbf{h}}_0^\top \mathbf{A}_0 \mathbf{x}_0 - \frac{\hat{h}_0^2}{\hat{r}_0^2} \mathbf{c}^\top \mathbf{x}_0 - 3\hat{h}_0^2 = 0 \quad (7.19)$$

with $\mathbf{c} = [\hat{\mathbf{r}}_0^\top \ \mathbf{0}_{1 \times 3}]^\top$, which is equivalent to

$$\mathbf{m}_3^\top \mathbf{z} + b_3 = 0 \quad (7.20)$$

where

$$\mathbf{m}_3 = \left[2\hat{\mathbf{h}}_0^\top \mathbf{A}_0 - \frac{\hat{h}_0^2}{\hat{r}_0^2} \mathbf{c}^\top \quad \mathbf{0}_{1 \times 14} \right]^\top, \quad \text{and} \quad b_3 = -3\hat{h}_0^2. \quad (7.21)$$

Boundary condition i_f) The final state shall perform the n th revolution about the central body. Mathematically, this is translated into

$$\mathbf{r}_f \cdot \mathbf{v}_0 = 0. \quad (7.22)$$

As it is written, the boundary condition only enforces that a revolution is completed at epoch t_f . Consequently, the boundary condition cannot assure that exactly n

revolutions are performed. However, the correct number of revolutions is achieved because the new solution is expected to be similar to the reference one for small enough δt_0 . After linearization, the boundary condition becomes

$$\hat{\mathbf{r}}_f \cdot \delta \mathbf{v}_0 + \hat{\mathbf{v}}_0 \cdot \delta \mathbf{r}_f = \mathbf{d}^\top \begin{bmatrix} \mathbf{x}_0 \\ \mathbf{x}_f \end{bmatrix} = 0 \quad (7.23)$$

with $\mathbf{d} = [\mathbf{0}_{1 \times 3} \ \hat{\mathbf{r}}_f^\top \ \hat{\mathbf{v}}_0^\top \ \mathbf{0}_{1 \times 3}]$. In a more compact form rewritten as

$$\mathbf{m}_4^\top \mathbf{z} + b_4 = 0 \quad (7.24)$$

with

$$\mathbf{m}_4 = [\mathbf{d}^\top \ \mathbf{0}_{1 \times 8}]^\top, \quad \text{and} \quad b_4 = 0 \quad (7.25)$$

Boundary condition ii_f) The Keplerian energy with respect to the central body $E = v^2/2 - \mu_t/r = \mathbf{v} \cdot \mathbf{v}/2 - \mu_t/\|\mathbf{r}\|$ at final forward time of the new BC orbit shall be equal to the final Keplerian energy of the reference final state. This is enforced to preserve capture in forward time, that is $(\mathbf{x}_0, t_0) \in \mathcal{W}_n$. The condition reads

$$\frac{\mathbf{v}_f \cdot \mathbf{v}_f}{2} - \frac{\mu_t}{\|\mathbf{r}_f\|} = \frac{\hat{\mathbf{v}}_f \cdot \hat{\mathbf{v}}_f}{2} - \frac{\mu_t}{\|\hat{\mathbf{r}}_f\|}, \quad (7.26)$$

then linearized as

$$\hat{\mathbf{v}}_f \cdot \delta \mathbf{v}_f + \mu_t \frac{\hat{\mathbf{r}}_f \cdot \delta \mathbf{r}_f}{\hat{r}_f^3} = \mathbf{j}_f^\top \mathbf{x}_f - \left(\hat{v}_f^2 + \frac{\mu_t}{\hat{r}_f} \right) = 0 \quad (7.27)$$

with $\mathbf{j}_f = \left[\frac{\mu_t}{\hat{r}_f^3} \hat{\mathbf{r}}_f^\top \ \hat{\mathbf{v}}_f^\top \right]^\top$. Rearranging terms, the condition can be written as

$$\mathbf{m}_5^\top \mathbf{z} + b_5 = 0 \quad (7.28)$$

where

$$\mathbf{m}_5 = \left[\mathbf{0}_{1 \times 6} \ \mathbf{j}_f^\top \ \mathbf{0}_{1 \times 8} \right]^\top, \quad \text{and} \quad b_5 = - \left(\hat{v}_f^2 + \frac{\mu_t}{\hat{r}_f} \right). \quad (7.29)$$

Boundary condition iii_f) The variation on the final eccentricity magnitude $e_f = \hat{e}_f + \delta e_f$ shall be null, then $\delta e_f = 0$. Hence, the condition can be written as

$$\mathbf{e}_f \cdot \mathbf{e}_f = \hat{\mathbf{e}}_f \cdot \hat{\mathbf{e}}_f. \quad (7.30)$$

Substituting $\mathbf{e} = \frac{\mathbf{v} \times \mathbf{h}}{\mu_t} - \frac{\mathbf{r}}{r}$ and linearizing, the following expression is derived

$$\begin{aligned} & \frac{(\hat{\mathbf{v}}_f \times \hat{\mathbf{h}}_f) \cdot (\delta \mathbf{v}_f \times \hat{\mathbf{h}}_f + \hat{\mathbf{v}}_f \times \delta \mathbf{h}_f)}{\mu_t^2} + \\ & - \frac{(\delta \mathbf{v}_f \times \hat{\mathbf{h}}_f) \cdot \hat{\mathbf{r}}_f + (\hat{\mathbf{v}}_f \times \delta \mathbf{h}_f) \cdot \hat{\mathbf{r}}_f + (\hat{\mathbf{v}}_f \times \hat{\mathbf{h}}_f) \cdot \delta \mathbf{r}_f}{\mu_t \hat{r}_f} + \\ & + \frac{[(\hat{\mathbf{v}}_f \times \hat{\mathbf{h}}_f) \cdot \hat{\mathbf{r}}_f] (\hat{\mathbf{r}}_f \cdot \delta \mathbf{r}_f)}{\mu_t \hat{r}_f^3} = \mathbf{q}^\top \mathbf{x}_f + \nu = 0 \end{aligned} \quad (7.31)$$

with

$$\mathbf{q} = \left[\alpha^\top + \beta^\top [\hat{\mathbf{v}}_f^\wedge]^2 \quad \beta^\top \left([\hat{\mathbf{h}}_f^\wedge] - [\hat{\mathbf{v}}_f^\wedge] [\hat{\mathbf{r}}_f^\wedge] \right) \right]^\top, \quad \alpha = \left(\frac{(\boldsymbol{\kappa} \cdot \hat{\mathbf{r}}_f) \hat{\mathbf{r}}_f^\top - \hat{r}_f^2 \boldsymbol{\kappa}^\top}{\mu_t \hat{r}_f^3} \right)^\top, \quad (7.32)$$

$$\beta = \frac{1}{\mu_t} \left(\frac{\hat{\mathbf{r}}_f^\top}{\hat{r}_f} - \frac{\boldsymbol{\kappa}^\top}{\mu_t} \right)^\top, \quad \nu = \frac{3}{\mu_t} \left(\frac{\boldsymbol{\kappa} \cdot \hat{\mathbf{r}}_f}{\hat{r}_f} - \frac{\boldsymbol{\kappa} \cdot \boldsymbol{\kappa}}{\mu_t} \right), \quad \text{and} \quad \boldsymbol{\kappa} = \hat{\mathbf{v}}_f \times \hat{\mathbf{h}}_f.$$

More compactly

$$\mathbf{m}_7^\top \mathbf{z} + b_7 = 0 \quad (7.33)$$

where

$$\mathbf{m}_7 = \left[\mathbf{0}_{1 \times 6} \quad \mathbf{q}^\top \quad \mathbf{0}_{1 \times 8} \right]^\top, \quad \text{and} \quad b_7 = \nu. \quad (7.34)$$

Boundary condition \mathbf{i}_b The Keplerian energy at the final backward time of the new ballistic capture orbit shall be equal to the final Keplerian energy of the reference final state. This is enforced to preserve escape in backward time, which means $(\mathbf{x}_0, t_0) \in \mathcal{X}_{-1}$. Similarly to Eq. (7.26), the condition is expressed as

$$\frac{\mathbf{v}_b \cdot \mathbf{v}_b}{2} - \frac{\mu_t}{\|\mathbf{r}_b\|} = \frac{\hat{\mathbf{v}}_b \cdot \hat{\mathbf{v}}_b}{2} - \frac{\mu_t}{\|\hat{\mathbf{r}}_b\|}, \quad (7.35)$$

and once linearized reads

$$\hat{\mathbf{v}}_b \cdot \delta \mathbf{v}_b + \mu_t \frac{\hat{\mathbf{r}}_b \cdot \delta \mathbf{r}_b}{\hat{r}_b^3} = \mathbf{j}_b^\top \mathbf{x}_b - \left(\hat{v}_b^2 + \frac{\mu_t}{\hat{r}_b} \right) = 0 \quad (7.36)$$

with $\mathbf{j}_b = \left[\frac{\mu_t}{\hat{r}_b^3} \hat{\mathbf{r}}_b^\top \quad \hat{\mathbf{v}}_b^\top \right]^\top$. Rearranging terms, the condition becomes

$$\mathbf{m}_6^\top \mathbf{z} + b_6 = 0 \quad (7.37)$$

where

$$\mathbf{m}_6 = \left[\mathbf{0}_{1 \times 12} \quad \mathbf{j}_b^\top \quad \mathbf{0}_{1 \times 2} \right]^\top, \quad \text{and} \quad b_6 = - \left(\hat{v}_b^2 + \frac{\mu_t}{\hat{r}_b} \right). \quad (7.38)$$

7.2.3 Three-point boundary value problem solved through multiple shooting

A 3PBVP [113, 114] consists in finding \mathbf{x}_0 , $t \in [t_b, t_f]$ with $t_b \leq t_0 \leq t_f$, such that

$$\dot{\mathbf{x}} = \mathbf{f}(\mathbf{x}, t), \quad \mathbf{g}(\mathbf{x}(t_b), \mathbf{x}(t_0), \mathbf{x}(t_f)) = \mathbf{0}. \quad (7.39)$$

The first equation is the state space representation of Eq. (2.1), while function \mathbf{g} specifies eight boundary conditions needed to well-pose the problem [110]. According to the multiple shooting approach, the problem presented in Eq. (7.39) can be solved for a finite set of variables [114, 115].

In multiple shooting, the solution is discretized over m and l grid points in forward and backward time, respectively. In forward time, the discretization is $t_0 < t_1 < \dots < t_{m-1} = t_f$, so meaning $\mathbf{s}_j = \mathbf{x}(t_j) = \mathbf{x}_j$ with $j = 1, 2, \dots, m-1$. In backward time, it is $t_b = t_{1-l} < \dots < t_{-1} < t_0$, that is $\mathbf{s}_k = \mathbf{x}(t_k) = \mathbf{x}_k$ with $k = -1, -2, \dots, 1-l$. The discretized solution at initial time is $\mathbf{s}_0 = \mathbf{x}(t_0) = \mathbf{x}_0$, the one at final forward time is $\mathbf{s}_{m-1} = \mathbf{x}(t_f) = \mathbf{x}_f$, and that at final backward time is $\mathbf{s}_{1-l} = \mathbf{x}(t_b) = \mathbf{x}_b$. Consequently, $m-1$ and $l-1$ segments are defined in forward and backward time, respectively, in which a 3PBVP is solved by enforcing continuity of solutions at both ends. Sensitivity is reduced by shortening the duration of the original problem. Defect vectors are

$$\begin{aligned}\zeta_j &= \varphi(\mathbf{s}_{j-1}, t_{j-1}; t_j) - \mathbf{s}_j, & t_j &= t_0 + j \frac{t_{m-1} - t_0}{m-1}, \\ \zeta_k &= \varphi(\mathbf{s}_{k+1}, t_{k+1}; t_k) - \mathbf{s}_k, & t_k &= t_0 - k \frac{t_{1-l} - t_0}{l-1},\end{aligned}\quad (7.40)$$

with $j = 1, \dots, m-1$ and $k = -1, \dots, 1-l$. Defects $\zeta_j = \zeta_j(\mathbf{s}_{j-1}, \mathbf{s}_j, t_{m-1})$ and $\zeta_k = \zeta_k(\mathbf{s}_{k+1}, \mathbf{s}_k, t_{1-l})$ depend on t_{m-1} and t_{1-l} via relations in Eq. (7.40) [112]. The new problem is to determine \mathbf{s}_j , \mathbf{s}_k , \mathbf{s}_0 , t_{m-1} , and t_{1-l} such that

$$\begin{aligned}\mathbf{g}(\mathbf{s}_0, \mathbf{s}_{m-1}, \mathbf{s}_{1-l}, t_{m-1}, t_{1-l}) &= \mathbf{0}, \\ \zeta_j &= \mathbf{0}, & j &= 1, \dots, m-1, \\ \zeta_k &= \mathbf{0}, & k &= -1, \dots, 1-l.\end{aligned}\quad (7.41)$$

In Eq. (7.41), there are $6(m+l-1) + 2$ unknowns and $6(m+l-2) + 8$ equations (8 boundary conditions and $6(m+l-2)$ defect constraints). Defects ζ_j are expanded as

$$\begin{aligned}\zeta_j &= \zeta_j(\mathbf{s}_{j-1}, \mathbf{s}_j, t_0, t_{m-1}) \approx \\ &\approx \hat{\zeta}_j + \frac{\partial \zeta_j}{\partial \mathbf{s}_{j-1}} \delta \mathbf{s}_{j-1} + \frac{\partial \zeta_j}{\partial \mathbf{s}_j} \delta \mathbf{s}_j + \frac{\partial \zeta_j}{\partial t_0} \delta t_0 + \frac{\partial \zeta_j}{\partial t_{m-1}} \delta t_{m-1}\end{aligned}\quad (7.42)$$

where $\hat{\zeta}_j = \mathbf{0}$. Indicating $\mathbf{f}(\mathbf{s}_j, t_j) = \mathbf{f}_j$, derivatives in Eq. (7.42) are computed as

$$\frac{\partial \zeta_j}{\partial \mathbf{s}_{j-1}} = \Phi(\mathbf{s}_{j-1}, t_{j-1}; t_j) = \Phi_{j-1}^j \quad (7.43)$$

$$\frac{\partial \zeta_j}{\partial \mathbf{s}_j} = \mathbf{I}_{6 \times 6} \quad (7.44)$$

$$\frac{\partial \zeta_j}{\partial t_0} = -\frac{m-j}{m-1} \Phi_{j-1}^j \mathbf{f}_{j-1} + \frac{m-j-1}{m-1} \mathbf{f}_j \quad (7.45)$$

$$\frac{\partial \zeta_j}{\partial t_{m-1}} = -\frac{j-1}{m-1} \Phi_{j-1}^j \mathbf{f}_{j-1} + \frac{j}{m-1} \mathbf{f}_j \quad (7.46)$$

they are evaluated at $(\hat{\mathbf{s}}_{j-1}, \hat{\mathbf{s}}_j, \hat{t}_0; \hat{t}_{m-1})$. Similarly, defects ζ_k are expanded as well. In matrix form, expansions can be written like

$$\zeta_{j|k} = \begin{bmatrix} \Phi_{j|k} & -\mathbf{I} & \mathbf{d}_{2,j|k} \end{bmatrix} \begin{bmatrix} \mathbf{s}_{j-1|k+1} \\ \mathbf{s}_{j|k} \\ t_{m-1|1-l} \end{bmatrix} + \mathbf{d}_{j|k} = 0 \quad (7.47)$$

where \mathbf{I} is the 6×6 identity matrix, and with

$$\begin{aligned}
 \Phi_{j-1|k+1}^{j|k} &= \Phi(\hat{\mathbf{s}}_{j-1|k+1}, \hat{\mathbf{t}}_{j-1|k+1}; \hat{\mathbf{t}}_{j|k}), \quad \mathbf{f}_{j|k} = \mathbf{f}(\hat{\mathbf{s}}_{j|k}, \hat{\mathbf{t}}_{j|k}), \\
 \mathbf{d}_{1,j|k} &= -\frac{(m|l) - |(j|k)|}{(m|l) - 1} \Phi_{j-1|k+1}^{j|k} \mathbf{f}_{j-1|k+1} + \frac{(m|l) - |(j|k)| - 1}{(m|l) - 1} \mathbf{f}_{j|k}, \\
 \mathbf{d}_{2,j|k} &= -\frac{|(j|k)| - 1}{(m|l) - 1} \Phi_{j-1|k+1}^{j|k} \mathbf{f}_{j-1|k+1} + \frac{|(j|k)|}{(m|l) - 1} \mathbf{f}_{j|k}, \quad \text{and} \\
 \mathbf{d}_{j|k} &= -\Phi_{j-1|k+1}^{j|k} \hat{\mathbf{s}}_{j-1|k+1} + \mathbf{d}_{1,j|k} \delta t_0 - \mathbf{d}_{2,j|k} \hat{\mathbf{t}}_{m-1|l-1} + \mathbf{I} \hat{\mathbf{s}}_{j|k}
 \end{aligned} \tag{7.48}$$

where δt_0 is given. Eventually, defects ζ_j and ζ_k are expressed in matrix form as

$$\zeta = \mathbf{D}\mathbf{s} + \mathbf{b}_d = \mathbf{0} \tag{7.49}$$

where defect, coefficient, variable, and constant matrices are

$$\zeta = [\zeta_1 \cdots \zeta_j \cdots \zeta_{m-1} \zeta_{-1} \cdots \zeta_k \cdots \zeta_{l-1}]^\top, \tag{7.50}$$

$$\mathbf{D} = \begin{bmatrix} & & & \mathbf{d}_{2,1} & & & & \\ & \mathbf{D}_f & & \mathbf{0}_{n_f \times n_b} & & \vdots & & \mathbf{0}_{n_f \times 1} \\ & & & & & \mathbf{d}_{2,m-1} & & \\ & & & & & & & \mathbf{d}_{2,-1} \\ \mathbf{D}_{b,(:,1:6)} & \mathbf{0}_{n_b \times n_f} & \mathbf{D}_{b,(:,7:n_b)} & \mathbf{0}_{n_b \times 1} & & \vdots & & \\ & & & & & & & \mathbf{d}_{2,1-l} \end{bmatrix}, \tag{7.51}$$

$$\mathbf{s} = [\mathbf{s}_0^\top \mathbf{s}_1^\top \cdots \mathbf{s}_{m-1}^\top \mathbf{s}_{-1}^\top \cdots \mathbf{s}_{l-1}^\top t_{m-1} t_{l-1}]^\top, \tag{7.52}$$

$$\mathbf{b}_d = [\mathbf{d}_1^\top \cdots \mathbf{d}_j^\top \cdots \mathbf{d}_{m-1}^\top \mathbf{d}_{-1}^\top \cdots \mathbf{d}_k^\top \cdots \mathbf{d}_{l-1}^\top]^\top \tag{7.53}$$

with $n_f = 6(m-1)$, $n_b = 6(l-1)$, and

$$\mathbf{D}_{f|b} = \begin{bmatrix} \Phi_0^{1|1} & -\mathbf{I} & \mathbf{0} & \cdots & \mathbf{0} \\ \mathbf{0} & \Phi_1^{2|2} & -\mathbf{I} & \cdots & \mathbf{0} \\ \vdots & & \ddots & \ddots & \vdots \\ \mathbf{0} & \cdots & \Phi_{m-3}^{m-2|2-l} & -\mathbf{I} & \mathbf{0} \\ \mathbf{0} & \cdots & \mathbf{0} & \Phi_{m-2}^{m-1|1-l} & -\mathbf{I} \end{bmatrix}. \tag{7.54}$$

The complete set of 8 linearized boundary conditions form a linear system that in matrix form reads

$$\bar{\mathbf{g}}(\mathbf{z}) = \mathbf{M}\mathbf{z} + \mathbf{b}_m = \mathbf{0} \tag{7.55}$$

where \mathbf{z} is the variable matrix previously defined in Section 7.1. The coefficient matrix \mathbf{M} and constant matrix \mathbf{b}_m are constructed as follows

$$\mathbf{M} = [\mathbf{M}_1^\top \mathbf{m}_2 \mathbf{m}_3 \mathbf{m}_3 \mathbf{m}_4 \mathbf{m}_5 \mathbf{m}_6 \mathbf{m}_7]^\top, \tag{7.56}$$

$$\mathbf{b}_m = [\mathbf{b}_1^\top b_2 b_3 b_4 b_5 b_6 b_7]^\top. \tag{7.57}$$

As previously shown, defects ζ_j and ζ_k can be expressed in matrix form as in Eq. (7.49). Eventually, the full system of $6(m+l-2)+8$ equations is built by combining Eqs. (7.49) and (7.55). It reads

$$\mathbf{A}\mathbf{s} = \mathbf{b} \quad (7.58)$$

where the coefficient and constant matrices are

$$\mathbf{A} = \begin{bmatrix} & & \mathbf{D} & & \\ \mathbf{M}_{(:,1:6)} & \mathbf{0} & \mathbf{M}_{(:,7:12)} & \mathbf{0} & \mathbf{M}_{(:,13:20)} \end{bmatrix}, \quad (7.59)$$

$$\mathbf{b} = - \left[\mathbf{b}_d^\top \quad \mathbf{b}_m^\top \right]^\top. \quad (7.60)$$

7.2.4 Generation of ballistic capture orbit family

The algorithm to generate a family of BC orbits is herewith discussed. First of all, an enough regular BC orbit $\gamma(\mathbf{x}_0^*, t_0^*) \in \mathcal{C}_{-1}^n$ is chosen. Such orbit is referred to as baseline and it is used as seed to generate the whole family of new BC orbits. Then, the desired number of revolutions n , the desired capture epoch increment δt_0 , and the desired sequence length in terms of steps number N_p are defined. If $\delta t_0 > 0$ (< 0), then the family is built in forward (backward) time. Before solving the sequence of 3PBVPs, the baseline starting point (\mathbf{x}_0^*, t_0^*) is checked to grant capture and belong to \mathcal{C}_{-1}^n .

Next, the sequence of 3PBVPs is solved. The number of forward points m is set equal to the number of revolutions n about the target plus 1. In this way, the number of forward segments equals the revolutions. The number of backward points l is set equal to 2, such that the escape leg is fully covered in one segment. Later, a loop iterating from 1 to N_p is performed. In the first iteration, the reference solution is set equal to the baseline one. For each iteration, the new capture epoch is updated to $t_0 = \hat{t}_0 + \delta t_0$, and the coefficient matrix \mathbf{A} and constant matrix \mathbf{b} are computed from the current reference solution $\gamma(\hat{\mathbf{x}}_0, \hat{t}_0)$. The linear system in Eq. (7.58) is solved, and the new BC IC (\mathbf{x}_0, t_0) is extracted from the variable \mathbf{s} . The set of nonlinear boundary conditions i_0, ii_0, iii_0 are enforced on (\mathbf{x}_0, t_0) . This is suggested because boundary conditions may not be exactly satisfied due to linearization and numerical noise.

If a new BC orbit is found, then results are stored, the current solution becomes the reference one, and the loop proceeds to the next iteration. Conversely, if the methodology fails and the current solution is not a capture orbit, then the loop is stopped. Eventually, results are saved for post-processing. The detailed procedure to generate a family of BC orbits is found in Algorithm 7.1.

Algorithm 7.1: Generation of BC orbit family.

Procedure INITIALIZATION

Define baseline capture epoch t_0^* ;
 Define baseline BC orbit IC \mathbf{x}_0^* ;
 Define revolutions number n of capture set \mathcal{C}_{-1}^n ;
 Define capture epoch step δt_0 ; \triangleright if $\delta t_0 \geq 0 \Rightarrow$ forw./backw. gen.
 Define 3PBVPs sequence number of steps N_p ;

Procedure COMPUTE FIRST BC ORBIT

Solve BC problem for (\mathbf{x}_0^*, t_0^*) exploiting WSB [25]; \triangleright w/ GRATIS [38]
If $(\mathbf{x}_0^*, t_0^*) \notin \mathcal{C}_{-1}^n$ \triangleright baseline IC (\mathbf{x}_0^*, t_0^*) not a BC orbit
 | Return;
End

Procedure SOLVE SEQUENCE OF 3PBVPs

Set number of forward points $m = n + 1$; \triangleright 1 seg. per revolution
 Set number of backward points $l = 2$; \triangleright only 1 seg. for escape
 Set reference starting point $(\hat{\mathbf{x}}_0, \hat{t}_0) = (\mathbf{x}_0^*, t_0^*)$;
 Set counter $i = 1$;

While $i \leq N_p$

Update new capture epoch $t_0 = \hat{t}_0 + \delta t_0$;
 Build \mathbf{M} and \mathbf{b}_m of linear. bound. conds. $\bar{\mathbf{g}}(\mathbf{z}) = \mathbf{0}$; \triangleright see Eq. (7.55)
 Build \mathbf{D} and \mathbf{b}_d of defects constraints $\zeta(\mathbf{s}) = \mathbf{0}$; \triangleright see Eq. (7.49)
 Build \mathbf{A} and \mathbf{b} of multiple shooting; \triangleright see Eq. (7.58)
 Solve linear system $\mathbf{A}\mathbf{s} = \mathbf{b}$ for variable \mathbf{s} ;
 Extract (\mathbf{x}_0, t_0) from variable vector \mathbf{s} ;
 Enforce boundary condition i_0 on (\mathbf{x}_0, t_0) ; \triangleright see Eq. (7.8)
 Enforce boundary condition ii_0 on (\mathbf{x}_0, t_0) ; \triangleright see Eq. (7.13)
 Enforce boundary condition iii_0 on (\mathbf{x}_0, t_0) ; \triangleright see Eq. (7.17)
 Solve BC problem for (\mathbf{x}_0, t_0) exploiting WSB [25]; \triangleright w/ GRATIS [38]
If $(\mathbf{x}_0, t_0) \in \mathcal{C}_{-1}^n$ \triangleright found new BC orbit, 3PBVP solved
 | Store results $(\mathbf{x}_0^{(i)}, t_0^{(i)}) = (\mathbf{x}_0, t_0)$;
 | Update reference capture epoch $\hat{t}_0 = t_0$;
 | Update reference BC orbit IC $\hat{\mathbf{x}}_0 = \mathbf{x}_0$;
 | Increment loop counter $i = i + 1$;

Else \triangleright failed to solve current 3PBVP
 | Break the loop;

End**End**

Save number of new orbits computed $N_{BC} = i - 1$;
 Save results;

Exit

Result: Family of new BC orbits having ICs $(\mathbf{x}_0^{(i)}, t_0^{(i)}) \forall i = 1, 2, \dots, N_{BC}$.

7.3 Results

The methodology presented in Section 7.2 is now applied to build two families of BC orbits²⁶. The first is a family of orbits belonging to \mathcal{C}_{-1}^1 while the second to \mathcal{C}_{-1}^6 . Families have been built starting from the same baseline capture orbit. The procedure in Algorithm 7.1 is carried out twice per family, both in forward and backward direction. The two resulting families have been unified in a unique, larger family with two branches stemming from the baseline capture orbit $\gamma(\mathbf{x}_0^*, t_0^*)$.

7.3.1 Baseline ballistic capture orbit

The baseline BC sets \mathcal{C}_{-1}^1 and \mathcal{C}_{-1}^6 are defined in the Mars-centered RTN@ t_i frame at baseline capture epoch $t_0^* = 0$ days set to December 9, 2023 at 12:00:00.00 (UTC). At this epoch, Mars' true anomaly with respect to the Sun is approximately equal to 270 deg, maximizing \mathcal{R}_c [50]. The selected plane is defined by inclination $i_0^* = 0$ deg, and RAAN $\Omega_0^* = 0$ deg. At the initial epoch t_0^* , sought trajectories have osculating eccentricity $e_0^* = 0.99$ [9], and true anomaly $\theta_0^* = 0$ deg. Let R_{\odot} be the radius of Mars in km, then the search space on the plane defined above is a circular crown centered at Mars, from radius $R_{\odot} + 100$ km up to radius $11R_{\odot}$. Hence, $(r_{p0}^*, \omega_0^*) \in [R_{\odot} + 100 \text{ km}, 11R_{\odot}] \times (0, 2\pi]$ rad and grid size set to $[339 \times 360]$.

The baseline BC orbit has been chosen based on its regularity. By visual inspection of capture sets \mathcal{C}_{-1}^1 and \mathcal{C}_{-1}^6 plots, a regular orbit (small regularity index S) present in both sets has been selected. Such plots are shown in Figure 7.3, where interior and exterior corridor branches are highlighted too [11]. The baseline BC orbit is marked with a red triangle and has coordinates $(r_{p0}^*, \omega_0^*) = (2.35R_{\odot}, 288 \text{ deg})$. The baseline capture orbit is presented in Figure 7.4. The two orbits shown are propagated starting from the same IC, however their number of revolutions is different. In Figure 7.4a, the post-capture leg is limited to the 1st revolution. Differently, the post-capture leg of the orbit represented in Figure 7.4b goes on up to the 6th revolution. EoM are written in the three-dimensional space, however only the xy -plane is shown in Figure 7.3 and no clues are provided about the out of plane motion. This is done for visualization purposes. The out of plane motion is small (but not null) in the ECLIPJ2000 frame and top-views allow a better understanding of the particle motion. The latter remark applies also to next plots.

²⁶EoM include gravitational attractions of the Sun, Mercury, Venus, Earth–Moon (B), Mars (central body), Jupiter (B), Saturn (B), Uranus (B) and Neptune (B), and SRP. To nondimensionalize EoM, a modified set of normalization units is used to avoid ill-conditioning. They are: $\bar{M}\bar{U} = 42828.376 \text{ km}^3 \text{ s}^{-2}$, $\bar{L}\bar{U} = 1.085772 \times 10^6 \text{ km}$ (i. e., Mars– $L_{2,\odot\odot}$ distance), $\bar{T}\bar{U} = 5.466913 \times 10^6 \text{ s}$, and $\bar{V}\bar{U} = 1.986079 \times 10^{-1} \text{ km s}^{-1}$.

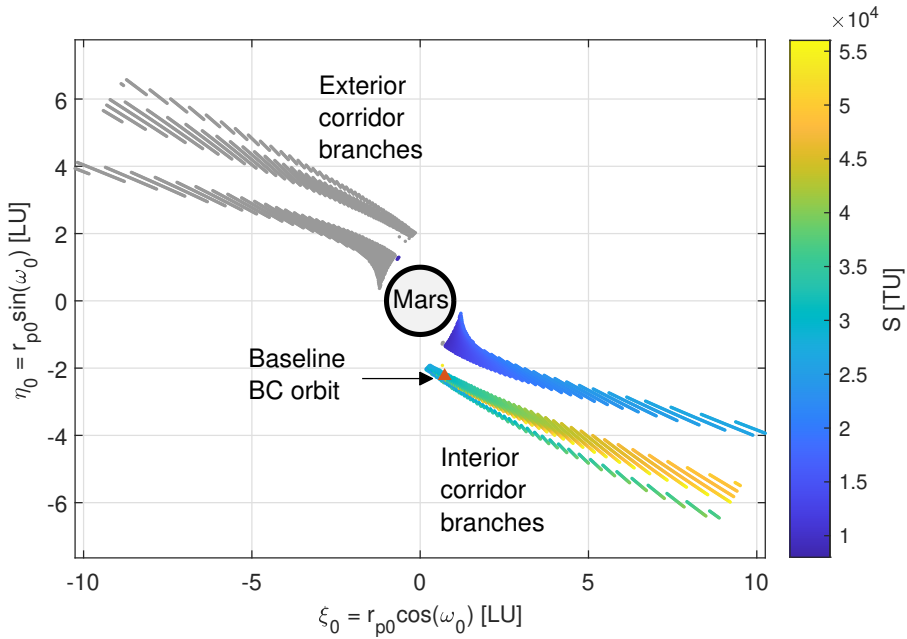
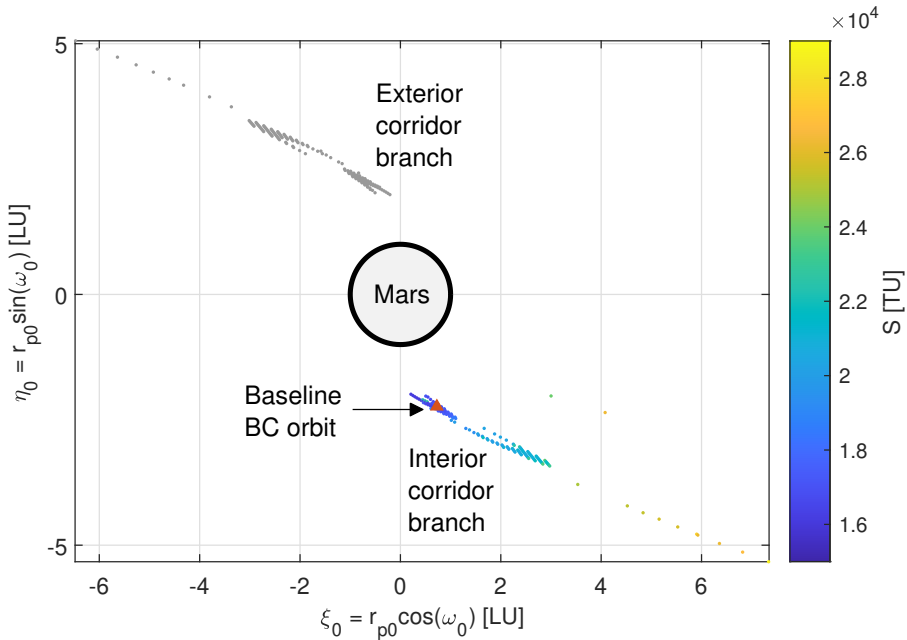
(a) Capture set \mathcal{C}_{-1}^1 .(b) Capture set \mathcal{C}_{-1}^6 .

Figure 7.3: Capture sets at epoch $t_0^* = 0$ days set to December 9, 2023 at 12:00:00.00 (UTC). Regularity index S of branches developing the interior BCC. In gray, branches developing the exterior BCC. Nondimensional coordinates on the orbital plane $i_0^* = \Omega_0^* = 0$ deg defined in the Mars-centered RTN@ t_0^* frame. Selected baseline capture orbit marked with red triangle.

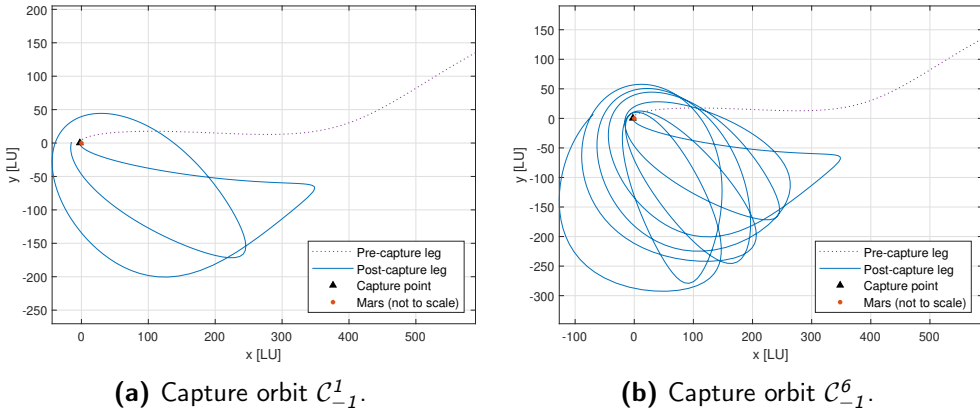


Figure 7.4: Baseline BC orbits at capture epoch $t_0^* = 0$ days set to December 9, 2023 at 12:00:00.00 (UTC). Pre-capture and post-capture legs represented as purple dotted and blue solid lines, respectively. Nondimensional coordinates in the Mars-centered ECLIPJ2000 frame, xy -plane views. Out of plane motion small but not null.

7.3.2 Families of ballistic capture orbits

The family of BC orbits belonging to C_{-1}^1 is constructed setting $n = 1$, $\delta t_0 = \pm 5$ days, and $N_p = 30$. On the other hand, the family of orbits belonging to C_{-1}^6 is built setting $n = 6$, $\delta t_0 = \pm 2$ days, and $N_p = 75$. The time step of family C_{-1}^6 is smaller compared to family C_{-1}^1 because of the greater difficulty for the algorithm in completing the sequences of 3PBVPs as the number of revolutions n increases. In the best case, the algorithm would return two families covering 300 days, from $t_0^* - 150$ to $t_0^* + 150$ days. Algorithm 7.1 is applied twice per family, both in forward and backward directions. In doing so, two sequences of orbits are obtained for each distinct family that are later combined.

Results are shown in Figure 7.5, where the families of BC orbits are drawn. Forward and backward sequences are represented with black solid and dotted lines, respectively. They are overlapped on a collection of capture set branches developing the interior BCC. The plotted sets span capture epoch from $t_0^* - 150$ days up to $t_0^* + 150$ days. Information about the regularity of solutions is expressed in terms of the normalized regularity index S_{rel} represented through color shading. A color code is used to highlight the generated orbits (marked with triangles) having the same capture epochs of reported capture sets. To enhance the visualization, close magnifications to Mars are shown in Figure 7.6.

About family C_{-1}^1 (plot in Figure 7.5a), the methodology successfully completed 27 steps in the forward direction, so reaching 135 days after the baseline capture epoch t_0^* . In backward direction, the algorithm never failed and completed all 30 steps, so providing solutions up to 150 days, before t_0^* . Overall, the baseline solution is extended for 285 days. The forward sequence failed in correspondence of the discontinuity located on the edge of the capture set branches characterized by larger regularity indexes (lighter branches).

Regarding family \mathcal{C}_{-1}^6 (plot in Figure 7.5b), 47 and 16 steps are successfully completed in the forward and backward directions, respectively. As a result, the algorithm provided solutions for 126 days, up to 94 days in the forward direction and -32 days in the backward one.

The algorithm performs better for family \mathcal{C}_{-1}^1 than for family \mathcal{C}_{-1}^6 , even though a smaller time step δt_0 is used for the second one. The reason could be found in the shape and size of capture sets. Indeed, sets \mathcal{C}_{-1}^1 are wide and dense, while sets \mathcal{C}_{-1}^6 are small and sparse. In particular, the sparsity of sets \mathcal{C}_{-1}^6 represents and harsh obstacle to overcome for the algorithm, so preventing the successful completion of the full sequence.

Selected BC orbits are plotted in Figure 7.7. They are the members of the families corresponding to the sets shown in Figure 7.5. The same color code of Figure 7.5 applies to Figure 7.7. As expected, orbits of the same family are really similar in shape. They are rotated about the target due to the revolution of the central body about the Sun. The orbit in purple is the baseline BC orbit in Figure 7.4. Mars' SOI is also represented for reference ($R_{\text{SOI}} = 170R_{\odot}$).

The families of BC orbits are now studied in detail. In particular, the distance from the central body and the Keplerian energy are considered of interest. In Figures 7.8 and 7.9, pre-capture and post-capture legs are drawn as dotted and solid lines, respectively. The curves are colored as the corresponding capture orbits shown in Figure 7.7. The color code is that of Figure 7.5.

The distance evolution of the families is presented in Figure 7.8. As clearly shown by the plots, orbits of both families cross Mars' SOI multiple times during the temporary capture. Furthermore, at the escape point, all orbits have already crossed the SOI. Therefore, the escape from Mars is always triggered by the zero crossing of the Keplerian energy. Most orbits fly far from the surface and all orbits shown in Figure 7.8 never cross the Exosphere limit located at an altitude of 230 km. However, some solutions fly very close to such limit. Specifically, the ones generated after $t_0^* + 100$ days, which are those succeeding the light blue curve in Figure 7.8a. These are orbits whose ICs are close to the previously mentioned discontinuity located near the edge in the less regular (lighter) branches of the capture sets shown in Figure 7.5. The last orbit of the forward sequence is that performing the closest passage to Mars. At the next step, the algorithm fails because the computed solution falls in the crash set \mathcal{K}_1 , thus impacting the target instead of preserving the weakly stable nature of the reference orbit $\gamma(\hat{\mathbf{x}}_0, \hat{t}_0)$.

The Keplerian energy trend is plotted in Figure 7.9. As already observed while commenting Figure 7.8, it is the Keplerian energy that triggers the escape. In fact, the Keplerian energy is always zero at the beginning of all pre-capture legs. Except for some occasional behaviors, the trend of Keplerian energy is quite similar for all orbits belonging to the same family, even though they are shifted in time. This is akin to previous observations on orbit shapes, and distances from target.

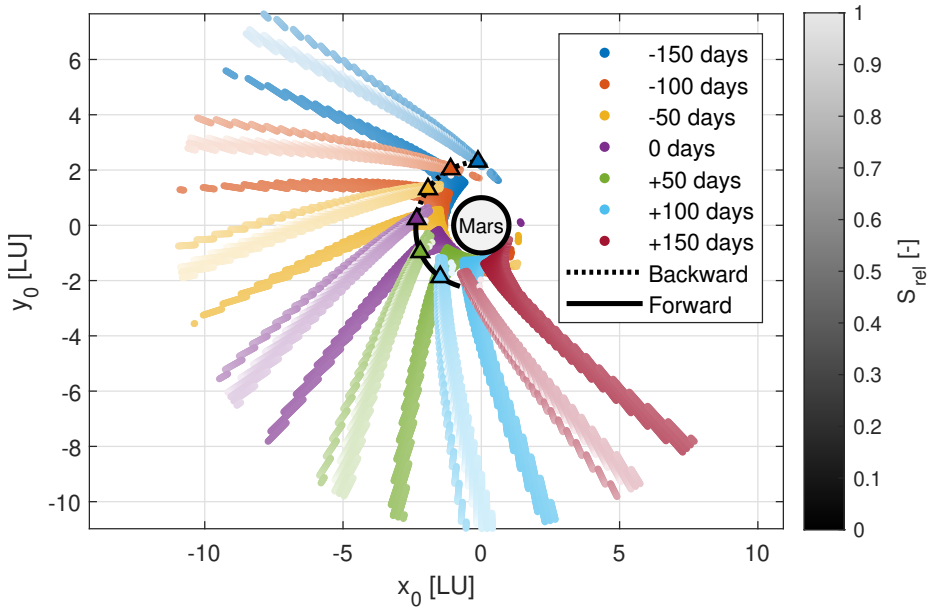
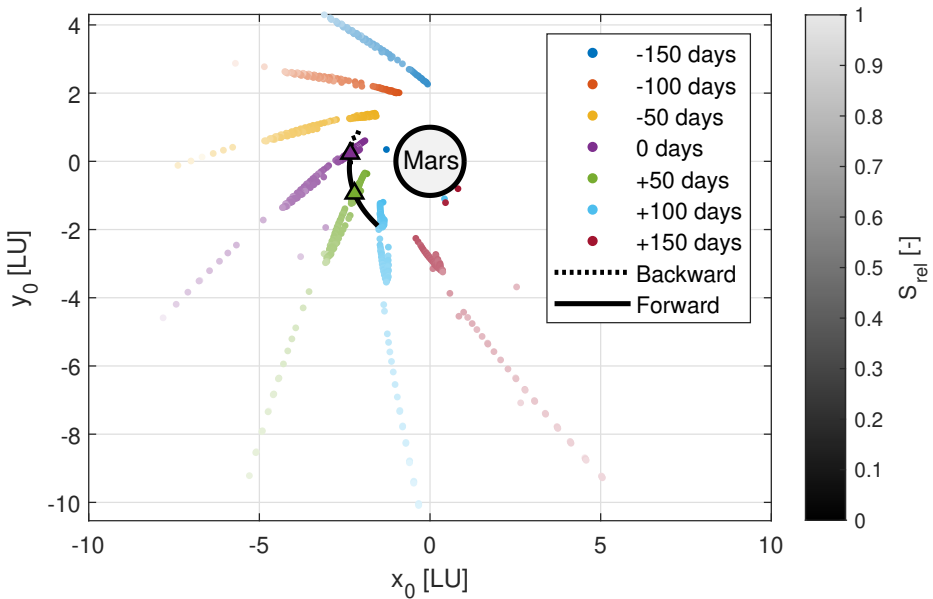
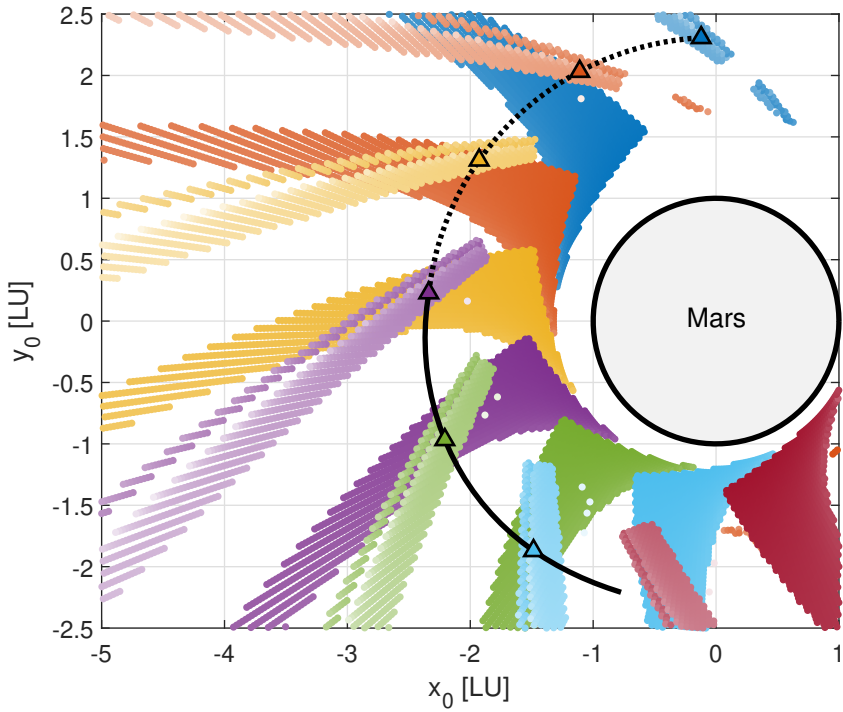
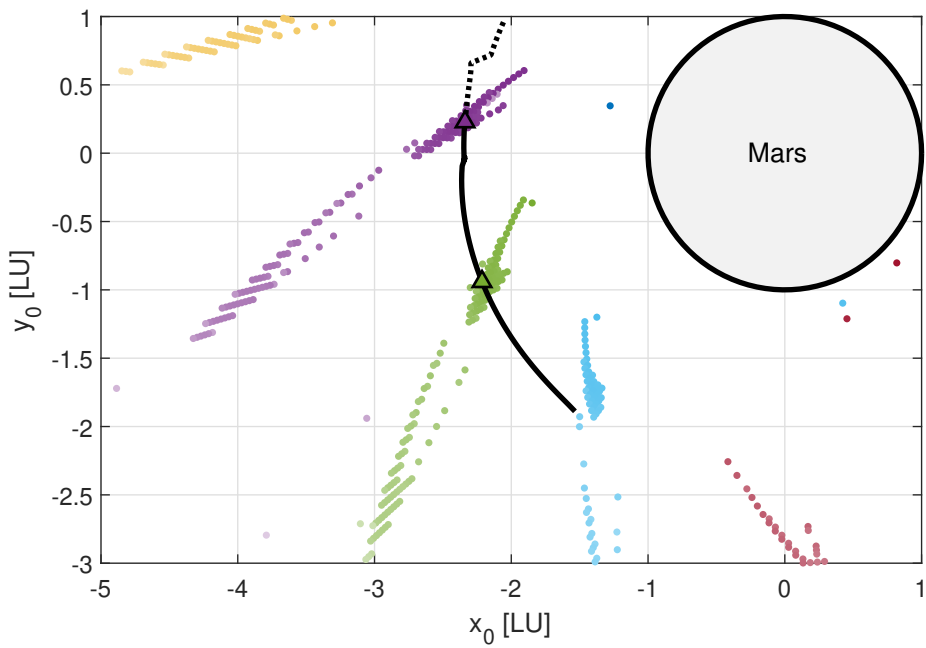
(a) Family and capture sets \mathcal{C}_{-I}^1 .(b) Family and capture sets \mathcal{C}_{-I}^6 .

Figure 7.5: Families of BC orbits generated with Algorithm 7.1. Black solid and dotted lines represent forward and backward sequences, respectively. Families overlapped on a collection of capture set branches developing the interior BCC and spanning from $t_0^* - 150$ up to $t_0^* + 150$ days. Baseline capture epoch $t_0^* = 0$ set to December 9, 2023 at 12:00:00.00 (UTC). Triangles mark peculiar BC orbits computed at the same epochs of the visualized capture sets. Correspondence depicted through color code. Normalized regularity index S_{rel} expressed through color shading. Nondimensional coordinates in the Mars-centered ECLIPJ2000 frame, xy -plane views. Out of plane contribution small but not null.

(a) Magnification C_{-1}^1 .(b) Magnification C_{-1}^6 .**Figure 7.6:** Magnifications of BC orbit families shown in Figure 7.5.

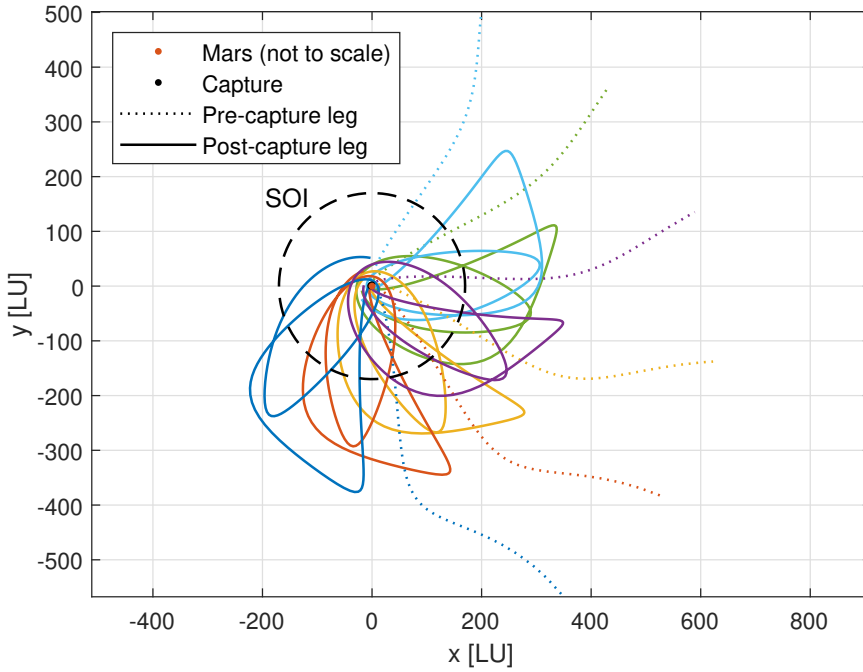
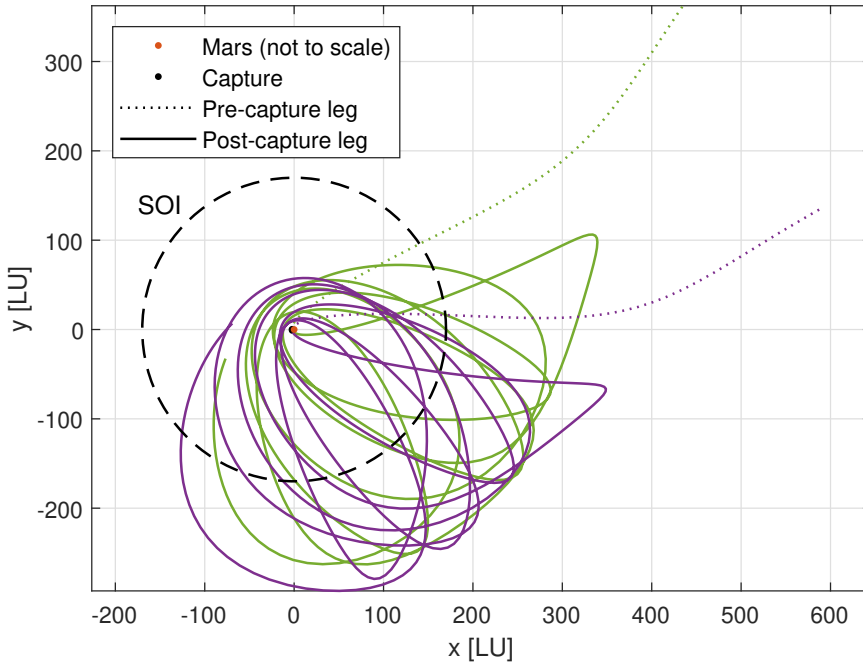
(a) Orbits family C_{-1}^1 .(b) Orbits family C_{-1}^6 .

Figure 7.7: BC orbits at peculiar capture epochs. Same color code used in Figure 7.5. Pre- and post-capture legs represented as dotted and solid lines, respectively. Nondimensional coordinates in the Mars-centered ECLIPJ2000 frame, xy -plane views. Out of plane motion small but not null.

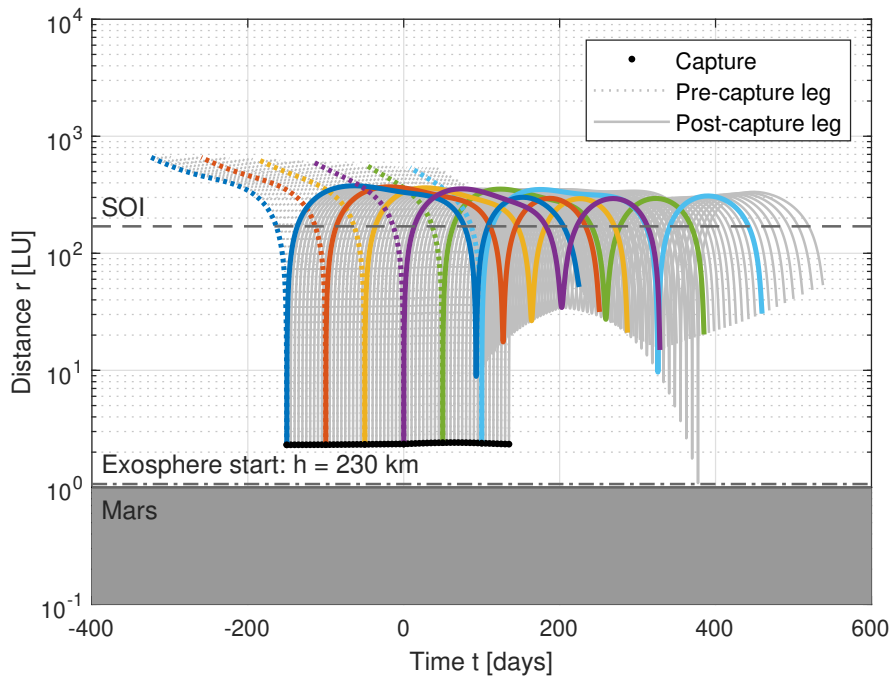
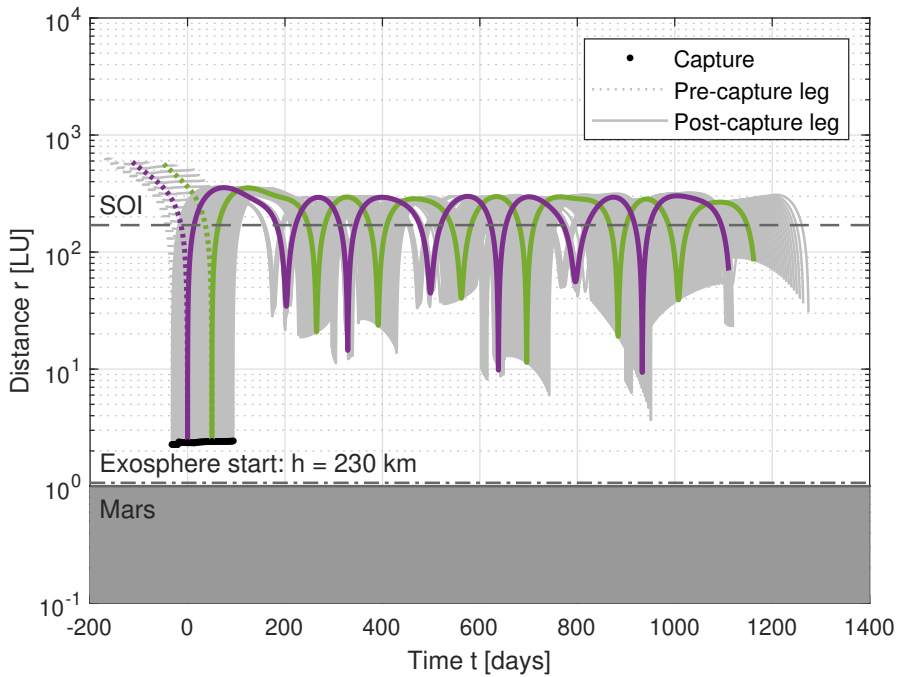
(a) Distances family \mathcal{C}_{-1}^1 .(b) Distances family \mathcal{C}_{-1}^6 .

Figure 7.8: Distance from Mars of BC orbit families generated with Algorithm 7.1. Curves colored as corresponding capture orbits shown in Figure 7.7. Same color code used in Figure 7.5. Pre- and post-capture legs represented as dotted and solid lines, respectively.

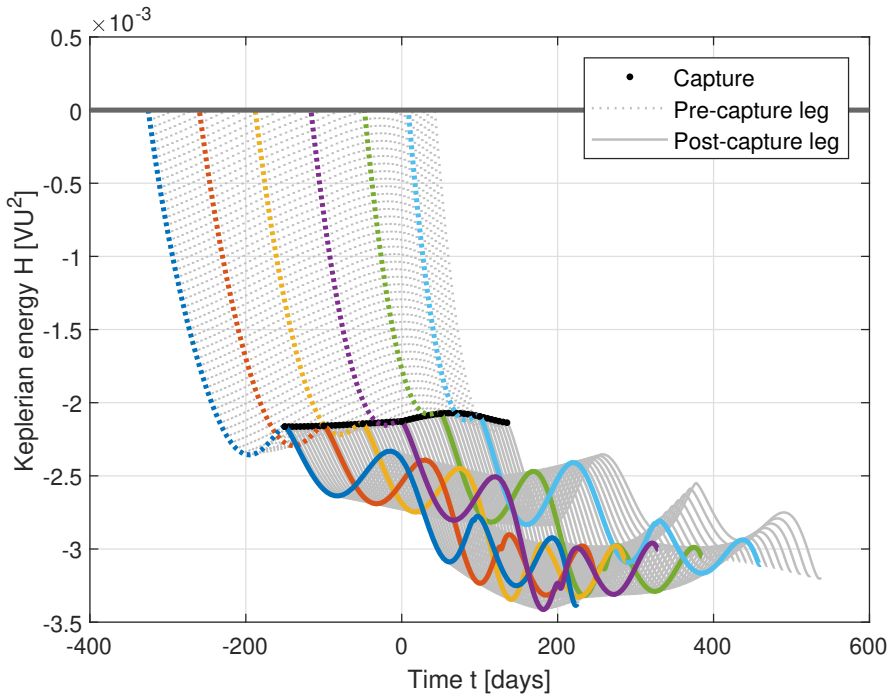
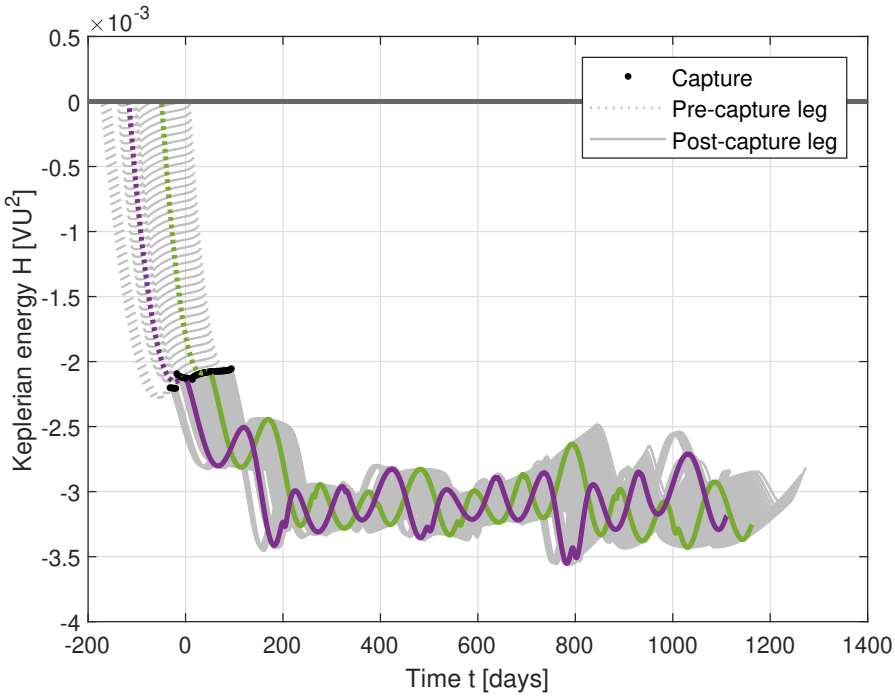
(a) Keplerian energies family C_{-1}^1 .(b) Keplerian energies family C_{-1}^6 .

Figure 7.9: Keplerian energy with respect to Mars of BC orbit families generated with Algorithm 7.1. Curves colored as corresponding capture orbits shown in Figure 7.7. Same color code used in Figure 7.5. Pre- and post-capture legs represented as dotted and solid lines, respectively.

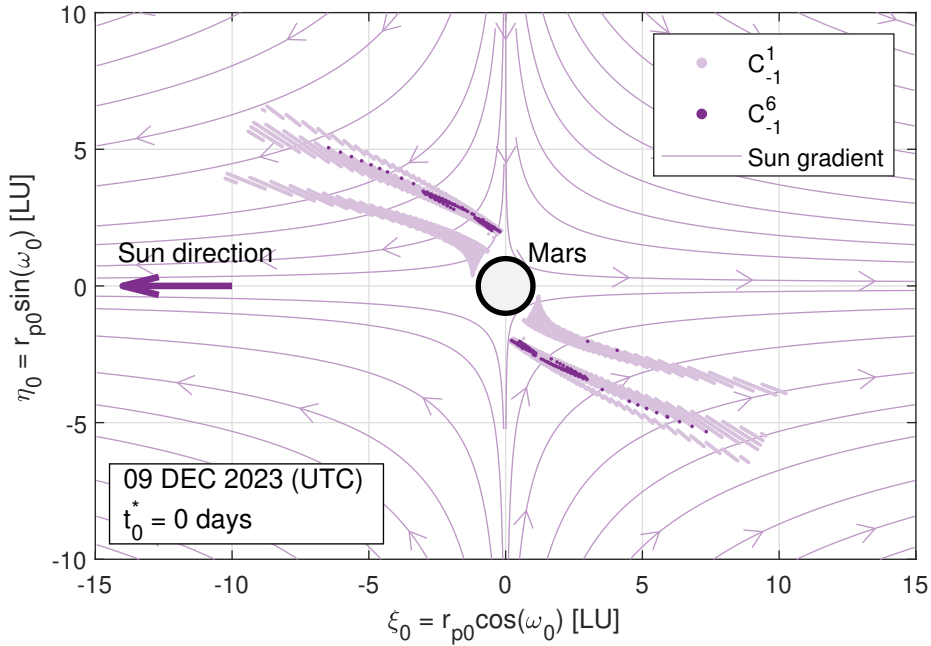


Figure 7.10: Capture sets C_{-1}^1 and C_{-1}^6 inspected against solar gravity gradient. Capture sets and solar gravity gradient computed at baseline capture epoch $t_0^* = 0$ days set to December 9, 2023 at 12:00:00.00 (UTC). Nondimensional coordinates on the orbital plane $i_0^* = \Omega_0^* = 0$ deg defined in the Mars-centered RTN@ t_0^* frame.

7.3.3 Inspection against solar gravity gradient

To better understand why a reference solution is corrected into a specific new capture orbit according to the methodology described in Section 7.2, the families are inspected against the solar gravity gradient. The solar gravity gradient is computed according to (see Section 3.4) [43, 52]. Specifically, the first order Taylor expansion about the origin (corresponding to Mars center) of the Sun gravitational attraction is evaluated on the domain of interest. The goal of this analysis is to identify some visible patterns or connections to shed some light on the physical motivation behind the effectiveness of the method.

Figure 7.10 shows an example of this analysis, where streamlines of the solar gravity gradient are shown on the background of baseline capture sets C_{-1}^1 and C_{-1}^6 . Results are represented in the Mars-centered RTN@ t_0^* frame. Consequently, the Sun direction is aligned with the $-x$ direction. In Figure 7.11, solar gravity gradient streamlines at peculiar capture epochs are compared against the two families of BC orbits. Results are plotted in the Mars-centered ECLIPJ2000 frame with color code akin to that in Figure 7.5. Sun directions corresponding to peculiar capture epochs are also reported near the frame origin. Neither trivial patterns nor connections between families and streamlines are recognized. Further investigation is necessary to physically justify how families are constructed along distinctive paths.

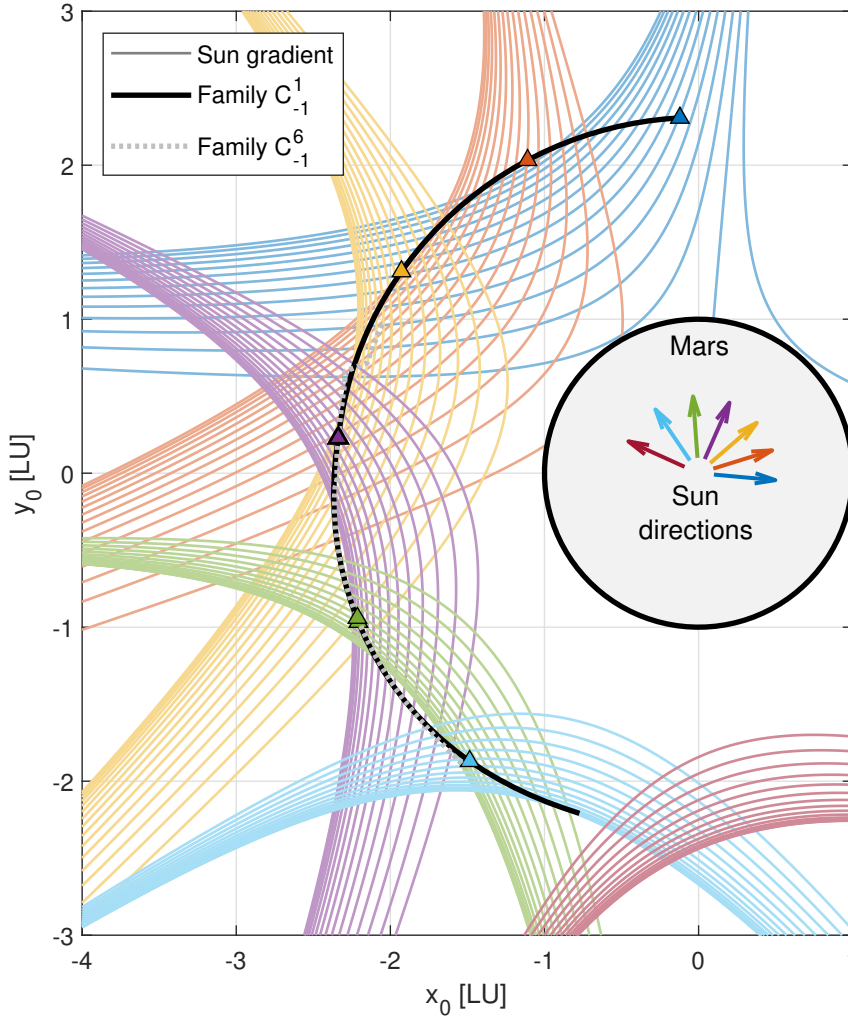


Figure 7.11: Families C_{-1}^1 and C_{-1}^6 of BC orbits generated with Algorithm 7.1 inspected against solar gravity gradient fields computed at peculiar capture epochs spanning from $t_0^* - 150$ days to $t_0^* + 150$ days. Baseline capture epoch $t_0^* = 0$ days set to December 9, 2023 at 12:00:00.00 (UTC). ICs of BC orbits at peculiar epochs marked by triangles. Same color code used in Figure 7.5. Nondimensional coordinate in the Mars-centered ECLIPJ2000 frame, xy -plane view. Out of plane contribution small but not null.

7.4 Final remarks

The problem of correcting the IC initial condition of a reference capture orbit, which solution is required for the successful application of the algorithm, is stated and discussed. The approach to tackle the problem is explained. Attention is given to steps including the flow expansion, the definition of the 8 necessary boundary conditions, and their linearization. Then, a 3PBVP is formulated and solved with the multiple shooting technique. As a result, a linear system is obtained that, once solved, provides the IC of a new BC orbit. Families of capture orbits are easily generated by solving a sequence of linear systems, so reducing the computational burden typically required for finding BC orbits via classical approaches (see Section 3.3).

The algorithm is proven successful in the generation of two families of orbits belonging to capture sets \mathcal{C}_{-1}^1 and \mathcal{C}_{-1}^6 . Based on results, the algorithm performs better when the revolutions number n is small. For $n = 1$, the method works smoothly and long sequences of BC orbits are built even for large time steps δt_0 . Conversely, for many revolutions, the method finds difficult to build long sequences of orbits due to the smallness and sparsity typical of capture sets exhibiting many revolutions about the target. The issue is mitigated by using a small time step δt_0 . Nevertheless, the algorithm constructs sequences of solutions spanning more than 100 days for both families. Shape, distance, and Keplerian energy of orbits are studied, so proving the method effectiveness in finding solutions really similar to each other, even over large time spans. The capability of generating wide families of capture orbits, both for few and many revolutions, and the limited computational complexity opens the possibility to the onboard implementation of the algorithm, even for autonomous, limited-capability platforms like CubeSats.

“Fall in love with some activity, and do it! Nobody ever figures out what life is all about, and it doesn’t matter. Explore the world. Nearly everything is really interesting if you go into it deeply enough. Work as hard and as much as you want to on the things you like to do the best. Don’t think about what you want to be, but what you want to do. Keep up some kind of a minimum with other things so that society doesn’t stop you from doing anything at all.”

Richard P. Feynman

Backbone of capture set

The chapter defines the backbone of a BC set and presents a methodology based on LDs for its derivation. The method constitutes one of the required building blocks of the ABC algorithm presented in Chapter 6. The effectiveness of LDs in extracting dynamical features is studied. The computation of the backbone is discussed in detail. The performance of the backbone is analyzed.

8.1 Problem statement

The backbone of a capture set is defined as the locus of points in a capture set \mathcal{C}_{-1}^1 also belonging to $\mathcal{C}_{-1}^{n \gg 1}$. This means that ICs constituting the backbone are expected to perform at least more than one (preferably many) revolution about the target planet. The advantage of the backbone is that it is computed on the capture set \mathcal{C}_{-1}^1 . This avoid propagating ICs for large final forward times typical of orbits belonging to capture sets featuring large revolution numbers n . Essentially, interesting capture solutions are inferred from the dynamical information obtained on a short finite horizon, so making the technique suitable for implementation on board spacecraft with limited resources akin to autonomous interplanetary CubeSats. The problem faced in this chapter can be stated as:

Problem. Find the locus of points in a capture set \mathcal{C}_{-1}^1 also belonging to capture sets $\mathcal{C}_{-1}^{n \gg 1}$. In particular, such locus of points is named backbone of the capture set and it is of interest because made of initial conditions performing many revolutions about the central body. A backbone is required to contain solutions belonging at least to capture sets $\mathcal{C}_{-1}^{n \geq 5}$.

Firstly, a methodology to derive a backbone must be developed. Secondly, according to the goal set in the problem statement, a backbone is required to contain solutions belonging to capture sets completing more than 5 revolutions.

8.2 Methodology

The approach to tackle the problem follows:

1. definition of LDs integrands suitable for astrodynamics purposes and computed over different forward and backward horizons;
2. computation of stationary points on several 1-dimensional sections of the forward LD scalar field propagated over a finite horizon comparable with weakly-stable set \mathcal{W}_1 and with constant initial pericenter radii r_{p0} ;
3. construction of the backbone as the parametric curve of stationary points computed at step 2;
4. inference of capture set $\mathcal{C}_{-1}^{n \gg 1}$ from the backbone computed at step 3.

In step 1, techniques capable of extracting dynamical insight about the system under study are exploited. This because the backbone must embed the qualitative long-term behavior of the sought $\mathcal{C}_{-1}^{n \gg 1}$ capture orbits.

Step 2 is heuristically justified in what follows. From the literature, abrupt changes in LD scalar fields are known to be separatrices for the dynamics [83, 93]. Conversely, smooth islands in the scalar field appear to feature solutions with similar qualitative behavior. The latter is supported by the findings of numerical experiments seeing the LD method applied to two very different scenarios of great interest for the astrodynamics community. The first is the Didymos binary asteroid case study [116], while the second is the ballistic capture phenomenon at Mars [105]. Our claim is that stationary points in 1-dimensional sections of a LD field correspond to solutions where the qualitative behavior is preserved if longer finite horizons are considered. Therefore, stationary points are thought to behave in the opposite way of abrupt changes. Consequently, they identify phase space locations where trajectories are more prone to retain their dynamical nature over time. To some extent, such trajectories are expected to be more robust as well.

Speaking of the problem at hand, not all stationary points of a 1-dimensional LD section are of interest. Indeed, only those confined within capture sets by the WSB are useful for the backbone computation. By assumption, the backbone is constructed interpolating a sequence of stationary points computed in the appropriate place of the phase space. Consequently, the backbone results being a curve expected to preserve its qualitative behavior on the long-term, so even over extended horizons. An educated initial guess granting the backbone confinement within a capture set is required for the success of the procedure.

Once a sequence of stationary points computed on 1-dimensional LD sections is obtained, the backbone is derived in step 3 as a parametric curve interpolating the same stationary points. In step 4, ICs belonging to capture sets $\mathcal{C}_{-1}^{n \gg 1}$ are inferred sampling the backbone. Eventually, the performance of the method is assessed. LDs suitable for astrodynamics purposes and the backbone construction are explored in what follows.

Table 8.1: Finite horizons.

Subset	Finite horizon	
	Time	[days]
$\sim \mathcal{W}_1$	τ_1	304.11
$\sim \mathcal{W}_2$	τ_2	447.76
$\sim \mathcal{W}_3$	τ_3	597.21
$\sim \mathcal{W}_4$	τ_4	729.39
$\sim \mathcal{W}_5$	τ_5	893.21
$\sim \mathcal{W}_6$	τ_6	1023.82
$\sim \mathcal{X}_{-1}$	τ_{-1}	228.68

8.2.1 Lagrangian descriptors suitable for astrodynamics

Several LD integrands are proposed in [83, 93] and reported in Table 4.1. However, alternative integrand definitions could be specified to address the specific needs of the problem at hand. Two integrands suitable for astrodynamics problems are introduced for this purpose. The first is a LD based on the Keplerian energy of the spacecraft with respect to the target body (i. e., Mars in this dissertation). This is named²⁷ M_9 . The second descriptor, called M_{10} , considers a metric derived from the spacecraft angular momentum even in this case referred to the target body. In mathematical means, they are

$$M_9(\mathbf{x}_0, t_0, \tau_b, \tau_f) = \int_{t_0 - \tau_b}^{t_0} \left| \frac{v^2}{2} - \frac{\mu_t}{r} \right|^{1/\tau_b} dt + \int_{t_0}^{t_0 + \tau_f} \left| \frac{v^2}{2} - \frac{\mu_t}{r} \right|^{1/\tau_f} dt \quad (8.1)$$

$$M_{10}(\mathbf{x}_0, t_0, \tau_b, \tau_f) = \int_{t_0 - \tau_b}^{t_0 + \tau_f} \|\mathbf{r} \times \mathbf{v}\|^{1/2} dt \quad (8.2)$$

where $\mathbf{x} = [\mathbf{r}^T \mathbf{v}^T]^T$ is the state variable; r and v are the magnitudes of position vector \mathbf{r} and velocity vector \mathbf{v} , respectively; μ_t is the gravitational parameter of the central body; τ_b and τ_f are the backward and forward finite horizons, respectively.

The choice of backward and forward finite horizons is key. In fact, extremely short finite horizons preclude revealing the underlying dynamical template of geometrical structures, so concealing transport patterns in the phase space [93, 105]. Conversely, unreasonably lengthy horizons furnish excessive information to process, thereby jeopardizing the method and leading to undesired outcomes [105]. Practical examples are provided and discussed in Section 8.3.1. The finite horizon choice being critical, a preliminary study is carried out to identify proper time spans for the LD scalar fields propagation. As a result, backward and forward horizons are selected as the escape time and aggregate revolution periods, respectively, of a reference capture orbit.

²⁷Subscripts are assigned in continuity with those used in Table 4.1.

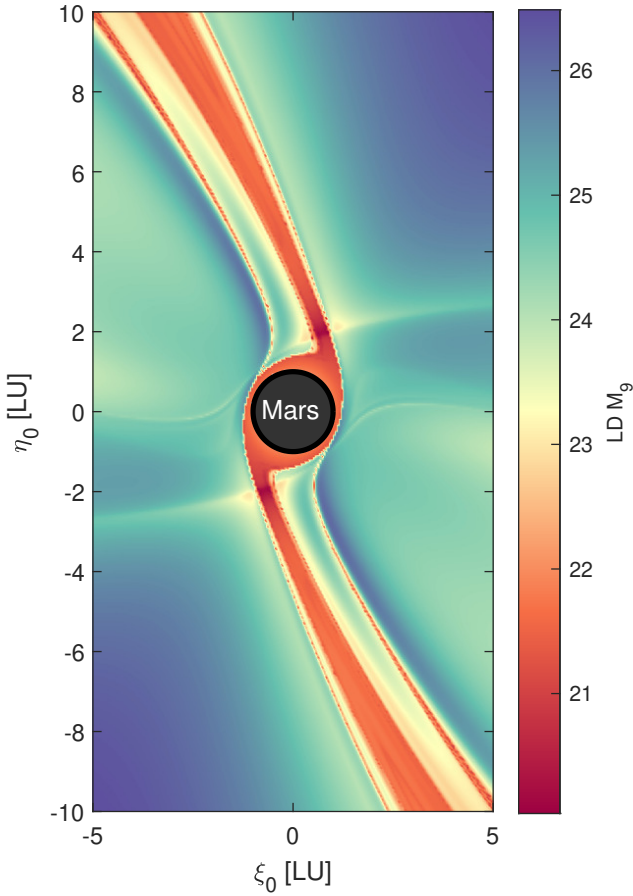


Figure 8.1: Energy-based LD field $\mathcal{M}_9(\tau_{-1}, \tau_6)$. Finite horizon comparable to capture set \mathcal{C}_{-1}^6 . Initial time epoch t_0 set to December 9, 2023 at 12:00:00.00 (UTC). Nondimensional coordinates on the orbital plane $i_0 = \Omega_0 = 0.2\pi$ rad defined in the Mars-centered RTN@ t_0 frame. Mars represented in black. Features of LD field resemble the typical shape of capture sets. Separatrices of the phase space easily recognized as abrupt changes.

The reference orbit is that belonging to \mathcal{C}_{-1}^6 and exhibiting minimum regularity coefficient $\Delta S_{\%}$ out of 10^3 trajectories computed²⁸:

- at capture epoch t_0 set to December 9, 2023 at 12:00:00.00 (UTC), so maximizing \mathcal{R}_c [50];
- with orbital plane defined by inclination and RAAN imposed to $i_0 = \Omega_0 = 0.2\pi$ rad, so maximizing Mars' capture ratio (see Figure 10 in [50]);
- setting osculating eccentricity $e_0 = 0.99$ [9];
- imposing true anomaly $\theta_0 = 0$ deg (i. e., assumed at pericenter);
- assuming constant initial pericenter radius $r_{p0} = 2.1$ LU;
- sampling 10^3 arguments of pericenter in the range [230, 260] deg.

The resulting reference capture orbit is not representative of the whole capture sets \mathcal{C}_{-1}^n with $n = 1, \dots, 6$. In fact, BC orbits generally manifest different times of flight both for pre- and post-capture legs as detailed in [69] and addressed

²⁸EoM include gravitational attractions of the Sun, Mercury, Venus, Earth–Moon (B), Mars (central body), Jupiter (B), Saturn (B), Uranus (B) and Neptune (B), and SRP. To nondimensionalize EoM, a modified set of normalization units is used to avoid ill-conditioning. They are: $\bar{M}\bar{U} = 42828.376 \text{ km}^3 \text{ s}^{-2}$, $\bar{L}\bar{U} = 1.085772 \times 10^6 \text{ km}$ (i. e., Mars– $L_{2,\odot\sigma}$ distance), $\bar{T}\bar{U} = 5.466913 \times 10^6 \text{ s}$, and $\bar{V}\bar{U} = 1.986079 \times 10^{-1} \text{ km s}^{-1}$.

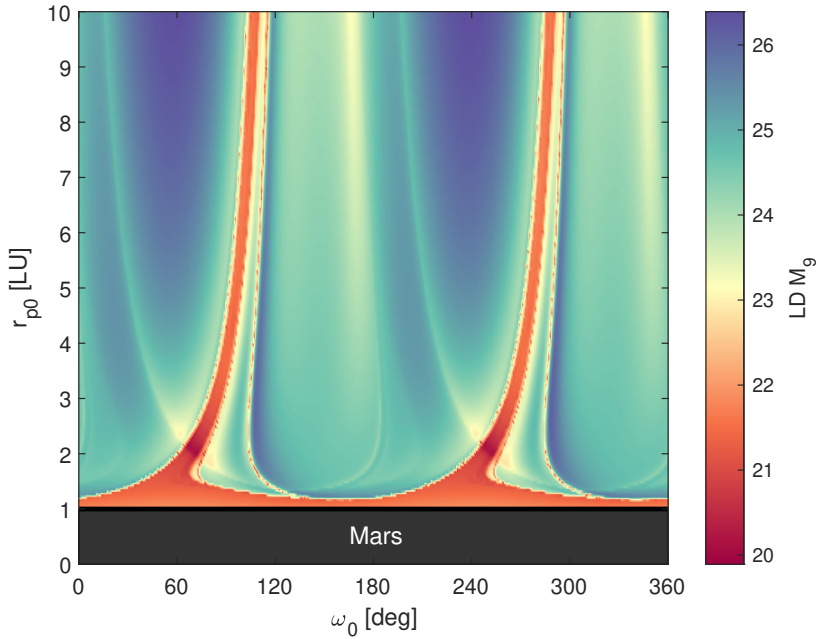


Figure 8.2: Energy-based LD field $\mathcal{M}_g(\tau_{-1}, \tau_6)$. Finite horizon comparable to capture set \mathcal{C}_{-1}^6 . Initial time epoch t_0 set to December 9, 2023 at 12:00:00.00 (UTC). Radius of pericenter r_{p0} and argument of pericenter ω_0 at capture epoch t_0 . Mars represented in black. Features of LD field resemble the shape of capture sets when represented as in [69]. Separatrices of the phase space easily recognized as abrupt changes.

in [68, 78, 105]. Nevertheless, the reference capture orbit is representative at least of those trajectories exhibiting high post-capture regularity and performing a close approach to Mars at an approximate distance of 2.1 LU. These are the most interesting solutions from operational perspectives. LD fields propagated over variable finite horizons were investigated in [117]. However, despite this being a legitimate approach, the resulting advantages did not justify the additional effort required for its implementation and computation.

Forward and backward finite horizons associated to the reference capture orbit are collected in Table 8.1. Each finite horizon is representative of a subset whose propagation time span is comparable to that of the chosen finite horizon itself. An example LD scalar field is propagated over a finite horizon comparable to capture set \mathcal{C}_{-1}^6 , so using $\tau_b = \tau_{-1}$ and $\tau_f = \tau_6$. For notation purposes, a LD scalar field is defined as $\mathcal{M}_i(\tau_b, \tau_f) := \{M_i(\mathbf{x}_0, t_0, \tau_b, \tau_f) | (\mathbf{x}_0, t_0) \in \Pi\}$, where Π is the set of ICs [105]. LD field $\mathcal{M}_g(\tau_{-1}, \tau_6)$ is shown in Figure 8.1 in Cartesian coordinates, while it is represented in Figure 8.2 using Keplerian elements. Patterns in Figure 8.1 resemble the usual shape of capture sets (see Chapters 3, 5, and 7). Differently, dynamical features highlighted in Figure 8.2 mirror capture sets as plotted in [69] and resemble the region identified in Figure 13 in [118], so confirming the role of the third-body perturbation in the BC mechanism.

Algorithm 8.1: Backbone construction.**Procedure** INITIALIZATION

Select LD and finite horizon (τ_b, τ_f) ; ▷ energy-based LD M_g
 Set first initial pericenter radius r_{p0} ; ▷ database/corrected IC
 Set first initial guess ω_0^G ; ▷ database/corrected IC
 Set pericenter radius increment Δr_{p0} and stationary points number N_{pnt} ;

Procedure BACKBONE CONSTRUCTION

For $i = 1 : N_{\text{pnt}}$
 Find stationary point ω_0^* of $M = M(\mathbf{x}_0(r_{p0}, \omega_0), \tau_b, \tau_f)$ with `fminunc`;
If `fminunc successful` ▷ stationary point found
 | Store result $(r_{p0}^{(i)}, \omega_0^{(i)}) = (r_{p0}, \omega_0^*)$;
Else ▷ stationary point not found
 | Break the loop;
End
 Increment initial pericenter radius $r_{p0} = r_{p0} + \Delta r_{p0}$;
 Update initial guess $\omega_0^G = \omega_0^*$;
End
 Construct backbone from $(r_{p0}^{(i)}, \omega_0^{(i)})$ with `cscvn`;

Exit

Result: Backbone as parametric variational cubic spline curve.

8.2.2 Backbone construction

The selected LD is propagated over the finite horizon $(\tau_b, \tau_f) = (0, \tau_1)$, so for a time span comparable to revolution periods for weakly-stable set \mathcal{W}_1 . Stationary points ω_0^* are searched between separatrices isolating weakly-stable orbits and on 1-dimensional sections along the initial argument of pericenter ω_0 at fixed initial pericenter radius r_{p0} . They are computed with the MATLAB[®]'s `fminunc` routine implementing a quasi-Newton optimization algorithm²⁹. The optimization is performed with central finite differences, optimality tolerance set to 10^{-6} , and step tolerance equal to 10^{-10} . An initial guess ω_0^G is used to initialize the procedure (e. g., taken from the BC database or belonging to a BC orbits family generated on board). After getting the first stationary point ω_0^* , next points are computed solving optimization problems for increasing values of r_{p0} by steps of Δr_{p0} . New initial guesses are set equal to the last stationary point ω_0^* computed, so numerically continuing the sequence. Once the desired range of Mars distances is covered (i. e., enough stationary points are computed), the backbone is built as a parametric variational cubic spline curve³⁰ [119]. The procedure is detailed in Algorithm 8.1.

²⁹Visit <https://www.mathworks.com/help/optim/ug/fminunc.html> and <https://www.mathworks.com/help/optim/ug/choosing-the-algorithm.html> for additional details [last accessed Dec 1, 2022].

³⁰For this purpose, MATLAB[®]'s `cscvn` routine is used, <https://www.mathworks.com/help/curvefit/cscvn.html> [last accessed Dec 1, 2022].

8.3 Results

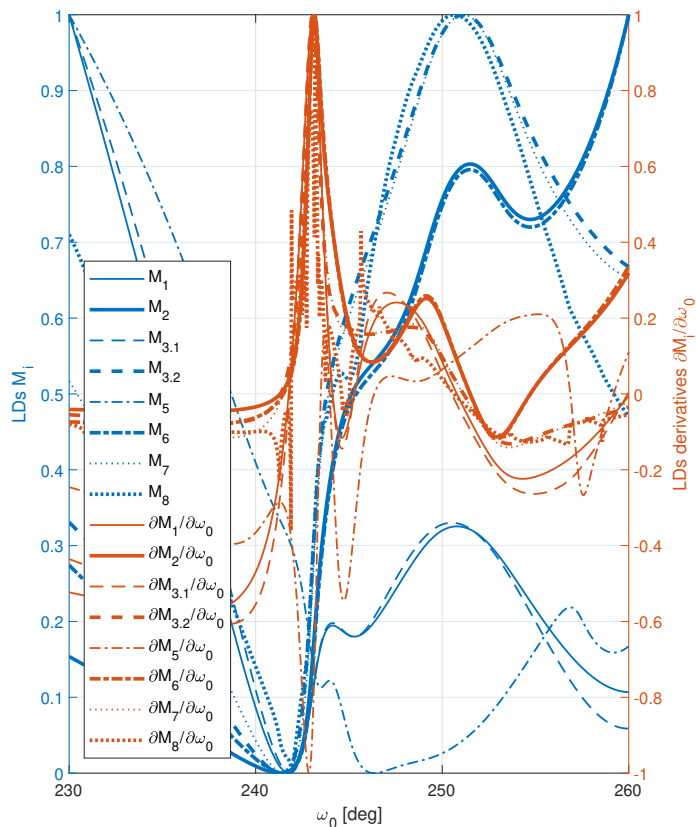
The backbone of the capture set \mathcal{C}_{-1}^I introduced in Section 8.2.1 is herewith constructed. Specifically, the backbone lying in the capture set portion developing into the interior subcorridor (see Chapter 5). The backbone is computed after selecting what appears to be the most suited LD.

8.3.1 Lagrangian descriptor selection

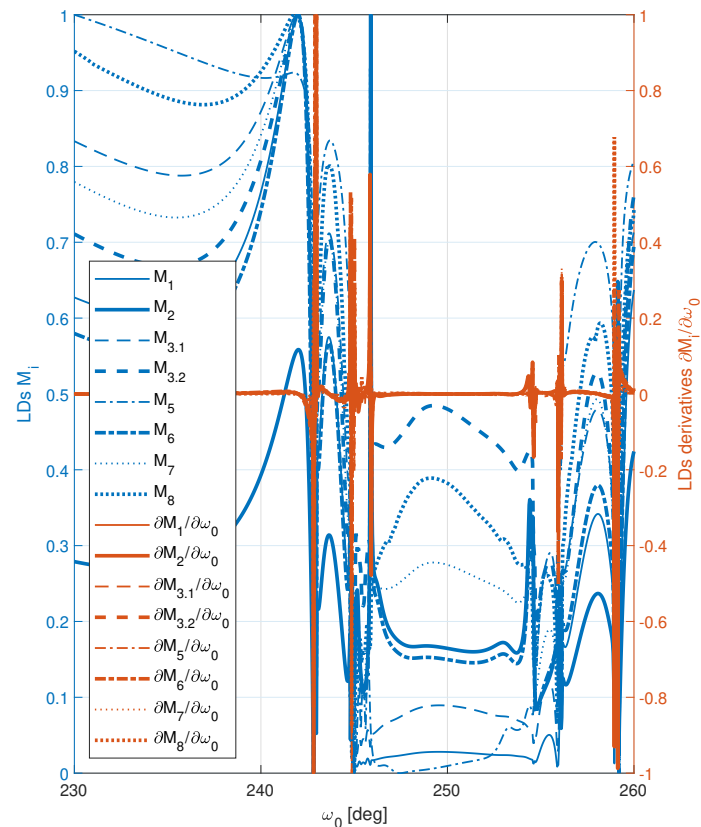
The selection is carried out studying the trends of several 1-dimensional LD sections propagated over different finite horizons. The investigation is performed fixing the initial pericenter radius $r_{p0} = 2.1\text{LU}$ and letting the initial argument of pericenter ω_0 vary in $[230, 260]\text{deg}$. The selected finite horizons are $(\tau_b, \tau_f) = (0, \tau_1)$ and $(\tau_b, \tau_f) = (0, \tau_6)$, therefore those comparable to weakly-stable sets \mathcal{W}_1 and \mathcal{W}_6 , respectively. Gradients along ω_0 computed with central finite differences are analyzed as well [120]. In Figure 8.3, trends for LDs specified in [83, 93] are shown. Those for astrodynamics LDs are plotted in Figure 8.4. Both trends (i. e., blue curves on left y -axes) and gradients (i. e., red curves on right y -axes) are normalized to their maximum values for a fair comparison. As expected, dynamical features (e. g., abrupt changes, edges) are not completely developed yet in Figures 8.3a and 8.4a. This because of the integration interval being insufficiently long [93]. LD trends are smooth and no remarkable discontinuities are detected in the gradients. Contrarily, many abrupt changes in the field and related discontinuities in the gradients are detected in Figures 8.3b and 8.4b.

Among the investigated descriptors, the Keplerian energy-based LD M_9 is preferred over other options for the following reasons. Firstly, M_9 seems extremely smooth when propagated on short horizons. This is a desirable property when solving optimization problems searching for stationary points. Unfortunately, some dynamical insight is lost due to the excessively short propagation interval, which is translated to accuracy loss in determining the exact backbone location. Hopefully, capture sets $\mathcal{C}_{-1}^{n \gg 1}$ can be still inferred from an approximation of the real backbone. Secondly, M_9 stationary points are expected to detect the phase space region featuring BC orbits with similar energetic behavior. Thirdly, a unique stationary point (i. e., a maximum) is visually detected³¹ at $\omega_0 \approx 250\text{deg}$, hence close to where the capture set branch developing the interior subcorridor is located (see Figure 5.9). Previous claims are confirmed by plots in Figure 8.5 where M_9 sections are inspected against subsets \mathcal{W} , \mathcal{X} , \mathcal{K} , \mathcal{D} , and \mathcal{C} . In fact, variations in the selected LD field does not match exactly the WSB (i. e., separatrices between sets). Nevertheless, the stationary point is correctly found within capture sets \mathcal{C}_{-1}^I and \mathcal{C}_{-1}^6 (i. e., light green background). The stationary point (i. e., dashed vertical line) shifts to the left from Figure 8.5a to Figure 8.5b, thereby proving the loss of dynamical insight for excessively short finite horizons. Nevertheless, the backbone can still be constructed even though some dynamical insight is lost.

³¹Over finite horizon $(\tau_b, \tau_f) = (0, \tau_1)$, so $\sim \mathcal{W}_1$, this is true also for LDs $M_{3.2}$, M_7 , and M_8 .

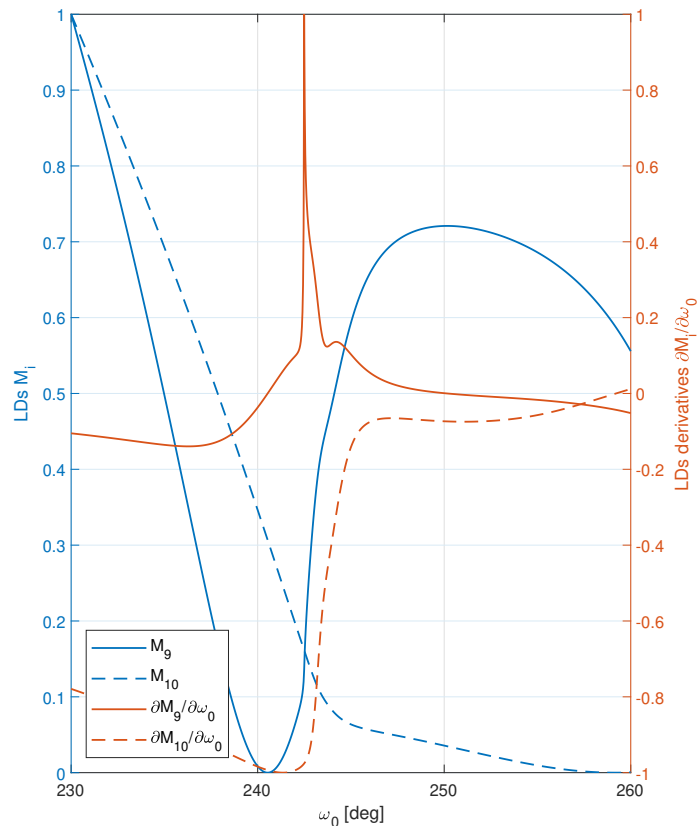


(a) Finite horizon $(\tau_b, \tau_f) = (0, \tau_1)$, so comparable to set \mathcal{W}_1 .

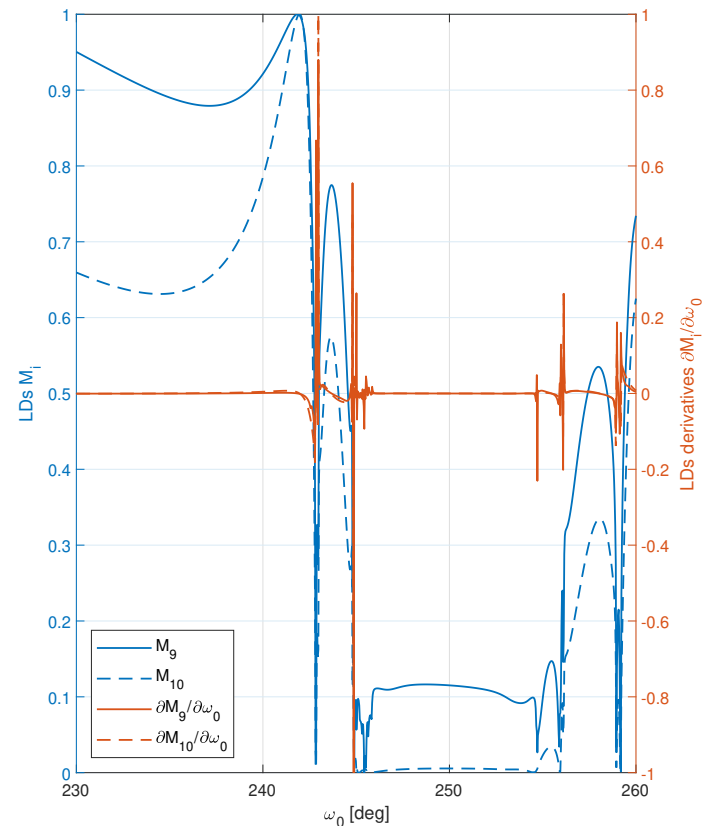


(b) Finite horizon $(\tau_b, \tau_f) = (0, \tau_6)$, so comparable to set \mathcal{W}_6 .

Figure 8.3: Study of 1-dimensional LD sections at constant initial pericenter radius $r_{p0} = 2.1$ LU. LDs defined by authors in [83]. LDs M_i (in blue, left y-axis) and gradients $\partial M_i / \partial \omega_0$ (in red, right y-axis) as a function of initial argument of pericenter ω_0 , with $i = \{1, 2, 3.1, 3.2, 5, 6, 7, 8\}$. LDs M_i and gradients $\partial M_i / \partial \omega_0$ both normalized to their maximum values. Dynamical features are more developed for longer finite horizons.

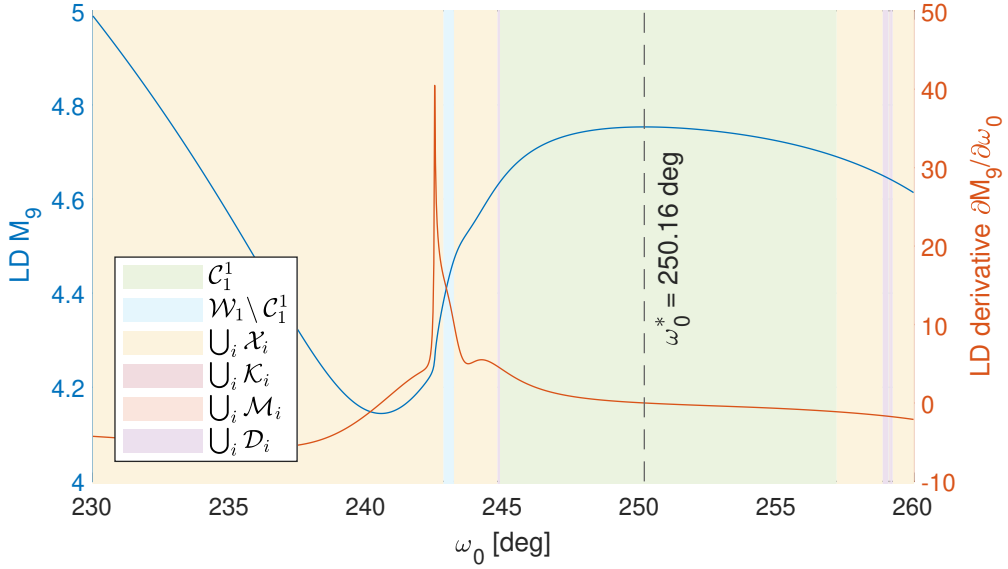


(a) Finite horizon $(\tau_b, \tau_f) = (0, \tau_1)$, so comparable to set \mathcal{W}_1 .

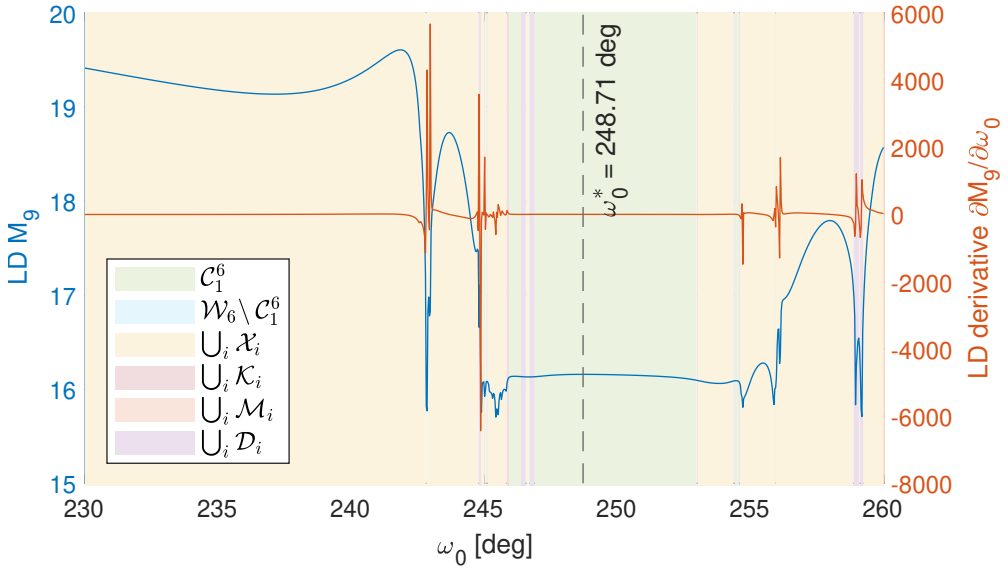


(b) Finite horizon $(\tau_b, \tau_f) = (0, \tau_6)$, so comparable to set \mathcal{W}_6 .

Figure 8.4: Study of 1-dimensional LD sections at constant initial pericenter radius $r_{p0} = 2.1\text{LU}$. Astrodynamics based LDs. LDs M_i (in blue, left y -axis) and gradients $\partial M_i/\partial\omega_0$ (in red, right y -axis) as a function of initial argument of pericenter ω_0 , with $i = \{9,10\}$. LDs M_i and gradients $\partial M_i/\partial\omega_0$ both normalized to their maximum values. Dynamical features are more developed for longer finite horizons.



(a) Finite horizon $(\tau_b, \tau_f) = (0, \tau_1)$, so comparable to set \mathcal{W}_1 .



(b) Finite horizon $(\tau_b, \tau_f) = (0, \tau_6)$, so comparable to set \mathcal{W}_6 .

Figure 8.5: Energy-based LD M_g (in blue, left y-axis) and gradient $\partial M_g / \partial \omega_0$ (in red, right y-axis) as a function of initial argument of pericenter ω_0 inspected against subsets \mathcal{W} , \mathcal{X} , \mathcal{K} , \mathcal{D} , and \mathcal{C} . Phase space 1-dimensional section at constant initial pericenter radius $r_{p0} = 2.1$ LU. LD stationary point of interest ω_0^* marked with dashed vertical line.

8.3.2 Backbone

The backbone is built as a curve of stationary points computed on 1-dimensional sections of the Lagrangian descriptor M_g . They are computed on a finite horizon comparable to the revolution period of \mathcal{C}_{-1}^I orbits. Before actually derive the backbone, some preliminary tests are performed to assure the effectiveness of the methodology. Specifically, 9 stationary points at various distances from Mars are computed with MATLAB[®]'s `fminunc` routine. In the peculiar problem under analysis, stationary points are maxima of 1-dimensional LD sections (see Figure 8.5). Consequently, the cost function is defined as $f(\omega_0) = -M_i(r_{p0}, \omega_0, \tau_b, \tau_f)$ with r_{p0} fixed, $t_b = 0$ and $\tau_f = \tau_1$, so transforming stationary points into minima.

Results are shown in Figure 8.6, where the performance of LD M_g is compared to that of M_g . LD M_g is examined in contrast because of its proved capability of highlighting dynamical features thanks to the clever choice of setting the integrand exponent $p = 1/\tau$ (see Table 4.1) [93]. In Figure 8.6, stationary points are marked as colored vertical dashed lines. Sections cover distances from 2 LU up to 6 LU. Both descriptors M_g and M_g decrease for larger distances from the target. At all distances, edges are not completely developed because of the short finite horizon chosen. However, limiting the finite horizon speeds up propagations of LDs and consequently the solution of the optimization problem. Descriptor M_g behaves consistently across the various sections, remaining smooth and preserving its trend (see Figure 8.6b). On the contrary, descriptor M_g changes trend at large distances, so making difficult the computation of the stationary point. Remarkably, stationary points exceed the WSB for sections at $r_{p0} = 5.5\text{LU}$ and 6.0LU .

Eventually, starting from the 1-dimensional section at $r_{p0} = 2.1\text{LU}$, a sequence of $N_{\text{opt}} = 25$ optimization problems is solved for increasing r_{p0} values by steps of $\Delta r_{p0} = 10^3\text{ km}$. Distances up to $\approx 9.2\text{LU}$ are covered. The resulting backbone is presented in Figure 8.7, while the complete list of stationary points is reported in Table 8.2. Scalar fields $\mathcal{M}_g(\tau_{-1}, \tau_1)$ and $\mathcal{M}_g(\tau_{-1}, \tau_6)$ are plotted in the background of Figures 8.7a, 8.7c and Figures 8.7b, 8.7d, respectively. Results in Figures 8.7a, 8.7b and Figures 8.7c, 8.7d are represented on the $\omega_0 r_{p0}$ -plane and $\xi_0 \eta_0$ -plane, respectively. The former are the initial Keplerian elements in the RTN@ t_0 frame, while the latter are the Cartesian coordinates on the orbital plane defined by inclination and RAAN set to $i_0 = \Omega_0 = 0.2\pi$ rad.

In all four plots, the backbone remains confined by separatrices visible in the fields. This confirms how the dynamical information revealed by stationary points obtained over short finite horizons (i. e., $\sim \mathcal{W}_1$) embeds insight on the long-term qualitative behavior of capture orbits. ICs belonging to the backbone preserve their dynamical peculiarities even after more than 3 times the time span considered to construct the backbone (i. e., $\tau_6 \approx 3.4\tau_1$, see Table 8.1). Despite the additional effort in solving the sequence of optimization problems to get the stationary points, supplementary dynamical knowledge about the future evolution of the system is extracted from LD fields propagated on relatively short finite horizons. Therefore, clues on capture sets $\mathcal{C}_{-1}^{n \gg 1}$ are supposedly inferable from the backbone.

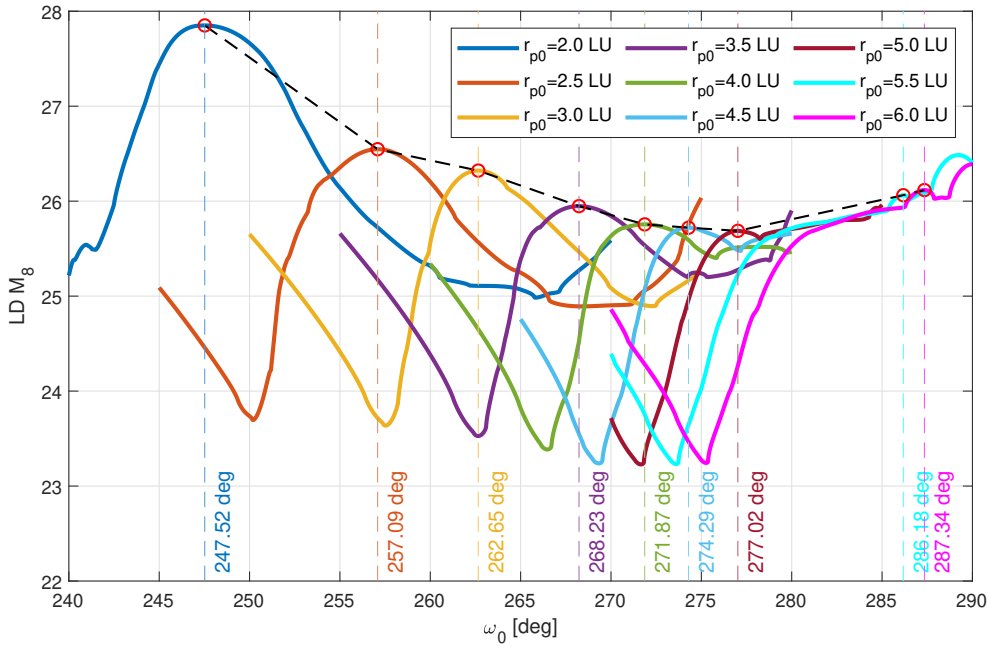
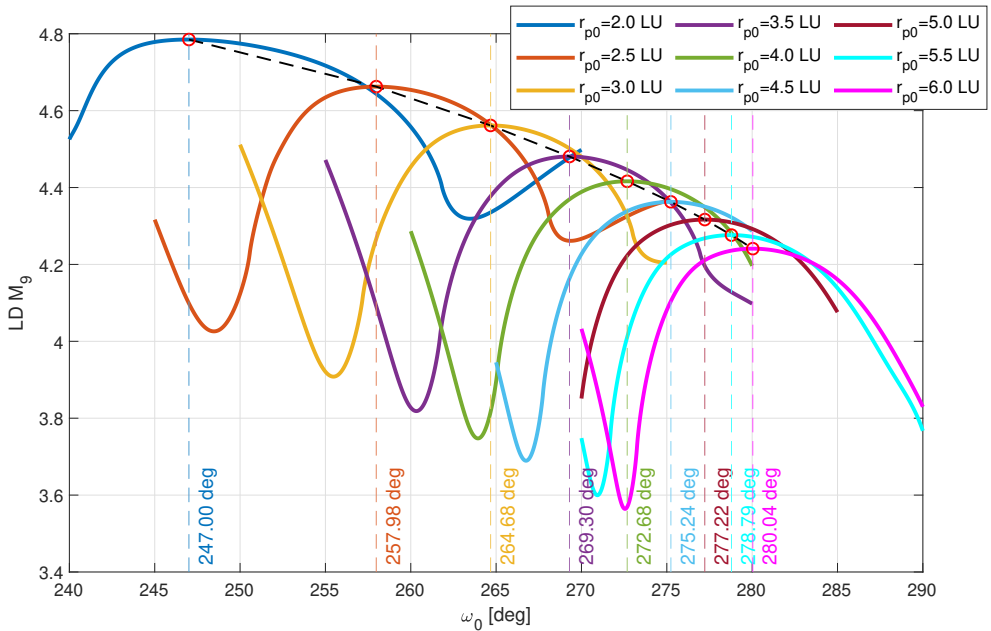
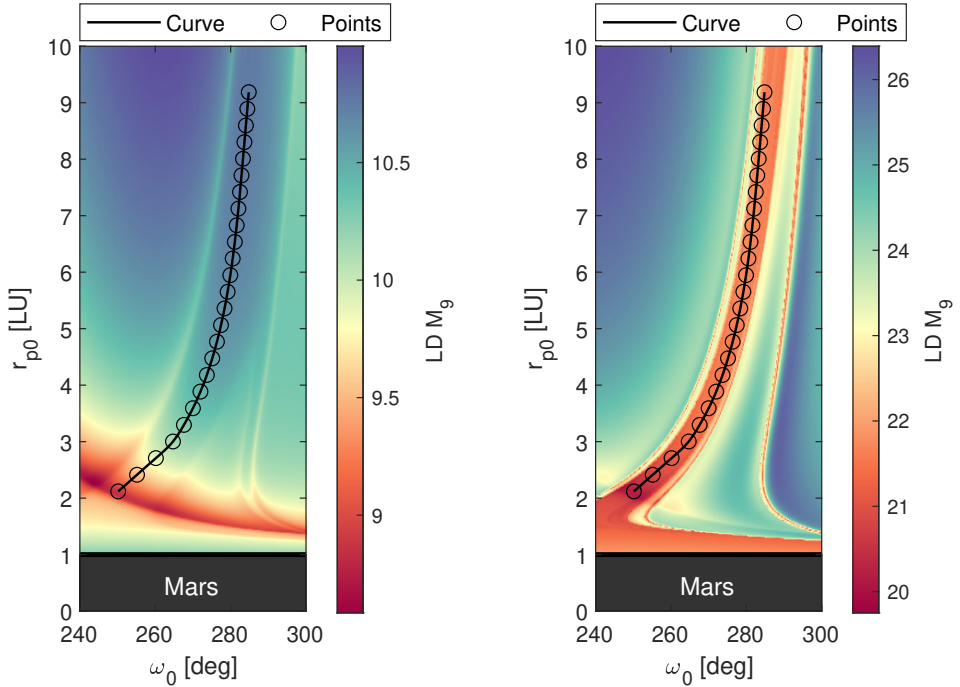
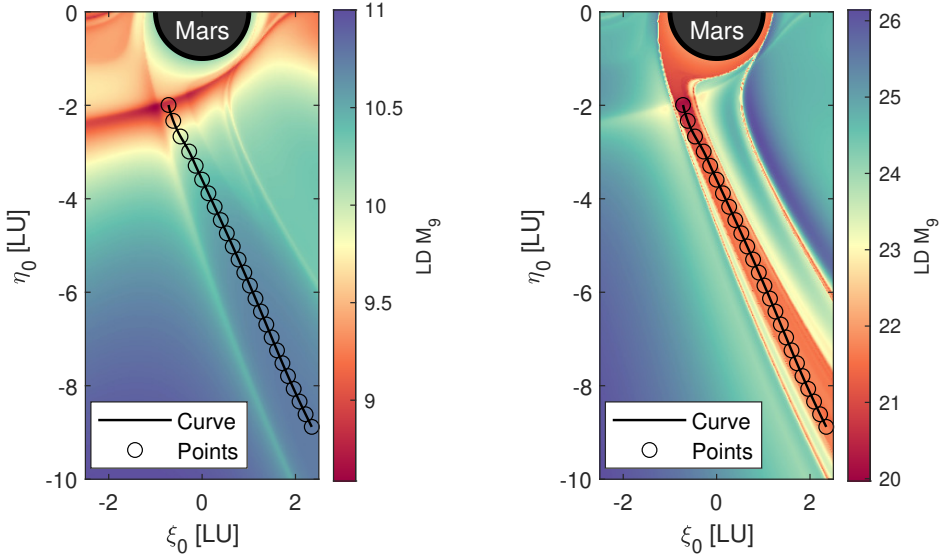
(a) Sections of LD M_8 .(b) Sections of Keplerian energy-based LD M_9 .

Figure 8.6: Stationary points ω_0^* of 1-dimensional LD sections evaluated at various initial pericenter radii r_{p0} . Stationary points marked as colored dashed vertical lines. Color code shown in the legend. Envelope of stationary points drawn as dashed black line. Finite horizon $(\tau_b, \tau_f) = (0, \tau_1)$, so comparable to weakly-stable set \mathcal{W}_1 .



(a) Finite horizon $(\tau_b, \tau_f) = (\tau_{-1}, \tau_1)$, so $\sim \mathcal{C}_{-1}^1$; representation in $\omega_0 r_{p0}$ -plane.

(b) Finite horizon $(\tau_b, \tau_f) = (\tau_{-1}, \tau_6)$, so $\sim \mathcal{C}_{-1}^6$; representation in $\omega_0 r_{p0}$ -plane.



(c) Finite horizon $(\tau_b, \tau_f) = (\tau_{-1}, \tau_1)$, so $\sim \mathcal{C}_{-1}^1$; representation in $\xi_0 \eta_0$ -plane.

(d) Finite horizon $(\tau_b, \tau_f) = (\tau_{-1}, \tau_6)$, so $\sim \mathcal{C}_{-1}^6$; representation in $\xi_0 \eta_0$ -plane.

Figure 8.7: Backbone (black solid line) inspected against energy-based LD scalar fields $\mathcal{M}_g(\tau_{-1}, \tau_f)$ for two values of τ_f and two coordinate sets. Mars represented as black rectangle (on top) and black circle (on bottom). Stationary points marked as empty black circles. Backbone lies within regions confined by dynamic separatrices (abrupt changes) featured by LD fields propagated over both short ($\sim \mathcal{C}_{-1}^1$) and long ($\sim \mathcal{C}_{-1}^6$) finite horizons. Backbone starting from $r_{p0} = 2.1$ LU, with $N_{\text{pnt}} = 25$ points by steps of $\Delta r_{p0} = 10^3$ km.

Table 8.2: Stationary points of backbone. Capture epoch t_0 set to December 9, 2023 at 12:00:00.00 (UTC). Initial Keplerian elements at RTN@ t_0 : orbital plane defined by inclination and RAAN set to $i_0 = \Omega_0 = 0.2\pi$ rad, osculating eccentricity $e_0 = 0.99$, and initial true anomaly $\theta_0 = 0$ rad.

Point (i)	Coordinates	
	$r_{p0}^{(i)}$ [LU]	$\omega_0^{(i)}$ [deg]
1	2.119	250.2
2	2.413	255.2
3	2.708	260.2
4	3.002	264.7
5	3.297	267.6
6	3.591	270.0
7	3.886	272.0
8	4.180	273.7
9	4.474	275.1
10	4.769	276.4
11	5.063	277.4
12	5.358	278.4
13	5.652	279.2
14	5.947	279.9
15	6.241	280.5
16	6.536	281.1
17	6.830	281.6
18	7.125	282.1
19	7.419	282.5
20	7.713	282.9
21	8.008	283.3
22	8.302	283.7
23	8.597	284.0
24	8.891	284.4
25	9.186	284.8

Table 8.3: Backbone performance. Analysis carried out sampling 10^3 backbone ICs.

Capture set \mathcal{C}_{-1}^n	Capture orbits	
	Revolutions n	Number
1	1000	100.0%
2	1000	100.0%
3	678	67.8%
4	446	44.6%
5	433	43.3%
6	337	33.7%
7	313	31.3%
8	304	30.4%
9	253	25.3%
10	199	19.9%

8.3.3 Performance analysis

A performance analysis is carried out to assess whether useful dynamical knowledge about $\mathcal{C}_{-1}^{n \gg 1}$ could be inferred or not from a backbone. Specifically, 10^3 ICs are uniformly sampled along the backbone constructed in Section 8.3.2. Then, ICs are classified with GRATIS into capture sets from \mathcal{C}_{-1}^1 up to \mathcal{C}_{-1}^{10} . The results in terms of absolute and relative number of BC orbits out of the whole sample are shown in Table 8.3. The totality of ICs belong to \mathcal{C}_{-1}^2 , more than the 30% is classified into \mathcal{C}_{-1}^6 , and almost the 20% is part of capture set \mathcal{C}_{-1}^{10} .

Figure 8.8 shows how ICs are classified by GRATIS into the ten capture sets considered. The initial pericenter radius r_{p0} and argument of pericenter ω_0 are plotted on the left y -axis in blue and right y -axis in red, respectively. The larger the number of revolutions n , the more discontinuous becomes the set of ICs granting temporary capture. The way in which the set is broken apart resembles the distinctive Cantor-like structure of the WSB consisting in the intricate network of manifolds supporting phase space transport [62, 63].

Capture set \mathcal{C}_{-1}^5 is studied in detail because of the goal set in the problem statement about inferring orbits classified into $\mathcal{C}_{-1}^{n \geq 5}$ (see Section 8.1). Post-capture legs, and subcorridor \mathcal{S}_{-1}^5 up to $t_0 - 600$ days are propagated from the set of ICs sampled on the backbone and belonging to \mathcal{C}_{-1}^5 . They are plotted in their entirety in Figure 8.9, while a magnification close to Mars' SOI is proposed in Figure 8.10. From the three views in Figure 8.9, the subcorridor \mathcal{S}_{-1}^5 (in light blue) appears much larger than that in Figure 5.11. Remarkably, the sample of ICs loses its capture properties starting from large distances with respect to the target. The most useful orbits from operational perspectives (i. e., those closely approaching Mars) retain the required dynamical behavior even on the long-term, thereby granting capture and successfully completing several revolutions about Mars.

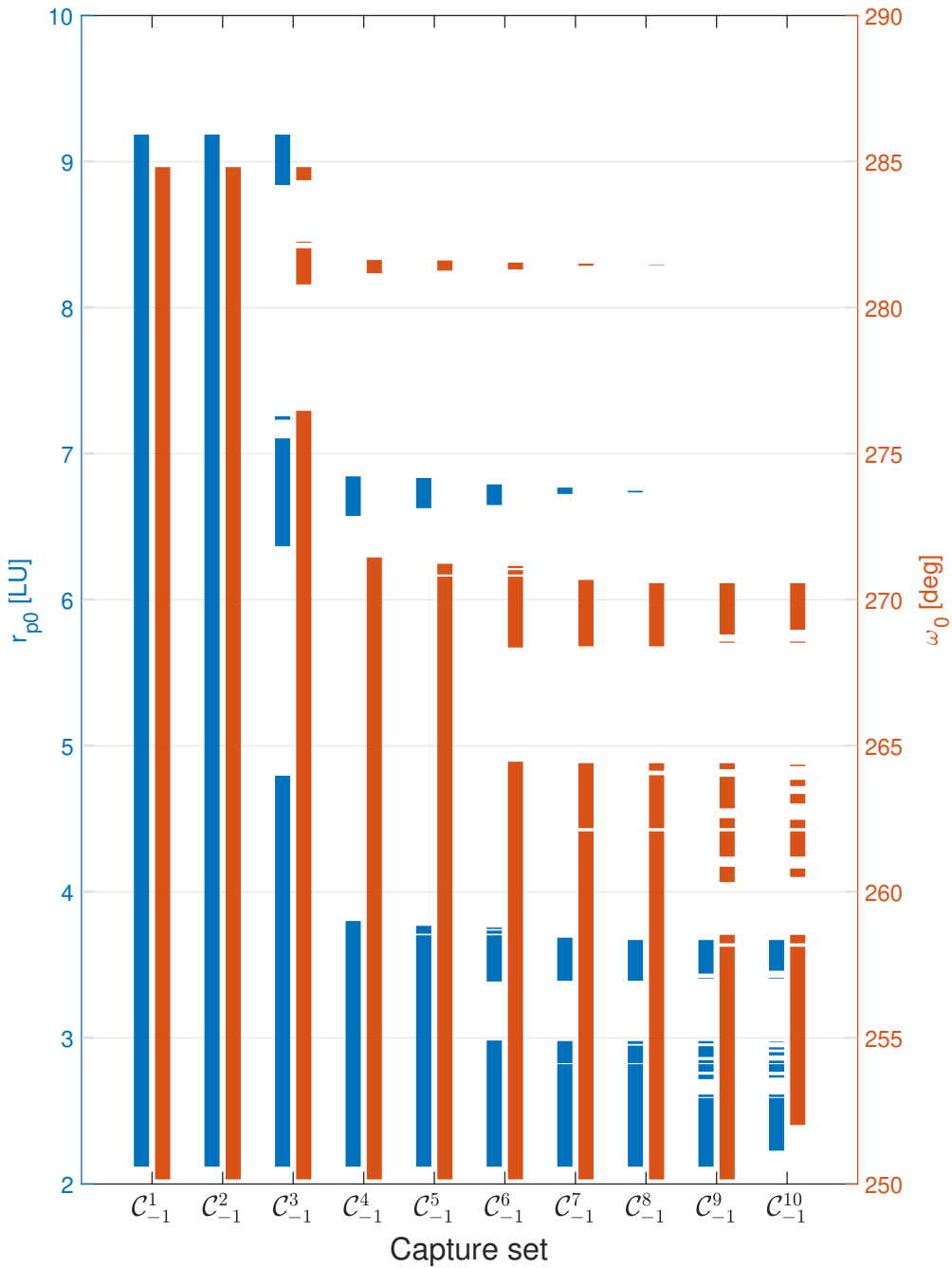


Figure 8.8: Analysis of backbone performance for several capture sets. Backbone ICs belonging to capture sets C_{-1}^n with $n = 1, \dots, 10$. Distributions of pericenter radii r_{p0} (in blue, left y -axis) and arguments of pericenter ω_0 (in red, right y -axis). Analysis carried out sampling 10^3 backbone ICs.

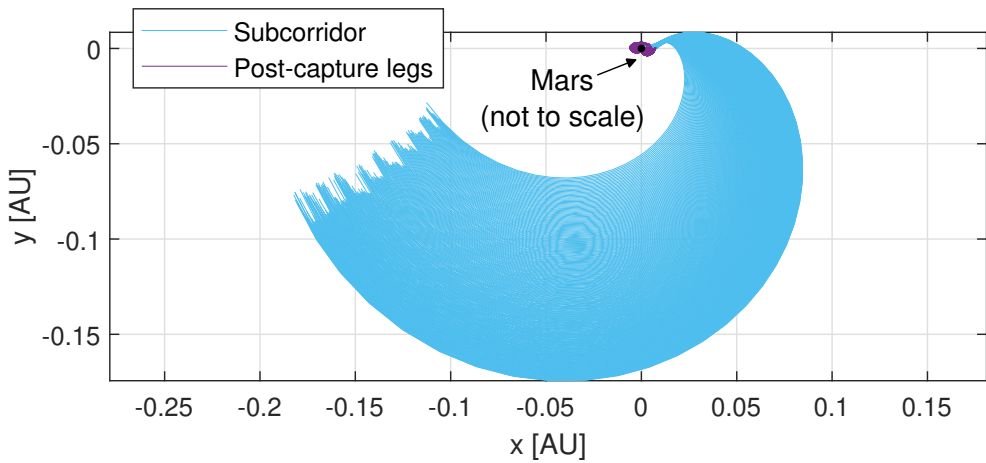
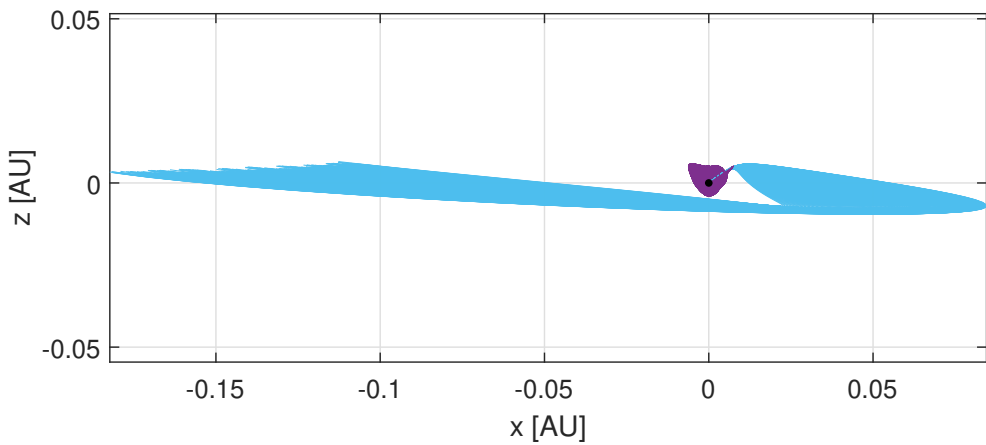
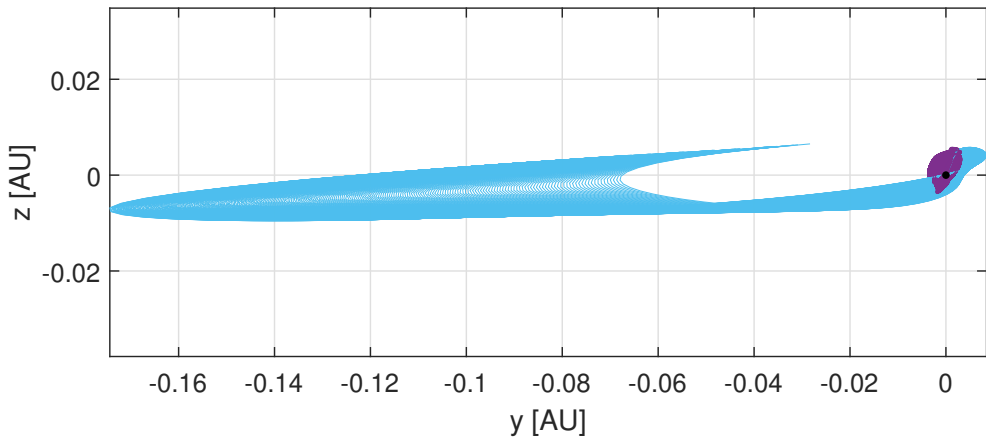
(a) View xy -plane.(b) View xz -plane.(c) View yz -plane.

Figure 8.9: Views in the physical space of subcorridor \check{S}_{-1}^5 far from Mars built sampling the backbone. Subcorridor backward propagated from t_0 to $t_0 - 600$ days. Trajectories plotted in the Mars-centered ECLIPJ2000 frame.

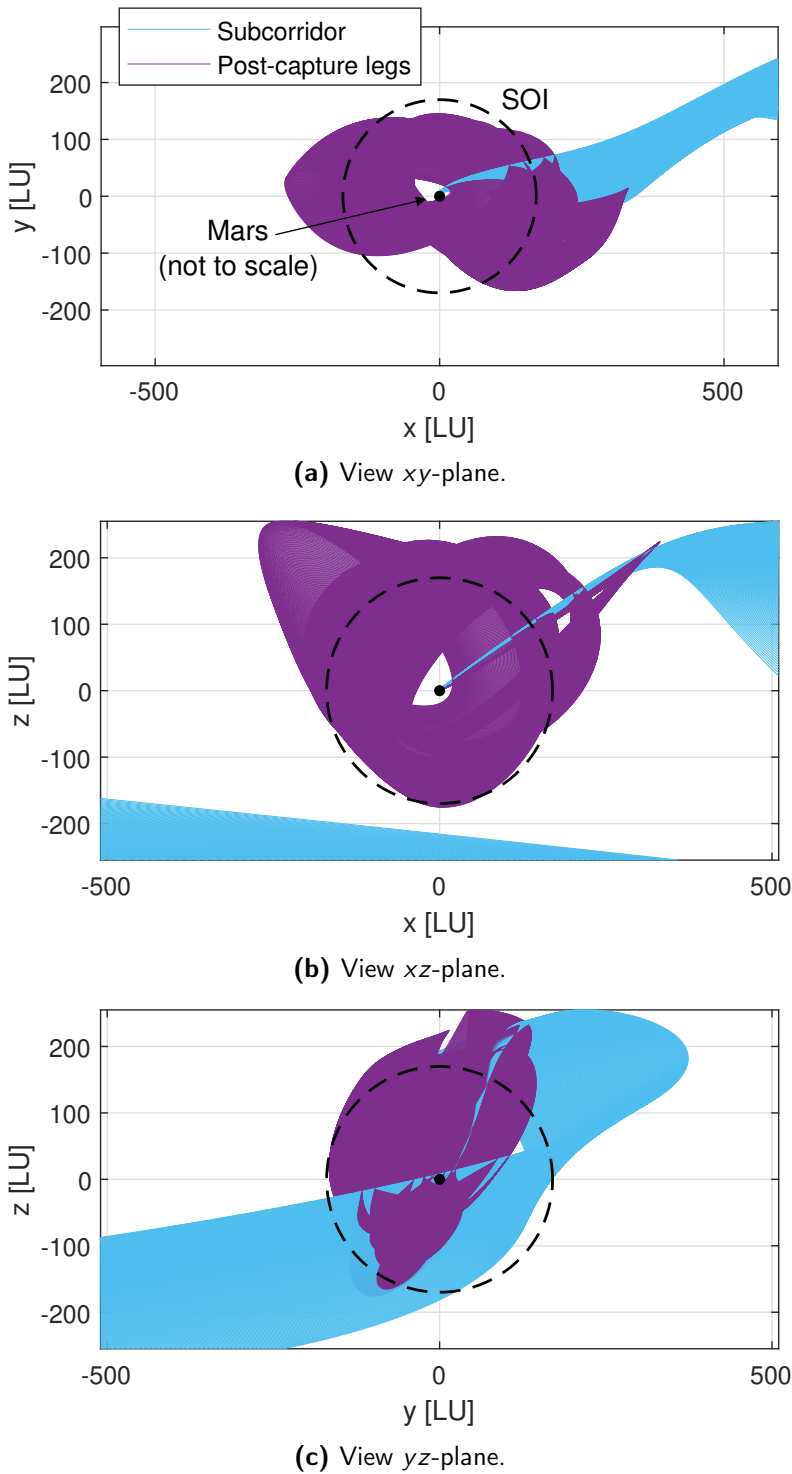


Figure 8.10: Views in the physical space of subcorridor \check{S}_{-1}^5 built sampling the backbone. Magnifications of subcorridor and post-capture legs close to Mars' SOI. Subcorridor backward propagated from t_0 to $t_0 - 600$ days. Trajectories plotted in the Mars-centered ECLIPJ2000 frame.

8.4 Final remarks

The method presented in this chapter is an alternative approach to present-day practices for designing BC orbits. The devised procedure leverages on the novel concept of capture set backbone from which ICs belonging to $\mathcal{C}_{-1}^{n \gg 1}$ are inferred. Construction of the backbone is made possible by exploiting the dynamical information embedded within LDs propagated on a short finite horizon. The knowledge extracted from metrics propagated over time intervals comparable to the revolution period typical of weakly-stable orbits in \mathcal{W}_1 is proved sufficient to deduce the location in the phase space of ICs performing several revolutions about Mars. The computationally demanding problem of designing orbits granting long-term temporary capture is unburdened by maximizing the descriptor M_g on selected 1-dimensional sections at constant initial pericenter radius, provided that the optimization is carried out within phase space regions bounded by the WSB. This novel design method being computationally light, it could potentially see implementation on board of autonomous, interplanetary CubeSats.

The proposed approach could be easily tailored to work with other descriptors. The number N_{pnt} of stationary points to compute and the step Δr_{p0} can be adjusted to overcome failings in solving the sequence of optimization problems. Decreasing both step Δr_{p0} and number N_{pnt} aids the numerical continuation in succeeding, in particular when using less smooth metrics. In the chapter, only heuristic arguments are provided to justify the methodology. However, it could be argued that maximizing the proposed Keplerian energy-based LD over finite horizons consistent with times of flight typical of orbits in weakly-stable set \mathcal{W}_1 is akin to minimize an integral over the same finite time of the spacecraft Keplerian energy. Indeed, the Keplerian energy of particles being temporarily captured oscillates between negative values (see Figure 7.9) up to the escape event, when the energy rapidly increases towards large positive values [50]. Finally, similarities between the backbone and kick-maps [121] seem to exist, so providing an alternative perspective to face the problem and potentially justify the backbone effectiveness with solid mathematical arguments.

Acknowledgments Potential connections between the backbone and the kick-maps were conjectured by Prof. C. Colombo while providing constructive feedback at the PhD final review held in October 2022. Due to time constraints, this research topic has not been investigated yet but could be easily part of future work.

O rapaz começou a entender que os presentimentos eram os rápidos mergulhos que a alma dava nesta corrente Universal de vida, onde a história de todos os homens está ligada entre si, e podemos saber tudo, porque tudo está escrito.

Paulo Coelho, *O Alquimista*

Synthesis of ballistic capture corridors

The chapter proposes a methodology to synthesize numerical approximation of BCCs, thereby covering steps v)–viii) of the ABC algorithm onboard block discussed in Section 6.2. A linear interpolation for inexpensive evaluation of states in the BCC is used. Far from capture, smooth parametric surfaces mapping corridor states to capture set ICs are computed and studied.

9.1 Problem statement

The goal of the BCC synthesis block foreseen in the ABC algorithm (see Figure 6.3) is to produce a numerical approximation of a subcorridor. The approximation is later made available to the autonomous guidance and control unit implemented onboard the limited-capability spacecraft. Ideally, the evaluation of the synthetic corridor shall be fast and inexpensive for spacecraft having limited onboard resources. In mathematical terms, our problem can be thus stated as follows:

Problem. Numerically synthesize the subcorridor $\check{\mathcal{D}}_{-1}^n = \{\gamma_b(\mathbf{x}_0, t_0) \mid \forall (\mathbf{x}_0, t_0) \in \mathcal{D}_{-1}^n\}$ as a function $\mathbf{x} = \psi(\lambda_{\odot}, \mathbf{p})$ of the solar longitude λ_{\odot} and parameters \mathbf{p} such that, given a solar longitude λ_{\odot}^* and parameters \mathbf{p}^* , the state $\mathbf{x}^* = \psi(\lambda_{\odot}^*, \mathbf{p}^*)$ is retrieved. In particular, the state \mathbf{x}^* must be targeted by the spacecraft to be temporarily captured by the central body at time epoch t_0 , so performing at least n revolutions about it.

9.2 Methodology

A numerical approximation of the corridor is built with the aim of a future onboard implementation. Firstly, a parametric representation of the corridor is carried out. Then, a linear interpolation between two corridor's Poincaré sections is performed to derive an intermediate section. Finally, states on the previously computed section

Algorithm 9.1: Synthesis of BCC.**Procedure** INITIALIZATION

Define set of parameters \mathbf{p} ; \triangleright e.g., $\mathbf{p} = [\xi_0, \eta_0]^\top$
 Define subcorridor domain \mathcal{D}_{-1}^n from \mathcal{C}_{-1}^n ; \triangleright e.g., circular shape
 Define number of interpolation nodes N_0 ;
 Define number of precomputed Poincaré sections N_{λ_\odot} ;
 Define solar longitude step $\Delta\lambda$ between subsequent Poincaré sections;

Procedure SAMPLE SELECTED DOMAIN

Select sampling rule; \triangleright e.g., Fibonacci lattice rule
 Sample N_0 nodes $\mathbf{x}_0^{(i)}$ over domain \mathcal{D}_{-1}^n ;
 Perform Delaunay triangulation on parameters $\mathbf{p}_0^{(i)}$;

Procedure CONSTRUCT PARAMETRIC SURFACES

Propagate nodes $\mathbf{x}_0^{(1)}$;
 Set solar longitude $\lambda_\odot^{(j)} = \lambda_\odot^{(1)}$;
For $j = 1 : N_{\lambda_\odot}$
 Derive parametric surfaces at $\lambda_\odot^{(j)}$; \triangleright numerical interp.
 Decrement solar longitude $\lambda_\odot^{(j)} = \lambda_\odot^{(j)} - \Delta\lambda_\odot$;
End
 Save results;

Exit

Result: Synthetic subcorridor $\check{\mathcal{S}}_{-1}^n$ expressed as $\mathbf{x} = \psi(\lambda_\odot, \mathbf{p})$.

are retrieved through a second linear interpolation. Overall, the methodology devised to tackle the problem envisages four steps:

1. sampling over the subcorridor domain \mathcal{D}_{-1}^n of N_0 interpolation nodes $\mathbf{x}_0^{(i)}$ with $i = 1, \dots, N_0$ according to Fibonacci lattice rule;
2. propagation of the N_0 nodes $\mathbf{x}_0^{(i)}$ sampled in step 1;
3. synthesis of subcorridor $\check{\mathcal{S}}_{-1}^n$ as a set of parametric surfaces $\mathbf{x} = \psi(\lambda_\odot, \mathbf{p})$ representative of N_{λ_\odot} precomputed Poincaré sections at $\lambda_\odot^{(j)}$ with $j = 1, \dots, N_{\lambda_\odot}$ and by steps of $\Delta\lambda_\odot$;
4. evaluation of state \mathbf{x}^* given solar longitude λ_\odot^* and parameters \mathbf{p}^* via two layers of linear interpolation:
 - i) between Poincaré sections at solar longitudes $\lambda_\odot^{(j)}$ and $\lambda_\odot^{(j+1)}$;
 - ii) on the Poincaré section computed at the desired solar longitude λ_\odot^* .

The detailed procedure to synthesize a corridor is found in Algorithm 9.1. On the other hand, precise steps to retrieve a state from a synthetic corridor are presented in Algorithm 9.2. The latter algorithm is made available to the autonomous guidance and control unit while solving the interplanetary cruise low-thrust optimal control problem [12]. Therefore, a mere evaluation of corridor target states is performed, so avoiding the propagation of several pre-capture legs. On the other hand, Algorithm 9.1 is called every time a synthetic corridor granting capture at a new desired epoch t_0 is requested.

Algorithm 9.2: Evaluation of synthetic BCC.**Procedure** INITIALIZATION

Define target Poincaré section setting solar longitude λ_{\odot}^* ;

Define target set of parameters \mathbf{p}^* ; \triangleright e. g. , $\mathbf{p}^* = [\zeta_0^*, \eta_0^*]^T$

Procedure EVALUATE TARGET STATE

Find Poincaré sections $\lambda_{\odot}^{(j)}$ and $\lambda_{\odot}^{(j+1)}$ closest to λ_{\odot}^* ;

For $i = 1 : N_0$

Get $\mathbf{x}^{(j,i)} = \psi(\lambda_{\odot}^{(j)}, \mathbf{p}^{(i)})$ and $\mathbf{x}^{(j+1,i)} = \psi(\lambda_{\odot}^{(j+1)}, \mathbf{p}^{(i)})$;

Interpolate $\mathbf{x}^{*(i)}$ from $\mathbf{x}^{(j,i)}$ and $\mathbf{x}^{(j+1,i)}$; \triangleright linear interp.

End

Interpolate \mathbf{x}^* at \mathbf{p}^* on Delaunay triangulation; \triangleright linear interp.

Return target state \mathbf{x}^* to autonomous guidance and control unit;

Exit

Result: Evaluation of target state $\mathbf{x}^* = \psi(\lambda_{\odot}^*, \mathbf{p}^*)$.

9.2.1 Parametric surfaces

The corridor is represented through parametric surfaces, miming what was done in [111] but applying the methodology to a non-autonomous system instead of an autonomous one. Cartesian coordinates (ξ_0, η_0) are used as parameters³². They are two independent variables describing the locations of ICs on the orbital plane in which the capture set is defined. Given a Poincaré section and the corresponding solar longitude λ_{\odot} , that corridor's section is completely described by six variables. Namely, they are the time interval $\Delta t = t - t_0$ (or alternatively the time epoch t), the projection of the position vector on the xy -plane (computed as $\sqrt{x^2 + y^2}$), the third component of the position vector z , and the three velocity components v_x , v_y , and v_z . In this way, the corridor's state on a Poincaré section is suitably mapped to the corresponding states at capture.

The grid used to numerically represent the parametric surfaces is constructed sampling the subcorridor domain with a Fibonacci lattice and subsequently performing a Delaunay triangulation. The Fibonacci lattice is a mathematical idealization of the sunflower pattern. It is generated with formulae [122]

$$l_i = l_0 \sqrt{i - 1/2} \quad (9.1)$$

$$\phi_i = 2\pi i \Phi^{-1} \quad (9.2)$$

where l_i and ϕ_i are the radial and azimuthal polar coordinates of each point (i) of the grid, while $\Phi = 1 + \Phi^{-1}$ is the golden ratio equal to $(1 + \sqrt{5})/2$. The Fibonacci grid is chosen for its several attributes, namely its geometric regularity, the almost homogeneous and isotropic resolution, and a lack of artificial symmetries. All features making the lattice suitable for numerical modeling [122].

³²This is not the only available option. Also other sets of parameters could be used, e. g., the radius and argument of pericenter (r_{p0}, ω_0) .

Given two Poincaré sections 1 and 2 separated by a small angle $\Delta\lambda_{\odot} = |\lambda_{\odot}^{(2)} - \lambda_{\odot}^{(1)}|$, thereby close enough to each other, the intermediate section at $\lambda_{\odot}^* = (\lambda_{\odot}^{(1)} + \lambda_{\odot}^{(2)})/2$ is derived by linear interpolation. The linear interpolation is carried out point by point between corresponding samples of the Fibonacci lattice. States on the interpolated section are evaluated by linearly interpolating the parametric surfaces numerically constructed on the Fibonacci lattice.

9.2.2 Performance of synthetic corridor

An assessment of synthetic corridor performance and goodness is carried out by evaluating a test point belonging to the corridor numerical approximation. The test point is arbitrary chosen as the center of the corridor since that is never a node of the Fibonacci lattice. Evaluations are compared against high-fidelity, point-wise propagations performed with GRATIS. Errors at insertion are computed for any tested solar longitudes as

$$e_{t_i} = |t_i - t_i^*|, \quad e_{r_i} = \|\mathbf{r}_i - \mathbf{r}_i^*\|, \quad e_{v_i} = \|\mathbf{v}_i - \mathbf{v}_i^*\| \quad (9.3)$$

where t_i^* , \mathbf{r}_i^* , and \mathbf{v}_i^* are the time epoch, position, and velocity of the high-fidelity solution, respectively. Additionally, also errors on time epoch and osculating elements at capture are estimated. They are computed between the new capture point³³, obtained by forward propagating the evaluated test point, and the initial osculating elements of the test point at time epoch t_0 . Hence,

$$\begin{aligned} e_{t_0} &= |t_0 - t_0^*|, \quad e_{r_0} = |r_0 - r_0^*|, \quad e_{e_0} = |e_0 - e_0^*|, \\ e_{i_0} &= |i_0 - i_0^*|, \quad e_{\Omega_0} = |\Omega_0 - \Omega_0^*|, \quad e_{\omega_0} = |\omega_0 - \omega_0^*|, \end{aligned} \quad (9.4)$$

where quantities marked with * superscript are the exact initial time epoch and osculating elements.

9.3 Results

The method is applied to synthesize the subcorridor \check{S}_{-1}^6 developed from the capture set \mathcal{C}_{-1}^6 presented in Chapter 5 (see Figure 5.3). The corridor is represented through parametric surfaces in Figure 9.1, where three sets of surfaces are shown. They are obtained performing a Delaunay triangulation on a Fibonacci lattice of 105 points. The first set, in yellow, refers to the Poincaré section at $\lambda_{\odot}^{(1)} = 90.05$ deg named *section 1*. The second one, colored in red and referred to as *section 2*, describes the Poincaré section at $\lambda_{\odot}^{(2)} = 89.95$ deg. Finally, the blue set includes parametric surfaces retrieved by linear interpolation of sections 1 and 2.

³³To find the new capture point is not trivial. For a generic state, neither the capture epoch nor the capture point location are known a priori. Generally speaking, capture is not even granted. However, if the IC forward propagated still belongs to a corridor, a new capture point is found inverting the methodology to construct BC orbits [25].

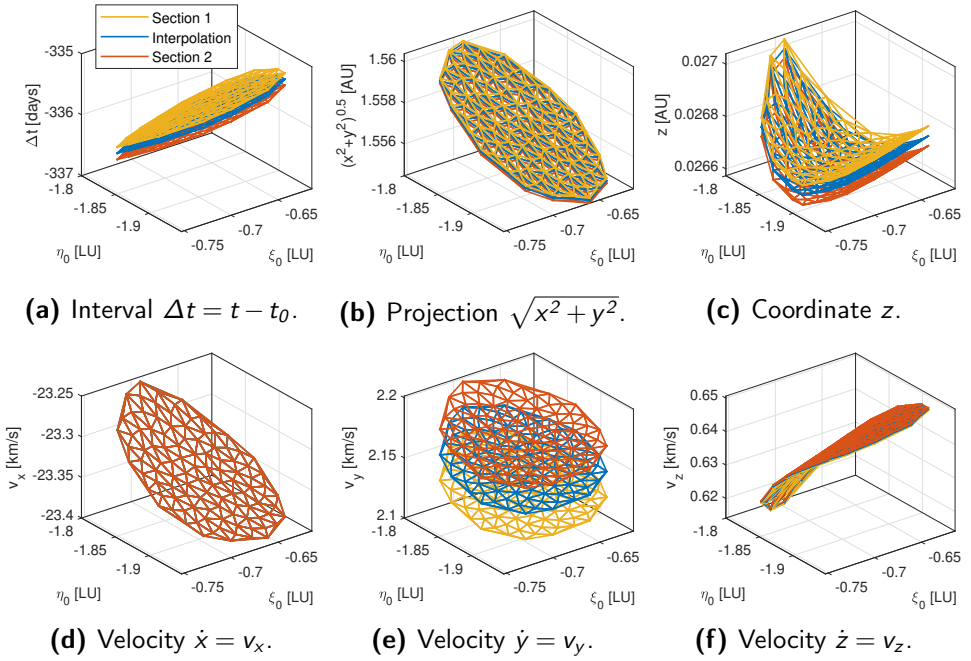
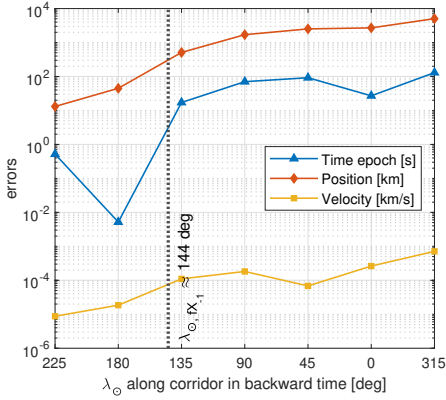


Figure 9.1: Subcorridor \mathcal{S}_{-1}^6 parametric surfaces of time epoch and Cartesian states at three Poincaré sections. States in Sun-centered ECLIPJ2000 frame. Parameters $\xi_0 = r_{p0} \cos(\omega_0)$ and $\eta_0 = r_{p0} \sin(\omega_0)$. Yellow and red surfaces at $\lambda_{\odot}^{(1)} = 90.05$ deg and $\lambda_{\odot}^{(2)} = 89.95$ deg, respectively. Blue surfaces linearly interpolated at $\lambda_{\odot}^* = 90$ deg. Delaunay triangulations on a Fibonacci lattice of 105 points.

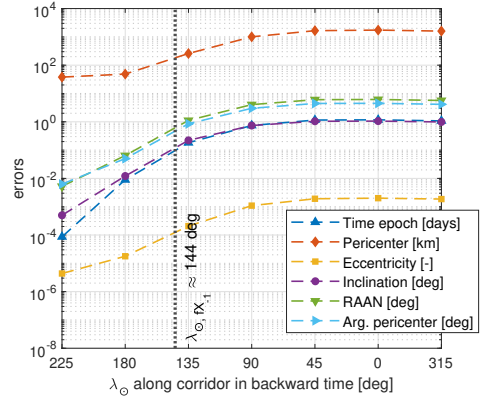
The center of the corridor is evaluated on all seven Poincaré sections drawn in Figure 5.10a. Two different synthetic corridors are tested, a coarse and a fine one. The former is built from Poincaré sections with step $\Delta\lambda_{\odot} = 0.1$ deg and approximated on a Fibonacci lattice of 105 points³⁴ (see Figure 9.1). The latter is derived from sections with step $\Delta\lambda_{\odot} = 0.01$ deg and Fibonacci lattice made of 715 points³⁵ (see Figure 5.9b). The test point evaluations are compared against the high-fidelity solution propagated with GRATIS (collected in Table 5.1 and Table 5.2). The errors at insertion are computed for any tested solar longitudes. Results are shown in Figure 9.2a, while plot in Figure 9.2b provides errors at capture. Figures 9.2c and 9.2d report the same errors when using the fine approximation. As expected, the fine approximation performs better, overall granting smaller errors than the coarse one both at insertion and capture. Errors are larger when interpolating far from capture, likely due to the stretching observed in Figure 5.13. However, they seem to stabilize after the corridor crosses the Poincaré section at $\lambda_{\odot} = 90$ deg. Regarding errors on insertion epoch and velocity, they seem to exhibit local maxima in correspondence of the corridor twisting, when $\lambda_{\odot} \approx 90$ deg.

³⁴Counting 21 complete clockwise spirals made of 5 points each.

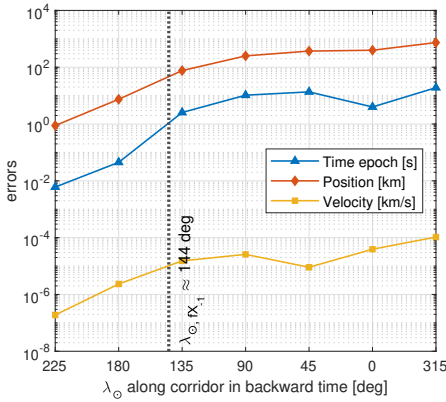
³⁵Counting 55 complete clockwise spirals made of 13 points each.



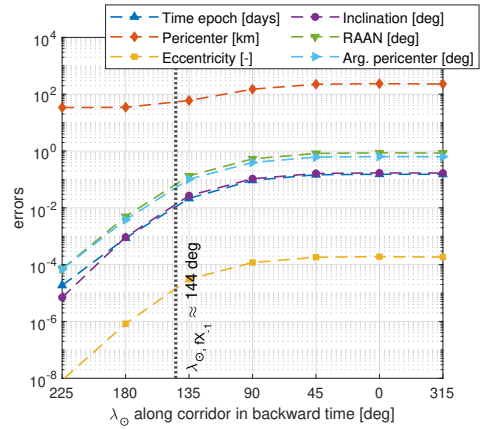
(a) Errors at insertion in subcorridor \check{S}_{-1}^6 , coarse approximation. Step $\Delta\lambda_{\odot} = 0.1$ deg and 105 points Fibonacci lattice.



(b) Errors at capture point, coarse approximation. Step $\Delta\lambda_{\odot} = 0.1$ deg and 105 points Fibonacci lattice.



(c) Errors at insertion in subcorridor \check{S}_{-1}^6 , fine approximation. Step $\Delta\lambda_{\odot} = 0.01$ deg and 715 points Fibonacci lattice.



(d) Errors at capture point, fine approximation. Step $\Delta\lambda_{\odot} = 0.01$ deg and 715 points Fibonacci lattice.

Figure 9.2: Errors of synthetic subcorridor \check{S}_{-1}^6 . Dotted black vertical lines mark approximate solar longitude $\lambda_{\odot,fx-1}$ at which a spacecraft escapes from Mars when flying on subcorridor's center trajectory in backward time. The x-axes are not monotone increasing because they represent solar longitude λ_{\odot} wrapped to 360 deg along subcorridor in backward time.

9.4 Final remarks

The mapping of capture conditions to interplanetary states has been discussed. Different interpolation schemes can be tested to find the best trade-off between computational effort and accuracy. Indeed, numerical experiments here omitted prove how too coarse approximations fail in representing corridors correctly. In particular, the method appears really sensitive to the step $\Delta\lambda_{\odot}$ used for reconstructing an intermediate Poincaré section. Alternative interpolation techniques like cubic spline or cubic convolution are expected to perform better than the simple, fast linear interpolation. This at the drawback of large computation efforts required both in terms of memory and time. In particular, cubic convolution interpolation was already proven successful when trying to approximate invariant manifolds in the restricted circular three body problem [111]. Nonetheless, priority to inexpensive interpolation methods has been given in this dissertation in light of the ultimate goal of implementing the ABC algorithm directly on board limited-capability, autonomous, interplanetary CubeSats.

“All we have to decide is what to do with the time that is given us.” – Gandalf

J. R. R. Tolkien, *The Fellowship of the Ring*

Conclusion

In conclusion, a critical discussion is presented summarizing the attained results and contributions that lead to answer the RQs. Furthermore, recommendations for future work are provided to drive potential next developments at best.

10.1 Summary of results

In Chapter 1, the following RQs were defined.

Research questions

- i) How can we characterize ballistic capture corridors?
- ii) How to synthesize high-fidelity ballistic capture corridors that are computationally inexpensive for onboard usage?
 - a) How can we generate new ballistic capture orbits on board?
 - b) To what extent can we exploit Lagrangian indicators to extract dynamical insight and build ballistic capture corridors?
 - c) How accurate are ballistic capture corridors constructed on board?

The characterization of BCCs was covered in Chapter 5, so answering RQ i) and achieving RO i). Dimension, shape, and peculiarities of corridors were studied to appraise their potential exploitation as pathways guaranteeing temporary capture at major planets for autonomous, deep-space CubeSats. On the other hand, RQ ii) was tackled in Chapters 6–9. Specifically, the comprehensive overview of the ABC algorithm was discussed in Chapter 6. Later, essential methods founding the algorithm (i. e., the generation of BC orbit families, the extraction of the backbone, and the synthesis of BCCs) were presented in detail. In Chapter 7, the computationally demanding problem of designing BC orbits through stable sets manipulation was unburdened by just solving a linear system, so answering RQ ii.a). A novel methodology to extract the backbone of a capture set was established in Chapter 8. The backbone could be used to construct capture sets

directly on board. Additionally, it finds application in the generation of BC orbit families when combined with the correction technique discussed in Chapter 7. This was made possible by exploiting LDs evaluated on a short finite horizon, therefore answering RQ ii.b). Finally, to answer RQ ii.c), the accuracy of synthetic corridors was assessed in Chapter 9. Errors at insertion and capture epoch for coarse and fine maps were estimated. All aforementioned outcomes concurred in achieving RO ii), so making the algorithm compatible with limited-capability, autonomous, interplanetary CubeSats.

Algorithms developed in Chapters 7–9 are advanced and complex. Their actual onboard implementation will strongly depend on the synergy with the autonomous CubeSat guidance and control unit. Determining the characteristic frequency with which new capture sets and BCCs are to be computed will be of paramount importance in assessing real feasibility for onboard implementations. Specifically, a high frequency could be problematic and prevent the successful application of the ABC algorithm. Nevertheless, we foresee a low characteristic frequency because new capture sets and BCCs are expected to be computed only when re-planning the capture about the target and not every time the interplanetary cruise is re-optimized, which occurs more frequently. Therefore, we are mildly positive about implementing the ABC successfully.

Overall, results presented in this dissertation aid in answering the ORQ of Pillar 3 and, consequently, the EXTREMA big RQ (see Section 1.2). Achieving ballistic capture at Mars without any a priori instruction is anything but trivial, in particular for limited-capability spacecraft akin to CubeSats. The answer to Pillar 3 ORQ is nowhere close to be exhaustively resolved. Nevertheless, the advancements discussed in this work will hopefully foster the necessary knowledge to ultimately engineer autonomous ballistic capture.

10.2 Recommendations for future work

Suggestions on possible future developments follow. Inclusion of stochastic dynamics in the EoM is advised to assess the robustness of the developed methods against uncertainties in the parameters and uncertainty continuous forces [109] (i. e., solar radiation pressure and residual non-modeled accelerations).

The boundary conditions of the 3PBVP formulated in Chapter 7 could be adapted to correct ICs not only belonging to \mathcal{C}_{-1}^n but to any generic sub-sets (i. e., \mathcal{W}_n , \mathcal{X}_n or \mathcal{K}_n) and to seek any desired initial Keplerian elements (or state coordinates) instead of the capture epoch. Investigating this possibility could be of interest to several applications.

The 3PBVP could be easily converted into an optimization problem similar to what is done in [114], the cost function being a quadratic form of the constraints or the correction magnitude for instance. This would allow relaxing boundary conditions ii_f) and i_b), and remove boundary condition iii_f) (i. e., the most strict). Adding constraints on regularity index S , repulsion rate ρ , or a specific LD could

be considered as well. This is expected to ease the search for new BC orbits at the cost of increasing the computational effort. However, by admitting some performance loss, the optimization could be forcibly stopped after a few iterations (in the limit even after just one if necessary) to reduce the computational burden, boost algorithm speed, and maintain the method suitable for limited-capability, autonomous spacecraft.

Starting from the aforementioned optimization problem statement, a low-thrust optimal control problem could be derived with the primary goal of making the temporary capture permanent. This means computing the thrust profile such that the \mathcal{C}_{-1}^n orbit on which the spacecraft is flying is transformed into a \mathcal{C}_{-1}^∞ orbit. The suggestion is to investigate both time-optimal and fuel-optimal approaches while considering that the latter may be likely more interesting from a practical point of view. The solving method (i. e., direct or indirect) should be selected based on the required performance. However, indirect methods are suggested considering the availability of really good initial guesses (i. e., BC orbits themselves).

The outcome of Chapter 8 is the result of an intuition supported by heuristic arguments and numerical experiments. Unfortunately, this is insufficient to prove the validity of the backbone because the mathematical proof is lacking. The recommendation is to provide a theoretical demonstration. It could be argued that clues on how to proceed may be possibly found in [62, 64, 93]. Finding strong mathematical evidence will be challenging but highly attractive. Additionally, potential points of contact and similarities between the backbone and kick-maps [121] should be investigated.

Although effective, the two-layer linear interpolation technique (see Section 9.2) used for on-the-fly evaluation of corridor states could be enhanced. In particular, an alternative procedure based on PCE could benefit in terms of both efficiency and accuracy [108]. The advice is to envisage a PCE based methodology to synthesize a corridor numerical approximation, so improving the proposed approach.

Attainability of BCCs pathways as viable options for autonomous CubeSats to achieve temporary capture at major planets according to their knowledge and dispersion errors must be proved. Specifically, this should be intended as a combined effort of Pillars 1, 2, and 3 in EXTREMA (see Figure 1.2).

Finally, assuring that the ABC algorithm is suitable for implementation on board to autonomous interplanetary CubeSats is mandatory. In this regard, a testing campaign assessing the performance and including V&V of the algorithm is strongly suggested. Firstly, in a processor-in-the-loop simulation. Then, in a hardware-in-the-loop experiment operated on relevant equipment.

See you space cowboy. . .

Hajime Yatate, *Cowboy Bebop*

Verification and validation campaign of GRATIS

In this appendix, the V&V of GRATIS is presented. According to the European Cooperation for Space Standardization (ECSS)³⁶ *verification* and *validation*, when referring to software, are defined as³⁷:

- **verification:** “*Process to confirm that adequate specifications and inputs exist for any activity, and that the outputs of the activities are correct and consistent with the specifications and inputs.*”, the status of the software following verification is *verified*;
- **validation:** “*Process to confirm that the requirements baseline functions and performances are correctly and completely implemented in the final product.*”, the status of the product following validation is *validated* and verification is a pre-requisite for validation.

Since no list of specifications and requirements are drafted for GRATIS, the focus in the validation campaign is to *i) verify* the correctness and consistency of the outputs provided some inputs, and *ii) validate* the correctness and completeness of the implemented functions in light of the toolkit purpose. To assess the V&V of GRATIS, the most important core routines are tested. In particular, the implemented DOPRI8 [40] integration scheme and the right-hand side (RHS) of the high-fidelity model. Three test plans for the DOPRI8, and a test plan and three benchmarks for the RHS are defined to assess their V&V. Then, the whole toolkit is tested against results found in literature to check the correct extraction and manipulation of stable sets.

³⁶<https://ecss.nl/standards/> [last accessed Dec 1, 2022].

³⁷From ECSS-E-ST-40C, third issue, 6 March 2009.

A.1 V&V of DOPRI8 integration scheme

The V&V of the implemented DOPRI8 propagation scheme, also named `my_ode78` or RK8(7)13M³⁸ throughout the manuscript, is carried out performing three test plans. The first test plan verified the correct implementation of the scheme. The second test checked the correct implementation of forward and backward propagation feature. The last one verified the correct implementation of the event location functionality. Finally, the scheme is compared to other numerical propagators available in the MATLAB[®]'s ode suite [39].

The whole DOPRI8's V&V campaign is performed in the context of the planar two-body problem. The planar two-body problem is selected for two reasons: it is frequently used by many authors, and it describes the major features of satellite motion very well [35, 123]. The nondimensional form of the equations is implemented in the RHS. Therefore, the attracting body had a gravitation parameter $\mu = 1$, and the propagated orbit is characterized by a semi-major axis $a = 1$. The revolution period resulted to be $T = 2\pi$. The differential equations of the dynamical system can be found in [35]. Moreover, a big advantage of using the planar two-body problem is that an exact solution exists. As a consequence, results can be verified and validated against it.

A.1.1 Test plan 1

To assess the correct implementation of the DOPRI8 scheme the test defined by [123] and used in [35] is used. The scheme is tested on five different problems D1 to D5 with eccentricities ranging from 0.1 to 0.9 by steps of 0.2. This because velocity variations in an eccentric orbit are crucial when testing a variable step numerical integration method like DOPRI8 [35].

The orbits are propagated starting from the pericenter and for 10 periods, from $t_0 = 0$ to $t_f = 20\pi$. For this test, the *RelTol* (relative tolerance error) is set to 10^{-14} . Errors are computed against the exact solution as

$$e_{\text{pos}} = \|\mathbf{r}^* - \mathbf{r}\|, \quad e_{\text{vel}} = \|\mathbf{v}^* - \mathbf{v}\| \quad (\text{A.1})$$

where \mathbf{r}^* and \mathbf{v}^* are the exact position and velocity.

The results of the five test problems are shown in Figure A.1. Position and velocity errors are shown on the left and on the right, respectively. The trends vary differently from D1 to D5. From the charts it seems that the numerical integration of D2 and D3 is more accurate with respect to others. As expected, D5's solution is the less accurate being the problem more eccentric. Nonetheless, position errors remain always under 10^{-10} . Similarly, apart from some exceptions for D5's solution, most of the times velocity errors are smaller than 10^{-10} . For comparison, the same

³⁸The notation RK $p(q)$ sM is used when referring to a Runge–Kutta method of order p , with an embedded step-size control of q th order, and a total of s stages [35].

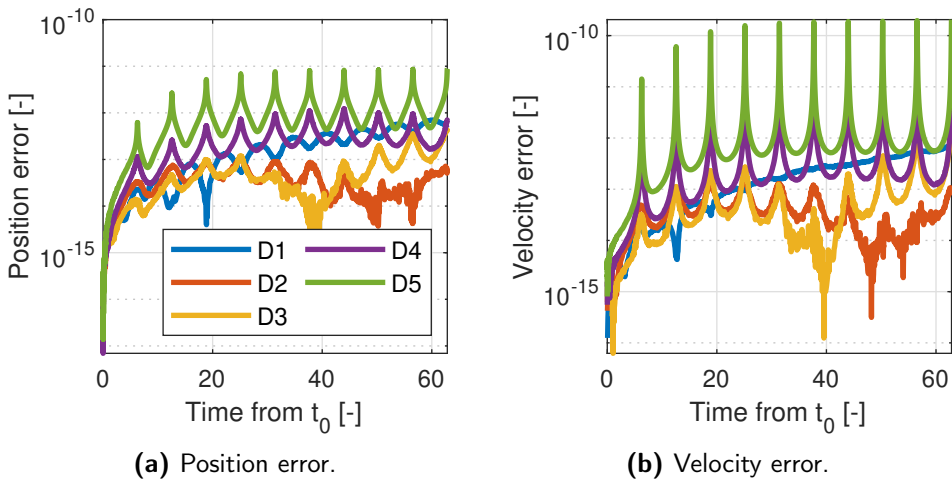


Figure A.1: Test plan 1 errors of `my_ode78`. Errors in nondimensional quantities. *RelTol* set to 10^{-14} .

test is run using MATLAB[®]'s `ode78`³⁹, `ode89`⁴⁰, and `ode113`⁴¹ with *AbsTol* (absolute tolerance error) set to 10^{-14} and *RelTol* set to 2.22045×10^{-14} . The latter because for smaller values MATLAB[®] displays a warning, notifying the user that *RelTol* has been increased to 2.22045×10^{-14} . From the results shown in Figure A.2, it seems that `my_ode78` performs better than `ode78`. However, different relative tolerances were used, therefore this comparison may be not completely fair. Results when using propagation schemes `ode89` and `ode113` are shown in Figures A.3 and A.4, respectively.

A.1.2 Test plan 2

The forward and backward integration capability of the scheme is checked propagating 10^3 random ICs forward for 10 periods, saving the final states, and then propagating backward the final states again for 10 periods to get back the ICs. The ICs are derived from a random vector of eccentricities and assuming the massless spacecraft at the pericenter. The random vector of eccentricities is obtained

³⁹`ode78` is a propagator based on an Verner's implementation of the RK formula (7,8) pair [124]. It is a method of 8th order with a 7th order continuous extension which requires four additional evaluations but only on steps requiring interpolation. <https://www.mathworks.com/help/matlab/ref/ode78.html> [last accessed Dec 1, 2022]

⁴⁰`ode89` is a propagator based on an Verner's implementation of the RK formula (8,9) pair [124]. It is a method of 9th order with an 8th order continuous extension which requires five additional evaluations but only on steps requiring interpolation. <https://www.mathworks.com/help/matlab/ref/ode89.html> [last accessed Dec 1, 2022]

⁴¹`ode113` is a multistep, VSVO, ABM, PECE solver of orders 1st to 13th. The highest order used appears to be 12th since a formula of order 13th is used to form the error estimate and the function does local extrapolation to advance the integration at order 13th. <https://www.mathworks.com/help/matlab/ref/ode113.html> [last accessed Dec 1, 2022].

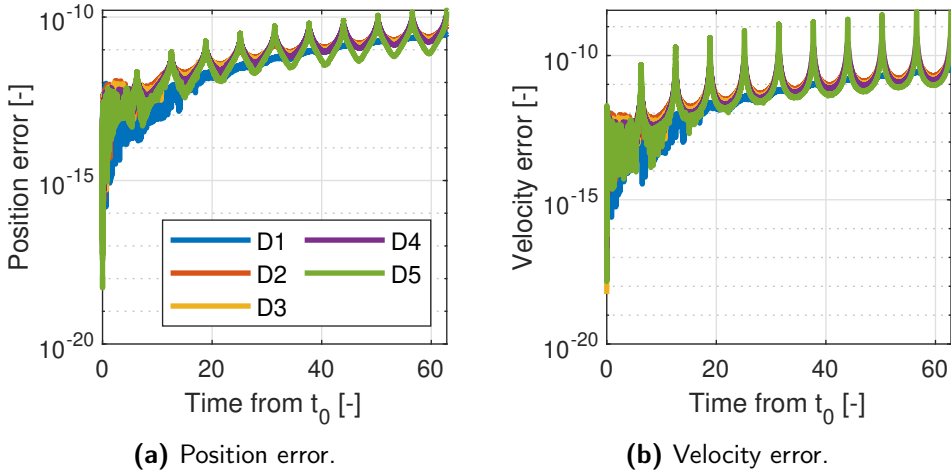


Figure A.2: Test plan 1 errors of `ode78`. Errors in nondimensional quantities. $RelTol$ set to 2.22045×10^{-14} and $AbsTol$ set to 10^{-14} .

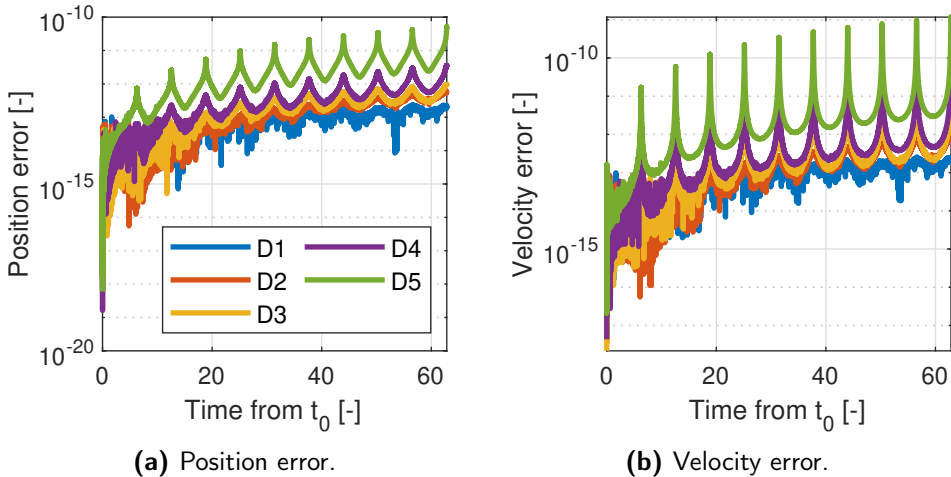


Figure A.3: Test plan 1 errors of `ode89`. Errors in nondimensional quantities. $RelTol$ set to 2.22045×10^{-14} and $AbsTol$ set to 10^{-14} .

with MATLAB[®]'s `rand`⁴² routine (which returns uniformly distributed random numbers) setting the seed to 0 and bounding the results between 0 and 0.99, so limiting the study to closed orbits. For this test, the $RelTol$ is set to 10^{-14} .

The plot in Figure A.5 shows the position and velocity errors for the test plan under study. The final states are compared against the corresponding exact ICs using Eq. (A.1). Errors strongly depend on the eccentricity but exhibit an erratic behavior for close eccentricity values. As expected, larger errors occur for eccentricities closer to the unity. As previously done, the test is run also propagating

⁴²<https://www.mathworks.com/help/matlab/ref/rand.html> [last accessed Dec 1, 2022].

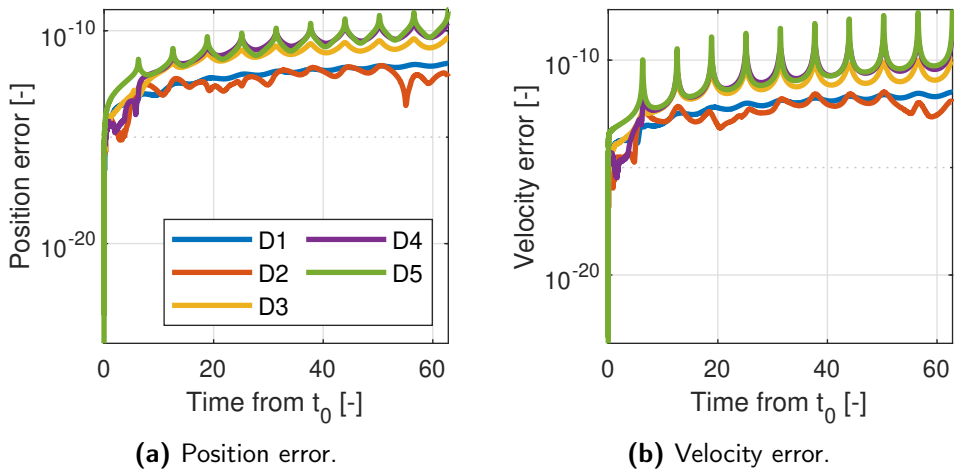


Figure A.4: Test plan 1 errors of `ode113`. Errors in nondimensional quantities. *RelTol* set to 2.22045×10^{-14} and *AbsTol* set to 10^{-14} .

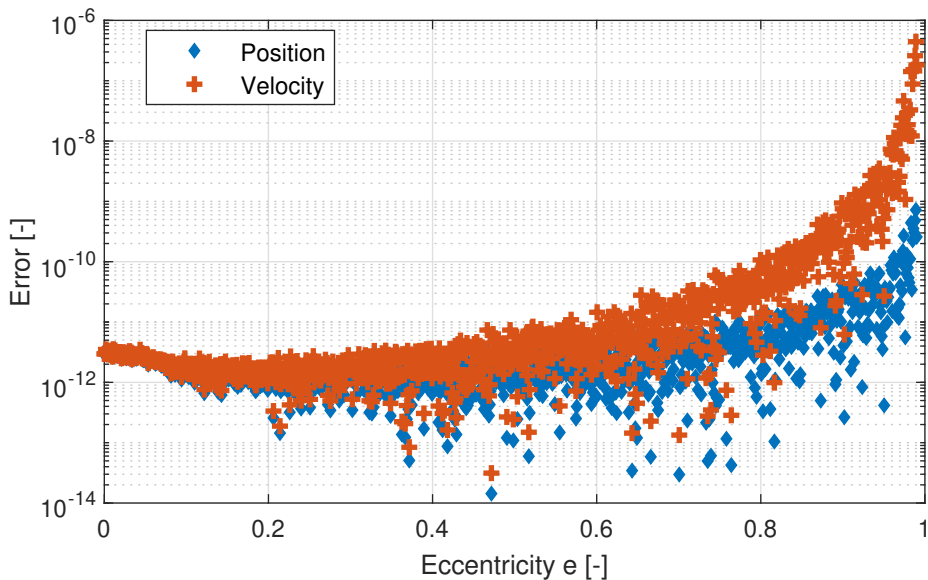


Figure A.5: Test plan 2 errors of `my_ode78`. Position error (blue diamonds) and velocity error (red crosses) in nondimensional quantities. *RelTol* set to 10^{-14} .

the equations with `ode78` scheme, see Figure A.6. In that case, *RelTol* is set to 2.22045×10^{-14} and *AbsTol* to 10^{-14} . As before, although the comparison is still not completely fair, `my_ode78` seems to perform better than `ode78`. Results from the tests carried out with propagation schemes `ode89` and `ode113` are shown in Figures A.7 and A.8, respectively. In both cases, *RelTol* is set to 2.22045×10^{-14} and *AbsTol* to 10^{-14} .

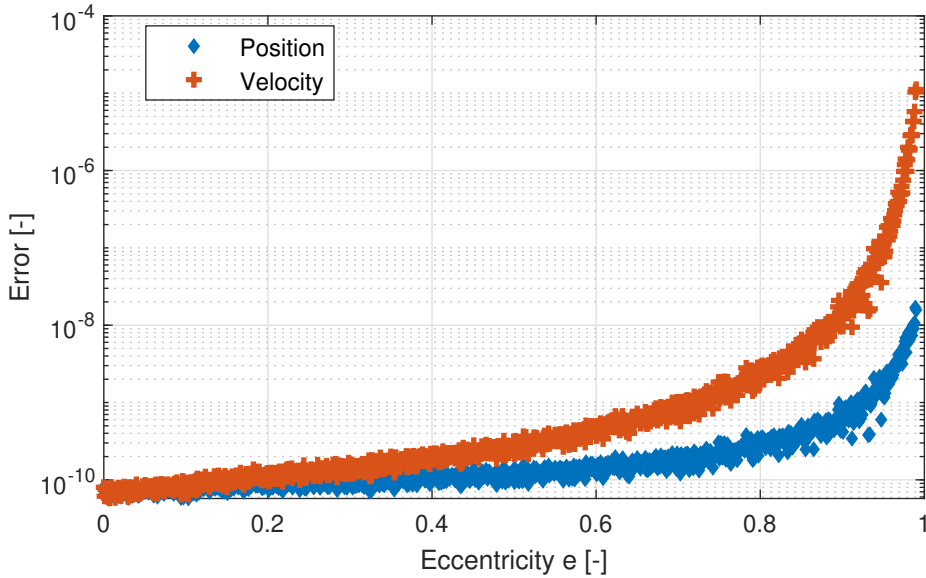


Figure A.6: Test plan 2 errors of `ode78`. Position error (blue diamonds) and velocity error (red crosses) in nondimensional quantities. $RelTol$ set to 2.22045×10^{-14} and $AbsTol$ set to 10^{-14} .

A.1.3 Test plan 3

The third test plan is used to V&V the event location functionality. The `my_ode78` of GRATIS implements the regula falsi method [120] for event location purposes. Differently, a variant of the regula falsi method called Illinois method [125] is implemented in MATLAB[®]'s routine `odezero` used by the integration schemes of the ode suite [39].

The same set of random eccentricities generated for the second test plan (see Section A.1.2) is used to generate the 10^3 needed for the third test. To assess the event location functionality, the massless particle is integrated starting from the pericenter. The scheme is requested to locate the events at which the true anomaly is equal to $\theta = \pi/2$. Half of the ICs are propagated forward, while the other half backward. Also in this case, the $RelTol$ is set to 10^{-14} .

The results of the test are shown in Figure A.9. Errors are computed against the exact solution at the event. Comparing the `my_ode78`'s outcome with the errors resulting from running the same test with `ode78` (see Figure A.10), as already suggested by the previous two tests, it can be claimed that `my_ode78` performs better than `ode78`. Results obtained using propagation schemes `ode89` and `ode113` are shown in Figures A.11 and A.12, respectively. Also in this case, when propagating with `ode78`, `ode89`, and `ode113`, tolerances $RelTol$ and $AbsTol$ are set to 2.22045×10^{-14} and 10^{-14} , respectively.

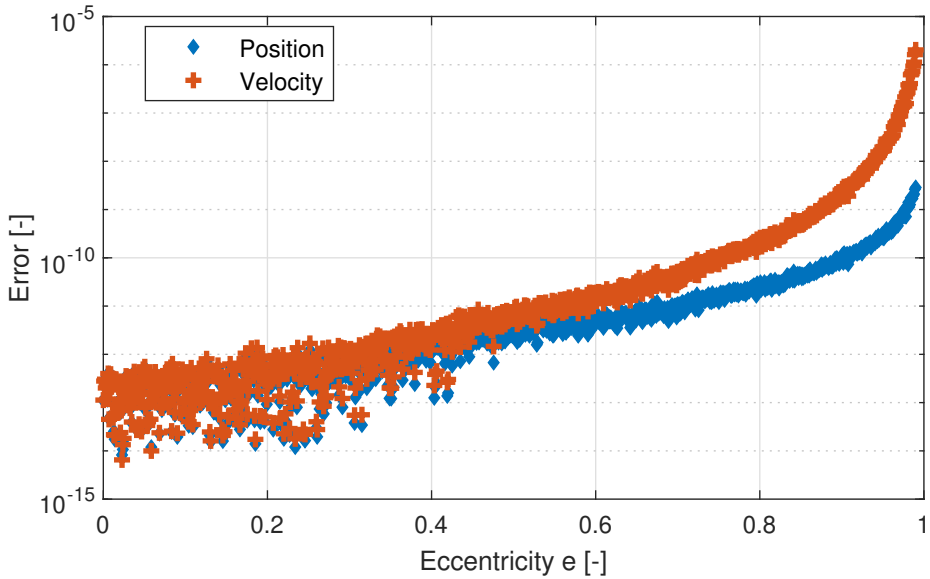


Figure A.7: Test plan 2 errors of `ode89`. Position error (blue diamonds) and velocity error (red crosses) in nondimensional quantities. $RelTol$ set to 2.22045×10^{-14} and $AbsTol$ set to 10^{-14} .

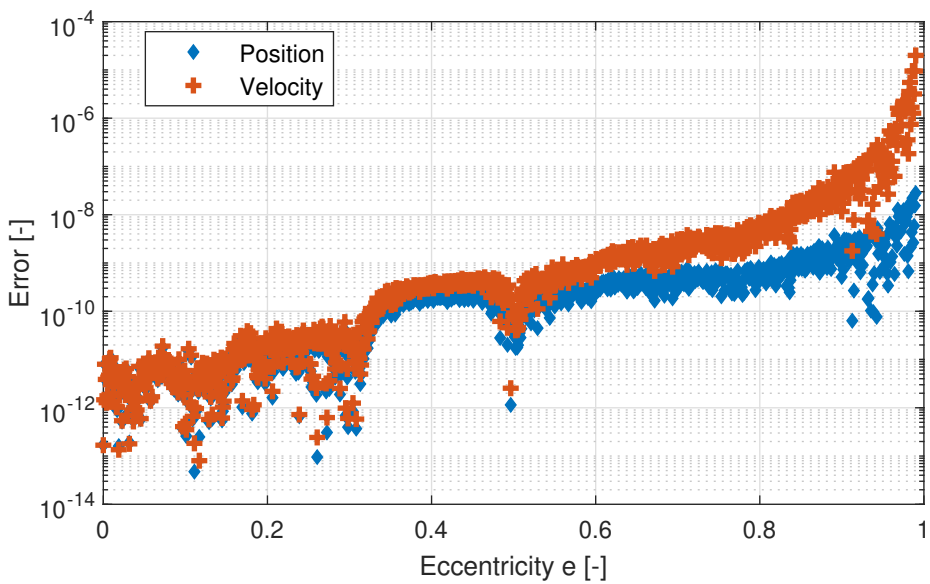


Figure A.8: Test plan 2 errors of `ode113`. Position error (blue diamonds) and velocity error (red crosses) in nondimensional quantities. $RelTol$ set to 2.22045×10^{-14} and $AbsTol$ set to 10^{-14} .

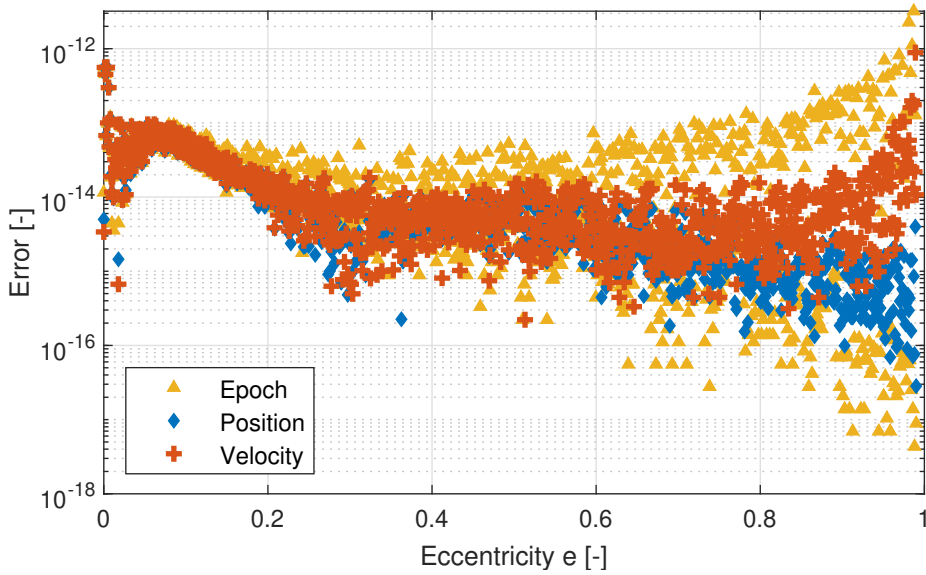


Figure A.9: Test plan 3 errors of `my_ode78`. Error on the event epoch (yellow triangles), position error (blue diamonds), and velocity error (red crosses) in nondimensional quantities. *RelTol* set to 10^{-14} .

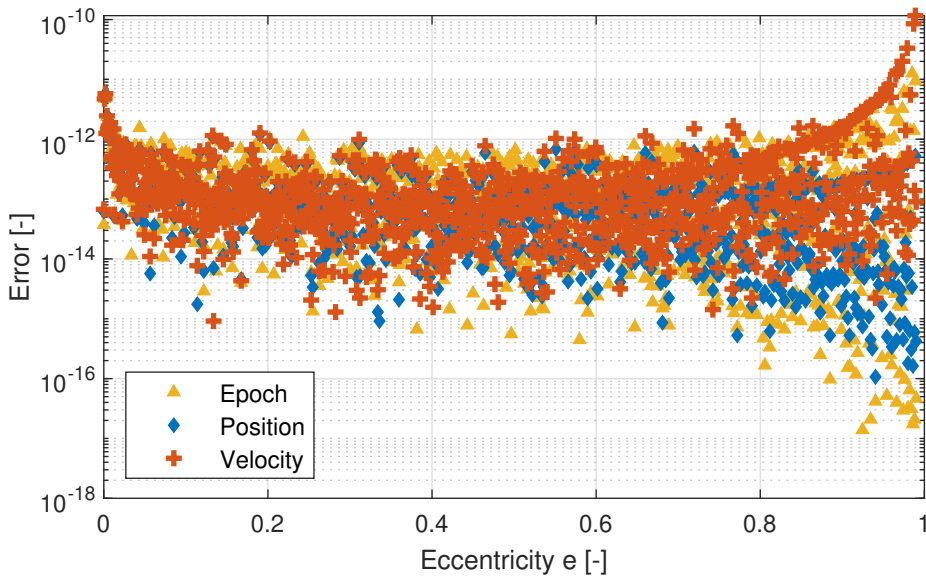


Figure A.10: Test plan 3 errors of `ode78`. Error on the event epoch (yellow triangles), position error (blue diamonds), and velocity error (red crosses) in nondimensional quantities. *RelTol* set to 2.22045×10^{-14} and *AbsTol* set to 10^{-14} .

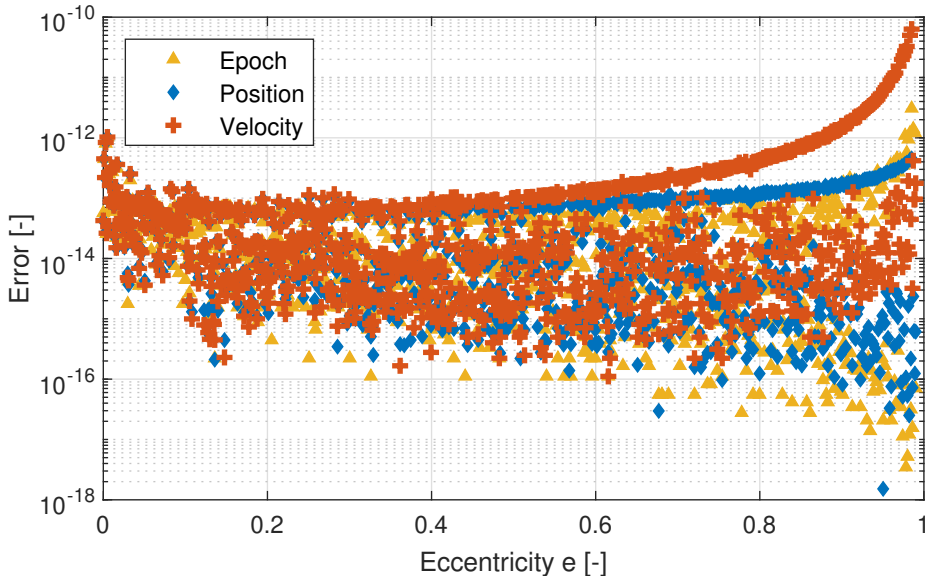


Figure A.11: Test plan 3 errors of `ode89`. Error on the event epoch (yellow triangles), position error (blue diamonds), and velocity error (red crosses) in nondimensional quantities. $RelTol$ set to 2.22045×10^{-14} and $AbsTol$ set to 10^{-14} .

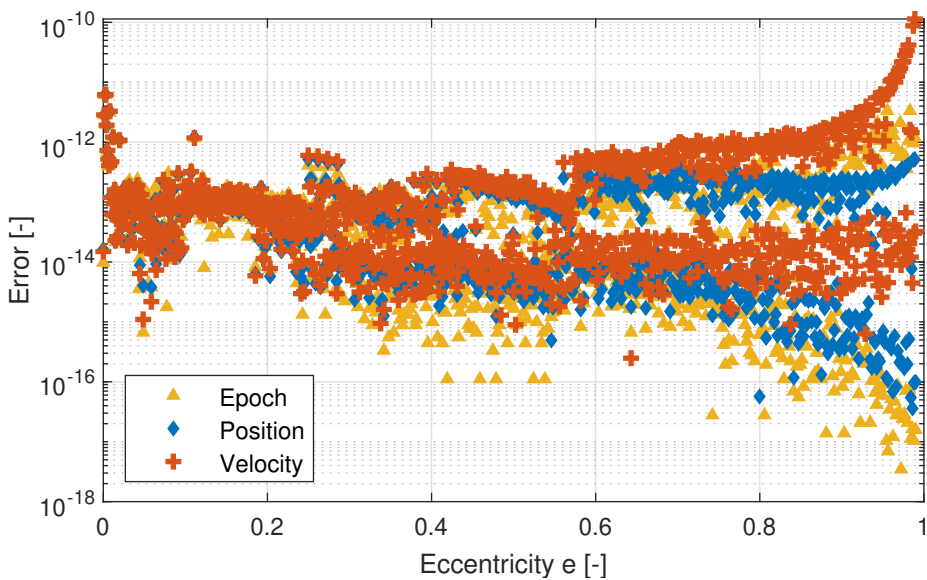


Figure A.12: Test plan 3 errors of `ode113`. Error on the event epoch (yellow triangles), position error (blue diamonds), and velocity error (red crosses) in nondimensional quantities. $RelTol$ set to 2.22045×10^{-14} and $AbsTol$ set to 10^{-14} .

A.2 Integration schemes comparison

Once the V&V campaign of the implemented DOPRI8 scheme is assured, its performance is compared to the ones of MATLAB[®]'s `ode45`⁴³, `ode78`, `ode89`, and `ode113`. The schemes are tested at different tolerances, specifically at 2.5×10^{-14} , 10^{-12} , 10^{-10} , 10^{-8} , and 10^{-6} . A set of 10^3 randomly generated ICs are propagated for 10 orbital revolutions and the final states are compared against the exact solutions. The massless particles are assumed to start from the pericenter of orbits having different eccentricities. The eccentricities are generated randomly using MATLAB[®]'s `randn`⁴⁴ routine (which returns normally distributed random numbers). Then, the output random eccentricities are scaled to obtain a normal distribution with mean $\mu = 0.7$ and standard deviation $\sigma = 0.05/3$ (so having $3\sigma = 0.05$).

The plot in Figure A.13 compares the number of function evaluations against the tolerance. At smaller tolerances, higher accuracy is expected. Then, Figure A.14 provide a rough idea about the computational times for single calls⁴⁵. Finally, the chart in Figure A.15 presents how position (solid curves) and velocity (dashed curves) errors vary for different tolerances and for the different integration schemes considered. All in all, there is evidence that the `my_ode78` delivers the best performance among the tested numerical propagation schemes.

⁴³`ode45` is a propagator based on an explicit RK formula (4,5) pair of Dormand and Prince [126]. It is a 7-stage method of 5th order with an embedded method of 4th order, also called DOPRI5 or RK5(4)7M [35]. The MATLAB[®]'s implementation uses a free interpolant of 4th order communicated privately by Dormand and Prince as specified in the help of the routine. <https://www.mathworks.com/help/matlab/ref/ode45.html> [last accessed Dec 1, 2022]

⁴⁴https://www.mathworks.com/help/matlab/ref/randn.html?searchHighlight=randn&s_tid=srchtitle [last accessed Dec 1, 2022]

⁴⁵Code written in MATLAB[®]R2021b and run on a Windows 10 Pro (OS type: 64-bit, x64-based processor; version: 20H2) machine having 16 GB of RAM, mounting 6x Intel[®] Core[™] i7-8700 CPU@3.20 GHz and a TOSHIBA DT01ACA100 1 TB.

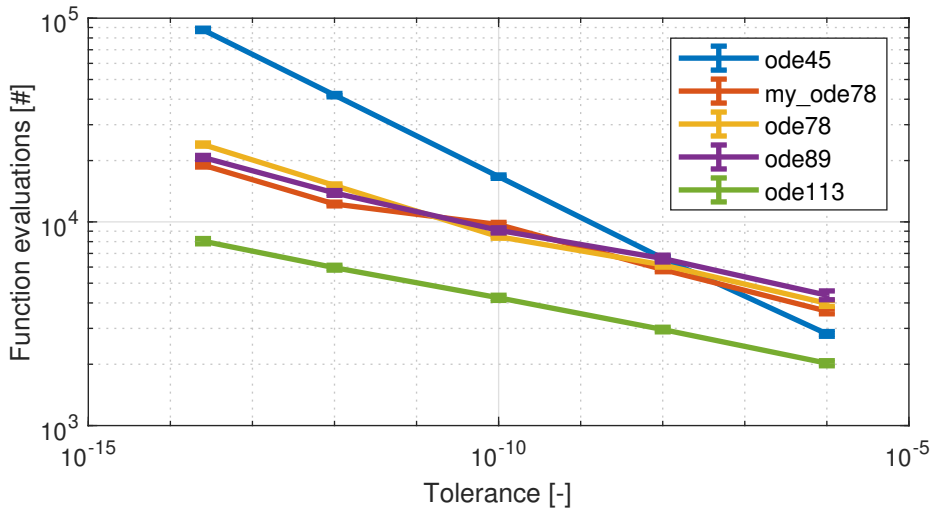


Figure A.13: Function evaluations comparison.

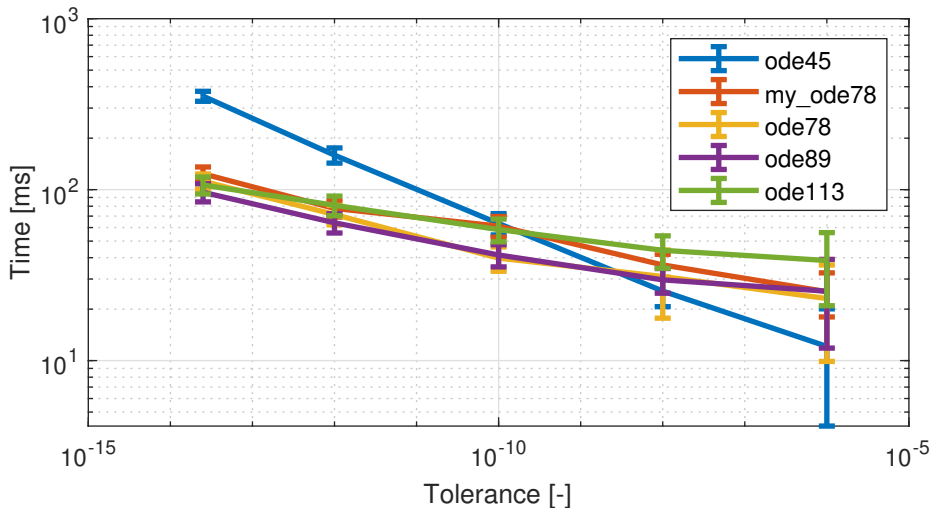


Figure A.14: Single call times comparison.

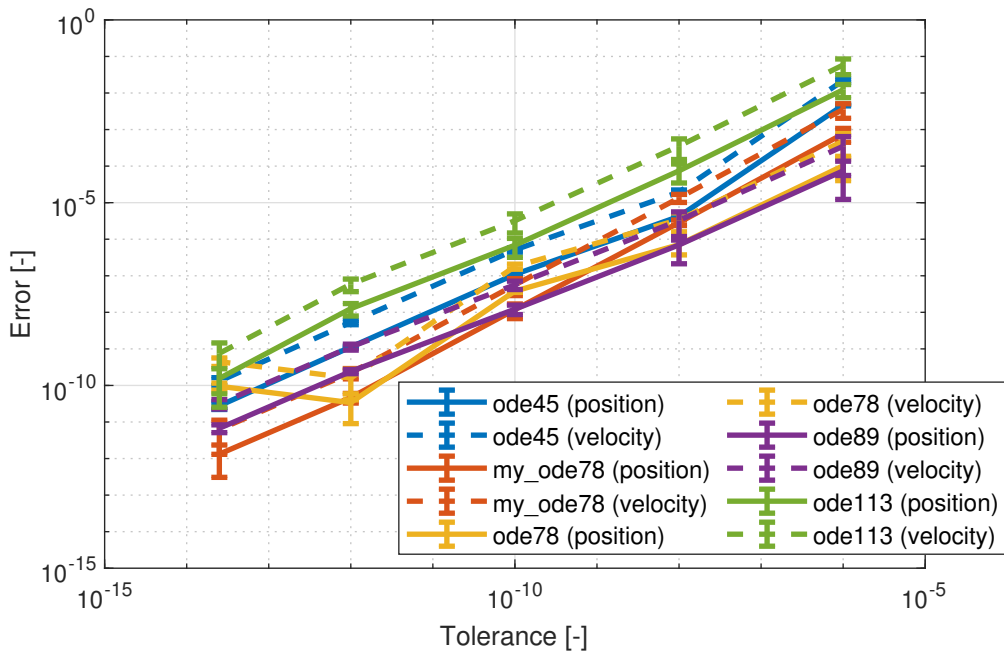


Figure A.15: Errors comparison. Position error (solid lines) and velocity error (dashed lines) in nondimensional quantities.

A.3 RHS V&V against GMAT

The goodness of the RHS is tested against the General Mission Analysis Tool (GMAT)⁴⁶ (release R2020a), which is an open source, platform independent, trajectory optimization and design system designed to model and optimize spacecraft trajectories in flight regimes ranging from low Earth orbit to lunar applications, interplanetary trajectories, and other deep space missions [127, 128]. General Mission Analysis Tool (GMAT) is developed by NASA and private industries.

A.3.1 Test plan definition

Ten ICs are propagated for 20 years both in GMAT and GRATIS. Then, errors on position and velocity are computed to compare the propagated trajectories. The initial epoch for the propagation is set to January 1, 2020 at 11:00:00.000 (UTC). The ICs Keplerian elements expressed in the J2000 frame centered at the Sun are collected in Table A.1. The ICs are generated randomly exploiting GMAT's random routine `rand` setting the seed to 1. The generated values are limited between lower and upper bounds. Bounds are collected in Table A.2.

GMAT comes with several embedded numerical integrator. According to the user guide⁴⁷, the **PrinceDormand78**⁴⁸ is the best all purpose integrator in GMAT. As a consequence, the **PrinceDormand78** is used for this test. The accuracy is set to 10^{-14} and the error control to **RSSStep**⁴⁹ mode.

⁴⁶<https://opensource.gsfc.nasa.gov/projects/GMAT/index.php> [last accessed Dec 1, 2022].

⁴⁷<http://gmat.sourceforge.net/docs/R2020a/html/index.html> [last accessed Dec 1, 2022].

⁴⁸An adaptive step, eighth order RK integrator with seventh order error control. Coefficients derived by Prince and Dormand [40]. It is the DOPRI8 implemented in GRATIS.

⁴⁹In GMAT, root sum square (RSS) relative error measured with respect to current step.

Table A.1: Ten ICs generated randomly exploiting GMAT's random routine `rand` setting the seed to 1. ICs expressed as Keplerian elements in the J2000 inertial frame centered at the Sun.

ID	Semi-major axis a_0 [km]	Eccentricity e_0 [-]	Inclination i_0 [deg]	RAAN Ω_0 [deg]	Argument of pericenter ω_0 [deg]	True anomaly θ_0 [deg]
1	$7.460\,942 \times 10^8$	$9.232\,318 \times 10^{-1}$	$2.306\,240 \times 10^1$	$3.596\,546 \times 10^2$	$8.499\,203 \times 10^1$	$1.427\,691 \times 10^2$
2	$7.045\,949 \times 10^8$	$8.378\,478 \times 10^{-1}$	$5.638\,923 \times 10^1$	$1.888\,373 \times 10^2$	$1.596\,430 \times 10^2$	$8.264\,780 \times 10^1$
3	$3.825\,848 \times 10^8$	$4.263\,916 \times 10^{-1}$	$1.690\,430 \times 10^2$	$2.802\,201 \times 10^2$	$2.577\,494 \times 10^2$	$2.889\,927 \times 10^2$
4	$6.571\,223 \times 10^8$	$8.208\,554 \times 10^{-1}$	$1.493\,286 \times 10^2$	$9.829\,799 \times 10^1$	$2.132\,755 \times 10^1$	$2.413\,901 \times 10^2$
5	$3.520\,106 \times 10^8$	$1.955\,754 \times 10^{-1}$	$5.213\,334 \times 10^1$	$5.116\,325 \times 10^1$	$2.819\,932 \times 10^2$	$1.485\,140 \times 10^2$
6	$5.195\,326 \times 10^8$	$2.955\,103 \times 10^{-1}$	$8.030\,421 \times 10^1$	$7.996\,484 \times 10^1$	$2.641\,110 \times 10^1$	$1.689\,259 \times 10^2$
7	$1.552\,388 \times 10^8$	$5.195\,514 \times 10^{-1}$	$1.505\,214 \times 10^1$	$3.300\,701 \times 10^2$	$3.277\,614 \times 10^2$	$1.076\,148 \times 10^2$
8	$4.880\,963 \times 10^8$	$9.469\,703 \times 10^{-1}$	$4.697\,622 \times 10^1$	$8.316\,555 \times 10^1$	$1.920\,415 \times 10^2$	$3.419\,777 \times 10^2$
9	$5.901\,162 \times 10^8$	$4.489\,227 \times 10^{-2}$	$2.519\,390 \times 10^1$	$2.852\,653 \times 10^2$	$1.072\,849 \times 10^1$	$3.179\,252 \times 10^2$
10	$6.753\,763 \times 10^8$	$3.738\,085 \times 10^{-1}$	$9.691\,645 \times 10^1$	$2.348\,276 \times 10^2$	$1.300\,540 \times 10^2$	$2.055\,631 \times 10^2$

Table A.2: Lower and upper bounds of ICs generated in GMAT.

Quantity	Symbol	Bounds	
		Lower	Upper
Semi-major axis	a_0 [AU]	0.5	5
Eccentricity	e_0 [-]	0	0.99
Inclination	i_0 [deg]	0	180
RAAN	Ω_0 [deg]	0	360
Argument of pericenter	ω_0 [deg]	0	360
True anomaly	θ_0 [deg]	0	360

The propagation is carried out having the Sun as central body and adding the third-body perturbations of the following: Mercury, Venus, Earth, Moon, Mars (B⁵⁰), Jupiter (B), Saturn (B), Uranus (B), Neptune (B), and Pluto (B). Moreover, also the contribution of the SRP and relativistic corrections (Schwarzschild solution, geodesic precession, and Lense-Thirring precession) are taken into account⁵¹. In GMAT, the SRP spherical area model is used. When using such model the user must provide the coefficient of reflectivity and the area needed to compute the SRP acceleration. Those were generated randomly with the GMAT's random routine `rand` setting the seed to 1. The parameters and the bounds used to generate them are collected in Tables A.3–A.4, respectively. For all ten cases, the spacecraft (or particle) mass is assumed 24 kg. After the numerical propagation, the ten trajectories are saved as SPICE's spacecraft ephemeris kernels (SPKs)⁵² [27, 28]. The plot in Figure A.16 shows the propagated trajectories in the J2000 inertial frame centered at the Sun.

According to the user guide, GMAT saves the spacecraft states from the first step after the initial epoch to the last step before the final epoch when writing spacecraft ephemeris as SPK. Therefore, in GRATIS, trajectories are propagated from January 1, 2020 at 12:00:00.000 (UTC), slightly after the previously defined initial epoch. The new ICs are retrieved with SPICE toolkit. ICs in Cartesian coordinates with respect to the Sun-centered J2000 frame are collected in Table A.5. To be consistent and perform a fair comparison, the propagation in GRATIS is performed with the Sun as central body and taking into account the same list of third-body perturbations used in GMAT. The SRP and relativistic corrections are taken into account as well. In GRATIS, the SRP model implemented is the *cannonball* or *spherical* model [129]. Regarding relativistic corrections, the Schwarzschild solution,

⁵⁰Here B stands for barycenter.

⁵¹In GMAT, this is done making a **ForceModel**, which is a model of the environmental forces and dynamics that affects the motion of a spacecraft. Numerous force models are supported. After them being configured, they are attached to the **Propagator** object using a **ForceModel** to numerically solve the orbital EoM, forward or backward in time.

⁵²SPICE is the information system developed by NAIF to assist NASA scientists and engineers in mission modeling, planning, interpreting scientific observations, and executing activities.

Table A.3: Spacecraft SRP parameters generated randomly exploiting GMAT's random routine `rand` setting the seed to 1.

ID	Reflectivity	SRP area
	C_r [-]	A_{SRP} [m ²]
1	1.387 911	6.730 486
2	1.534 414	9.148 224
3	1.092 801	5.229 710
4	1.593 066	6.749 376
5	1.034 171	6.277 897
6	1.096 172	9.043 365
7	1.584 389	5.702 529
8	1.493 060	5.451 945
9	1.540 788	4.535 004
10	1.637 836	1.350 517

Table A.4: Lower and upper bounds of SRP spacecraft parameters generated in GMAT.

Quantity	Symbol	Bounds	
		Lower	Upper
Reflectivity coefficient	C_r [-]	1	2
SRP area	A_{SRP} [m ²]	0.1	10

the geodesic precession, and the Lense-Thirring precession are considered [31]. The kernels embedded in GMAT (LSK, SPK, and PCK) are exported from GMAT and imported in GRATIS for consistency. Always for consistency, the same values of solar constant $G_{\text{sc}} = 1367 \text{ W m}^{-2}$ and astronomical unit $\text{AU} = 149597870.691 \text{ km}$ used by GMAT are temporary adopted in GRATIS. The numerical propagation is carried out with `my_ode78`. RelTol is set to 10^{-14} .

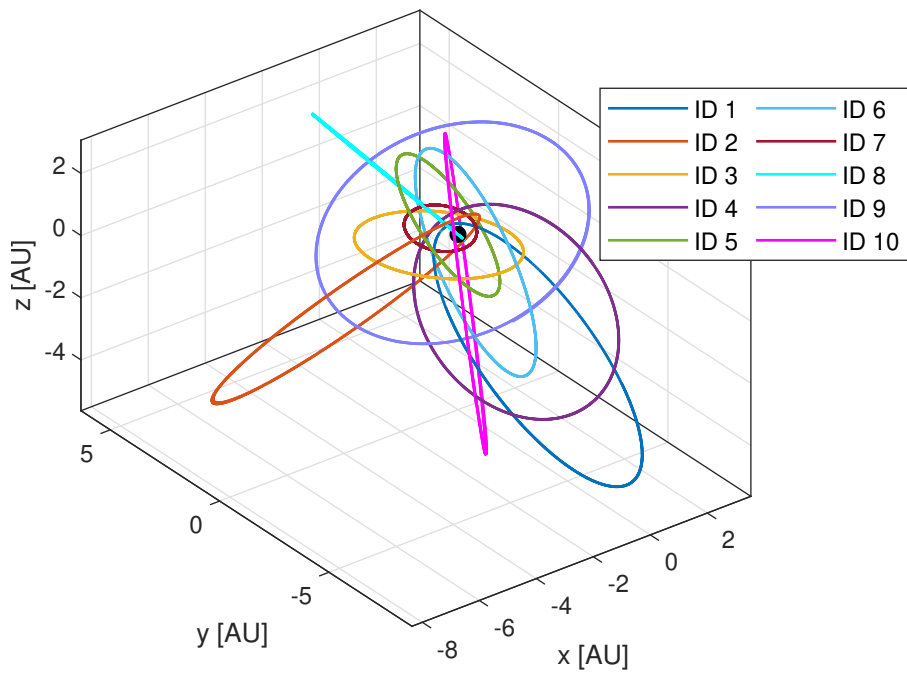


Figure A.16: The ten trajectories numerically propagated in GMAT. J2000 inertial frame centered at the Sun.

Table A.5: ICs numerically propagated in GRATIS. Cartesian coordinates in the J2000 inertial frame centered at the Sun.

ID	Position			Velocity		
	x_0 [km]	y_0 [km]	z_0 [km]	v_{x0} [km s ⁻¹]	v_{y0} [km s ⁻¹]	v_{z0} [km s ⁻¹]
1	$-2.812\,408 \times 10^8$	$-2.816\,169 \times 10^8$	$-1.206\,211 \times 10^8$	-6.337 448	-18.854 44	-8.043 600
2	$7.279\,361 \times 10^7$	$1.054\,357 \times 10^8$	$-1.399\,204 \times 10^8$	-17.431 16	14.894 80	-26.172 29
3	$-1.717\,034 \times 10^7$	$2.742\,466 \times 10^8$	$-6.149\,131 \times 10^6$	23.508 25	-6.942 320	-4.240 546
4	$-2.916\,564 \times 10^8$	$-8.771\,567 \times 10^7$	$-1.786\,731 \times 10^8$	11.021 89	19.043 77	8.098 486
5	$-9.815\,784 \times 10^7$	$2.530\,155 \times 10^8$	$3.023\,949 \times 10^8$	-12.872 11	-8.736 863	5.848 701
6	$-8.292\,633 \times 10^7$	$-6.393\,833 \times 10^8$	$-1.741\,599 \times 10^8$	2.329 370	1.849 327	-11.538 72
7	$9.208\,641 \times 10^7$	$9.207\,275 \times 10^7$	$3.381\,439 \times 10^7$	-9.085 801	31.586 02	6.142 329
8	$-4.767\,362 \times 10^6$	$-2.597\,080 \times 10^7$	$1.760\,367 \times 10^6$	67.468 74	-2.578 705	-72.106 29
9	$-1.306\,118 \times 10^8$	$-5.402\,236 \times 10^8$	$-1.261\,884 \times 10^8$	13.792 91	-4.199 088	5.739 615
10	$-4.243\,075 \times 10^8$	$-6.777\,568 \times 10^8$	$-3.592\,251 \times 10^8$	-2.099 945	-0.862 171 3	10.056 50

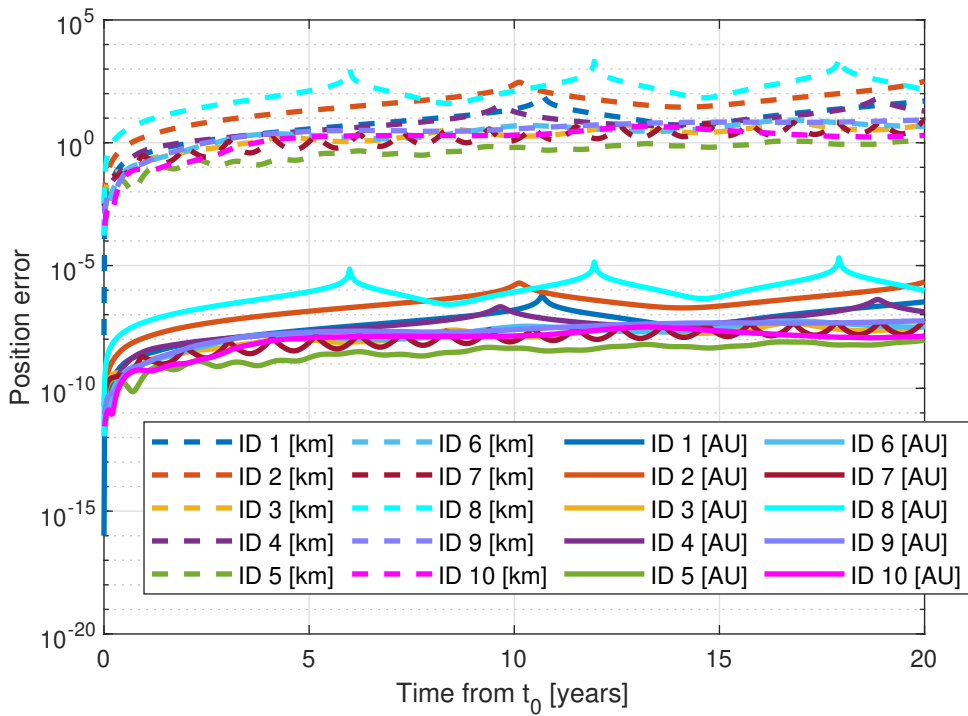


Figure A.17: Position error of GRATIS against GMAT. Units of measurement for y-axis shown in the legend.

A.3.2 Results and discussion

GRATIS and GMAT performances are evaluated in terms of their position and velocity errors. Errors are computed according to Eq. (A.1). The chart in Figure A.17 shows the error on the position while the velocity error is presented in Figure A.18. The maximum error of the whole propagation and the error at the final epoch are found in Table A.6.

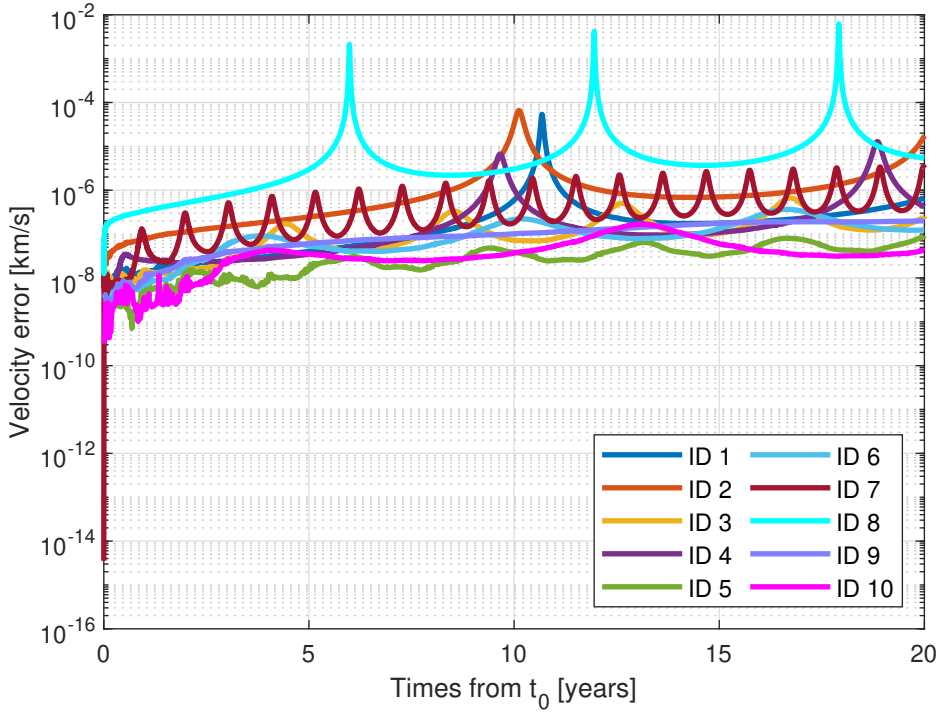


Figure A.18: Velocity error of GRATIS against GMAT.

Table A.6: Position and velocity errors of GRATIS against GMAT.

ID	Final errors		Maximum errors	
	$e_{\text{pos},f}$ [km]	$e_{\text{vel},f}$ [km s ⁻¹]	$e_{\text{pos},\text{max}}$ [km]	$e_{\text{vel},\text{max}}$ [km s ⁻¹]
1	4.982×10^1	6.544×10^{-7}	8.836×10^1	5.364×10^{-5}
2	3.224×10^2	1.748×10^{-5}	3.224×10^2	6.570×10^{-5}
3	5.337	2.512×10^{-7}	7.101	6.671×10^{-7}
4	1.947×10^1	4.167×10^{-7}	6.177×10^1	1.284×10^{-5}
5	1.351	9.083×10^{-8}	1.351	9.083×10^{-8}
6	4.688	1.245×10^{-7}	8.313	3.675×10^{-7}
7	7.421	3.234×10^{-6}	7.587	3.472×10^{-6}
8	1.417×10^2	5.484×10^{-6}	3.091×10^3	6.172×10^{-3}
9	8.465	2.013×10^{-7}	8.465	2.013×10^{-7}
10	2.019	4.184×10^{-8}	4.716	1.680×10^{-7}

Table A.7: IC of Siding Spring comet (C/2013 A1). Cartesian coordinates in the J2000 inertial frame centered at the Sun.

Initial condition at		
$t_0 = \text{January 1, 2014 at 12:00:00.000 (UTC)}$		
x_0	$2.325\,487 \times 10^8$	km
y_0	$4.662\,406 \times 10^8$	km
z_0	$-2.838\,604 \times 10^8$	km
v_{x0}	1.298 172	km s^{-1}
v_{y0}	$-2.101\,254 \times 10^1$	km s^{-1}
v_{z0}	2.144 944	km s^{-1}

A.4 Siding Spring comet (C/2013 A1) benchmark

C/2013 A1⁵³, or Siding Spring, is an Oort cloud hyperbolic comet. It was discovered on January 3, 2013. On October 19, 2014, it had a close encounter with Mars, passing at a distance of approximately 140 000 km. For this benchmark, the ephemeris of Siding Spring made available by the JPL is used as ground truth to assess GRATIS performance. The ephemeris of Siding Spring⁵⁴ (SPK file `siding_spring_s46.bsp`) has been retrieved from JPL's NAIF website.

A.4.1 Benchmark definition

Siding Spring trajectory is propagated both with GRATIS and GMAT. Then, resulting trajectories are compared each other and against the real ephemeris retrieved by NAIF website. The propagations are carried out from January 1, 2014 at 12:00:00.000 (UTC) to December 25, 2015 at 12:00:00.000 (UTC) (approximately 723 days). The following kernels are used for retrieving the IC and propagating it: `naif0012.tls`, `pck00010.tpc`, and `gm_de440.tpc`⁵⁵. The ephemerides of the planets and the Moon are already included within Siding Spring's SPK.

The IC expressed in Cartesian coordinates in the Sun-centered J2000 frame is presented in Table A.7. In GRATIS, the numerical propagation is carried out with `my_ode78` setting `RelTol` to 10^{-14} . On the other hand, in GMAT, the `PrinceDormand78` is used, with accuracy parameter set to 10^{-14} and error control mode set to `RSSStep`. For this benchmark, the kernels used in GRATIS are imported in GMAT for consistency.

⁵³<https://ssd.jpl.nasa.gov/sbdb.cgi?ID=dK13A010> [last accessed Dec 1, 2022].

⁵⁴Data available at: https://naif.jpl.nasa.gov/pub/naif/generic_kernels/spk/comets/siding_spring_s46.bsp [retrieved Dec 1, 2022].

⁵⁵Data available at: https://naif.jpl.nasa.gov/pub/naif/generic_kernels/lsk/naif0012.tls, and [~/generic_kernels/pck/pck00010.tpc](https://naif.jpl.nasa.gov/pub/naif/generic_kernels/pck/pck00010.tpc) [retrieved Dec 1, 2022]. The `gm_de440.tpc` PCK kernel consistent with the ephemerides DE440s is custom made, courtesy of Dr. C. Giordano. In fact, it is not released yet.

The propagation is performed having the Sun as central body and adding the third-body perturbations of the following: Mercury, Venus, Earth, Moon, Mars, Phobos, Deimos, Jupiter (B), Saturn (B), Uranus (B), Neptune (B), and Pluto (B). SRP acceleration and relativistic corrections (Schwarzschild solution, geodesic precession, and Lense-Thirring precession) are taken into account. To compute the reflectivity coefficient and area-to-mass ratio some assumptions are needed. The albedo of the comet is assumed $\varepsilon = 0.04$ (average between 0.02 and 0.06 [130]). Since it is estimated that Siding Spring has a radius between 400^{56} and 700 m^{57} , the radius is assumed 500 m (average value). Lastly, a density of 600 kg m^{-3} is assumed (average for comets) [131]. The reflectivity coefficient is computed as

$$C_r = 1 + \varepsilon \quad (\text{A.2})$$

therefore resulting equal to 1.04. Assuming a spherical shape, the area-to-mass ratio is computed as

$$\frac{A_{\text{SRP}}}{m} = \frac{3}{4R\rho} \quad (\text{A.3})$$

where R is the radius and ρ the density of the body, equal to $2.2727 \times 10^{-6} \text{ m kg}^{-2}$.

A.4.2 Results and discussion

The propagated trajectories and the one from HORIZONS System are compared in Figure A.19. In Figure A.20, the xy -plane is shown. In the plots, the unit of measure LU corresponds to 1 AU. To compare the results, the errors on position and velocity are computed according to Eq. (A.1). Results are shown in Figure A.21. The maximum errors and the errors at the final epoch are found in Table A.8. When compared to GMAT, GRATIS performs very well. On the other hand, errors are larger when both GMAT and GRATIS are compared to the Siding Spring ephemeris released by JPL. Very likely, that is because the RHS of JPL takes into account more perturbing contributions than the ones considered in this benchmark [30].

⁵⁶<https://www.uahirise.org/releases/siding-spring/> [last accessed Dec 1, 2022].

⁵⁷<https://www.nasa.gov/content/goddard/nasas-swift-satellite-tallies-water-production-of-mars-bound-comet> [last accessed Dec 1, 2022].

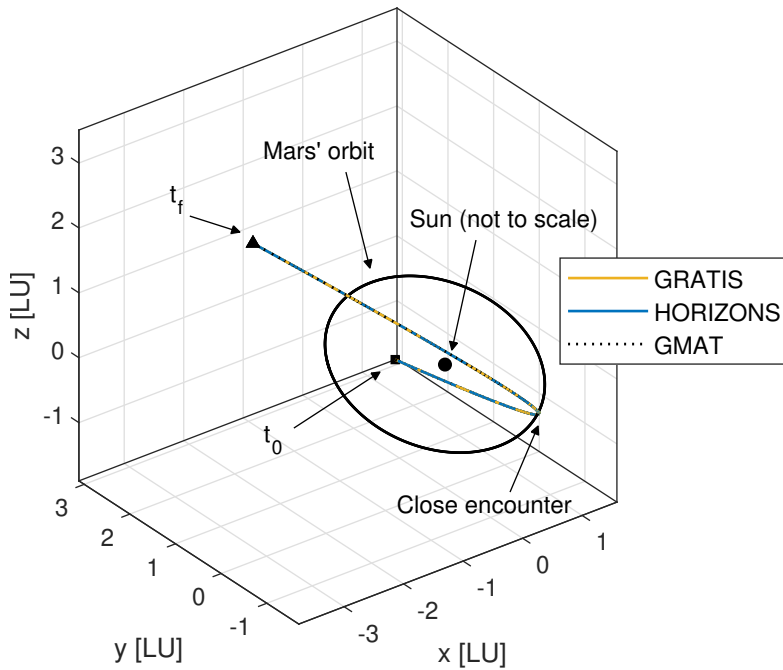


Figure A.19: Trajectory comparison for Siding Spring comet benchmark. J2000 inertial frame centered at the Sun. Here LU corresponds to 1 AU.

Table A.8: Position and velocity errors of Siding Spring comet benchmark.

Final errors		Maximum errors	
$e_{\text{pos},f}$ [km]	$e_{\text{vel},f}$ [km s ⁻¹]	$e_{\text{pos},\text{max}}$ [km]	$e_{\text{vel},\text{max}}$ [km s ⁻¹]
<i>GRATIS vs. GMAT:</i>			
2.839×10^{-1}	7.818×10^{-9}	2.839×10^{-1}	1.616×10^{-7}
<i>GRATIS vs. HORIZONS:</i>			
2.177	4.742×10^{-8}	2.177	9.179×10^{-8}
<i>GMAT vs. HORIZONS:</i>			
2.156	4.794×10^{-8}	2.156	2.631×10^{-7}

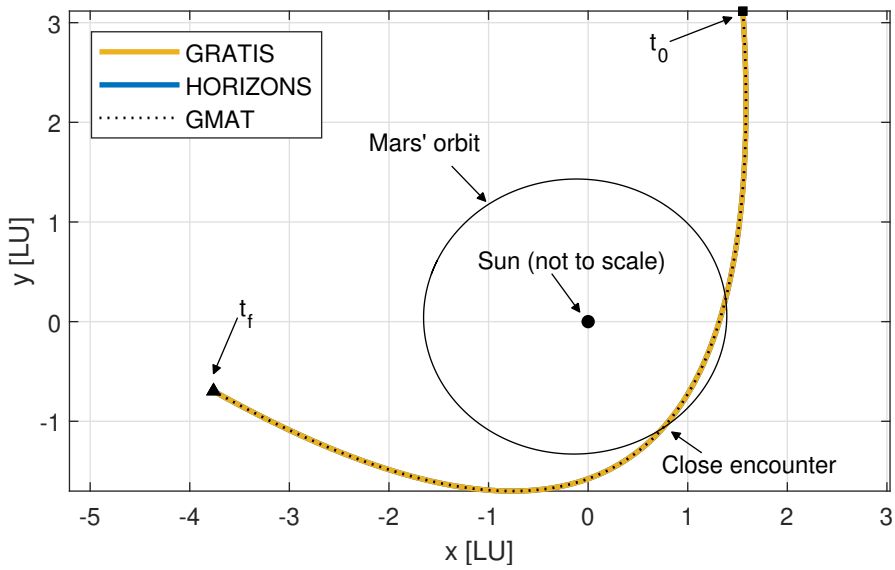


Figure A.20: Trajectory comparison for Siding Spring comet benchmark, xy -plane. J2000 inertial frame centered at the Earth. Here LU corresponds to 1 AU.

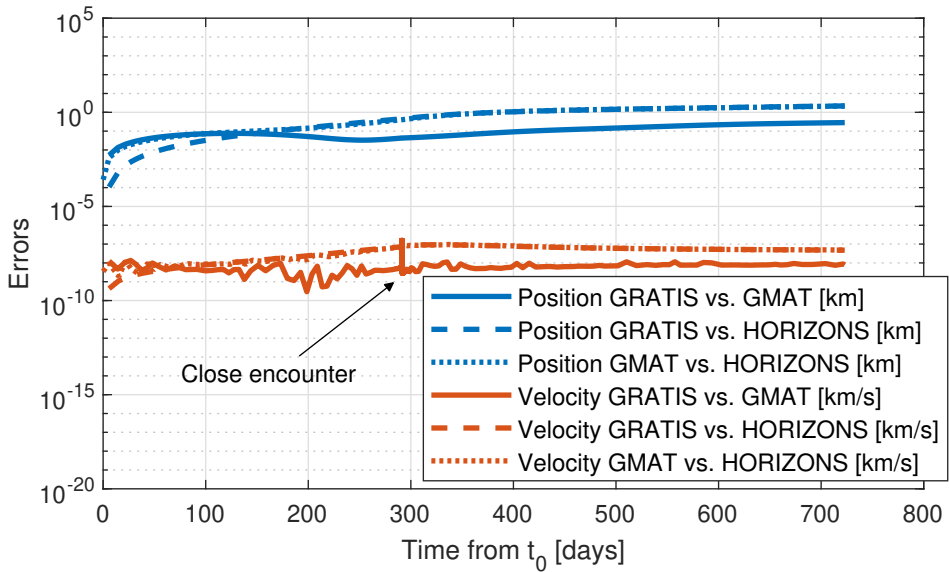


Figure A.21: Position and velocity errors for Siding Spring comet benchmark.

Table A.9: IC of 2006 RH₁₂₀. Cartesian coordinates in the J2000 inertial frame centered at the Earth.

Initial condition at $t_0 = \text{April 1, 2006 at 12:00:00.000 (UTC)}$		
x_0	$3.988\,125 \times 10^6$	km
y_0	$3.786\,330 \times 10^6$	km
z_0	$3.095\,485 \times 10^5$	km
v_{x0}	$-1.488\,339$	km s^{-1}
v_{y0}	$-3.621\,496 \times 10^{-1}$	km s^{-1}
v_{z0}	$-3.338\,711 \times 10^{-1}$	km s^{-1}

A.5 2006 RH₁₂₀ benchmark

2006 RH₁₂₀⁵⁸ (RH₁₂₀ for short) is a tiny near-Earth asteroid and fast rotator with a diameter of approximately 2-3 m [132]. Classified as an Apollo near-Earth object (NEO), it can be temporarily captured by Earth–Moon system while orbiting the Sun. That because of periodical close approaches with the Earth–Moon system. Indeed, it was in Earth orbit from September 2006 to June 2007. As a consequence of its temporary capture, its orbit is well-known. The ephemeris of RH₁₂₀ has been retrieved from JPL’s HORIZONS System⁵⁹ and used as ground truth.

A.5.1 Benchmark definition

The body trajectory is propagated both in GRATIS and GMAT and results are compared against the real ephemeris. The IC is set to April 1, 2006 at 12:00:00.000 (UTC) and propagated forward for 500 days. The same set of generic kernels used for the Siding spring benchmark is used (see Section A.4). The SPK `de440s.bsp`⁶⁰ is used for retrieving ephemerides of the major bodies [30].

The IC expressed in Cartesian coordinates in the Earth-centered J2000 frame is presented in Table A.9. The same integration schemes and tolerance settings of Section A.4 are used for this benchmark. The kernels employed in GRATIS are imported in GMAT for consistency.

This time, propagation is carried out having the Earth as central body and adding the third-body perturbations of the following: Sun, Mercury, Venus, Moon, Mars (B), Jupiter (B), Saturn (B), Uranus (B), Neptune (B), and Pluto (B). The contributions of SRP acceleration, NSG perturbation, and relativistic corrections (Schwarzschild solution, geodesic precession, and Lense-Thirring precession) are

⁵⁸<https://ssd.jpl.nasa.gov/sbdb.cgi?sstr=2006+RH120;orb=1> [last accessed Dec 1, 2022].

⁵⁹Data available at: <https://ssd.jpl.nasa.gov/?horizons> [retrieved Dec 1, 2022].

⁶⁰Data available at: https://naif.jpl.nasa.gov/pub/naif/generic_kernels/spk/planets/de440s.bsp [retrieved Dec 1, 2022].

Table A.10: Position and velocity errors of 2006 RH₁₂₀ benchmark.

Final errors		Maximum errors	
$e_{\text{pos},f}$ [km]	$e_{\text{vel},f}$ [km s ⁻¹]	$e_{\text{pos},\text{max}}$ [km]	$e_{\text{vel},\text{max}}$ [km s ⁻¹]
<i>GRATIS vs. GMAT:</i>			
3.321×10^{-1}	1.217×10^{-7}	3.764×10^{-1}	8.518×10^{-7}
<i>GRATIS vs. HORIZONS:</i>			
3.810×10^3	1.421×10^{-3}	4.811×10^3	1.084×10^{-2}
<i>GMAT vs. HORIZONS:</i>			
3.810×10^3	1.421×10^{-3}	4.811×10^3	1.084×10^{-2}

considered. The asteroid parameters needed to evaluate the SRP acceleration are computed with Eqs. (A.2) and (A.3) and assuming the following: albedo $\varepsilon = 0.18$ (most typical near-Earth asteroid (NEA) albedo for S-type asteroids [133, 134]), radius $R = 3.3\text{m}$ [134], and density $\rho = 2710\text{kg m}^{-3}$ (typical value for S-type asteroids [135]). Therefore, the reflectivity coefficient and area-to-mass ratio used for this benchmark are $C_r = 1.18$ and $A/m = 8.3864 \times 10^{-5}\text{ m}^2\text{ kg}^{-1}$, respectively. The terms of the infinite series modeling NSG are considered up to degree $n_{\text{deg}} = 4$ and order $n_{\text{ord}} = 4$. The coefficients to evaluate the NSG perturbation are retrieved from the EGM96 Earth's gravity field model. Data are publicly available in the file `egm1996_to360_tide_free_sha.tab`. They are archived in the Office of Geomatics's website⁶¹.

A.5.2 Results and discussion

The propagated trajectories are compared to the real ephemeris coming from the HORIZONS System. Figure A.22 shows a three-dimensional comparison of the trajectories in the J2000 inertial frame centered at the Earth, while Figure A.23 presents the same comparison from different points of view. In the plots, the unit of measure LU corresponds to Earth's radius. Position and velocity errors computed according to Eq. (A.1) are plotted in Figure A.24. The maximum errors and the errors at the final epoch are collected in Table A.10. Also in this benchmark, GRATIS performs very well when compared to GMAT. Differently, errors against the HORIZON System's ephemeris are larger.

⁶¹Data publicly available at: <https://earth-info.nga.mil/index.php?dir=wgs84&action=wgs84> [retrieved Dec 1, 2022].

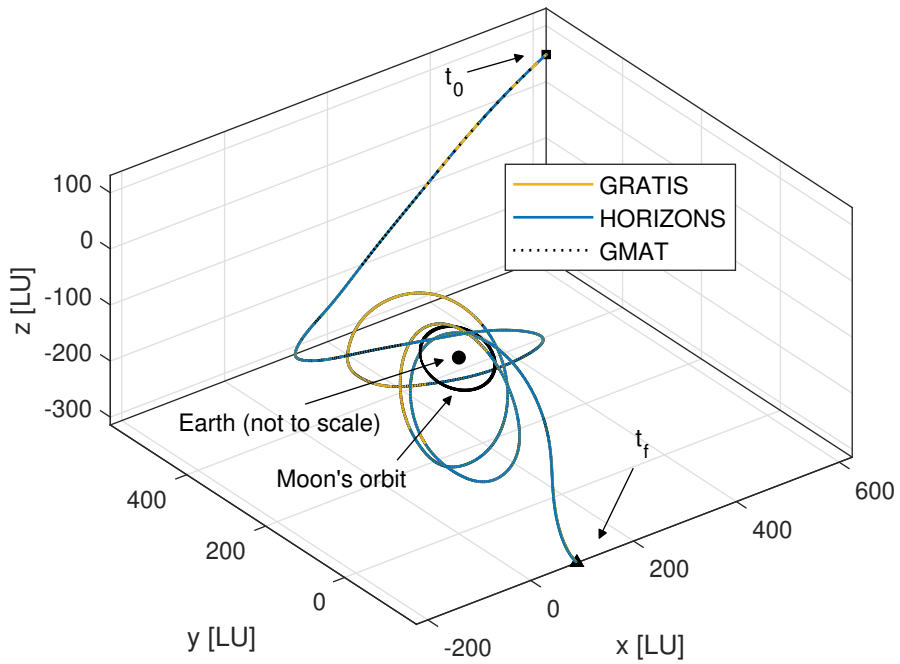


Figure A.22: Trajectory comparison for 2006 RH₁₂₀ benchmark. J2000 inertial frame centered at the Earth. Here LU corresponds to Earth's radius.

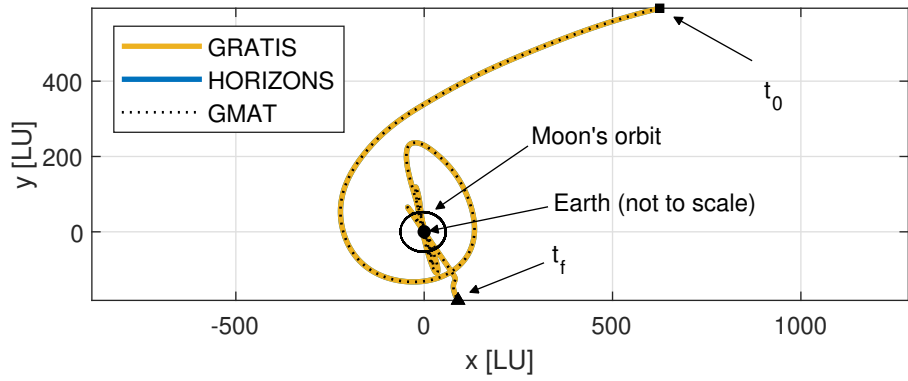
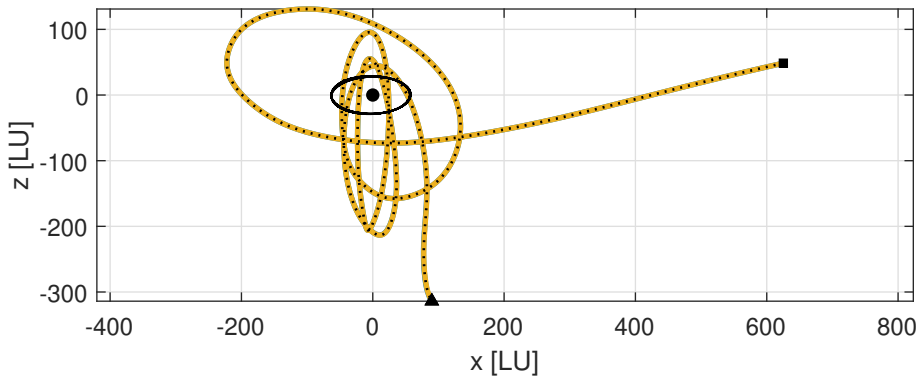
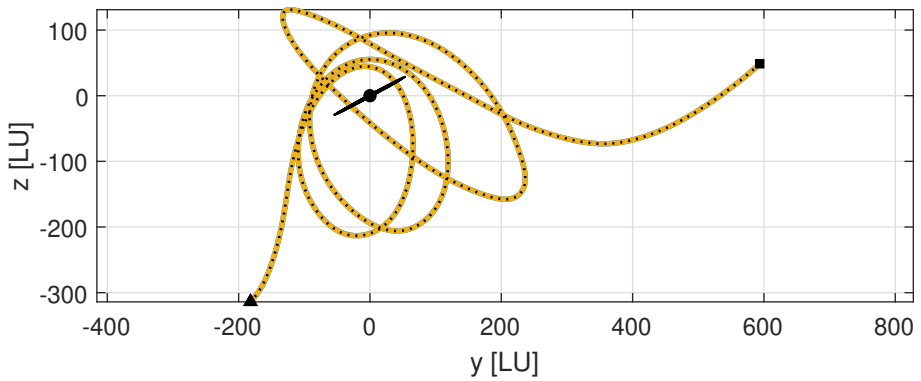
(a) xy -plane.(b) xz -plane.(c) yz -plane.

Figure A.23: Trajectory comparison for 2006 RH₁₂₀ benchmark. J2000 inertial frame centered at the Earth. Here LU corresponds to Earth's radius.

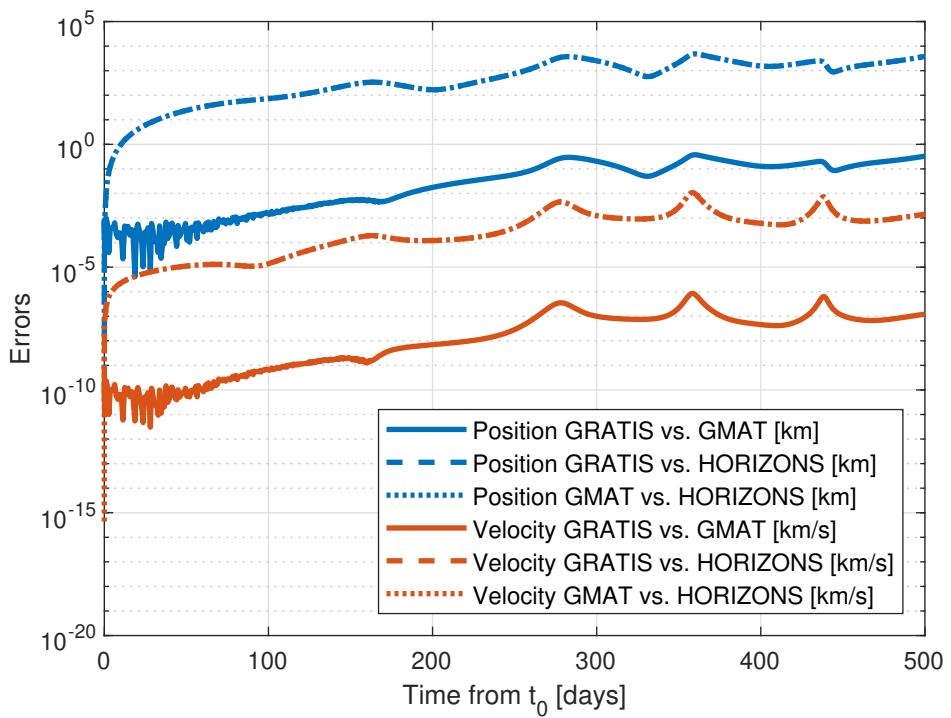


Figure A.24: Position and velocity errors for 2006 RH₁₂₀ benchmark.

Table A.11: IC of 2020 CD₃. Cartesian coordinates in the J2000 inertial frame centered at the Earth.

Initial condition at		
$t_0 = \text{September 18, 2017 at 10:31:22.261 (UTC)}$		
x_0	$8.276\,758 \times 10^4$	km
y_0	$8.144\,092 \times 10^4$	km
z_0	$-1.637\,116 \times 10^5$	km
v_{x0}	$5.829\,108 \times 10^{-1}$	km s^{-1}
v_{y0}	$-1.705\,912$	km s^{-1}
v_{z0}	$-5.538\,911 \times 10^{-1}$	km s^{-1}

A.6 2020 CD₃ benchmark

2020 CD₃⁶² (CD₃ for short) is a tiny near-Earth asteroid or minimoon [136]. Similarly to RH₁₂₀, it ordinarily orbits the Sun but periodically makes close approach to the Earth–Moon system. In those occasions, it can temporarily enter Earth orbit through ballistic capture. It is categorized as an Apollo object. Its ephemeris is retrieved from JPL’s HORIZONS System and used as reference for GRATIS performance evaluation.

A.6.1 Benchmark definition

As previously done, the first step is to propagate the trajectory both in GRATIS and GMAT. The second step is to compare the propagated trajectories to the ephemeris of the HORIZONS System. The epoch of the IC is selected to be September 18, 2017 at 10:31:22.261 (UTC), corresponding to the first Earth close encounter as shown in Figure A.25. The IC is propagated backward up to December 31, 2020 at 12:00:00.0000 (UTC) and forward up to January 1, 2017 at 12:00:00.0000 (UTC). The same set of generic kernels and major solar system bodies ephemerides (SPK kernels) used for RH₁₂₀ is employed for this benchmark.

The IC expressed in Cartesian coordinates in the Earth-centered J2000 frame is presented in Table A.11. The same integration schemes and tolerance settings of Section A.4 are used for this benchmark. Also in this case, the kernels used in GRATIS are imported in GMAT for consistency.

As done in Section A.5, propagation is carried out having the Earth as central body and adding the third-body perturbations of the following: Sun, Mercury, Venus, Moon, Mars (B), Jupiter (B), Saturn (B), Uranus (B), Neptune (B), and Pluto (B). The contributions of SRP acceleration, NSG perturbation, and relativistic corrections (Schwarzschild solution, geodesic precession, and Lense-Thirring precession) are considered. The minimoon parameters needed to evaluate the SRP acceleration

⁶²<https://ssd.jpl.nasa.gov/sbdb.cgi?sstr=54000953> [last accessed Dec 1, 2022].

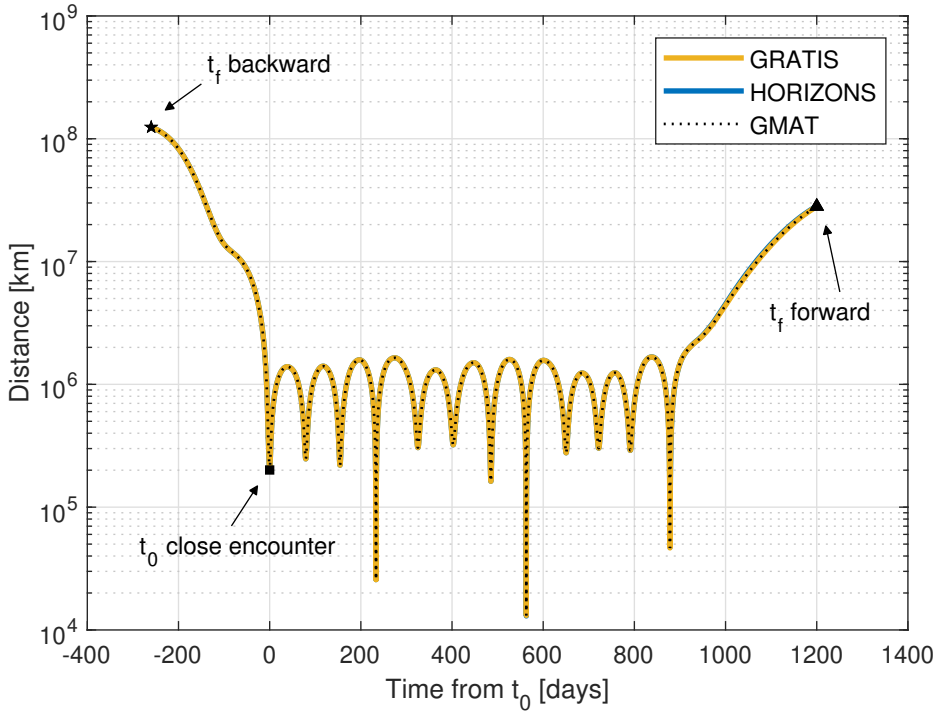


Figure A.25: 2020 CD₃ distance from Earth.

are computed with Eq. (A.2) and Eq. (A.3) and assuming the following [137]: albedo $\varepsilon = 0.35$, radius $R = 0.9$ m, and density $\rho = 2100 \text{ kg m}^{-3}$ [137]. Therefore, the reflectivity coefficient and area-to-mass ratio used for this benchmark resulted to be $C_r = 1.35$ and $A/m = 3.9683 \times 10^{-4} \text{ m}^2 \text{ kg}^{-1}$, respectively. The terms of the infinite series modeling NSG are considered up to degree $n_{\text{deg}} = 4$ and order $n_{\text{ord}} = 4$. The coefficients to evaluate the NSG perturbation are retrieved from the EGM96 Earth's gravity field model.

A.6.2 Results and discussion

The comparison between the two propagated trajectories and the HORIZONS System ephemeris in the three-dimensional space is shown in Figure A.26 while Figure A.27 provides the view of the xy -plane. The magnification of the temporary capture is provided in Figures A.28–A.29 where trajectories are represented in three-dimensional space and in the xy -plane, respectively. In the plots, the unit of measure LU corresponds to Earth's radius. Figure A.30 shows the position and velocity errors, while Table A.12 collects the maximum errors together with the errors at the final epochs of the forward and backward legs. The difference between the two propagated trajectories is small, confirming the goodness of GRATIS' RHS. Differently, differences are larger when the numerically propagated trajectories are compared to the ephemeris available in the HORIZONS System.

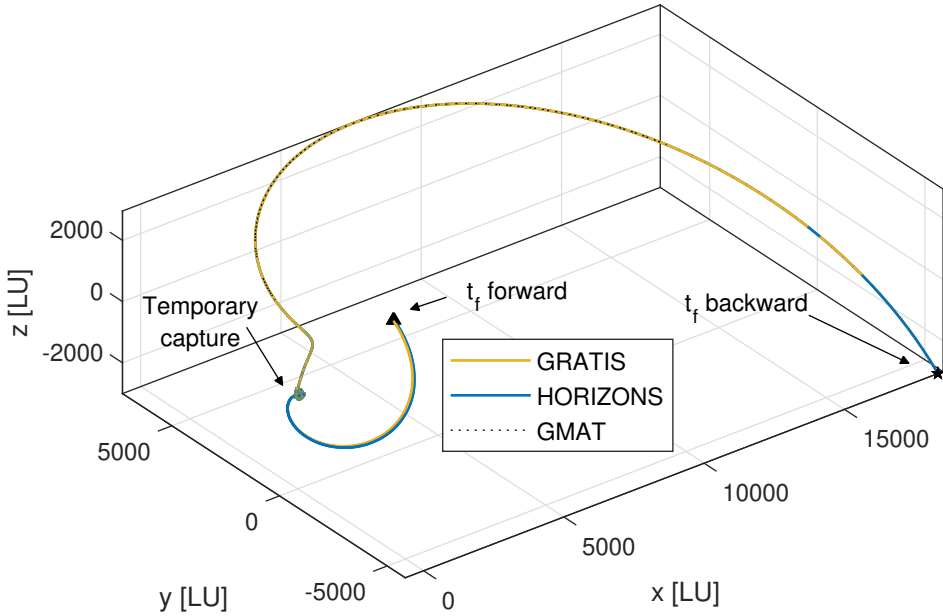


Figure A.26: Trajectory comparison for 2020 CD₃ benchmark. J2000 inertial frame centered at the Earth. Here LU corresponds to Earth's radius.

Table A.12: Position and velocity errors for 2020 CD₃ benchmark.

Final errors (backward)		Final errors (forward)		Maximum errors	
$e_{\text{pos},b}$ [km]	$e_{\text{vel},b}$ [km s ⁻¹]	$e_{\text{pos},f}$ [km]	$e_{\text{vel},f}$ [km s ⁻¹]	$e_{\text{pos},\text{max}}$ [km]	$e_{\text{vel},\text{max}}$ [km s ⁻¹]
<i>GRATIS vs. GMAT:</i>					
1.061×10^{-1}	1.766×10^{-8}	1.653×10^1	2.479×10^{-6}	2.101×10^1	1.721×10^{-4}
<i>GRATIS vs. HORIZONS:</i>					
4.500×10^2	8.066×10^{-5}	3.000×10^5	4.498×10^{-2}	3.897×10^5	2.532
<i>GMAT vs. HORIZONS:</i>					
4.498×10^2	8.066×10^{-5}	3.000×10^5	4.498×10^{-2}	3.898×10^5	2.532

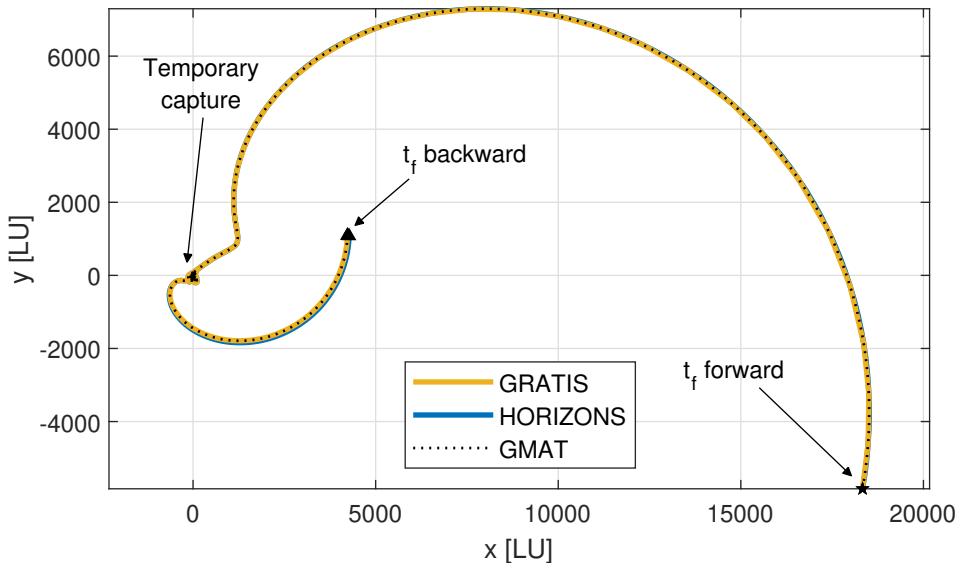


Figure A.27: Trajectory comparison for 2020 CD₃ benchmark, xy -plane. J2000 inertial frame centered at the Earth. Here LU corresponds to Earth's radius.

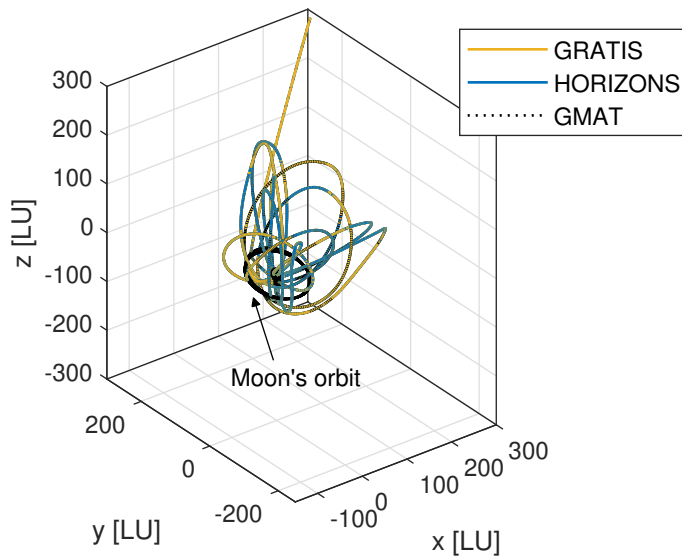


Figure A.28: Trajectory comparison for 2020 CD₃ benchmark, magnification. J2000 inertial frame centered at the Earth. Here LU corresponds to Earth's radius.

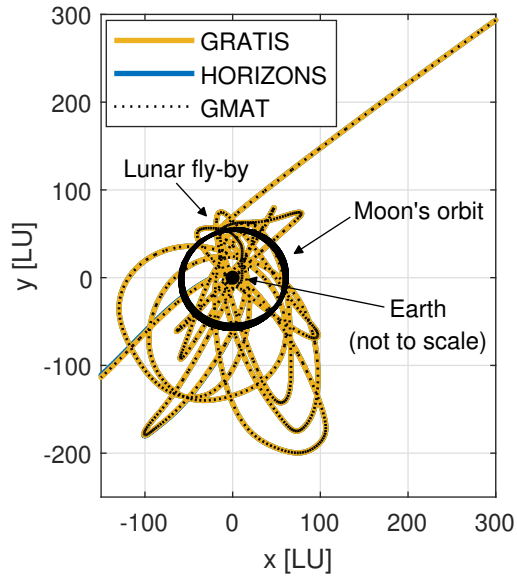


Figure A.29: Trajectory comparison for 2020 CD₃ benchmark, magnification xy -plane. J2000 inertial frame centered at the Earth. Here LU corresponds to Earth's radius.

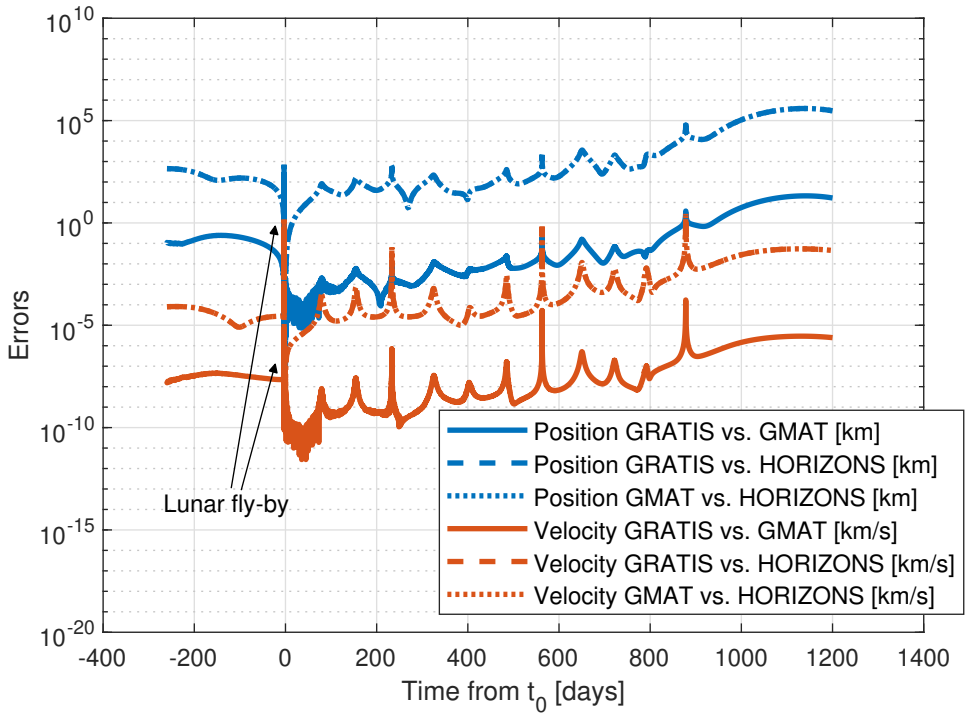


Figure A.30: Position and velocity errors for 2020 CD₃ benchmark.

A.7 V&V of stable sets extraction and manipulation

To assess the V&V of GRATIS in terms of stable sets extraction and manipulation some of the results published in [25] are reproduced. In [25], the authors presented three different case studies of capture: at Mercury, at Europa, and at the Earth. To numerically propagate the equation of motions, they used a 7th/8th order Runge–Kutta–Fehlberg⁶³ scheme with automatic step-size control and integration tolerance set to 10^{-12} [25]. The implemented DOPRI8 and the same tolerance are used to test GRATIS against the results reported in [25].

For consistency, the same kernels used by the authors are used to replicate the results. In particular, the JPL planetary ephemerides DE430 [138] are used to retrieve the precise states of the Sun, planets, and other bodies needed to compute the acceleration acting on the spacecraft (or particle). Ephemerides of the central body (or secondary), the primary, and the other perturbing bodies are publicly available⁶⁴. Regarding the generic kernels, based on the publishing date of the article, the following kernels are selected to be used in the V&V campaign: `naif0010.tls`, `pck00010.tpc`, and `gm_de431.tpc`⁶⁵.

A.7.1 Benchmark Sun–Mercury

For this benchmark the settings follow [25]: *i*) $t_0 = 2458891.70$ days, corresponding to February 12, 2020 at 04:48:00.000 (UTC); *ii*) $e_0 = 0.95$; *iii*) $i_0 = 45.04$ deg and $\Omega_0 = 202.50$ deg; *iv*) $r_{p0} \in [R + \epsilon, R_{SOI}]$ ($\epsilon = 1$ km) and $\omega_0 \in [0, 2\pi)$ uniformly discretized with 548 and 360 points, respectively; *v*) $n = 6$; *vi*) gravitational attractions of the Sun, Mercury, Venus, Jupiter (B), and Saturn (B). Note that, according to [25], ICs are expressed in the body mean equator of date frame (BME), a non-rotating frame frozen at the initial epoch and usually indicated as $BME@t_0$.

The plots in Figure A.31 replicates the results of Figures 6a and 6d of [25]. The number of points belonging to \mathcal{W}_1 , \mathcal{W}_{-1} , \mathcal{W}_6 , and \mathcal{C}_{-1}^6 is 25 596, 19 529, 2807, and 994, respectively (while it was 25 534, 19 686, 2801, and 986 in [25]). The curves in Figure A.32 are the reproduction of Figures 7a and 7b. Results of Figure A.32 are reproduced using the same ICs of Table 4 in [25]. The plots of Figure A.32 are slightly different compared to the ones in [25]. On the other hand, the charts in Figure A.33, showing the distance and the Keplerian energy of the solution characterized by the minimum stability index S_{\min} (more recently also

⁶³The scheme is the same explicit embedded RK of order 8th and step-size control with order 7th, performing 13 functions evaluations currently implemented in GRATIS.

⁶⁴Data available at: https://naif.jpl.nasa.gov/pub/naif/generic_kernels/spk/planets/de430.bsp, [~/spk/satellites/a_old_versions/jup310.bsp](https://naif.jpl.nasa.gov/pub/naif/generic_kernels/spk/satellites/a_old_versions/jup310.bsp), [~/spk/satellites/a_old_versions/sat360.bsp](https://naif.jpl.nasa.gov/pub/naif/generic_kernels/spk/satellites/a_old_versions/sat360.bsp), [~/spk/satellites/ura111.bsp](https://naif.jpl.nasa.gov/pub/naif/generic_kernels/spk/satellites/ura111.bsp), [~/spk/satellites/a_old_versions/nep081.bsp](https://naif.jpl.nasa.gov/pub/naif/generic_kernels/spk/satellites/a_old_versions/nep081.bsp), and [~/spk/satellites/a_old_versions/plu043.bsp](https://naif.jpl.nasa.gov/pub/naif/generic_kernels/spk/satellites/a_old_versions/plu043.bsp) [retrieved Dec 1, 2022].

⁶⁵Data available at: https://naif.jpl.nasa.gov/pub/naif/generic_kernels/lsk/a_old_versions/naif0010.tls, [~/generic_kernels/pck/pck00010.tpc](https://naif.jpl.nasa.gov/pub/naif/generic_kernels/pck/pck00010.tpc), and [~/generic_kernels/pck/gm_de431.tpc](https://naif.jpl.nasa.gov/pub/naif/generic_kernels/pck/gm_de431.tpc) [retrieved Dec 1, 2022].

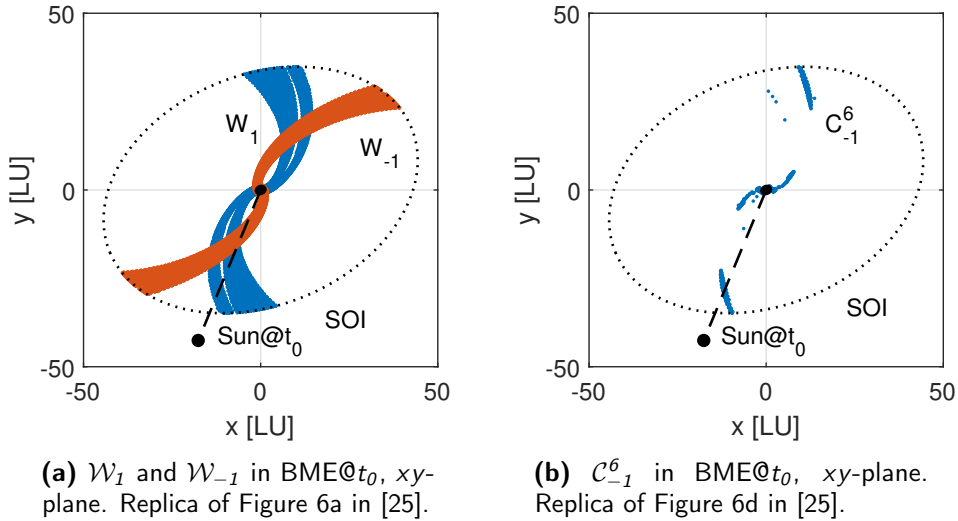


Figure A.31: Stable and capture sets at Mercury. Replicas of results in [25]. Here LU corresponds to Mercury's radius.

called regularity index [54]), are very similar. Very likely, since the phenomenon under analysis is chaotic and therefore very sensitive to small variation in the ICs, it could be possible that running analysis on a different machine resulted in slightly different output. However, the solution obtained with the implemented `my_ode78` and characterized by the minimum regularity index behaves very similarly to the one discussed in [25]. In conclusion, it seems that the current version of GRATIS correctly reproduced the results for the capture at Mercury case study in [25].

A.7.2 Benchmark Jupiter–Europa

For this benchmark the settings follow [25]: *i*) $t_0 = 2458852.19$ days, corresponding to January 3, 2020 at 16:33:35.999 (UTC); *ii*) $e_0 = 0.95$; *iii*) $i_0 = 45.00$ deg and $\Omega_0 = 233.82$ deg; *iv*) $r_{p0} \in [R + \epsilon, R_{\text{SOI}}]$ ($\epsilon = 1$ km) and $\omega_0 \in [0, 2\pi)$ uniformly discretized with 408 and 360 points, respectively; *v*) $n = 6$; *vi*) gravitational attractions of the Sun, Jupiter, Saturn (B), Io, Ganymede, Callisto, and Europa. ICs are expressed in the BME.

The plots in Figure A.34 replicates the results of Figures 9a and 9b of [25]. This time the number of points belonging to \mathcal{W}_1 , \mathcal{W}_{-1} , \mathcal{W}_6 , and \mathcal{C}_{-1}^6 is 5594, 5342, 190, and 174, respectively (differently, it was 5601, 5410, 190 and 173 in the original work). Curves in Figure A.35 reproduce Figures 11a and 11b. Also in this case, the plots of Figure A.32 are reproduced using the same ICs of Table 4 from [25]. Figure A.36 represents the Keplerian energy and the distance of the IC characterized by the minimum regularity index. Charts in Figures A.35–A.36 do not show the approaching leg, which is instead present in the originals. After visual comparison, it looks like that GRATIS correctly reproduced the results of the

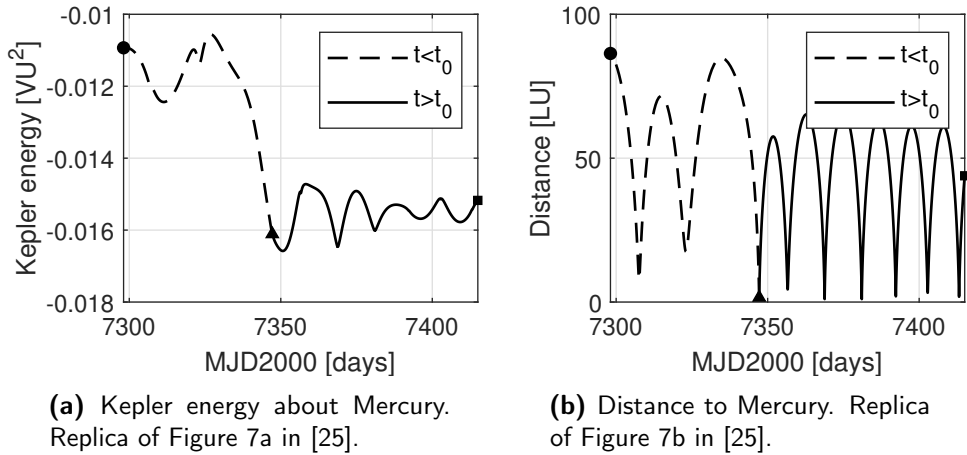


Figure A.32: Kepler energy and distance profiles of the sample solution at Mercury from Table 4 of [25] (backward integration dashed, forward integration solid). Replicas of results in [25]. Here LU corresponds to Mercury's radius while VU is the velocity on the circular orbit about Mercury having radius equal to LU.

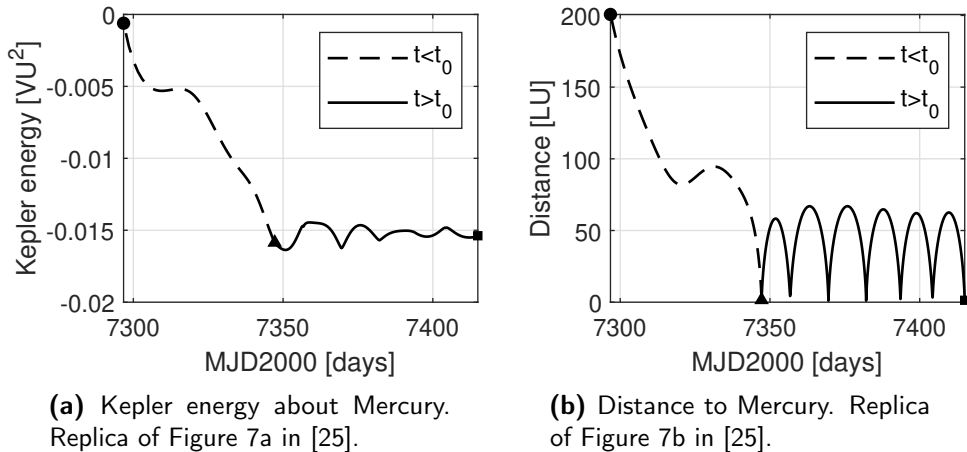


Figure A.33: Kepler energy and distance profiles of the solution having IC characterized by minimum regularity index S_{\min} at Mercury (backward integration dashed, forward integration solid). Here LU corresponds to Mercury's radius while VU is the velocity on the circular orbit about Mercury having a radius equal to LU.

capture at Europa too. Indeed, as it happened for the first case study, the plots from Figure A.35 slightly differ from the originals but the ones in Figure A.36 are very similar.

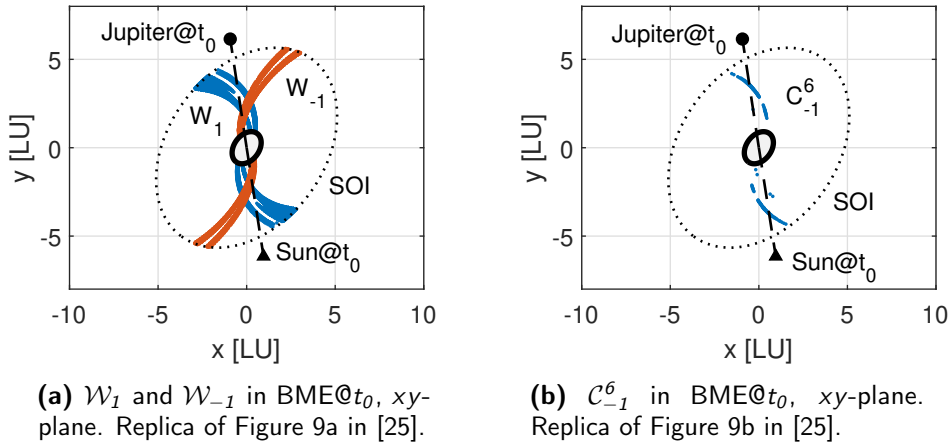


Figure A.34: Stable and capture sets at Europa. Replicas of results in [25]. Here LU corresponds to Europa's radius.

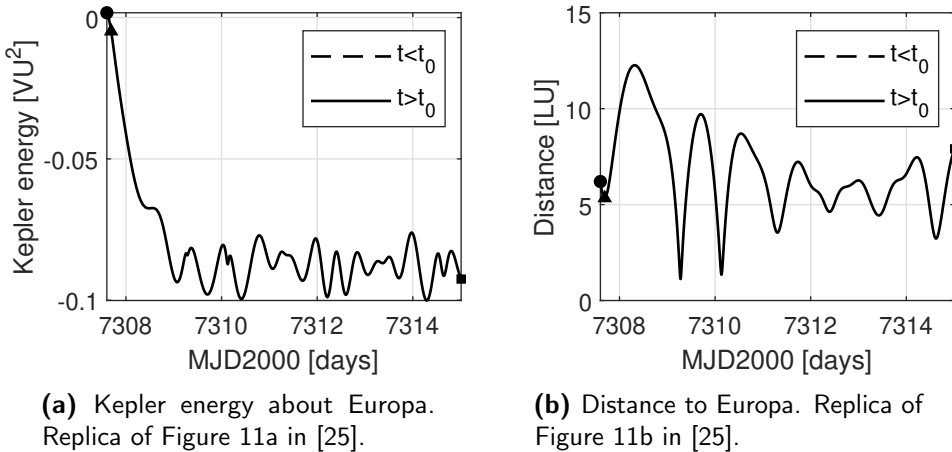


Figure A.35: Kepler energy and distance profiles of the sample solution at Europa from Table 4 of [25] (backward integration dashed, forward integration solid). Replicas of results in [25]. Here LU corresponds to Europa's radius while VU is the velocity on the circular orbit about Europa having radius equal to LU.

A.7.3 Benchmark Sun–Earth

For this benchmark the settings follow [25]: *i*) $t_0 = 2458888.82$ days, corresponding to February 9, 2020 at 07:40:47.999 (UTC); *ii*) $e_0 = 0.95$; *iii*) $i_0 = 45.89$ deg and $\Omega_0 = 272.54$ deg; *iv*) $r_{p0} \in [R + \epsilon, R_{SOI}]$ ($\epsilon = 1$ km) and $\omega_0 \in [0, 2\pi]$ uniformly discretized with 919 and 720 points, respectively; *v*) $n = 6$; *vi*) gravitational attractions of the Sun, the Earth, the Moon, Jupiter (B), and Saturn (B). ICs conditions are expressed in the BME.

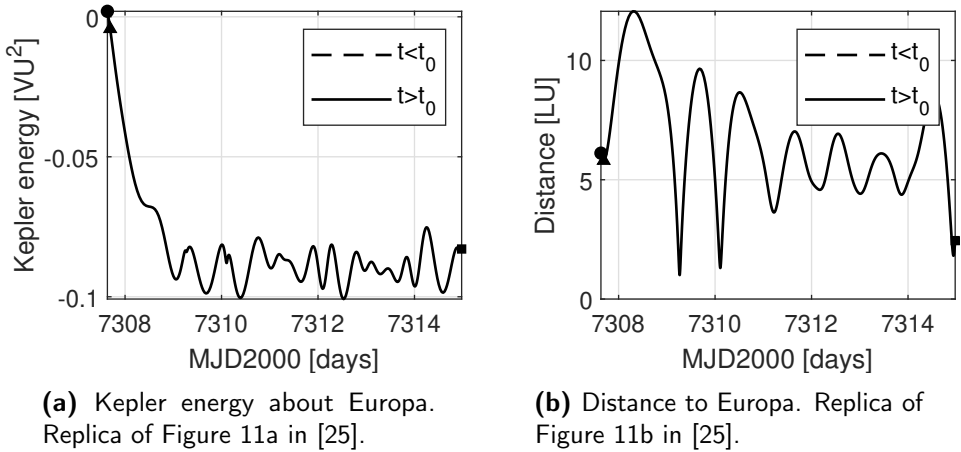
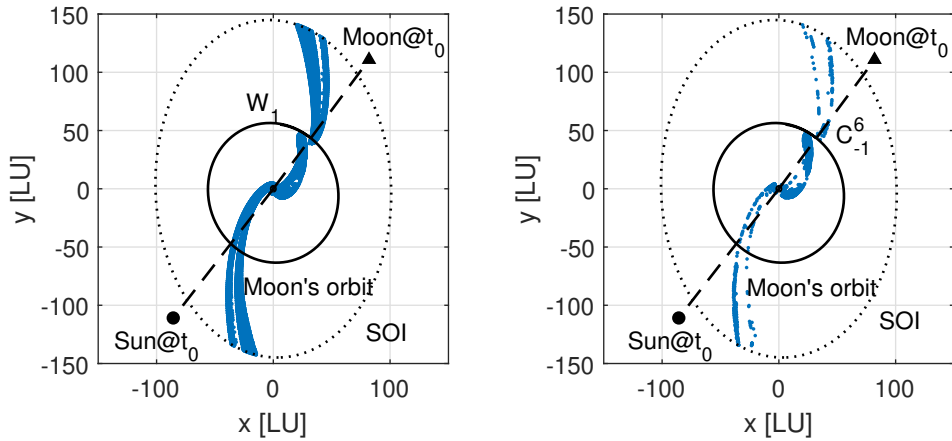


Figure A.36: Kepler energy and distance profiles of the solution having IC characterized by minimum regularity index S_{\min} at Europa (backward integration dashed, forward integration solid). Here LU corresponds to Europa's radius while VU is the velocity on the circular orbit about Europa having a radius equal to LU.

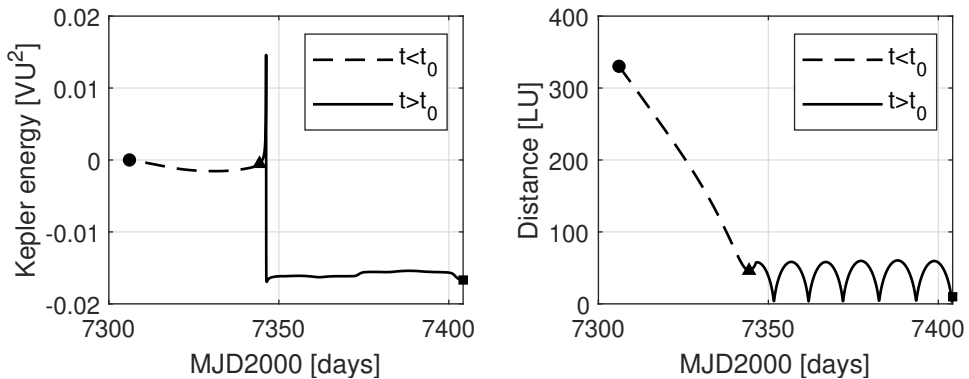
The plots in Figure A.37 replicate results of Figures 13a and 13b in [25]. To \mathcal{W}_1 , \mathcal{W}_{-1} , \mathcal{W}_6 , and \mathcal{C}_{-1}^6 belong 55 406, 56 835, 14 476, and 4472 points, respectively (instead, in [25], the points were 55 522, 56 770, 15 363, and 4498). The charts in Figure A.38 reproduce Figures 15a and 15c. The plots of Figure A.38 are reproduced using the same ICs collected in Table 4 targeting Earth. Figure A.39 shows the same quantities but for the solution characterized by the minimum regularity index when propagating with the implemented DOPRI8. This time, is the former that is more similar to the originals. Indeed, also if the solution with minimum regularity index has almost the same Keplerian energy and distance histories, some differences can be found. In particular in the peak value of the Keplerian energy just after the capture. All in all, GRATIS V&V campaign about extraction and manipulation of sets is considered successful as also this last case study is reproduced correctly.



(a) W_I and W_{-I} in $BME@t_0$, xy -plane. Replica of Figure 13a in [25].

(b) C_{-1}^6 in $BME@t_0$, xy -plane. Replica of Figure 13b in [25].

Figure A.37: Stable and capture sets at Earth. Replicas of results in [25]. Here LU corresponds to Earth's radius.



(a) Kepler energy about Earth. Replica of Figure 15a in [25].

(b) Distance to Earth. Replica of Figure 15c in [25].

Figure A.38: Kepler energy and distance profiles of the sample solution at Earth from Table 4 of [25] (backward integration dashed, forward integration solid). Replicas of results in [25]. Here LU corresponds to Earth's radius while VU is the velocity on the circular orbit about Earth having radius equal to LU.

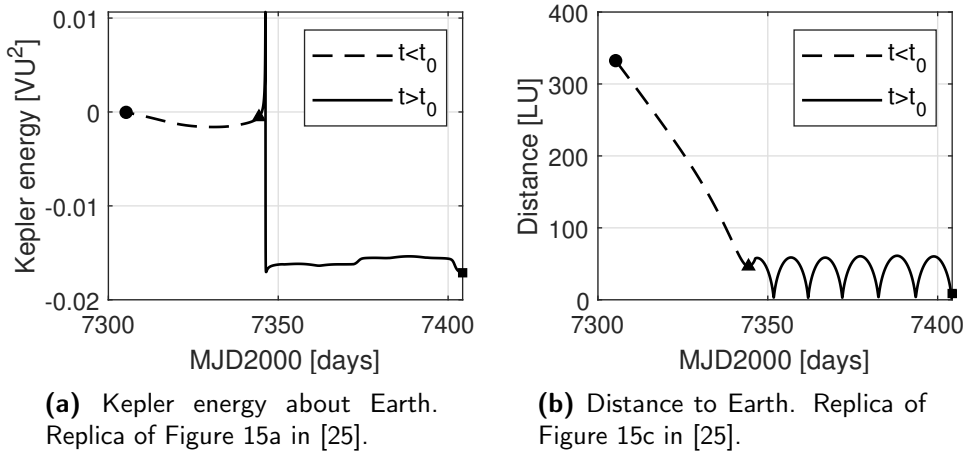


Figure A.39: Kepler energy and distance profiles of the solution having IC characterized by minimum regularity index S_{\min} at Earth (backward integration dashed, forward integration solid). Here LU corresponds to Earth's radius while VU is the velocity on the circular orbit about Earth having a radius equal to LU.

References

- [1] Poghosyan A and Golkar A. "CubeSat evolution: Analyzing CubeSat capabilities for conducting science missions". In: *Progress in Aerospace Sciences* 88 (2017), pp. 59–83. DOI: [10.1016/j.paerosci.2016.11.002](https://doi.org/10.1016/j.paerosci.2016.11.002).
- [2] Bandyopadhyay S, Foust R, Subramanian GP, Chung SJ, and Hadaegh FY. "Review of formation flying and constellation missions using nanosatellites". In: *Journal of Spacecraft and Rockets* 53.3 (2016), pp. 567–578. DOI: [10.2514/1.a33291](https://doi.org/10.2514/1.a33291).
- [3] Kalita H, Asphaug E, Schwartz S, and Thangavelautham J. "Network of nano-landers for in-situ characterization of asteroid impact studies". In: (2017). DOI: [10.48550/arXiv.1709.02885](https://doi.org/10.48550/arXiv.1709.02885).
- [4] Hein AM, Saidani M, and Tollu H. "Exploring potential environmental benefits of asteroid mining". In: *69th International Astronautical Congress 2018*. 2018.
- [5] Di Domenico G et al. "The ERC-funded EXTREMA project: Achieving self-driving interplanetary CubeSats". In: *Modeling and Optimization in Space Engineering — New Concepts and Approaches*. Accepted on March 31, 2022. In press. Springer.
- [6] Di Domenico G, Andreis E, Morelli AC, Merisio G, et al. "Toward self-driving interplanetary CubeSats: The ERC-funded project EXTREMA". In: *72nd International Astronautical Congress*. 2021.
- [7] Turan E, Speretta S, and Gill E. "Autonomous navigation for deep space small satellites: Scientific and technological advances". In: *Acta Astronautica* (2022). DOI: [10.1016/j.actaastro.2021.12.030](https://doi.org/10.1016/j.actaastro.2021.12.030).
- [8] Morselli A, Di Domenico G, Andreis E, Morelli AC, Merisio G, et al. "The EXTREMA orbital simulation hub: A facility for GNC testing of autonomous interplanetary CubeSat". In: *45 Symposium*. 2022, pp. 1–13.

- [9] Topputo F and Belbruno E. “Earth–Mars transfers with ballistic capture”. In: *Celestial Mechanics and Dynamical Astronomy* 121.4 (2015), pp. 329–346. DOI: [10.1007/s10569-015-9605-8](https://doi.org/10.1007/s10569-015-9605-8).
- [10] Aguiar G and Topputo F. “A technique for designing Earth–Mars low-thrust transfers culminating in ballistic capture”. In: *7th International Conference on Astrodynamics Tools and Techniques (ICATT)*. 2018, pp. 1–8.
- [11] Merisio G and Topputo F. “Characterization of ballistic capture corridors aiming at autonomous ballistic capture at Mars”. In: *2021 AAS/AIAA Astrodynamics Specialist Conference*. 2021, pp. 1–21.
- [12] Morelli AC, Merisio G, et al. “A convex guidance approach to target ballistic capture corridors at Mars”. In: *44th AAS Guidance, Navigation and Control Conference*. 2022, pp. 1–24.
- [13] Andreis E, Franzese V, and Topputo F. “Onboard orbit determination for deep-space CubeSats”. In: *Journal of guidance, control, and dynamics* (2022), pp. 1–14. DOI: [10.2514/1.G006294](https://doi.org/10.2514/1.G006294).
- [14] Andreis E, Panicucci P, Franzese V, and Topputo F. “A robust image processing pipeline for planets line-of-sight extraction for deep-space autonomous Cubesats navigation”. In: *44th AAS Guidance, Navigation and Control Conference*. 2022, pp. 1–19.
- [15] Andreis E, Franzese V, and Topputo F. “An overview of autonomous optical navigation for deep-space CubeSats”. In: *72nd International Astronautical Congress (IAC 2021)*. 2021, pp. 1–11.
- [16] Morelli AC, Hofmann C, and Topputo F. “Robust low-thrust trajectory optimization using convex programming and a homotopic approach”. In: *IEEE Transactions on Aerospace and Electronic Systems* (2021). DOI: [10.1109/TAES.2021.3128869](https://doi.org/10.1109/TAES.2021.3128869).
- [17] Morelli AC, Hofmann C, and Topputo F. “A homotopic approach for robust low-thrust trajectory design through convex optimization”. In: *72nd International Astronautical Congress (IAC 2021)*. 2021, pp. 1–11.
- [18] Topputo F and Belbruno E. “Computation of weak stability boundaries: Sun–Jupiter system”. In: *Celestial Mechanics and Dynamical Astronomy* 105.1-3 (2009), pp. 3–17. DOI: [10.1007/s10569-009-9222-5](https://doi.org/10.1007/s10569-009-9222-5).
- [19] Hyeraci N and Topputo F. “Method to design ballistic capture in the elliptic restricted three-body problem”. In: *Journal of guidance, control, and dynamics* 33.6 (2010), pp. 1814–1823. DOI: [10.2514/1.49263](https://doi.org/10.2514/1.49263).
- [20] Topputo F, Merisio G, et al. “Meteoroids detection with the LUMIO lunar CubeSat”. In: *Icarus* 389 (2023), p. 115213. DOI: [10.1016/j.icarus.2022.115213](https://doi.org/10.1016/j.icarus.2022.115213).

- [21] Cervone A et al. “Lumio: A CubeSat for observing and characterizing micro-meteoroid impacts on the lunar far side”. In: *Acta Astronautica* 195 (2022), pp. 309–317. DOI: [10.1016/j.actaastro.2022.03.032](https://doi.org/10.1016/j.actaastro.2022.03.032).
- [22] Merisio G and Topputo F. “Present-day model of lunar meteoroids and their impact flashes for LUMIO mission”. In: *Icarus* 389 (2023), p. 115180. DOI: [10.1016/j.icarus.2022.115180](https://doi.org/10.1016/j.icarus.2022.115180).
- [23] Suggs RM, Moser DE, Cooke WJ, and Suggs RJ. “The flux of kilogram-sized meteoroids from lunar impact monitoring”. In: *Icarus* 238. Supplement C (2014), pp. 23–36. DOI: [10.1016/j.icarus.2014.04.032](https://doi.org/10.1016/j.icarus.2014.04.032).
- [24] Bernardini N et al. “Exploiting coherent patterns for the analysis of qualitative motion and the design of bounded orbits around small bodies”. In: *73rd International Astronautical Congress (IAC 2022)* (Paris, France). 2022, pp. 1–16.
- [25] Luo Z-F, Topputo F, Bernelli Zazzera F, and Tang GJ. “Constructing ballistic capture orbits in the real Solar System model”. In: *Celestial Mechanics and Dynamical Astronomy* 120.4 (2014), pp. 433–450. DOI: [10.1007/s10569-014-9580-5](https://doi.org/10.1007/s10569-014-9580-5).
- [26] Archinal BA et al. “Report of the IAU working group on cartographic coordinates and rotational elements: 2009”. In: *Celestial Mechanics and Dynamical Astronomy* 109.2 (2011), pp. 101–135. DOI: [10.1007/s10569-010-9320-4](https://doi.org/10.1007/s10569-010-9320-4).
- [27] Acton C. “Ancillary data services of NASA’s navigation and ancillary information facility”. In: *Planetary and Space Science* 44.1 (1996), pp. 65–70. DOI: [10.1016/0032-0633\(95\)00107-7](https://doi.org/10.1016/0032-0633(95)00107-7).
- [28] Acton C, Bachman N, Semenov B, and Wright E. “A look towards the future in the handling of space science mission geometry”. In: *Planetary and Space Science* 150 (2018), pp. 9–12. DOI: [10.1016/j.pss.2017.02.013](https://doi.org/10.1016/j.pss.2017.02.013).
- [29] Gómez G, Jorba A, Masdemont J, and Simó C. “Study of the transfer from the Earth to a halo orbit around the equilibrium point L1”. In: *Celestial Mechanics and Dynamical Astronomy* 56.4 (1993), pp. 541–562. DOI: [10.1007/BF00696185](https://doi.org/10.1007/BF00696185).
- [30] Park RS, Folkner WM, Williams JG, and Boggs DH. “The JPL planetary and lunar ephemerides DE440 and DE441”. In: *The Astronomical Journal* 161.3 (2021), p. 105. DOI: [10.3847/1538-3881/abd414](https://doi.org/10.3847/1538-3881/abd414).
- [31] Huang C, Ries JC, Tapley BD, and Watkins MM. “Relativistic effects for near-Earth satellite orbit determination”. In: *Celestial Mechanics and Dynamical Astronomy* 48.2 (1990), pp. 167–185. DOI: [10.1007/BF00049512](https://doi.org/10.1007/BF00049512).
- [32] Topputo F et al. “Envelop of reachable asteroids by M-ARGO CubeSat”. In: *Advances in Space Research* 67.12 (2021), pp. 4193–4221. DOI: [10.1016/j.asr.2021.02.031](https://doi.org/10.1016/j.asr.2021.02.031).

- [33] Gottlieb RG. *Fast gravity, gravity partials, normalized gravity, gravity gradient torque and magnetic field: Derivation, code and data*. Tech. rep. 188243, prepared for Lyndon B. Johnson Space Center under contract NAS9-17885. 1993, pp. 1–62.
- [34] Milani A and Gronchi G. *Theory of orbit determination*. Cambridge University Press, 2010. DOI: [10.1017/cbo9781139175371.002](https://doi.org/10.1017/cbo9781139175371.002).
- [35] Montenbruck O and Gill E. *Satellite orbits models, methods and applications*. Springer, 2000. DOI: [10.1007/978-3-642-58351-3](https://doi.org/10.1007/978-3-642-58351-3).
- [36] Haller G. “A variational theory of hyperbolic Lagrangian coherent structures”. In: *Physica D: Nonlinear Phenomena* 240.7 (2011), pp. 574–598.
- [37] Meiss JD. *Differential dynamical systems*. SIAM, 2007. DOI: [10.1137/1.9780898718232](https://doi.org/10.1137/1.9780898718232).
- [38] Topputo F et al. “Trajectory design in high-fidelity models”. In: *7th International Conference on Astrodynamics Tools and Techniques (ICATT)*. 2018, pp. 1–9.
- [39] Shampine LF and Reichelt MW. “The MATLAB ode suite”. In: *SIAM journal on scientific computing* 18.1 (1997), pp. 1–22. DOI: [10.1137/s1064827594276424](https://doi.org/10.1137/s1064827594276424).
- [40] Prince PJ and Dormand JR. “High order embedded Runge–Kutta formulae”. In: *Journal of computational and applied mathematics* 7.1 (1981), pp. 67–75. DOI: [10.1016/0771-050x\(81\)90010-3](https://doi.org/10.1016/0771-050x(81)90010-3).
- [41] Belbruno E and Miller J. “Sun-perturbed Earth-to-Moon transfers with ballistic capture”. In: *Journal of Guidance, Control, and Dynamics* 16.4 (1993), pp. 770–775. DOI: [10.2514/3.21079](https://doi.org/10.2514/3.21079).
- [42] Belbruno E and Carrico J. “Calculation of weak stability boundary ballistic lunar transfer trajectories”. In: *Astrodynamics Specialist Conference*. 2000, p. 4142. DOI: [10.2514/6.2000-4142](https://doi.org/10.2514/6.2000-4142).
- [43] Circi C and Teofilatto P. “On the dynamics of weak stability boundary lunar transfers”. In: *Celestial Mechanics and Dynamical Astronomy* 79.1 (2001), pp. 41–72. DOI: [10.1023/A:1011153610564](https://doi.org/10.1023/A:1011153610564).
- [44] Ivashkin V. “On trajectories of Earth–Moon flight of a particle with its temporary capture by the Moon”. In: *Doklady Physics*. Vol. 47. Springer. 2002, pp. 825–827. DOI: [10.1134/1.1526433](https://doi.org/10.1134/1.1526433).
- [45] Belbruno E and Miller J. *A ballistic lunar capture trajectory for the Japanese spacecraft Hiten*. Tech. rep. IOM 312/904-1731-EAB. Jet Propulsion Laboratory, 1990, pp. 90–4.
- [46] Racca G et al. “SMART-1 mission description and development status”. In: *Planetary and space science* 50.14-15 (2002), pp. 1323–1337. DOI: [10.1016/S0032-0633\(02\)00123-X](https://doi.org/10.1016/S0032-0633(02)00123-X).

- [47] Chung M et al. "Trans-lunar cruise trajectory design of GRAIL (Gravity Recovery and Interior Laboratory) mission". In: *AIAA/AAS Astrodynamics Specialist Conference*. 2010, p. 8384. DOI: [10.2514/6.2010-8384](https://doi.org/10.2514/6.2010-8384).
- [48] Benkhoff J et al. "BepiColombo-mission overview and science goals". In: *Space Science Reviews* 217.8 (2021), pp. 1–56. DOI: [10.1007/s11214-021-00861-4](https://doi.org/10.1007/s11214-021-00861-4).
- [49] Schuster A and Jehn R. "Influence of the Mercury gravity field on the orbit insertion strategy of BepiColombo". In: *Aerospace Science and Technology* 39 (2014), pp. 546–551. DOI: [10.1016/j.ast.2014.06.003](https://doi.org/10.1016/j.ast.2014.06.003).
- [50] Luo Z-F and Topputo F. "Analysis of ballistic capture in Sun–planet models". In: *Advances in Space Research* 56.6 (2015), pp. 1030–1041. DOI: [10.1016/j.asr.2015.05.042](https://doi.org/10.1016/j.asr.2015.05.042).
- [51] Luo Z-F and Topputo F. "Mars orbit insertion via ballistic capture and aerobraking". In: *Astrodynamics* 5.2 (2021), pp. 167–181. DOI: [10.1007/s42064-020-0095-4](https://doi.org/10.1007/s42064-020-0095-4).
- [52] Giordano C and Topputo F. "Aeroballistic capture at Mars: Modeling, optimization, and assessment". In: *Journal of Spacecraft and Rockets* (2022), pp. 1–15. DOI: [10.2514/1.A35176](https://doi.org/10.2514/1.A35176).
- [53] Luo Z-F and Topputo F. "Capability of satellite-aided ballistic capture". In: *Communications in Nonlinear Science and Numerical Simulation* 48 (2017), pp. 211–223. DOI: [10.1016/j.cnsns.2016.12.021](https://doi.org/10.1016/j.cnsns.2016.12.021).
- [54] Dei Tos DA, Russell RP, and Topputo F. "Survey of Mars ballistic capture trajectories using periodic orbits as generating mechanisms". In: *Journal of Guidance, Control, and Dynamics* 41.6 (2018), pp. 1227–1242. DOI: [10.2514/1.g003158](https://doi.org/10.2514/1.g003158).
- [55] Belbruno E. "Lunar capture orbits, a method of constructing Earth Moon trajectories and the lunar GAS mission". In: *19th International Electric Propulsion Conference*. American Institute of Aeronautics and Astronautics, 1987, pp. 1–9. DOI: [10.2514/6.1987-1054](https://doi.org/10.2514/6.1987-1054).
- [56] Belbruno E. *Capture dynamics and chaotic motions in celestial mechanics*. Princeton University Press, 2004, pp. 1–211. DOI: [10.1515/9780691186436](https://doi.org/10.1515/9780691186436).
- [57] García F and Gómez G. "A note on weak stability boundaries". In: *Celestial Mechanics and Dynamical Astronomy* 97.2 (2007), pp. 87–100. DOI: [10.1007/s10569-006-9053-6](https://doi.org/10.1007/s10569-006-9053-6).
- [58] Sousa Silva P and Terra M. "Applicability and dynamical characterization of the associated sets of the algorithmic weak stability boundary in the lunar sphere of influence". In: *Celestial Mechanics and Dynamical Astronomy* 113.2 (2012), pp. 141–168. DOI: [10.1007/s10569-012-9409-z](https://doi.org/10.1007/s10569-012-9409-z).

- [59] Topputo F, Belbruno E, and Gidea M. “Resonant motion, ballistic escape, and their applications in astrodynamics”. In: *Advances in Space Research* 42.8 (2008), pp. 1318–1329. DOI: [10.1016/j.asr.2008.01.017](https://doi.org/10.1016/j.asr.2008.01.017).
- [60] Belbruno E, Topputo F, and Gidea M. “Resonance transitions associated to weak capture in the restricted three-body problem”. In: *Advances in Space Research* 42.8 (2008), pp. 1330–1351. DOI: [10.1016/j.asr.2008.01.018](https://doi.org/10.1016/j.asr.2008.01.018).
- [61] Belbruno E and Green J. “When leaving the Solar system: Dark matter makes a difference”. In: *Monthly Notices of the Royal Astronomical Society* 510.4 (2022), pp. 5154–5163. DOI: [10.1093/mnras/stab3781](https://doi.org/10.1093/mnras/stab3781).
- [62] Belbruno E, Gidea M, and Topputo F. “Weak stability boundary and invariant manifolds”. In: *SIAM Journal on Applied Dynamical Systems* 9.3 (2010), pp. 1061–1089. DOI: [10.1137/090780638](https://doi.org/10.1137/090780638).
- [63] Belbruno E, Gidea M, and Topputo F. “Geometry of weak stability boundaries”. In: *Qualitative Theory of Dynamical Systems* 12.1 (2013), pp. 53–66. DOI: [10.1007/s12346-012-0069-x](https://doi.org/10.1007/s12346-012-0069-x).
- [64] Belbruno E. “Relation between solutions of the Schrödinger equation with transitioning resonance solutions of the gravitational three-body problem”. In: *Journal of Physics Communications* 4.1 (2020), p. 015012. DOI: [10.1088/2399-6528/ab693f](https://doi.org/10.1088/2399-6528/ab693f).
- [65] Topputo F, Vasile M, and Bernelli-Zazzera F. “Low energy interplanetary transfers exploiting invariant manifolds of the restricted three-body problem”. In: *The Journal of the Astronautical Sciences* 53.4 (2005), pp. 353–372. DOI: [10.1007/BF03546358](https://doi.org/10.1007/BF03546358).
- [66] Haller G. “Lagrangian coherent structures”. In: *Annual Review of Fluid Mechanics* 47 (2015), pp. 137–162. DOI: [10.1146/annurev-fluid-010313-141322](https://doi.org/10.1146/annurev-fluid-010313-141322).
- [67] Wittig A et al. “Propagation of large uncertainty sets in orbital dynamics by automatic domain splitting”. In: *Celestial Mechanics and Dynamical Astronomy* 122.3 (2015), pp. 239–261. DOI: [10.1007/s10569-015-9618-3](https://doi.org/10.1007/s10569-015-9618-3).
- [68] Manzi M and Topputo F. “A flow-informed strategy for ballistic capture orbit generation”. In: *Celestial Mechanics and Dynamical Astronomy* 133.11 (2021), pp. 1–16. DOI: [10.1007/s10569-021-10048-2](https://doi.org/10.1007/s10569-021-10048-2).
- [69] Caleb T, Merisio G, Di Lizia P, and Topputo F. “Stable sets mapping with Taylor differential algebra with application to ballistic capture orbits around Mars”. In: *Celestial Mechanics and Dynamical Astronomy* 134.5 (2022), pp. 1–22. DOI: [10.1007/s10569-022-10090-8](https://doi.org/10.1007/s10569-022-10090-8).
- [70] Luo ZF. “The role of the mass ratio in ballistic capture”. In: *Monthly Notices of the Royal Astronomical Society* 498.1 (2020), pp. 1515–1529. DOI: [10.1093/mnras/staa2366](https://doi.org/10.1093/mnras/staa2366).

- [71] Shadden SC, Lekien F, and Marsden JE. “Definition and properties of Lagrangian coherent structures from finite-time Lyapunov exponents in two-dimensional aperiodic flows”. In: *Physica D: Nonlinear Phenomena* 212.3-4 (2005), pp. 271–304. DOI: [10.1016/j.physd.2005.10.007](https://doi.org/10.1016/j.physd.2005.10.007).
- [72] Gawlik ES, Marsden JE, Du Toit PC, and Campagnola S. “Lagrangian coherent structures in the planar elliptic restricted three-body problem”. In: *Celestial mechanics and dynamical astronomy* 103.3 (2009), pp. 227–249.
- [73] Short CR, Blazevski D, Howell KC, and Haller G. “Stretching in phase space and applications in general nonautonomous multi-body problems”. In: *Celestial Mechanics and Dynamical Astronomy* 122.3 (2015), pp. 213–238. DOI: [10.1007/s10569-015-9617-4](https://doi.org/10.1007/s10569-015-9617-4).
- [74] Pérez-Palau D, Masdemont JJ, and Gómez G. “Tools to detect structures in dynamical systems using jet transport”. In: *Celestial mechanics and dynamical astronomy* 123.3 (2015), pp. 239–262. DOI: [10.1007/s10569-015-9634-3](https://doi.org/10.1007/s10569-015-9634-3).
- [75] Sánchez-Martín P, Masdemont JJ, and Romero-Gómez M. “From manifolds to Lagrangian coherent structures in galactic bar models”. In: *Astronomy & Astrophysics* 618 (2018), A72. DOI: [10.1051/0004-6361/201833451](https://doi.org/10.1051/0004-6361/201833451).
- [76] Ferrari F and Alessi EM. “Dynamical transitions in the N-body granular problem to identify breakup limits of rubble-pile asteroids”. In: *European Planetary Science Congress. 2022*, EPSC2022–162. DOI: [10.5194/epsc2022-162](https://doi.org/10.5194/epsc2022-162).
- [77] Tyler J and Wittig A. “An improved numerical method for hyperbolic Lagrangian coherent structures using differential algebra”. In: *Journal of Computational Science* (2022), p. 101883. DOI: [10.1016/j.jocs.2022.101883](https://doi.org/10.1016/j.jocs.2022.101883).
- [78] Tyler J and Wittig A. “Three-dimensional Lagrangian coherent structures in the elliptic-restricted three-body problem”. In: *arXiv preprint arXiv:2209.11561* (2022). DOI: [10.48550/arXiv.2209.11561](https://doi.org/10.48550/arXiv.2209.11561).
- [79] Kelley DH, Allshouse MR, and Ouellette NT. “Lagrangian coherent structures separate dynamically distinct regions in fluid flows”. In: *Physical Review E* 88.1 (2013), p. 013017. DOI: [10.1103/PhysRevE.88.013017](https://doi.org/10.1103/PhysRevE.88.013017).
- [80] Laskar J. “Frequency analysis for multi-dimensional systems. Global dynamics and diffusion”. In: *Physica D: Nonlinear Phenomena* 67.1-3 (1993), pp. 257–281. DOI: [10.1016/0167-2789\(93\)90210-R](https://doi.org/10.1016/0167-2789(93)90210-R).
- [81] Laskar J. “Introduction to frequency map analysis”. In: *Hamiltonian systems with three or more degrees of freedom*. Springer, 1999, pp. 134–150. DOI: [10.1007/978-94-011-4673-9_13](https://doi.org/10.1007/978-94-011-4673-9_13).

- [82] Froeschlé C and Lega E. “On the measure of the structure around the last KAM torus before and after its break-up”. In: *Chaos in Gravitational N-Body Systems*. Springer, 1996, pp. 21–31. DOI: [10.1007/978-94-009-0307-4_2](https://doi.org/10.1007/978-94-009-0307-4_2).
- [83] Mancho AM, Wiggins S, Curbelo J, and Mendoza C. “Lagrangian descriptors: A method for revealing phase space structures of general time dependent dynamical systems”. In: *Communications in Nonlinear Science and Numerical Simulation* 18.12 (2013), pp. 3530–3557. DOI: [10.5194/npg-21-677-2014](https://doi.org/10.5194/npg-21-677-2014).
- [84] Benettin G, Galgani L, and Strelcyn J. “Kolmogorov entropy and numerical experiments”. In: *Physical Review A* 14.6 (1976), p. 2338. DOI: [10.1103/PhysRevA.14.2338](https://doi.org/10.1103/PhysRevA.14.2338).
- [85] Cincotta PM and Simó C. “Simple tools to study global dynamics in non-axisymmetric galactic potentials–i”. In: *Astronomy and Astrophysics Supplement Series* 147.2 (2000), pp. 205–228. DOI: [10.1051/aas:2000108](https://doi.org/10.1051/aas:2000108).
- [86] Froeschlé C, Lega E, and Gonczi R. “Fast Lyapunov indicators. Application to asteroidal motion”. In: *Celestial Mechanics and Dynamical Astronomy* 67.1 (1997), pp. 41–62. DOI: [10.1023/A:1008276418601](https://doi.org/10.1023/A:1008276418601).
- [87] Lega E and Froeschlé C. “Fast Lyapunov indicators comparison with other chaos indicators application to two and four dimensional maps”. In: *The Dynamical Behaviour of our Planetary System*. Springer, 1997, pp. 257–275. DOI: [10.1007/978-94-011-5510-6_18](https://doi.org/10.1007/978-94-011-5510-6_18).
- [88] Darriba LA, Maffione NP, Cincotta PM, and Giordano CM. “Comparative study of variational chaos indicators and ODEs’ numerical integrators”. In: *International Journal of Bifurcation and Chaos* 22.10 (2012), p. 1230033. DOI: [10.1142/S0218127412300339](https://doi.org/10.1142/S0218127412300339).
- [89] Hadjighasem A, Farazmand M, Blazeovski D, Froyland G, and Haller G. “A critical comparison of Lagrangian methods for coherent structure detection”. In: *Chaos: An Interdisciplinary Journal of Nonlinear Science* (2017). DOI: [10.1063/1.4982720](https://doi.org/10.1063/1.4982720).
- [90] Guzzo M and Lega E. “A study of the past dynamics of comet 67P/Churyumov-Gerasimenko with fast Lyapunov indicators”. In: *Astronomy & Astrophysics* 579 (2015), A79. DOI: [10.1051/0004-6361/201525878](https://doi.org/10.1051/0004-6361/201525878).
- [91] Guzzo M and Lega E. “Geometric chaos indicators and computations of the spherical hypertube manifolds of the spatial circular restricted three-body problem”. In: *Physica D: Nonlinear Phenomena* 373 (2018), pp. 38–58. DOI: [10.1016/j.physd.2018.02.003](https://doi.org/10.1016/j.physd.2018.02.003).

- [92] Farazmand M and Haller G. “Erratum and addendum to “A variational theory of hyperbolic Lagrangian coherent structures” [Physica D 240 (2011) 574–598]”. In: *Physica D: Nonlinear Phenomena* 241.4 (2012), pp. 439–441. DOI: [10.1016/j.physd.2011.09.013](https://doi.org/10.1016/j.physd.2011.09.013).
- [93] Lopesino C, Balibrea-Iñiesta F, García-Garrido VJ, Wiggins S, and Mancho AM. “A theoretical framework for Lagrangian descriptors”. In: *International Journal of Bifurcation and Chaos* 27.01 (2017), pp. 1730001, 1–25. DOI: [10.1142/S0218127417300014](https://doi.org/10.1142/S0218127417300014).
- [94] Haller G. “Distinguished material surfaces and coherent structures in three-dimensional fluid flows”. In: *Physica D: Nonlinear Phenomena* 149.4 (2001), pp. 248–277. DOI: [10.1016/S0167-2789\(00\)00199-8](https://doi.org/10.1016/S0167-2789(00)00199-8).
- [95] Haller G and Yuan G. “Lagrangian coherent structures and mixing in two-dimensional turbulence”. In: *Physica D: Nonlinear Phenomena* 147.3–4 (2000), pp. 352–370. DOI: [10.1016/S0167-2789\(00\)00142-1](https://doi.org/10.1016/S0167-2789(00)00142-1).
- [96] Farazmand M and Haller G. “Computing Lagrangian coherent structures from their variational theory”. In: *Chaos: An Interdisciplinary Journal of Nonlinear Science* 22.1 (2012), p. 013128. DOI: [10.1063/1.3690153](https://doi.org/10.1063/1.3690153).
- [97] Farazmand M and Haller G. “Attracting and repelling Lagrangian coherent structures from a single computation”. In: *Chaos: An Interdisciplinary Journal of Nonlinear Science* 23.2 (2013), p. 023101. DOI: [10.1063/1.4800210](https://doi.org/10.1063/1.4800210).
- [98] Mendoza C, Mancho A, and Wiggins S. “Lagrangian descriptors and the assessment of the predictive capacity of oceanic data sets”. In: *Nonlinear Processes in Geophysics* 21 (2014), pp. 677–689. DOI: [10.5194/npg-21-677-2014](https://doi.org/10.5194/npg-21-677-2014).
- [99] Ruiz-Herrera A. “Some examples related to the method of Lagrangian descriptors”. In: *Chaos: An Interdisciplinary Journal of Nonlinear Science* (2015). DOI: [10.1063/1.4922182](https://doi.org/10.1063/1.4922182).
- [100] Ruiz-Herrera A. “Performance of Lagrangian descriptors and their variants in incompressible flows”. In: *Chaos: An Interdisciplinary Journal of Nonlinear Science* (2016). DOI: [10.1063/1.4966176](https://doi.org/10.1063/1.4966176).
- [101] García Garrido V. *A tutorial on the method of Lagrangian descriptors*. Tech. rep. 2019, pp. 1–13. DOI: [10.6084/m9.figshare.11340818.v2](https://doi.org/10.6084/m9.figshare.11340818.v2).
- [102] Ros Roca X. *Computation of Lagrangian coherent structures with application to weak stability boundaries (MSc thesis)*. Politecnico di Milano, Milan, Italy, 2015.
- [103] Parkash AS. *Application of Lagrangian coherent structures to the computation and understanding of ballistic capture trajectories (MSc thesis)*. Delft University of Technology, Delft, Netherlands, 2019. URL: <http://resolver.tudelft.nl/uuid:23c04f74-ef77-4565-a29a-324bb861b2ba>.

- [104] Blazeviski D and Haller G. “Hyperbolic and elliptic transport barriers in three-dimensional unsteady flows”. In: *Physica D: Nonlinear Phenomena* 273 (2014), pp. 46–62. DOI: [10.1016/j.physd.2014.01.007](https://doi.org/10.1016/j.physd.2014.01.007).
- [105] Quinci A, Merisio G, and Topputo F. “Qualitative study of ballistic capture at Mars via Lagrangian descriptors”. In: *Communications in Nonlinear Science and Numerical Simulation* (-). Submitted on April 13, 2022. Under review.
- [106] Sousa Silva PA and Terra MO. “Diversity and validity of stable-unstable transitions in the algorithmic weak stability boundary”. In: *Celestial Mechanics and Dynamical Astronomy* 113.4 (2012), pp. 453–478. DOI: [10.1007/s10569-012-9418-y](https://doi.org/10.1007/s10569-012-9418-y).
- [107] Di Ruzza S, Pousse A, and Alessi EM. “On the co-orbital asteroids in the solar system: Medium-term timescale analysis of the quasi-coplanar objects”. In: *Icarus* 390 (2023), p. 115330. DOI: [10.1016/j.icarus.2022.115330](https://doi.org/10.1016/j.icarus.2022.115330).
- [108] Jones BA, Doostan A, and Born GH. “Nonlinear propagation of orbit uncertainty using non-intrusive polynomial chaos”. In: *Journal of Guidance, Control, and Dynamics* 36.2 (2013), pp. 430–444. DOI: [10.2514/1.57599](https://doi.org/10.2514/1.57599).
- [109] Giordano C. *Analysis, design, and optimization of robust trajectories for limited-capability small satellites (PhD thesis)*. Politecnico di Milano, Milan, Italy, 2021. URL: <http://hdl.handle.net/10589/177695>.
- [110] Bolle A and Circi C. “A hybrid, self-adjusting search algorithm for optimal space trajectory design”. In: *Advances in Space Research* 50.4 (2012), pp. 471–488. DOI: [10.1016/j.asr.2012.04.026](https://doi.org/10.1016/j.asr.2012.04.026).
- [111] Topputo F. “Fast numerical approximation of invariant manifolds in the circular restricted three-body problem”. In: *Communications in Nonlinear Science and Numerical Simulation* 32 (2016), pp. 89–98. DOI: [10.1016/j.cnsns.2015.08.004](https://doi.org/10.1016/j.cnsns.2015.08.004).
- [112] Dei Tos DA and Topputo F. “High-fidelity trajectory optimization with application to saddle-point transfers”. In: *Journal of Guidance, Control, and Dynamics* 42.6 (2019), pp. 1343–1352. DOI: [10.2514/1.g003838](https://doi.org/10.2514/1.g003838).
- [113] Armellin R and Topputo F. “A sixth-order accurate scheme for solving two-point boundary value problems in astrodynamics”. In: *Celestial Mechanics and Dynamical Astronomy* 96.3 (2006), pp. 289–309. DOI: [10.1007/s10569-006-9047-4](https://doi.org/10.1007/s10569-006-9047-4).
- [114] Dei Tos DA and Topputo F. “Trajectory refinement of three-body orbits in the real solar system model”. In: *Advances in Space Research* 59.8 (2017), pp. 2117–2132. DOI: [10.1016/j.asr.2017.01.039](https://doi.org/10.1016/j.asr.2017.01.039).

- [115] Mingotti G, Topputo F, and Bernelli-Zazzera F. “Transfers to distant periodic orbits around the Moon via their invariant manifolds”. In: *Acta Astronautica* 79 (2012), pp. 20–32. DOI: [10.1016/j.actaastro.2012.04.022](https://doi.org/10.1016/j.actaastro.2012.04.022).
- [116] Raffa S, Merisio G, et al. “Finding regions of bounded motion in binary asteroid environment using Lagrangian descriptors”. In: *Communications in Nonlinear Science and Numerical Simulation* (-). Submitted on March 14, 2022. Under review (2nd round).
- [117] Quinci A. *Qualitative study of ballistic capture at Mars via Lagrangian descriptors (MSc thesis)*. Politecnico di Milano, Milano, Italy, 2022. URL: <http://hdl.handle.net/10589/186116>.
- [118] Alessi EM and Pergola P. “Two options for the Callisto’s exploration”. In: *Acta Astronautica* 72 (2012), pp. 185–197. DOI: [10.1016/j.actaastro.2011.09.003](https://doi.org/10.1016/j.actaastro.2011.09.003).
- [119] Lee ETY. “Choosing nodes in parametric curve interpolation”. In: *Computer-Aided Design* 21.6 (1989), pp. 363–370. DOI: [10.1016/0010-4485\(89\)90003-1](https://doi.org/10.1016/0010-4485(89)90003-1).
- [120] Quarteroni A, Sacco R, and Saleri F. *Numerical mathematics*. Springer New York, 2007. DOI: [10.1007/b98885](https://doi.org/10.1007/b98885).
- [121] Alessi EM and Sánchez JP. “Semi-analytical approach for distant encounters in the spatial circular restricted three-body problem”. In: *Journal of Guidance, Control, and Dynamics* 39.2 (2016), pp. 351–359. DOI: [10.2514/1.G001237](https://doi.org/10.2514/1.G001237).
- [122] Swinbank R and Purser RJ. “Fibonacci grids: A novel approach to global modelling”. In: *Quarterly Journal of the Royal Meteorological Society: A journal of the atmospheric sciences, applied meteorology and physical oceanography* 132.619 (2006), pp. 1769–1793. DOI: [10.1256/qj.05.227](https://doi.org/10.1256/qj.05.227).
- [123] Hull TE, Enright WH, Fellen BM, and Sedgwick AE. “Comparing numerical methods for ordinary differential equations”. In: *SIAM Journal on Numerical Analysis* 9.4 (1972), pp. 603–637. DOI: [10.1137/0709052](https://doi.org/10.1137/0709052).
- [124] Verner JH. “Numerically optimal Runge–Kutta pairs with interpolants”. In: *Numerical Algorithms* 53.2 (2010), pp. 383–396. DOI: [10.1007/s11075-009-9290-3](https://doi.org/10.1007/s11075-009-9290-3).
- [125] Dowell M and Jarratt P. “A modified regula falsi method for computing the root of an equation”. In: *BIT Numerical Mathematics* 11.2 (1971), pp. 168–174. DOI: [10.1007/bf01934364](https://doi.org/10.1007/bf01934364).
- [126] Dormand JR and Prince PJ. “A family of embedded Runge–Kutta formulae”. In: *Journal of computational and applied mathematics* 6.1 (1980), pp. 19–26. DOI: [10.1016/0771-050x\(80\)90013-3](https://doi.org/10.1016/0771-050x(80)90013-3).

- [127] Hughes SP, Qureshi RH, Cooley SD, and Parker JJ. "Verification and validation of the general mission analysis tool (GMAT)". In: *AIAA/AAS astrodynamics specialist conference*. 2014, p. 4151. DOI: [10.2514/6.2014-4151](https://doi.org/10.2514/6.2014-4151).
- [128] Hughes SP. "General Mission Analysis Tool (GMAT)". In: *6th International Conference on Astrodynamics Tools and Techniques (ICATT)*. 2016.
- [129] Scheeres D, Rosengren A, and McMahon J. "The dynamics of high area-to-mass ratio objects in earth orbit: The effect of solar radiation pressure". In: *Proceedings of the AAS/AIAA Space Flight Mechanics Meeting, number AAS*. 2011, pp. 11–178.
- [130] Buratti BJ, Choukroun M, and Bauer JM. "The low albedo of comets". In: *AGU Fall Meeting Abstracts*. 2016, P43A–2083.
- [131] Britt DT, Consolmagno GJ, and Merline WJ. "Small body density and porosity: New data, new insights". In: *37th Annual Lunar and Planetary Science Conference*. 2006, p. 2214.
- [132] Barbee BW and Chodas PW. "Near-Earth asteroids 2006 RH120 and 2009 BD: Proxies for maximally accessible objects?" In: *2015 AAS/AIAA Astrodynamics Specialist Conference*. 2015.
- [133] Binzel RP, Lupishko DF, Di Martino M, Whiteley RJ, and Hahn GJ. "Physical properties of near-Earth objects". In: *Asteroids III* 255.271 (2002).
- [134] Kwiatkowski T et al. "Photometry of 2006 RH120: An asteroid temporarily captured into a geocentric orbit". In: *Astronomy & Astrophysics* 495.3 (2009), pp. 967–974. DOI: [10.1051/0004-6361:200810965](https://doi.org/10.1051/0004-6361:200810965).
- [135] Krasinsky GA, Pitjeva EV, Vasilyev MV, and Yagudina E. "Hidden mass in the asteroid belt". In: *Icarus* 158.1 (2002), pp. 98–105. DOI: [10.1006/icar.2002.6837](https://doi.org/10.1006/icar.2002.6837).
- [136] Naidu SP et al. "Preccovery observations confirm the capture time of asteroid 2020 CD3 as Earth's minimoon". In: *The Astrophysical Journal Letters* 913.1 (2021), p. L6. DOI: [10.1016/j.icarus.2015.05.032](https://doi.org/10.1016/j.icarus.2015.05.032).
- [137] Bolin BT et al. "Characterization of temporarily captured minimoon 2020 CD3 by Keck time-resolved spectrophotometry". In: *The Astrophysical Journal Letters* 900.2 (2020), p. L45. DOI: [10.3847/2041-8213/abae69](https://doi.org/10.3847/2041-8213/abae69).
- [138] Folkner WM, Williams JG, Boggs DH, Park RS, and Kuchynka P. *The planetary and lunar ephemerides DE430 and DE431*. Interplanetary Network Progress Report, 196(1).

List of figures

1.1	Fleets of miniaturized probes	2
1.2	Overview of the EXTREMA project objectives and structure	4
1.3	Earth–Mars low-thrust transfer culminating in ballistic capture at Mars	5
1.4	Temporal distribution of detected lunar impacts of LUMIO lunar CubeSat	8
1.5	LUMIO lunar CubeSat scientific return	8
1.6	Forward LD scalar field in the spatial perturbed BER4BP	9
1.7	Levels of LD in the perturbed BER4BP	9
2.1	Contributions of individual terms in Eq. (2.1)	18
2.2	Poincaré map \mathcal{P}	22
2.3	Material surfaces $\mathcal{M}(t)$	23
3.1	Illustration of particle stability	27
3.2	Sets relations according to the algorithmic definition of WSB	28
3.3	Capture sets \mathcal{C}_{-1}^1 and \mathcal{C}_{-1}^6 inspected against solar gravity gradient . .	29
3.4	\mathcal{C}_{-1}^1 trajectory inspected against the solar gravity gradient	30
3.5	Qualitative and quantitative indexes of ten \mathcal{C}_{-1}^6 capture sets	33
3.6	Capture sets \mathcal{C}_{-1}^6	34
4.1	Attracting and repelling LCSs	38
4.2	Qualitative behavior of two example points straddling a stable manifold	40
4.3	Advection map	41
4.4	The role of coherent structures	42
5.1	Illustration of BCC definitions	49
5.2	Capture set \mathcal{C}_{-1}^2	52
5.3	Capture set \mathcal{C}_{-1}^6	53
5.4	BCCs from t_0 to t_0-600 days	54
5.5	Trends of heliocentric osculating elements of BCCs	56
5.6	Rates of heliocentric osculating elements for BCCs	57
5.7	Time snapshot at t_0-600 days of $\check{\mathcal{B}}_{-1}^2$	58
5.8	Time snapshot at t_0-600 days of $\check{\mathcal{B}}_{-1}^6$	59
5.9	Detail of capture set \mathcal{C}_{-1}^6	61
5.10	Subcorridor envelope $\partial\check{\mathcal{S}}_{-1}^6$	62

5.11	Views subcorridor envelope $\partial\check{\mathcal{S}}_{-1}^6$ far from Mars	63
5.12	Views subcorridor envelope $\partial\check{\mathcal{S}}_{-1}^6$ at a closer range from Mars	64
5.13	Poincaré sections of subcorridor $\check{\mathcal{S}}_{-1}^6$	66
6.1	ABC algorithm flowchart	70
6.2	ABC algorithm on-ground tasks	71
6.3	ABC algorithm onboard tasks	72
7.1	Correction of capture orbit	76
7.2	Representation of flow expansion.	77
7.3	Capture sets at epoch t_0^*	87
7.4	Baseline BC orbits at capture epoch t_0^*	88
7.5	Families of BC orbits	90
7.6	Families of BC orbits – Magnifications	91
7.7	BC orbits at peculiar capture epochs	92
7.8	Distance from Mars of BC orbit families	93
7.9	Keplerian energy with respect to Mars of BC orbit families	94
7.10	Capture sets inspected against solar gravity gradient	95
7.11	Families of BC orbits inspected against solar gravity gradient	96
8.1	Energy-based LD field $\mathcal{M}_g(\tau_{-1}, \tau_6)$, finite horizon $\sim \mathcal{C}_{-1}^6$, $\xi_0\eta_0$ -plane.	102
8.2	Energy-based LD field $\mathcal{M}_g(\tau_{-1}, \tau_6)$, finite horizon $\sim \mathcal{C}_{-1}^6$, $\omega_0 r_{p0}$ -plane	103
8.3	Study of 1-dimensional LD sections	106
8.4	Study of 1-dimensional LD sections for astrodynamics based integrands	107
8.5	Inspection of energy-based LD against subsets \mathcal{W} , \mathcal{X} , \mathcal{K} , \mathcal{D} , and \mathcal{C}	108
8.6	Stationary points ω_0^* at various pericenter radii r_{p0}	110
8.7	Backbone	111
8.8	Analysis of backbone performance	114
8.9	Views backbone subcorridor $\check{\mathcal{S}}_{-1}^5$ far from Mars	115
8.10	Views backbone subcorridor $\check{\mathcal{S}}_{-1}^5$ at a closer range from Mars	116
9.1	Subcorridor $\check{\mathcal{S}}_{-1}^6$ parametric surfaces	123
9.2	Errors of synthetic subcorridor $\check{\mathcal{S}}_{-1}^6$	124
A.1	Test plan 1 errors of my_ode78	133
A.2	Test plan 1 errors of ode78	134
A.3	Test plan 1 errors of ode89	134
A.4	Test plan 1 errors of ode113	135
A.5	Test plan 2 errors of my_ode78	135
A.6	Test plan 2 errors of ode78	136
A.7	Test plan 2 errors of ode89	137
A.8	Test plan 2 errors of ode113	137
A.9	Test plan 3 errors of my_ode78	138
A.10	Test plan 3 errors of ode78	138
A.11	Test plan 3 errors of ode89	139

A.12 Test plan 3 errors of <code>ode113</code>	139
A.13 Function evaluations comparison	141
A.14 Single call times comparison	141
A.15 Errors comparison	142
A.16 The ten trajectories numerically propagated in GMAT	147
A.17 Position error of GRATIS against GMAT	149
A.18 Velocity error of GRATIS against GMAT	150
A.19 Trajectory comparison for Siding Spring comet benchmark	153
A.20 Trajectory comparison for Siding Spring comet benchmark, xy -plane .	154
A.21 Position and velocity errors for Siding Spring comet benchmark	154
A.22 Trajectory comparison for 2006 RH ₁₂₀ benchmark	157
A.23 Trajectory comparison for 2006 RH ₁₂₀ benchmark, plane views	158
A.24 Position and velocity errors for 2006 RH ₁₂₀ benchmark	159
A.25 2020 CD ₃ distance from Earth	161
A.26 Trajectory comparison for 2020 CD ₃ benchmark	162
A.27 Trajectory comparison for 2020 CD ₃ benchmark, xy -plane	163
A.28 Trajectory comparison for 2020 CD ₃ benchmark, magnification	163
A.29 Trajectory comparison for 2020 CD ₃ benchmark, magnification xy -plane	164
A.30 Position and velocity errors for 2020 CD ₃ benchmark	164
A.31 Stable and capture sets at Mercury	166
A.32 Sample solution at Mercury	167
A.33 IC characterized by minimum regularity index S_{\min} at Mercury	167
A.34 Stable and capture sets at Europa	168
A.35 Sample solution at Europa	168
A.36 IC characterized by minimum regularity index S_{\min} at Europa	169
A.37 Stable and capture sets at Earth	170
A.38 Sample solution at Earth	170
A.39 IC characterized by minimum regularity index S_{\min} at Earth	171

List of tables

2.1	Spacecraft parameters for SRP evaluation	17
2.2	Nondimensionalization units	24
4.1	Class of LDs with integrand and used norm	44
4.2	LCS-like methods trade-off	46
5.1	Positions of center in Poincaré sections	67
5.2	Velocities of center in Poincaré sections	67
5.3	Time epochs intervals Δt_c at which center crosses Poincaré sections .	67
8.1	Finite horizons	101
8.2	Stationary points of backbone	112
8.3	Backbone performance	113
A.1	Ten ICs generated randomly in GMAT	144
A.2	Bounds of ICs generated in GMAT	145
A.3	Spacecraft SRP parameters generated randomly in GMAT	146
A.4	Bounds of SRP spacecraft parameters generated in GMAT	146
A.5	ICs numerically propagated in GRATIS	148
A.6	Position and velocity errors of GRATIS against GMAT	150
A.7	IC of Siding Spring comet (C/2013 A1)	151
A.8	Position and velocity errors for Siding Spring comet benchmark	153
A.9	IC of 2006 RH ₁₂₀	155
A.10	Position and velocity errors for 2006 RH ₁₂₀ benchmark	156
A.11	IC of 2020 CD ₃	160
A.12	Position and velocity errors for 2020 CD ₃ benchmark	162

List of algorithms

7.1	Generation of BC orbit family	85
8.1	Backbone construction	104
9.1	Synthesis of BCC	120
9.2	Evaluation of synthetic BCC	121

List of acronyms

3PBVP three-point boundary value problem.

ABC autonomous ballistic capture.

ABM Adams–Bashforth–Moulton.

ASI Agenzia Spaziale Italiana.

BC ballistic capture.

BCC ballistic capture corridor.

BER4BP bi-elliptic restricted 4-body problem.

BME body mean equator of date frame.

CGST Cauchy–Green strain tensor.

CNES Centre National d'Études Spatiales.

CR3BP circular restricted three-body problem.

DA differential algebra.

DART Deep-space Astrodynamics Research & Technology.

DOPRI8 Dormand–Prince 8th-order embedded Runge–Kutta.

DRO distant retrograde orbit.

ECSS European Cooperation for Space Standardization.

EoM Equations of motion.

ER3BP elliptic restricted three-body problem.

ERC European Research Council.

ESA European Space Agency.

ESH EXTREMA simulation hub.

FLI fast Lyapunov indicator.

FTLE finite-time Lyapunov exponent.

- GMAT** General Mission Analysis Tool.
GNC guidance, navigation, and control.
GRATIS GRavity Tidal Slide.
GSTP General Support Technology Programme.
- IC** initial condition.
ICRF International Celestial Reference Frame.
- JAXA** Japan Aerospace Exploration Agency.
JPL Jet Propulsion Laboratory.
- LCS** Lagrangian coherent structure.
LD Lagrangian descriptor.
LSK leap seconds kernel.
LUMIO Lunar Meteoroid Impacts Observer.
- MEGNO** mean exponential growth factor of nearby orbits.
MMX Martian Moons eXploration.
- NAIF** Navigation and Ancillary Information Facility.
NASA National Aeronautics and Space Administration.
NEA near-Earth asteroid.
NEO near-Earth object.
NSG non-spherical gravity.
- ORQ** operational research question.
- PCE** polynomial chaos expansion.
PCK planetary constant kernel.
PDE partial differential equation.
PECE predictor-corrector.
PhD Philosophiæ Doctor.
- R&T** Research and Technology.
RAAN right ascension of the ascending node.
RHS right-hand side.
RK Runge–Kutta.
RO research objective.
RPF roto-pulsating frame.
RQ research question.
RSS root sum square.
RTN@ t_i radial-tangential-normal of date frame.
- SOI** sphere of influence.
SPK spacecraft ephemeris kernel.
SRP solar radiation pressure.

SSTO Sun-synchronous terminator orbit.

STM state transition matrix.

V&V verification and validation.

VSVO variable-step, variable-order.

WSB weak stability boundary.

Colophon

This manuscript was typeset in \LaTeX . The style was inspired by Dr. D. A. DeiTos's doctoral dissertation *Trajectory Optimization of Limited Control Authority Spacecraft in High-Fidelity Models* (2017).